1-1-2016

Neural Circuitry Deficits Associated With Dysfunctional Myelin

Kathleen June Maheras
Wayne State University,

NEURAL CIRCUITRY DEFICITS ASSOCIATED WITH MYELIN DYSFUNCTION

by

KATHLEEN JUNE MAHERAS

DISSERTATION

Submitted to the Graduate School

of Wayne State University,

Detroit, Michigan

in partial fulfillment of the requirements

for the degree of

DOCTOR OF PHILOSOPHY

2015

MAJOR: MOLECULAR BIOLOGY AND GENETICS

Approved By:

_____

Advisor Date

_____

_____

_____

DEDICATION

This work is dedicated to my family who offered their unconditional love and encouragement throughout my graduate work. From the bottom of my heart, thank you!

ACKNOWLEDGEMENTS

I wish to express my sincere gratitude to my dissertation advisor, Dr Alexander Gow. His continual guidance and relentless hard work have inspired and shaped the independent scientist I have become.

TABLE OF CONTENTS

LIST OF TABLES

LIST OF FIGURES

CHAPTER 1 – INTRODUCTION

Six hundred million years ago, the first multicellular organisms, the earliest metazoans, evolved from their unicellular ancestors, the colonial flagellate eukaryotes. Development of multicellularity was attained when unicellular organisms began to stick together, work together, and specialize. The presence of intercellular junctions partitioned the new multicellular organism, generating internal compartments. Each newly created compartment would further evolve a unique composition benefitting the organism, allowing it to adapt to different environments, and evolve into more complex species. Intercellular junctions contribute to the ascension, diversification, and transformation of unicellular organisms into the diverse animal kingdom.

The primary purpose of early intercellular junctions in metazoans was to protect the organism from the external environment. As multicellular organisms increased in complexity, intercellular junctions developed specialized functions, while retaining their most basic function of forming a barrier. Today, intercellular junctions have evolved to adhere cells together, preserve structural integrity, allow remodeling to occur in changing environments, and permit passage of select molecules. Three main categories of intercellular junctions have evolved: adherens, gap, and tight junctions.

Diversity of intercellular junctions permits functional specialization

Intercellular junctions, which are of four major categories, function to maintain a physical association between cells, allow intercellular communication, and participate in tissue organization. The first type of intercellular junction, the adherens

junction, molds the shape of multicellular structures by indirectly linking their actin cytoskeletons. All intercellular junctions are comprised of three basic structural proteins: integral membrane proteins, cytoplasmic proteins, and cytoskeletal proteins. The integral proteins of adherens junctions are largely comprised of the cadherin family of type-1 transmembrane proteins (Yoshida and Takeichi, 1982; Yoshida-Noro et al., 1984). The extracellular domains of cadherins interact with either *trans* (opposing) or *cis* (neighboring) cadherins forming dimers or tetramers. The cytoplasmic domains of cadherins bind to members of the catenin family of cytoplasmic proteins. These protein complexes are anchored to actin filaments, thereby stabilizing the junction in the membrane.

The second category of adhesive junction is the desmosome, which provides focal mechanical strength to epithelial and endothelial cell layers by attaching the plasma membrane to intermediate filaments. Desmosomes are comprised of cadherins and integral membrane proteins known as desmogleins and desmocollins (Buxton et al., 1993; Holton et al., 1990; Koch et al., 1990). These single-pass transmembrane proteins interact in *trans* with neighboring desmogleins and desmocollins at their extracellular domains. The cytoplasmic domains bind to anchoring proteins such as plakoglobin, plakophilin, or desmoplakin, which in turn are bound to intermediate filaments. While desmosomes function to adhere two cells together, hemidesmosomes anchor each cell to the basement membrane or extracellular matrix (Borradori and Sonnenberg, 1999).

Gap junctions are the third type of intercellular junctions that interact in *trans* to form channels between cells and permit direct cell-to-cell communication. These

junctions are comprised of the connexin family of polytopic four transmembrane domain proteins. Connexins interact in *cis* to form hexamers known as connexons. Opposing connexons form the characteristic gap junction, allowing small metabolites and water to freely pass, thereby coupling the cells chemically and electrically (Alberts et al., 2008).

The hypotheses developed and examined within this dissertation work revolve around the function of tight junctions, which are the final category of intercellular junctions. Tight junctions were first observed in the 1960s and form circumferential bands between plasma membranes of apposing cells by interactions in *trans* that focally fuse the cell membranes and eliminate the paracellular space (Farquhar and Palade, 1963). Tight junctions are permeable to water and selectively permeable to ions but otherwise seal the extracellular spaces between cells and serve to generate two compartments, the contents of which can be independently regulated (Angelow and Yu, 2007; Furuse and Tsukita, 2006; Van Itallie and Anderson, 2004, 2006). Tight junctions are the principal component for establishing and maintaining the apical and basolateral domains of polarized epithelial and endothelial cell layers (Mugnaini and Schnapp, 1974; Shin et al., 2006). In addition to the archival tight junctions between apposing cells, which are known as heterotypic junctions, autotypic tight junctions are found between bilayers of a single cell such as the membrane sheaths of myelinating cells in the central and peripheral nervous systems (Dermietzel, 1974; Tetzlaff, 1978). The functional characterization of autotypic tight junctions in CNS myelin sheaths is the foundation for this dissertation work.

Claudins constitute the principal integral membrane protein of tight junctions

Probing cultured rat fibroblasts, cardiac muscle, and epithelial cells from small intestine and liver identified a candidate integral membrane protein of tight junctions. The probe was comprised of a fusion protein containing cDNA of zonula occludens (ZO-1). The ZO family of proteins comprises a major component of the cytoplasmic proteins of tight junctions (Itoh et al., 1993). The fusion protein interacted with a novel 65 kDa transmembrane protein designated occludin. Using immunoelectron microscopy and freeze-fracture replica electron microscopy, occludin was localized at tight junctions in epithelial and endothelial cells (Fujimoto, 1995; Furuse et al., 1993). Transfection studies demonstrated that newly synthesized chick occludin can be delivered and incorporated into existing human and bovine epithelial cell tight junctions (Furuse et al., 1994) and increased transepithelial resistance (McCarthy et al., 1996). However, knockout studies in mice show that occludin is not the main integral membrane protein of tight junctions (Gow et al., 1999; Morita et al., 1999b).

Two key experiments extensively investigating the function of occludin refuted the hypothesis that occludin is necessary for tight junction formation. First, when peptides raised against occludin were transfected into epithelial cells, occludin was excluded from tight junction strands. Interestingly, epithelial cell morphology remained unaltered (Wong and Gumbiner, 1997). Second, deletion of the occludin gene by homologous recombination in embryonic stem cells yielded a mouse with morphological normal tight junctions in many tissues (Saitou et al., 1998). Reassessing the original cell fraction in which occludin was identified, Furuse et al. (1998) discovered a novel 22 kDa protein. When sequenced, the putative

transmembrane protein had disparate sequence to occludin and was designated claudin (Cldn), from the Latin word 'to close.' This protein was quickly found to be a member of a large family of proteins with broad and overlapping expression patterns in polarized cells (Fanning et al., 1998; Furuse et al., 1998; Morita et al., 1999a; Morita et al., 1999c; Simon et al., 1999).

The claudin family of proteins has increased to at least 24 members in mammals with similar structures, divergent sequences, and hallmark conserved elements (Angelow et al., 2008; Furuse and Tsukita, 2006; Van Itallie and Anderson, 2006). Claudins are polytopic membrane proteins consisting of four transmembrane domains with amino and carboxyl termini both located in the cytoplasm and two extracellular domains. Conserved features include a GLWxxC (8 – 10 aa) motif within the first cytoplasmic domain and a PSD95 / Dlgs1 / ZO-1 (PDZ) domain near the carboxyl-terminus for binding the cytoplasmic tight junction proteins: ZO-1, -2, and -3.

The expression of claudins is essential for tight junction function, whereas occludin is considered an accessory protein (reviewed in Alberts et al., 2008; Nelson and Fuchs, 2010). Evaluation of genetic knockout or mutations reiterates the indispensible function of claudin family members, *in vivo*, for tight junction formation (reviewed in Furuse, 2009). The loss of Cldn1 leads to an epidermal barrier deficit resulting in water loss and neonate death (Furuse et al., 2002); altered ionic permeability and subsequent hair cell degeneration and congenital deafness arise from to the loss of Cldn14 (Ben-Yosef et al., 2003; Wilcox et al., 2001); the absence of Cldn15 in produces megaintestine (Tamura et al., 2008); loss of Cldn16

(paracelllin-1) results in hypomagnesaemia, hypercalciuria and nephrocalcinosis (Weber et al., 2000); and finally, renal magnesium wasting and renal failure are seen in the absence of Cldn 19 (Konrad et al., 2006). The first claudin shown to demonstrate dysfunction of tight junction in several tissues, Cldn11, is the primary focus of this dissertation work.

Functional role of Claudin 11 homotypic tight junctions

Claudin11 forms parallel tight junction strands in several tissues including Sertoli cells of the testis, basal cells of the stria vascularis, and CNS myelin sheaths (Bronstein et al., 1997; Gow et al., 2004; Gow et al., 1999; Kitajiri et al., 2004; Morita et al., 1999b). Functional analyses assessing the role of Cldn11 tight junctions has been simplified by the tendency for Cldn11 to form single claudin tight junctions (Gow et al., 1999).

Studies exploring the function of Cldn11 tight junctions were first completed in Sertoli cells of the testis. The loss of Cldn11 results in disappearance of the characteristic parallel tight junction intramembranous strands, hypogonadism and azoospermia (Gow et al., 1999). Arrested spermatogenesis and abnormal morphology of seminiferous tubules were excluded as the source for male sterility; instead, the phenotype originates from disruption of the tightly controlled blood-testis barrier, causing early spermatocyte death (Gow et al., 1999).

Within the inner ear, Cldn11 expression is restricted to basal cells of the stria vascularis (Gow et al., 2004; Kitajiri et al., 2004). Claudin11 knockout (*Cldn11*$^{-/-}$) mice were characterized to elucidate the function of tight junctions on audition. *Cldn11*$^{-/-}$ mice lack an endocochlear potential with minimal disruption to potassium

ion homeostasis in the endolymph or perilymph. Morphometric analyses reveal mice have normal inner ear cellular morphology, inner and outer hair cell organization, and a normal compliment of spiral ganglion neurons. Psychoacoustic analysis confirmed the critical function of the endocochlear potential on hearing sensitivity and demonstrates that *Cldn11*$^{-/-}$ mice have increased hearing thresholds to approximately 70 dB SPL by six weeks of age (Gow et al., 2004).

Structure and composition of CNS myelin membrane

The dissertation work herein centers on the function of Cldn11 tight junctions within CNS myelin sheaths. Pre-myelinating oligodendrocytes extend numerous processes that contact nearby axons, expand into large trapezoid membrane sheets, and wrap segments of the axons in multiple layers (Figure 1.1A). Initially these sheets contain cytoplasm (Figure 1.1A, light grey), which is extruded during membrane compaction and confined to an outer channel (Figure 1.1A, dark grey). The asymmetric trapezoid shape of the flattened myelin sheath generates distinct compartments once myelination compaction has occurred (Figure1.1C). At the lateral edges, membrane loops containing the cytoplasm comprise the paranodal region. The compact myelin region, known as the internode, spans from paranode to paranode (Figure 1.1A, dark grey). Lastly, unmyelinated segments between myelin sheaths are known as nodes of Ranvier at which voltage-gated Na^+ channels are localized to propagate action potentials (Figure1.1C).

Myelin sheaths are an extension of the plasma membrane of oligodendrocytes. The composition of myelin is 40 % water; the dry mass is comprised of 70 % lipids and cholesterol and 30 % protein, more than half of which

is proteolipid protein (PLP) (Folch and Lees, 1951). The function of PLP within the myelin membrane remains unknown, however it is thought to involve adhesion and stabilization of compact myelin (Boison et al., 1995; Boison and Stoffel, 1994; Greer and Lees, 2002). Myelin basic protein (MBP), accounts for 30 % of total myelin protein, is localized to the major dense line (MDL) observed in transmission electron micrographs of compact myelin and is thought to stabilize opposing membrane layers (Omlin et al., 1982). The MDL is formed from the cytoplasmic faces of apposing plasma membranes. The two external surfaces of the plasma membrane form the minor dense line, or intraperiod line (IPL) in electron micrographs. The protein with the third largest concentration in CNS myelin is Cldn11, comprises 7 % of total protein. As extensively described above, Cldn11 forms autotypic in myelin and comprises the diffusion barrier that forms the intramyelinic compartment (Figure 1.1, red) (Gow et al., 1999; Morita et al., 1999b). Remaining minor protein components include 2',3'-Cyclic Nucleotide 3' Phosphodiesterase (CNP), myelin associated glycoprotein (MAG), myelin oligodendrocyte basic protein (MOBP), myelin oligodendrocyte glycoprotein (MOG), Nogo (Chen et al., 2000), OMGP, Sirtuin 2 (SirT2), and stathmin.

Claudin 11 tight junctions in CNS myelin

For half a century, myelin tight junction were known morphologically as the radial component which appears as rod-like thickenings within the intraperiod lines (IPLs) of compact myelin has been documented from transmission and freeze fracture electron microscopy (Peters, 1961, 1964; Reale et al., 1975; Staehelin, 1974; Tabira et al., 1978). Recently, Cldn11 was confirmed to comprise the only

Figure 1.1 – Schematic illustrating key features of the myelin membrane

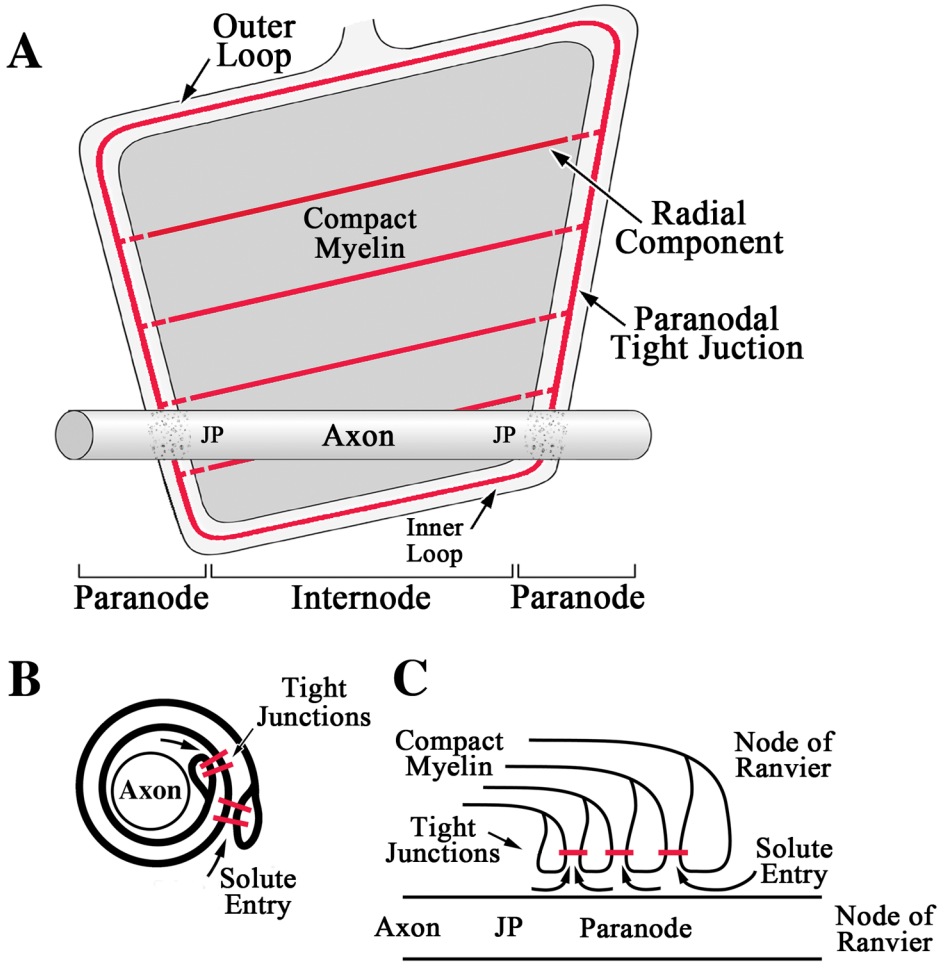

(A) A CNS myelin sheath is unraveled revealing the structure and organization of the multilayered myelin membrane. Myelin begins as a flat trapezoid sheet filled with cytoplasm extruded to an outer channel along the perimeter upon maturation and compaction. **(B)** Cross section through the internode showing myelin wraps, paranodal loops, and Cldn11 tight junctions (red) forming the electrically tight barrier between successive layers of myelin. **(C)** Location of membrane domains on the axon are also shown: node of Ranvier, paranodal myelin, juxtaparanodal region (JP), and the remaining axon internode (Axon) The location of Cldn11 tight junctions are indicated in red. This figure was modified and reprinted with permission from the corresponding author (Gow, 2008)

family member in the radial component (Gow et al., 1999). Claudin 11 tight junctions are also present in the paranode, forming a continuous barrier between apposing layers of myelin membrane. Elimination of Cldn11 in CNS myelin has revealed the contribution of tight junctions to myelin sheath function.

Ultrastructural analyses indicate that the absence of Cldn11 tight junctions neither perturbs compaction and thickness of myelin sheaths, nor disrupts axoglial junctions. Phenotypic assessment reveals a slight tremor which does not arise from neuronal loss or axonal degeneration (Gow et al., 1999). Interestingly, an increase in latency of the visual evoked potentials (VEPs) from *Cldn11*$^{-/-}$ mice suggests slowed conduction velocity (Michaelson et al., 1996; Strain and Tedford, 1993). These findings recapitulate more recent studies in the auditory pathway.

The loss of Cldn11 in the stria vascularis of the cochlea accounts for the observable increase in hearing threshold, however the well-differentiated waveforms of the auditory brainstem response (ABR) suggest overall preservation of the auditory pathway with dysfunction being limited to a delay in the latency of Wave V latency. Wave V latency is a commonly used proxy for conduction velocity along central myelinated fibers of the auditory pathway (Gow et al., 2004). Thus the ABR data suggest slowed conduction in the auditory brainstem, data from visual and auditory pathways demonstrate global dysfunction of myelinated axons within the CNS of *Cldn11*$^{-/-}$ mice.

Function of CNS myelin

The high lipid and low water content of myelin generates a high resistance / low capacitance structure that insulates axons. During axon depolarization, the

electrically tight myelin membrane reduces current leakage into the compact myelin region, restricting depolarization events to the nodes of Ranvier. Electrical signals propagate from node to node, depolarizing the axonal membrane at these regions compared to the entire axonal length in a process known as saltatory conduction. Conduction velocity along myelinated fibers is proportional to the axonal diameter, unlike unmyelinated axons, for which conduction velocity is proportional to the square root of the diameter. The influence myelin has on conduction velocity is functionally equivalent to increasing axonal thickness by100 (Kandel et al., 2000).

The passive properties of neurons, tau (time constant) and lambda (length constant), specify action potential propagation. Lambda is the critical component determining the distance along an axon a depolarizing event can travel and still trigger a subsequent depolarizing event. Lambda is thought of as a safety factor specifying the integrity of conduction along an axon in the absence of internodes or presence of dysfunctional internode segments. If lambda is smaller than the distance between myelin internodes, signal propagation becomes impaired. This consequence is commonly seen in multiple sclerosis (MS) when demyelination leads to the absence of several internodes along an axon, reducing action potential propagation.

The time constant, tau, is the calculated time it takes the membrane potential of a neuron to reach 63 % of its steady state value. Tau regulates temporal summation by dictating the time course of synaptic potentials. A shorter tau represents a quicker change in membrane potential resulting from a stimulus. Additionally, a shorter tau increases the likelihood that two consecutive inputs will

summate and depolarize the cell membrane enough to fire an action potential (Kandel et al., 2000).

Function of Claudin 11 tight junctions in CNS myelin membrane

Initial hypotheses from several studies posited that Cldn11 tight junctions in CNS myelin stabilize the myelin membrane and generate an immune privileged compartment (Mugnaini and Schnapp, 1974; Tabira et al., 1978). These hypotheses have proved untenable, and more recent data indicate that Cldn11 tight junctions preserve electrochemical gradients in similar fashion to epithelia (Devaux and Gow, 2008; Gow et al., 2004; Kitajiri et al., 2004). Noteworthy electrophysiology experiments conducted in *Cldn11*$^{-/-}$ mice established the mechanism by which Cldn11 tight junctions function in CNS myelin (Devaux and Gow, 2008; Gow et al., 2004; Gow and Devaux, 2008).

Slowed conduction velocity in the visual and auditory pathways has been demonstrated in *Cldn11*$^{-/-}$ mice (Gow et al., 2004; Gow et al., 1999; Kitajiri et al., 2004). Compound action potentials (CAPs) measuring electrical potential from *ex vivo* optic nerves of *Cldn11*$^{+/+}$ and *Cldn11*$^{-/-}$ mice demonstrate the loss of tight junctions significantly impacts CAP velocities along myelinated fibers (Figure 1.2) (Devaux and Gow, 2008). Three components of the CAP are visible, corresponding to large (1st), medium (2nd), and small (3rd) diameter fibers, respectively. The onset delay in medium and small diameter fibers is unmistakable in *Cldn11*$^{-/-}$ mice compared to controls, with significant reductions in conduction velocity of 20 and 50 %, respectively. Axon diameters of the medium and small components were estimated to be approximately 1.2 and 0.7 μm. Conduction velocity along large

diameter fibers, estimated at > 2 μm, are not significantly impacted (Devaux and Gow, 2008).

The absence of Cldn11 tight junctions does not alter the ultrastructure of myelin sheaths except for the absence of radial components. Detailed analyses reveal myelin thickness, compaction, and internode length are preserved. The distribution of voltage-gated ion channels within nodes, or underneath the myelin sheaths remain normal (Devaux and Gow, 2008). In view of this preservation of architecture, a novel computational model was developed to describe conduction along small diameter myelinated fibers, accounting for the critical contribution of tight junctions within the myelin membrane.

Early computational models describing saltatory conduction in myelinated fibers are depicted as a double-cable circuit comprised of resistors (longitudinal component of the fiber) and capacitors (axonal surface) (Brill et al., 1977; Halter and Clark, 1991; Hartline and Colman, 2007; Waxman and Bennett, 1972). These models were simple and predominantly based on large diameter myelinated axons of the peripheral nervous system (PNS), rather than the vast number of small diameter myelinated fibers of the CNS (Blight, 1985). Compared to such double cable models (DCM) (Halter and Clark, 1991; McIntyre et al., 2002), the revised tight junction model (TJM), specifies tight junctions as a series resistance with myelin membrane to reduce capacitive charging of the membrane. Scaling the DCM to the electrophysiological and morphological dimensions of optic nerve axons does not yield a conducting model. However, the addition of tight junctions in the TJM better reflects the experimental data obtained. This finding suggests that tight junctions

Figure 1.2 – Compound action potentials from *Cldn11*$^{-/-}$ mice indicate slowed conduction velocity in small diameter fibers

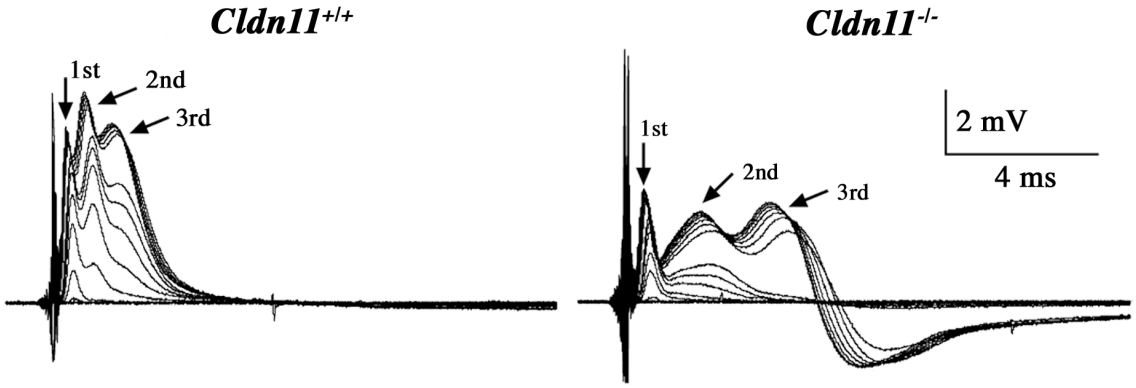

Representative compound action potentials (CAPs) collected from isolated optic nerves in *Cldn11*$^{+/+}$ and *Cldn11*$^{-/-}$ mice showing three components (arrows) elicited by square voltage pulses with varied amplitudes. The components correspond to large, medium, and small diameter axons, respectively, within the optic nerve fiber bundles. This figure was modified and reprinted with permission from the corresponding author (Devaux and Gow, 2008).

play an important role in action potential propagation for small diameter fibers (Devaux and Gow, 2008; Gow and Devaux, 2008).

Small diameter myelinated fibers are found throughout the brain, especially in grey matter regions (Aboitiz et al., 1992). The majority of neural circuits require signal information integration via small myelinated fibers, from multiple sensory modalities, as well as refinement from feed forward / back networks. If slowed conduction velocity occurs along these fibers, errors in information processing and synchrony will likely arise and may lead to the development of behavioral abnormalities. The disconnection hypothesis discussed in Chapter 2 is consistent with disrupted communication along small diameter myelinated fibers as an etiology of cognitive disease.

Cognitive diseases such as Schizophrenia (SZ) are thought to originate from altered neural connectivity and disconnection of brain regions (Benes, 2000; Friston, 1999; Nuechterlein and Dawson, 1984). Reduced in white matter volume and integrity are apparent from functional magnetic resonance imaging (fMRI) and diffusion tensor imaging (DTI) scans, and in molecular analyses of post mortem tissue (Camchong et al., 2011; Davis et al., 2003; Flynn et al., 2003; Lawrie and Abukmeil, 1998). Surprisingly, reduced myelin protein and gene transcripts are the most prominent changes detected in post mortem patients (Haroutunian et al., 2007; Katsel et al., 2005; McCullumsmith et al., 2007; Tkachev et al., 2003). Not surprisingly, many symptoms plaguing SZ patients are common in other neurological disorders (Davis et al., 2003; Denier et al., 2007; Feinstein et al., 1992; Kopala et al., 2000), which suggests a fundamental deficit.

Investigating the consequence of dysfunctional myelin on neural processing

Many published studies suggest that white matter dysfunction, neural processing deficits, and myelin gene misregulation may play a role in cognitive diseases. However, because of the complex etiology of cognitive disorders, the specific contribution of dysfunctional myelin cannot be determined from clinical studies. Therefore, the overall goal of this dissertation is to elucidate the phenotype associated with dysfunctional myelin in *Cldn11*$^{-/-}$ mice, focusing on neural processing and the development of behavior abnormalities.

The second chapter of this dissertation examined anesthesia regimes needed for subsequent experiments using evoked potentials to characterize a neural circuit in the auditory brainstem. This circuit is employed as a model of neural processing because it is a well-characterized system, easy to interrogate, and has been studied in depth for decades. Information gained from this simple model system can be extrapolated to higher order brain networks that are more challenging to investigate directly. To obtain acoustic information from animal models, a straightforward approach is to use an anesthetic cocktail, allowing for uninterrupted signal measurement with minimal noise influence from awake activity.

Various anesthetics confer differing levels of sedation and alter recorded brain wave activity. The potential for altering neural circuitry and interfering with evoked responses is significant and is addressed in Chapter 2. Previous work in our laboratory and others has determined that one of the oldest anesthetics, 2,2,2-tribromoethanol, is a safe agent effective well below lethal doses and minimally influences evoked brainstem responses (Gow et al., 1999; Zheng et al., 1999). The

challenge in Chapter 2 was to develop a new anesthetic regime that increases anesthesia time without sacrificing data quality or altering waveform characteristics.

Once established, the new anesthetic cocktail is used for more advanced acoustic studies, which is the focus of Chapter 3. Here, the consequence of dysfunctional myelin on neural processing is examined using the *Cldn11*$^{-/-}$*Tg*$^{+/-}$ mouse model. Using the auditory brainstem as a model, neural processing is investigated by measuring sound lateralization in azimuth plane. Two primary auditory features, intensity and timing, are relayed from each ear and are first processed in the superior olivary complex (SOC). Due to the head size and position of the ears in mice, sound intensity differences between left and right wars are principally used for localization

The focus of Chapter 3 is to measure the output of the signal integrators in the SOC when differing sound intensities are presented to each ear. Altering intensity cues played to each ear simulates the lateralization of a sound source from the perspective of neural processing in the LSO. Herein, we find that *Cldn11*$^{-/-}$*Tg*$^{+/-}$ respond abnormally to intensity differences suggesting altered in sound lateralization circuitry. Unexpectedly, the output generated by LSO allow us to comment on a debate in the auditory field regarding models that account for neural processing in the SOC. Our data support the contemporary two-neuron hypothesis (Dingle et al., 2012; Phillips, 2008; Phillips and Hall, 2005; Phillips et al., 2012; Yost, 1974), rather than the classical Jeffress model (Jeffress, 1948). Because small diameter, myelinated fibers are found along the auditory pathway, we hypothesize that slowed conduction velocity along small diameter ipsilateral fibers between the cochlear

nucleus and SOC can disrupt the integration of auditory signals. These data demonstrate that dysfunctional myelin can alter neural processing which has significant implications for higher order brain function in general.

If dysfunctional myelin alters neural processing in the auditory brainstem, then probing higher order integration networks, such as those responsible for behavior, should also reveal deficits. Chapter 4 explores this hypothesis in a quantifiable manner through behavioral testing of *Cldn11*$^{-/-}$ *Tg*$^{+/-}$ mice. Behavior is the observed response of an animal to an environmental cue or stimulation, typically through integration of sensory signals. Because small diameter myelinated fibers are prevalent in sensory integration networks, we hypothesize that *Cldn11*$^{-/-}$*Tg*$^{+/-}$ mice will exhibit abnormal behavioral phenotypes. Through anecdotal evidence and the use of several behavioral tasks to assess behavior, we find that *Cldn11*$^{-/-}$*Tg*$^{+/-}$ mice are less anxious than controls. However this conclusion is somewhat uncertain because of technical difficulties encountered during testing. The most unexpected finding from Chapter 4 is the possibility that dysfunctional myelin may also perturb neurotransmitter levels in the ventral hippocampus. These data, combined with the neural processing abnormalities in the brainstem suggest that dysfunctional myelin could underlie some behavioral disorders.

CHAPTER 2– increased anesthesia time with low impact on auditory evoked potentials using and avertin-chloral hydrate cocktail

INTRODUCTION

In 1929, a German physiologist and psychiatrist, Hans Berger, published the first-ever recorded spontaneous brain activity from a human (Berger, 1929). This groundbreaking discovery and newly developed technique established the fundamentals of electroencephalography (EEG) as we know it today. Further progress was made when sensory stimulation of the brain during sleep was shown to have consistent alterations to the EEG (Davis, 1939), however the magnitude of baseline activity far exceeded that of the sensory evoked activity. To combat this, the process known as signal averaging was introduced (Clark et al., 1961). The premise of averaging uses the fact that sensory evoked responses have a temporal relationship with the stimulus, whereas baseline neural activity is random and does not. Thus, baseline EEGs could be mathematically removed from an averaged trace and what remains was the neural response to a sensory evoked stimulus (Jacobson, 1994).

Evoked potentials can be induced using visual, somatosensory, and auditory stimuli

There are three types of sensory stimuli that can be used to elicit an evoked response: visual, somatosensory and auditory. Visual evoked potentials (VEPs) use light stimulus to induce photic electroretinograms (Adrian and Matthews, 1934), whereas somatosensory evoked potentials (SEPs) use electrical stimulation of peripheral nerves and muscles to measure action potential volleys along sensory

and motor fibers (Dawson, 1947). All three techniques of sensory evoked potentials have been extensively studied and routinely used in clinical settings for diagnostic purposes. The remainder of this chapter will focus on the use of auditory evoked potentials (AEPs). Readers are directed elsewhere for excellent descriptions of the two aforementioned evoked potentials (Chiappa, 1997; Niedermeyer and Lopes da Silva, 2005).

The basis of AEPs is contingent on the ability to audiologically stimulate and record electrical activity in the brain. As previously mentioned, the change a sensory stimulus elicits in baseline EEGs is small. To enhance signal detection, a number of techniques that modify the EEG have been employed. For instance, signal averaging allows for subtraction of baseline neural activity, pre-amplification of signals allows for enhanced detection when responses are small (microvolts), and the use of a band pass filters can eradicate unwanted noise, optimizing collection results.

To further enhance and define different types of auditory responses which occur in the brain, AEPs can be divided into three categories based on the latency each response occurs: short (0 – 10 msec), middle (10 – 40 msec) and long / late (> 50 msec). These are known as the auditory brainstem response (ABR), middle latency response (MLR) and the long latency response (LLR) respectively.

Each of the three AEPs is not only defined by the latency of occurrence, but also by the characteristic series of waves (or peaks) and troughs (valleys) elicited. Waveforms of AEPs can be named based on the polarity of the wave, the latency of occurrence, or sequential order (Jacobson, 1994). The ABR has five, sometimes six,

distinct waves that present 0 to 10 msec post stimulus. Standard nomenclature used to identify ABR waves comes independently from two groups in which Roman numerals I through V (sometimes VI) were used to label positive waves, preventing confusion if a waveform was either missing or altered in a disease state (Jewett and Williston, 1971; Lev and Sohmer, 1972). The first wave occurs approximately 1.2 – 2 msec post stimulus, depending upon electrode placement. Each succeeding waves occurs in approximately 1 msec intervals thereafter.

Contrasting nomenclature of the ABR, MLR wave identification is commonly described by the polarity of the waves: N for negative and P for positive. Polarity is combined with a lower case letter in alphabetical order. Earlier alphabetical letters designate earlier wave latency (Goldstein and Rodman, 1967). At best, optimal filter settings will differentiate six waveforms: V (retained from the ABR), P_0, N_a, P_a, N_b and P_b. In contrast to the crisp, sharp waveforms of the ABR, MLR waves tend to be broader, spanning a greater latency range, thus, naming waves based on the latency they occur would become varied and problematic. The N_a trough spans approximately 15 – 30 msec, the P_a peak between 30 – 40 msec, and the P_b peak between 46 – 55 msec (Hall, 1992).

Similar to MLRs, LLRs waveform nomenclature is based on the polarity of the waveforms. To differentiate from MLRs, polarity is combined with numerical digits, indicating wave order appearance (Williams et al., 1962). At the earliest latencies, wave P_b from the MLR is sometimes present, followed by characteristic LLR waves P1, N1, P2, N2 and P3 (sometimes referred to as P300 under certain stimulus conditions). Wave P1 is typically present between 40 – 70 msec, followed N1

ranging from 90 – 150 msec, P2 between 160 – 300 msec, N2 around 275 msec, and finally P3 at approximately 300 msec (Hall, 1992). Of these waves, N1 and P2 are seen most reliably.

Auditory evoked responses waveforms are generated from nuclei along the ascending auditory pathway

All three categories of auditory evoked responses have characteristic waveforms that arise at somewhat predictable latencies post stimulus. Therefore, it is reasonable to conclude that these signals are being generated from brain structures along the ascending auditory pathway and cortical regions. Determination of specific signal generators for the longer AEPs (MLRs and LLRs) are difficult to assign because as nerve signals traverse along the ascending pathway, information becomes widely dispersed within and between auditory cortices, integrated with information from other sensory systems, and further processed in a more complex manner, such as language recognition. What little information we do know about the signal generators of these waveforms has come from examining patients with auditory lesions, and yet, data is still controversial and discordant between patients. Interrogating the auditory cortices experimentally is more challenging due to the location of structures and the nature of auditory information integration. In contrast, the ABR is the best characterized and most AEP and will be the focus of scrutiny for this thesis.

A combination of techniques have allowed for the anatomical and physiological characterization of ABR waveforms. Early studies employed far and near field recordings in animals and humans. More recently, refined techniques such

as surgical lesioning, single unit recordings, and targeted ablation of neurons has uncovered the ABR waveform generators. Wave I in humans and animals is generated from the distal portion of the auditory nerve as it leaves the cochlea and enters the internal auditory canal (Hashimoto et al., 1981; Jewett and Williston, 1971; Moller and Jannetta, 1981, 1982, 1983a; Sohmer and Feinmesser, 1967). Because of its long length in humans, the proximal portion of the auditory nerve additionally gives rise to Wave II (Moller, 1985; Moller and Jannetta, 1981, 1982, 1983a; Moller et al., 1988; Moller et al., 1995).

In smaller animals commonly used in audiology studies (cats, bats, and rodents), the short length of the auditory nerve cannot account for Wave II generation, and thus, Wave II most likely arises from within the cochlear nucleus (Fisch and Ruben, 1962; Moller and Jannetta, 1983b). As a consensus, the cochlear nucleus also gives rise to Wave III of the ABR in humans, whereas MNTB principle cells are responsible for Wave III generation in rodents (Jalabi et al., 2013).

The third-order neurons in the superior olivary complex are responsible for the generation of Wave IV in both humans and small animals. Driving factors include intracranial recordings, as well as consideration of wave amplitude, broadness of waves, known orientation of neurons in major nuclei, and approximate relay times along fiber tracts (Moore, 1987).

Wave V originates from the lateral lemniscus (LL) fibers terminating in the inferior colliculus (IC) (Moller et al., 1995). Uncertainty still remains about the precise signal generators of the occasional ABR waves (V – VI), due to the auditory

pathway's heavy contralateral trajectory and strong decussation of fibers across the midline.

With a general consensus for the ABR signal generators in humans and animals, more complex studies interrogating the auditory pathway and the resulting changes to the ABR can be quite informative. One crucial element in the collection and interrogation of AEPs that must be reviewed is the use of anesthesia during acquisition.

Anesthesia drugs are frequently administered in AEP studies

The use of rodent models for AEP studies has increased markedly in recent decades. In contrast to clinical and research studies of audition in humans using surface electrodes, many simple animal experiments are performed using subdermal electrodes under anesthesia. The least invasive method for examining the auditory pathway is to administer a short-term anesthetic, which avoids more complex surgical procedures involving the insertion of intracranial electrodes, and the subsequent complications associated with recovery and postoperative infection. Injectable anesthetics are typically administered via venous, peritoneal, muscular or subcutaneous routes depending on the differing properties of the drugs and their absorption rates (2008; Flecknell, 1996). The most commonly recommended anesthetics for use in rodents include inhaled agents, barbiturates, and dissociative agents.

Anesthetic drugs most commonly used for auditory studies in rodents have been limited to a combination of a dissociative anesthetic with a powerful sedative / analgesic such as ketamine / xylazine, which confers effective anesthesia over a

period of 1 – 2 hrs. However, when compared with AEP measures in awake mice, ketamine / xylazine anesthesia has been shown to alter waveform structure, increase wave latencies by as much as 1 msec, and decrease wave amplitudes up to 20 % (McGee et al., 1983; van Looij et al., 2004), Additionally, if injected at high doses, it causes significant respiratory depression in rodents and requires prolonged post-procedure recovery (2008). Similarly, volatile inhaled anesthetics such as isoflurane have been also reported to alter ABR waveform morphology, decrease wave amplitudes and increase wave latencies and hearing thresholds in rodents (Santarelli et al., 2003; Stronks et al., 2010). The centrally derived waveforms (Waves III – V) are predominantly affected in a dose dependent manner. Alternatively, more mild fast acting drugs such as 2,2,2-tribromoethanol (TBE) have also been employed (Forrest et al., 1996; Gow et al., 2004; Zheng et al., 1999).

Tribromoethanol is an effective anesthesia with rapid onset and recovery times. A major advantage of this drug is its safety in rodents, with therapeutic doses far below the lethal dose. Furthermore, it neither impairs ABR nor MLR evoked responses nor significantly suppresses respiration (Gow et al., 2004). However, TBE is a relatively short-acting drug at doses useful for AEPs, which confines auditory experiments to 25 – 30 min in duration, thereby limits experimental complexity and the extent of data collection.

The goal of this chapter has been to develop an anesthesia regimen that increases the effective anesthesia time in mice, compared to a single dose of TBE, without significantly compromising the quality of ABRs acquired using subdermal electrodes. Accordingly, we compared our standard regimen of 375 mg / kg TBE

with a drug combination comprising 375 mg / kg TBE followed after 5 min by 200 mg / kg chloral hydrate (CH). Our data show that we can increase effective anesthesia almost two-fold without compromising ABR quality.

MATERIALS AND METHODS

Mice

The Department of Laboratory and Animal Resources at Wayne State University maintained all mice in this study. All experiments on mice were performed in accordance with an Institutional Animal Care and Use Committee protocol approved by the Wayne State University Animal Investigation Committee. The mice used in this study were between six weeks and four months of age and were on a randomly mixed background strain comprised of C57BL / 6J and 129. We observed only mild age – dependent ABR threshold increases, which were consistent with previous studies on this mixed background (Gow et al., 2004).

Chemicals

A 40 x stock solution of TBE (Sigma, St Louis, MO) (100 % weight / volume) was prepared by dissolving 10 grams (g) of TBE in 6.2 ml of 2-methylbutan-2-ol (Sigma, St Louis, MO) and adjusting to 10 milliliters (ml). The stock was aliquoted at 250 μl in 1.5 ml plastic tubes (Thermo Fisher Scientific, Waltham, MA) and stored at - 20°C. Working solutions of 2.5 % TBE were prepared from a fresh aliquot of stock dissolved by vortexing in 9.75 ml sterile PBS, pH 7.4 (Cellgro, Mannassas, VA). Working solutions were stored away from light at 4°C up to two weeks.

Chloral hydrate (Sigma, St Louis, MO) was prepared as a 2 % working solution by dissolving 0.5 g in 25 ml of sterile PBS. Working solutions were stored sterile and away from light at 25°C. The PBS was filter – sterilized using a 10 ml disposable syringe (Luer-Lok tip, BD Falcon, Franklin Lakes NJ) with a 0.22 μm filter attachment (Millipore, Carrigtwohill, Ireland).

Anesthesia

Mice were anesthetized by intraperitoneal (IP) injection with fresh TBE in sterile PBS at a dose of 375 mg / kg (TBE cohort) as previously described (Gow et al., 2004), and placed on a 39°C heating pad for experimentation. The mice were monitored for the absence of tail, foot, and ear reflexes, as well as reduced respiratory rate, which are all indications of effective anesthesia. Alternatively, mice received a combination of fresh 375 mg / kg, IP, TBE in sterile PBS followed by 200 mg / kg, IP, CH in sterile PBS (TBE-CH cohort) five min after TBE anesthesia was confirmed. After the completion of experiments, the mice were allowed to recover in a separate cage on a 39°C heating pad until they regained normal activity and could be placed back in their home cage. The mice were monitored periodically in their home cage for 24 hrs to ensure they remained active and healthy.

Auditory brainstem response measurements

After confirming anesthesia, the fur along the top of the head and middle of the back of each mouse was sterilized / moistened with alcohol prep pads (Triad Group, INC, Hartland WI). Exposing the eyes to the alcohol pad was avoided. Subdermal platinum electrodes (Grass Technologies, West Warwick, RI) were then placed at the right and left mastoids (negative), vertex (reference) and hindquarters along the midline (ground). Ten min post TBE injection, and at subsequent 10 min intervals, mice were presented with 1,024 pure-tone stimuli in 10 dB SPL decrements from 80 – 20 dB SPL at 32 kHz (102 μsec duration; Blackman envelope – constant rise and fall similar to a Gaussian curve) and a stimulus rate of 29.1 / sec. Both right and left ears were tested successively and ipsilateral

electroencephalography recordings were pre-amplified (100,000 x), band pass filtered (0.3 – 3 kHz) and recorded for 12.5 msec (Sepwin software version 5.1, Intelligent Hearing Systems, Miami, FL).

Amplitudes of the ABR waves were measured from the first derivative of the wave peak to that of the following trough and latencies were measured from the stimulus onset to the first derivative of each wave peak. Plots of ABR wave amplitude or latency versus stimulus intensity exhibited negative slopes for all mice, as expected. Hearing thresholds were approximated as the lowest stimulus intensity that could evoke an ABR Wave I response.

To examine the amplitudes of Waves I, III and V as functions of anesthesia time, we initially plotted absolute amplitudes. Although we observed low inter – animal variability for Wave I data, there was significant stochastic variability for Waves III and V that was not correlated with anesthesia time or stimulus intensity. Alternate plots of sensation level (defined as $SL = A_{stim} - A_{thres}$, where A_{stim} is the stimulus amplitude and A_{thresh} is the threshold amplitude) as a function of anesthesia time did not resolve this variability (Wave III: Appendix B.1; Wave V: Appendix B.2).

Peritoneal cavity examination

Mice received two IP injections, one day apart, of sterile PBS, 375 mg / kg TBE in sterile PBS or TBE followed by 200 mg / kg CH in sterile PBS. The anesthetized mice were allowed to fully recover on a 39°C heating pad then placed back in their home cages and monitored for 24 hrs. Three days after the second injection, the mice were sacrificed and their peritoneal cavities were immediately exposed and photographed (Coolpix 950, Nikon, Melville, NY) followed by a detailed

analysis of the abdominal organs for signs of persistent anesthesia – induced pathology. Two independent observers blinded to the injected agent evaluated the organs using several criteria: general appearance, organ color and size relative to one another, signs of inflammation, vasodilation and the presence or absence of ascites. Eight mice were examined including two sterile PBS injected controls, three TBE and three TBE-CH injected mice.

Statistics

Statistical analyses were performed using GraphPad Prism (version 5, La Jolla, CA). The latency / intensity data comparing TBE and TBE-CH in Figure 2.3A and B were fit with a one-phase exponential decay algorithm. Regression coefficients, R^2, were also calculated. The data for each 10 min interval were analyzed using a one-way ANOVA with Bonferroni post-hoc testing to compare matching intensities between the anesthetic treatments. For Figures 2.4 – 2.9, normalized (to the 50 min time point) amplitudes or latencies of Waves I, III and V from each animal, and the average values from the cohort, were fit using linear regression constrained at (50,1). *F*-tests were used to identify significant deviances of the regression line slopes from zero. In Figure 2.10, normalized (to the Day 0 data point) average weights were fit using linear regression constrained at (0,1). *F*-test was used to determine if the slope of the regression line differs from zero.

RESULTS

Minimal differences in ABR thresholds and Wave latencies for TBE versus TBE-CH anesthesia

To ascertain the impact of a TBE-CH anesthetic cocktail on mouse AEPs, we verified several characteristic features of the ABRs (Figure 2.1A). First, the five characteristic peaks and troughs of the ABR arising from generators are evoked during anesthesia: spiral ganglion neurons, cochlear nucleus, MNTB, SOC, and termination of lateral lemniscus fibers into the inferior colliculus (Buchwald and Huang, 1975). Second, the latency of each of these waves occurs at characteristic intervals. The first wave (Wave I) arises approximately 1.5 msec post-stimulus, followed by Waves II – V at roughly one msec intervals thereafter. Third, the latency of each wave increases slightly as the stimulus intensity is progressively decreased (i.e. ABRs are right-shifted as stimulus intensity decreases).

Fourth, the lowest stimulus intensity that elicits an identifiable ABR Wave I approximates the hearing threshold of the mice (Figure 2.1B), the time course of which is not statistically different between mice anesthetized with TBE (ANOVA; $F_{2,10}$ = 0.6410, p = 0.5471) or TBE-CH (ANOVA; $F_{4,25}$ = 1.190 p = 0.3393). Regression lines for these threshold series have positive slopes (p < 0.05); however, the average threshold change is negligible at < 7 %. Finally, there are no statistical differences in the Wave I latencies between the anesthesia groups at any stimulus intensity (Table 2.1), indicating that both drug regimens have similar initial effects on the ABRs. Moreover, we find no statistical differences from an ANOVA (Table 2.2, Figure 2.2) between the cohorts for interpeak latencies of the total ABR (Waves V –

I; $F_{5,26}$ = 0.2966, p = 0.91), the peripherally derived ABR components (Waves III – I; $F_{5,25}$ = 0.8094, p = 0.55), or centrally derived components (Waves V – III; $F_{5,25}$ = 0.4545, p = 0.81).

We also compared Wave I latencies as a function of stimulus intensity at 10 min intervals between 10 – 30 min for the TBE and TBE-CH cohorts (Figure 2.3A), after which the TBE group regain consciousness. The average latencies of Wave I for all intensities (80 – 30 dB SPL) are adequately described by a one-phase exponential decay model using non-linear regression (0.66 < R^2 < 0.83). The regression lines for each group converge with time, but never differ by more than 4 % on the ordinate axis at any stimulus intensity or time point, and the ordinate intercepts are not statistically significant at any time point (p > 0.37). Moreover, the Wave I latencies between the 10 and 30 min time points differ by no more than 4 % within each cohort. In addition, we examined the central Wave V latencies as a function of stimulus intensity at 10 min intervals from 10 – 30 min between anesthetic groups (Figure 2.3B, Table 2.3). The average latencies of Wave V for all intensities (80 – 30 dB SPL) can be similarly described using a one-phase exponential decay model using non-linear regression (0.41 < R^2 < 0.63), similar to Wave I. Taken together, these data indicate that there are negligible differences in ABR waveforms, latencies or hearing thresholds between the treatment groups over the time course of the experiment.

ABR amplitudes and latencies are modestly altered by TBE-CH

To determine the effects of TBE-CH on Wave I amplitudes with time, we measured ABRs in anesthetized mice at 10 min intervals for 50 min at 32 kHz. Our

Figure 2.1 – ABR threshold series from TBE and TBE-CH anesthetized mice

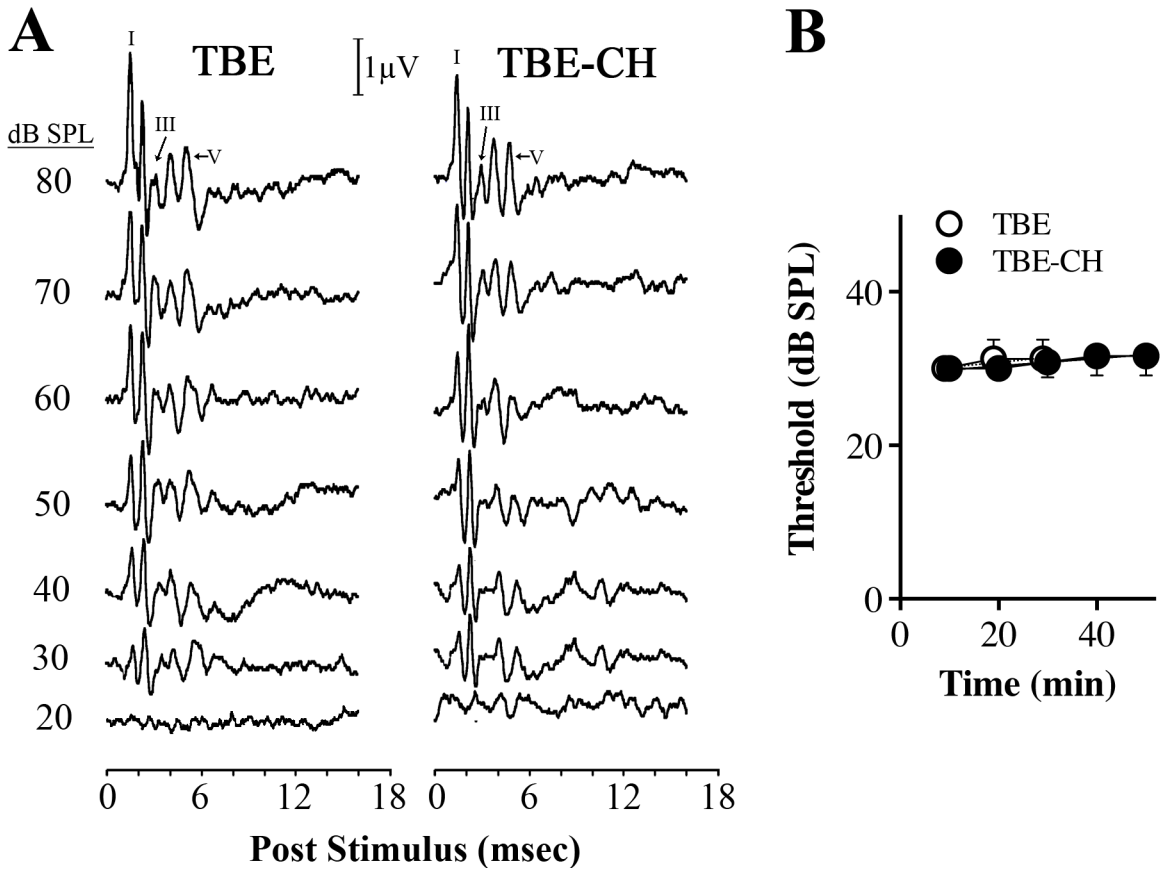

(**A**) Representative ABR intensity series from TBE (TBE) or TBE-CH (TBE-CH) anesthetized mice measured at 10 min intervals post-injection anesthesia. (**B**) ABR hearing thresholds from TBE (TBE) and TBE-CH (TBE-CH) anesthetized mice measured at 10 min intervals post-anesthesia.

Table 2.1 – *F* and *p* values for one-way ANOVAs comparing Wave I latencies between the TBE and TBE-CH cohorts (Figure 2.3A).

Intensity	10 min		20 min		30 min	
dB SPL	$F_{11,48}$	*p*	$F_{11,42}$	*p*	$F_{11,42}$	*p*
80	1.524	>0.05	1.170	>0.05	1.016	>0.05
70	1.560	>0.05	1.170	>0.05	0.811	>0.05
60	1.923	>0.05	1.188	>0.05	0.982	>0.05
50	2.431	>0.05	1.476	>0.05	1.076	>0.05
40	1.742	>0.05	1.476	>0.05	1.529	>0.05
30	2.468	>0.05	1.257	>0.05	0.154	>0.05

Bonferroni post hoc reveals no statistically significant differences between corresponding intensities.

Figure 2.2 – Interpeak latencies from TBE and TBE-CH at 10 min intervals

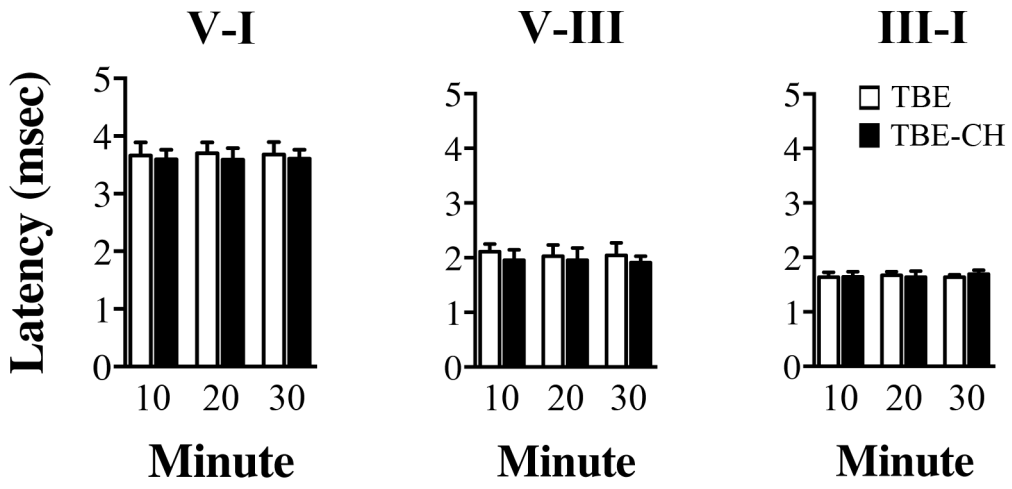

Interpeak latencies were calculated for Waves V – I, V – III, and III – I at 10 min intervals for 30 min comparing TBE and TBE-CH anesthesia affects. There are no statistically significant changes for any interpeak latency (Table 2.3).

Table 2.2 – Interpeak latencies of TBE (TBE) and TBE-CH (TBE-CH) anesthetized mice at 10 min intervals.

Anesthesia	V – I		III – I		V – III	
Time (min)	TBE	TBE-CH	TBE	TBE-CH	TBE	TBE-CH
10	3.75 ± 0.13	3.60 ± 0.14	1.64 ± 0.09	1.64 ± 0.10	2.11 ± 0.14	1.95 ± 0.19
20	3.70 ± 0.19	3.59 ± 0.20	1.67 ± 0.07	1.64 ± 0.11	2.03 ± 0.21	1.96 ± 0.22
30	3.68 ± 0.22	3.60 ± 0.16	1.64 ± 0.05	1.69 ± 0.07	2.04 ± 0.23	1.91 ± 0.07
40		3.63 ± 0.13		1.74 ± 0.10		1.89 ± 0.11
50		3.56 ± 0.14		1.65 ± 0.09		1.91 ± 0.16

Figure 2.3 – ABR Wave I and V latency / intensity graphs from TBE and TBE-CH anesthetized cohorts

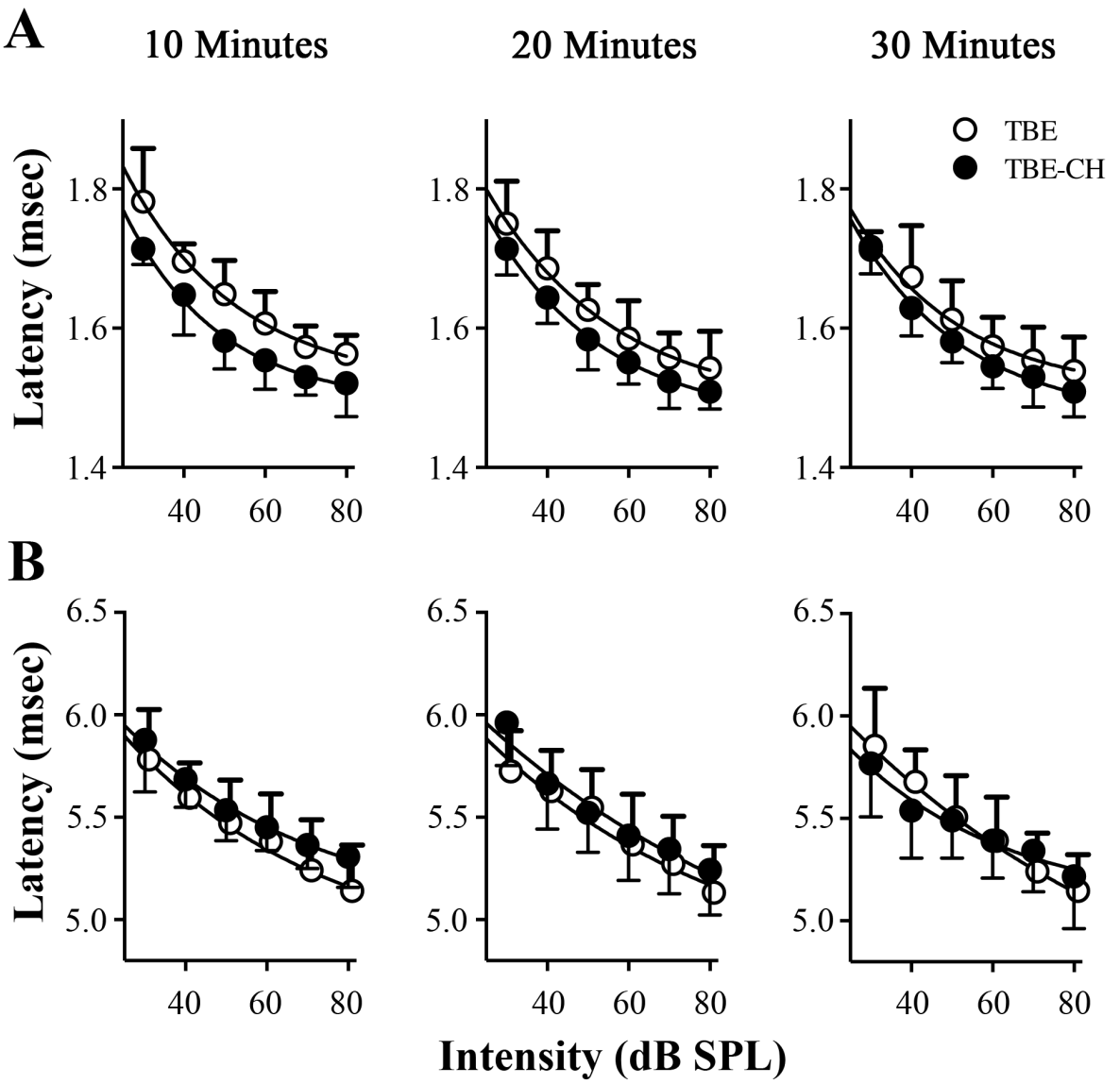

(A) Quantified latency – intensity series of ABR Waves I under TBE (TBE) or TBE-CH (TBE-CH) anesthesia at 10 min post-injection intervals. Data are plotted as mean ± SD for five mice per treatment. See Table 1 for corresponding one-way ANOVA *p* values (**B**) Quantified latency-intensity series ABR Waves V under TBE (TBE) or TBE-CH (TBE-CH) anesthesia at 10 min post-injection intervals. Data are plotted as mean ± SD for five mice per treatment. See Table 2.2 for corresponding one-way ANOVA *p* values.

Table 2.3 – *F* and *p* values for one-way ANOVAs comparing Wave V latencies between the TBE and TBE-CH cohorts (Figure 2.3B).

Intensity dB SPL	10 min		20 min		30 min	
	$F_{11,48}$	*p*	$F_{11,42}$	*p*	$F_{11,42}$	*p*
80	1.524	>0.05	1.170	>0.05	1.016	>0.05
70	1.560	>0.05	1.170	>0.05	0.811	>0.05
60	1.923	>0.05	1.188	>0.05	0.982	>0.05
50	2.431	>0.05	1.476	>0.05	1.076	>0.05
40	1.742	>0.05	1.476	>0.05	1.529	>0.05
30	2.468	>0.05	1.257	>0.05	0.154	>0.05

Bonferroni post hoc reveals no statistically significant differences between corresponding intensities.

previous studies have shown this to be the optimal stimulus frequency for hearing experiments, providing greatest amplitudes and lowest thresholds (Gow et al., 2004). Amplitudes of the waves were obtained from 80 dB SPL to approximately 30 dB SPL, depending on the hearing threshold of individual mice. At a stimulus intensity of 80 dB SPL (Figure 2.4A), we observe consistent and statistically significant reductions in Wave I amplitudes (α = 0.05; Table 2.4) at early time points during anesthesia, as indicated by the positive slopes of the regression lines for all mice. Regression lines at other stimulus intensities between 70 – 30 dB SPL also have positive slopes for most of the mice (Figure 2.4B – F). Furthermore, the regression lines for the average amplitudes differ statistically from zero (α = 0.05; Table 2.4).

Despite these non-zero slopes, the physiological effect of TBE-CH on Wave I amplitudes is relatively small. Thus, the average amplitude we observe at 80 dB SPL after 10 min of anesthesia is reduced by 19 %, compared to the 50 min time point when the mice are beginning to regain consciousness. At lower stimulus intensities, average reductions in amplitudes are 12 % at 70 dB SPL (Figure 2.4B) and at most 6 % for 60 – 30 dB SPL stimuli. Around the hearing threshold of 30 dB SPL, the anesthesia has little affect on Wave I amplitudes.

Similar to Wave I amplitudes, the regression lines for normalized Wave I latencies (Figure 2.5) are statistically non-zero for most individual mice (α = 0.05; Table 2.5), and all of the averaged data down to the hearing threshold have negative slopes. Nevertheless the absolute changes in the latencies, which are increased at early time points, are minimal. Thus, for all stimulus intensities between 80 – 30 dB SPL, we observe an increase of 3 % or less compared to the 50 min time point.

Figure 2.4 – Normalized amplitudes of Wave I from TBE-CH anesthetized mice

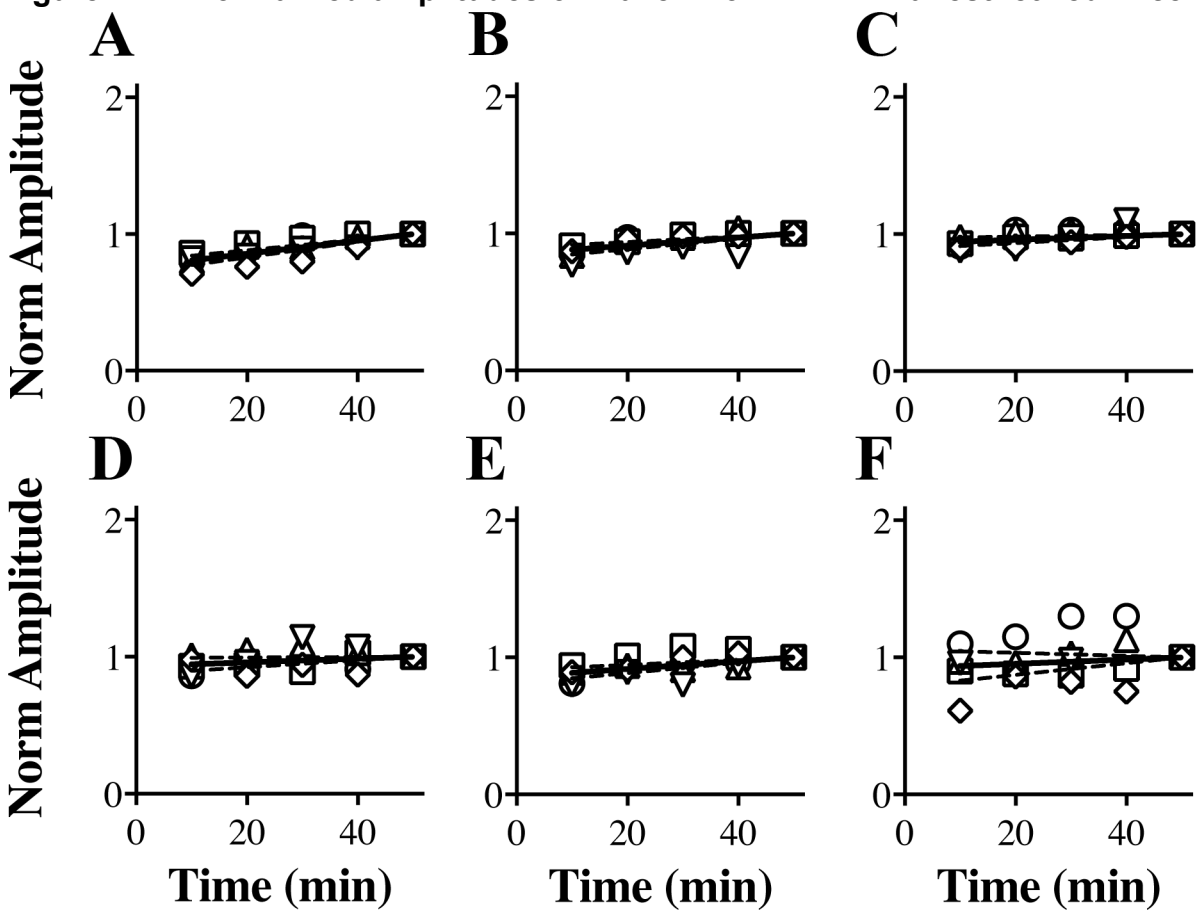

ABR threshold series were obtained at 10 min intervals during anesthesia for 50 min. Normalized Wave I amplitudes are plotted as a function of time for stimulus intensities of 80 dB SPL (**A**), 70 dB SPL (**B**), 60 dB SPL (**C**), 50 dB SPL (**D**) 40 dB SPL (**E**) and 30 dB SPL (**F**). The data for each mouse are normalized to amplitude at 50 min and the average linear regression line constrained at (50,1) is shown (solid line) ± 95 % CI (dashed lines). See Table 2.4 for corresponding linear regression *p* values.

Table 2.4 – Tabulated *p* values of normalized Wave I amplitudes from TBE-CH anesthetized mice (Figure 2.4).

Stimulus	*p* values, $F_{1,3}$					
(dB SPL)	Mouse 1	Mouse 2	Mouse 3	Mouse 4	Mouse 5	Group
80	***0.006***	***0.004***	***0.001***	***0.001***	***<0.001***	***<0.001***
70	***0.030***	***0.005***	0.054	***0.006***	***0.009***	***0.003***
60	0.542	***0.005***	0.732	0.112	***<0.001***	0.051
50	0.060	0.051	0.139	0.588	0.137	***0.022***
40	***0.004***	0.977	***0.006***	***0.006***	***0.030***	***<0.001***
30	0.127	***0.009***	0.090	1.000	***0.010***	0.239

F-tests were used to identify statistically significant differences between the null hypothesis ($m = 0$), that regression line slopes do not differ from zero, for several mice (bold, italicized).

Together, these data demonstrate that the TBE-CH anesthesia causes at most, minor reductions in Wave I ABR amplitudes and negligible changes in latencies.

The size and stability of Waves I provide the greatest sensitivity for measuring changes in ABRs, but anesthetics typically have less impact on Wave I compared to subsequent waves, particularly those derived from central signal generators. Thus, to determine the effect of TBE-CH anesthesia on the major centrally derived components, we examined normalized amplitudes and latencies of ABR Waves III (Figure 2.6, Table 2.6 and Figure 2.7, Table 2.7) and Waves V (Figure 2.8, Table 2.8 and Figure 2.9, Table 2.9).

The Wave III amplitudes (Figure 2.6) are qualitatively similar to the Wave I data in that the slopes of the regression lines are positive; however the rates of change with time are much greater. Thus, maximal average amplitudes at 10 min are 1.5 – 3 fold smaller than those at 50 min, which suggests that Wave III may be strongly affected by TBE-CH. Unexpectedly, the magnitudes of the amplitude data are independent of stimulus intensity, which suggests a stochastic effect of the combination anesthesia. In contrast to the amplitude changes, the normalized average Wave III latencies (Figure 2.7) are invariant with stimulus intensity or anesthesia time and the slopes of the regression lines are zero ($\alpha = 0.05$). Together, these data suggest that the Wave III amplitudes vary in a stochastic rather than systematic manner, which may argue against a strong suppression and more toward increased amplitude variability during anesthesia. Indeed, this variability is reflected in the large 95 % confidence intervals in the 80 – 30 dB SPL data.

Figure 2.5 – Normalized latencies of Wave I from TBE-CH anesthetized mice

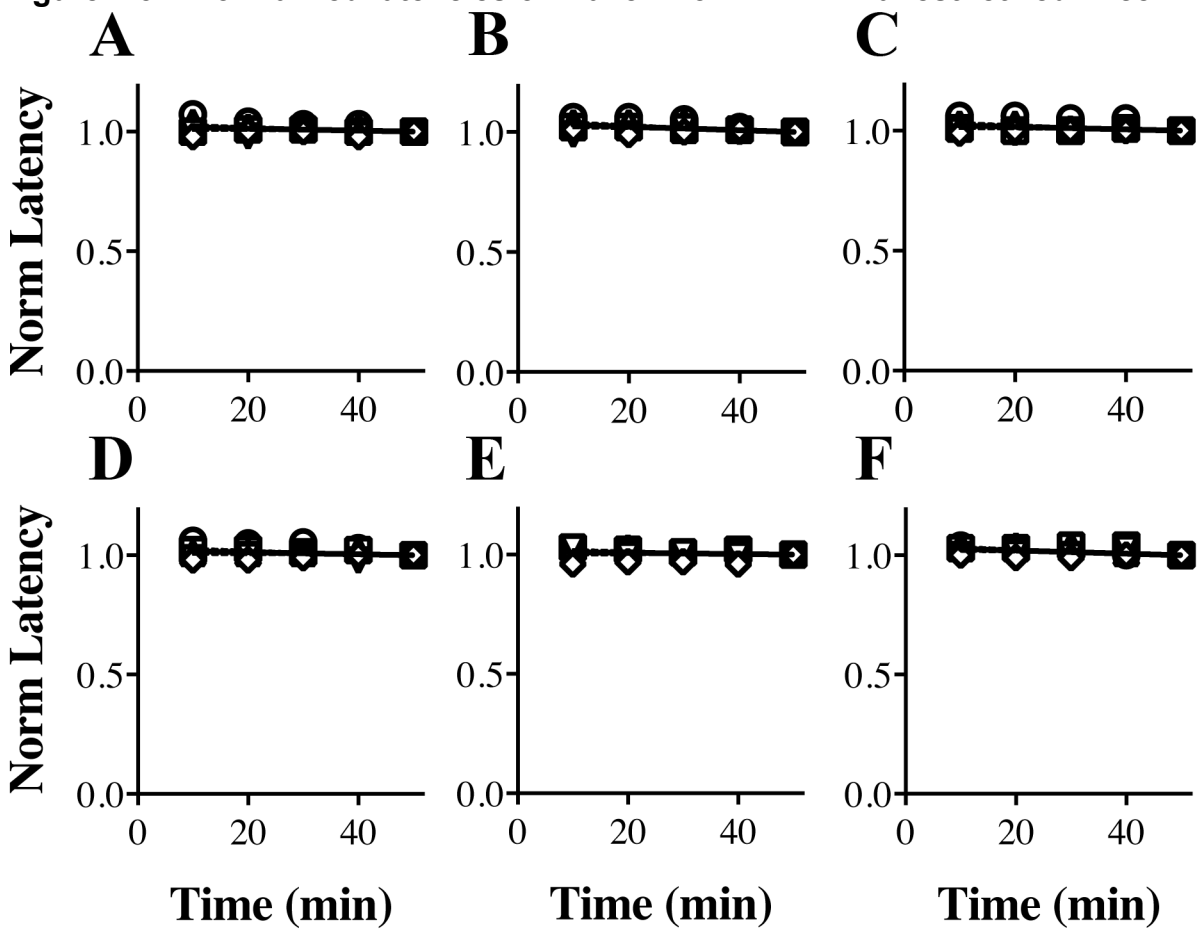

ABR threshold series were obtained at 10 min intervals during anesthesia for 50 min. Normalized Wave I latencies are plotted as a function of time for stimulus intensities of 80 dB SPL (**A**), 70 dB SPL (**B**), 60 dB SPL (**C**), 50 dB SPL (**D**) 40 dB SPL (**E**) and 30 dB SPL (**F**). The data for each mouse are normalized to the latency at 50 min and the average linear regression line constrained at (50,1) is shown (solid line) ± 95 % CI (dashed lines). See Table 2.5 for corresponding linear regression *p* values.

Table 2.5 – Tabulated *p* values for normalized Wave I latencies from TBE-CH anesthetized mice (Figure 2.5).

Stimulus	*p* values, $F_{1,3}$					
(dB SPL)	Mouse 1	Mouse 2	Mouse 3	Mouse 4	Mouse 5	Group
80	***0.001***	0.166	***0.004***	0.236	0.166	***<0.001***
70	***0.001***	***0.001***	***0.002***	***0.670***	0.689	***0.002***
60	***0.005***	***0.166***	***0.001***	0.261	0.099	***0.004***
50	***0.001***	***0.010***	0.112	0.193	***0.001***	***0.005***
40	***0.046***	***0.004***	***0.003***	0.052	***0.014***	0.148
30	***0.004***	***0.031***	***0.002***	0.501	0.166	***<0.001***

F-tests were used to identify statistically significant differences between the null hypothesis ($m = 0$), that regression line slopes do not differ from zero, for several mice (bold, italicized).

Figure 2.6 – Normalized amplitudes of Wave III from TBE-CH anesthetized mice

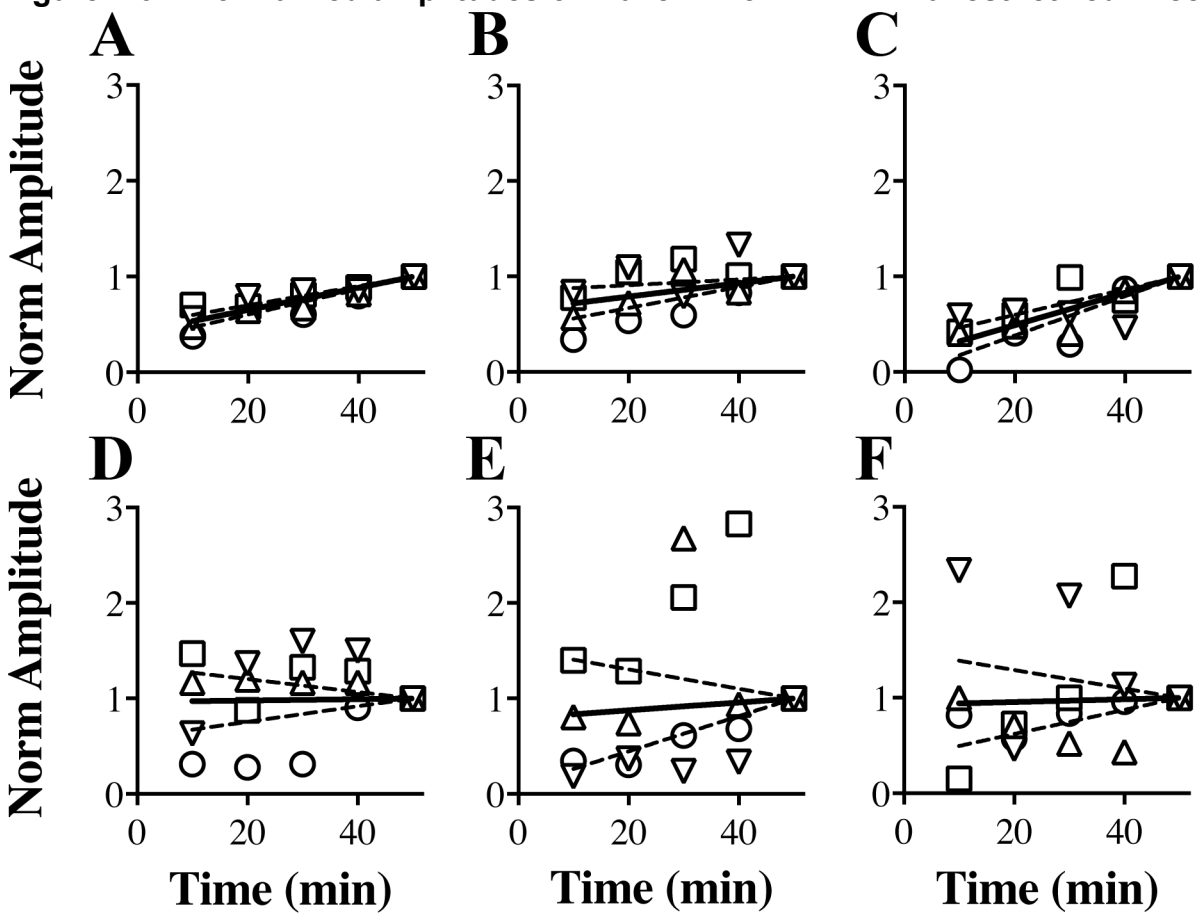

ABR threshold series were obtained at 10 min intervals during anesthesia for 50 min. Normalized Wave V amplitudes are plotted as a function of time for stimulus intensities of 80 dB SPL (**A**), 70 dB SPL (**B**), 60 dB SPL (**C**) 50 dB SPL (**D**) 40 dB SPL (**E**) and 30 dB SPL (**F**). The data for each mouse are normalized to amplitude at 50 min and the average linear regression line constrained at (50,1) is shown (solid line) ± 95 % CI (dashed lines). See Table 2.6 for corresponding linear regression *p* values.

Table 2.6 – Tabulated *p* values of normalized Wave III amplitudes from TBE-CH anesthetized mice (Figure 2.6).

Stimulus	*p* values, $F_{1,3}$				
(dB SPL)	Mouse 1	Mouse 2	Mouse 3	Mouse 4	Group
80	***<0.001***	***<0.001***	***<0.001***	***<0.001***	***<0.001***
70	***<0.001***	0.662	*0.025*	0.701	***0.002***
60	***<0.001***	***0.008***	***0.002***	***0.028***	***<0.001***
50	***0.002***	0.132	***0.010***	0.619	0.874
40	***<0.001***	0.270	0.724	***0.007***	0.551
30	***0.021***	0.503	0.258	0.198	0.789

F-tests were used to identify statistically significant differences between the null hypothesis ($m = 0$), that regression line slopes do not differ from zero, for several mice (bold, italicized).

Figure 2.7 – Normalized latencies of Wave III from TBE-CH anesthetized mice

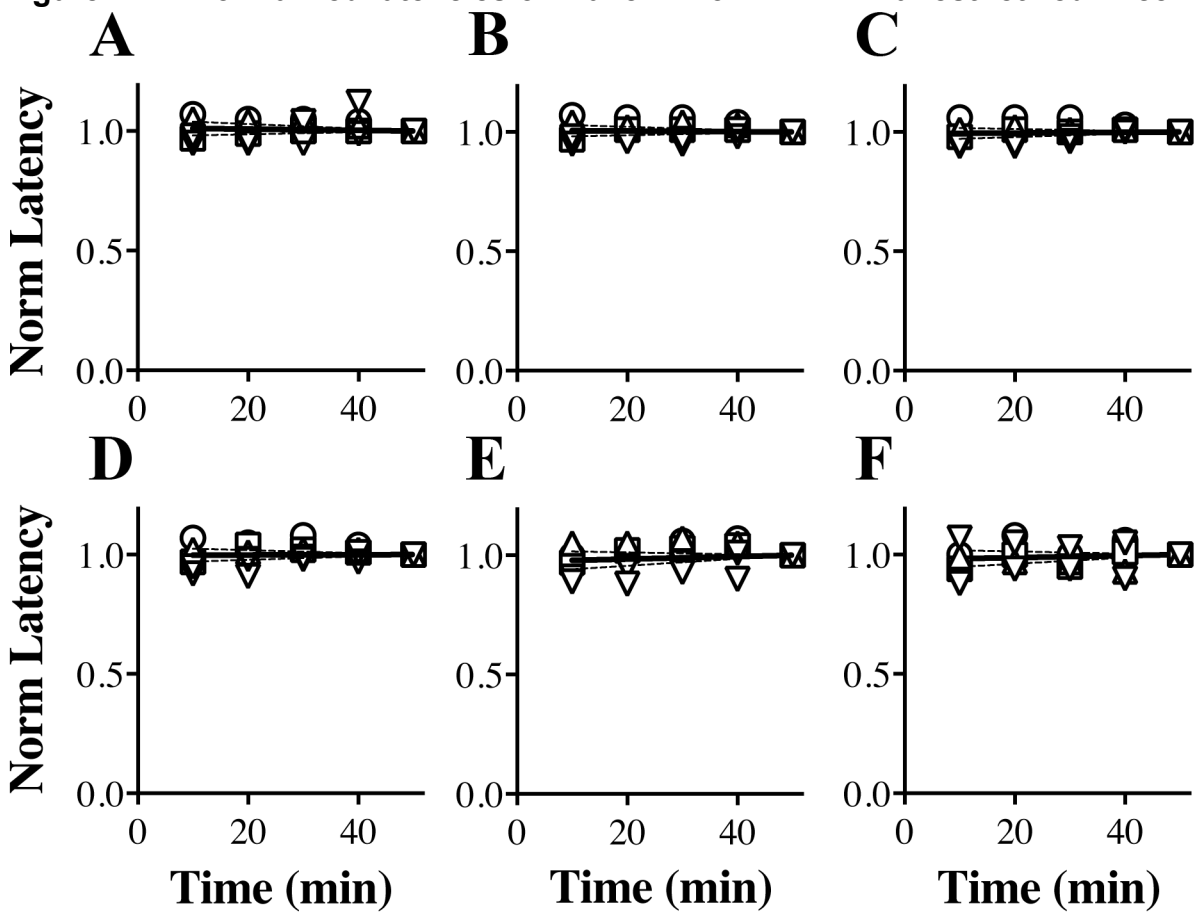

ABR threshold series were obtained at 10 min intervals during anesthesia for 50 min. Normalized Wave V latencies are plotted as a function of time for stimulus intensities of 80 dB SPL (**A**), 70 dB SPL (**B**), 60 dB SPL (**C**) 50 dB SPL (**D**) 40 dB SPL (**E**) and 30 dB SPL (**F**). The data for each mouse are normalized to amplitude at 50 min and the average linear regression line constrained at (50,1) is shown (solid line) ± 95 % CI (dashed lines). See Table 2.7 for corresponding linear regression *p* values.

Table 2.7 – Tabulated *p* values of normalized Wave III latencies from TBE-CH anesthetized mice (Figure 2.7).

Stimulus	*p* values, $F_{1,3}$					
(dB SPL)	Mouse 1	Mouse 2	Mouse 3	Mouse 4	Mouse 5	Group
80	***0.001***	***0.026***	***0.002***	1	***0.002***	0.453
70	0.001	0.541	0.015	0.070	<0.001	0.644
60	***0.002***	0.566	***0.015***	***0.010***	***<0.001***	0.600
50	***0.008***	0.752	***0.028***	***0.020***	***0.003***	0.872
40	0.391	0.823	***0.020***	***0.004***	***0.007***	0.250
30	0.261	0.076	0.232	***0.004***	***0.013***	0.324

F-tests were used to identify statistically significant differences between the null hypothesis ($m = 0$), that regression line slopes do not differ from zero, for several mice (bold, italicized).

Figure 2.8 shows normalized amplitudes of Waves V at 10 min intervals up to 50 min under combination TBE-CH anesthesia, and normalized amplitudes are shown from 80 – 30 dB SPL. The regression lines of the averaged amplitude data between 80 – 50 dB SPL have non-zero slopes ($\alpha = 0.05$), with maximum amplitudes of 10 – 21 % greater than the 50 min time point. At 40 and 30 dB SPL, average Waves V regression line slopes was zero, attributable to the variable increase or decrease of amplitudes as time progressed. However, in contrast to the Wave I (Figure 2.4) and Wave III data (Figure 2.6), slopes of the regression lines in Figure 2.8 are negative, which indicates that Wave V amplitudes are supernormal at early anesthesia time points and decrease as the mice approach consciousness. In addition, the magnitudes of these changes are independent of stimulus intensity. These data suggest that TBE-CH does not depress Wave V amplitudes but rather enhances them, which differs from other common anesthetic combinations used in the hearing field such as ketamine / xylazine. However, we cannot rule out the possibility of stochastic anesthesia effects, similar to the Wave III amplitudes, because of the large variability in the amplitudes between mice.

Wave V latencies for 80 – 30 dB SPL are shown in Figure 2.9. The average regression line for the 80 – 30 dB SPL latencies have a zero slope ($\alpha = 0.05$). The greatest variation in Wave V latency occurs at 30 dB SPL, however the latencies are 2 % greater at 10 min than at 50 min. These data demonstrate that there is little effect of TBE-CH on Wave V latencies even though the drug combination generally increases the amplitudes of these waves in our study cohort.

Figure 2.8 – Normalized amplitudes of Wave V from TBE-CH anesthetized mice

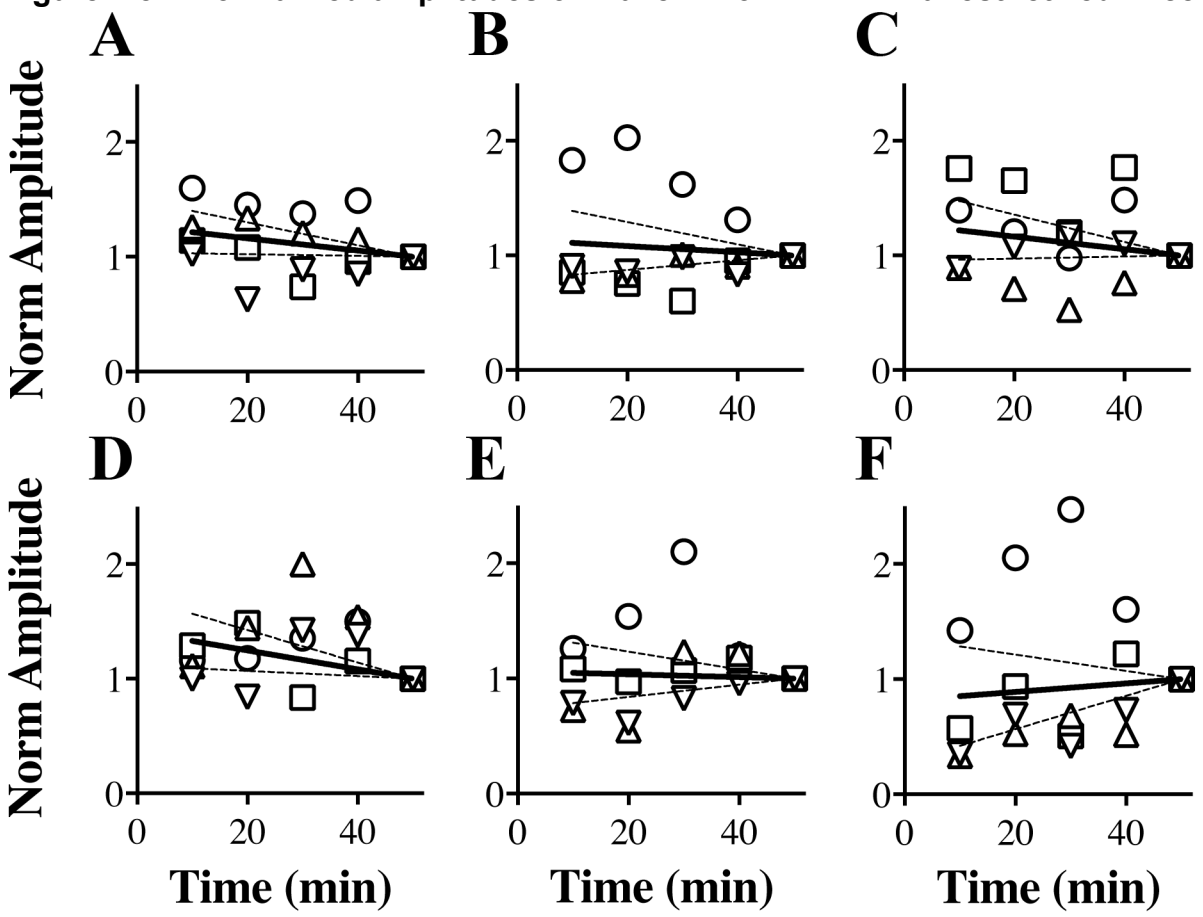

ABR threshold series were obtained at 10 min intervals during anesthesia for 50 min. Normalized Wave V amplitudes are plotted as a function of time for stimulus intensities of 80 dB SPL (**A**), 70 dB SPL (**B**), 60 dB SPL (**C**) 50 dB SPL (**D**) 40 dB SPL (**E**) and 30 dB SPL (**F**). The data for each mouse are normalized to amplitude at 50 min and the average linear regression line constrained at (50,1) is shown (solid line) ± 95 % CI (dashed lines). See Table 2.8 for corresponding linear regression *p* values.

Table 2.8 – Tabulated *p* values of normalized Wave V amplitudes from TBE-CH anesthetized mice (Figure 2.8).

Stimulus	*p* values, $F_{1,3}$				
(dB SPL)	Mouse 1	Mouse 2	Mouse 3	Mouse 4	Group
80	***0.006***	0.787	***0.002***	0.197	***0.026***
70	***0.001***	0.053	***0.011***	0.073	0.417
60	0.097	***0.021***	0.094	0.729	0.089
50	0.152	0.099	0.168	0.658	***0.009***
40	0.100	0.325	0.290	***0.009***	0.700
30	0.065	0.118	***0.004***	***0.005***	0.716

F-tests were used to identify statistically significant differences between the null hypothesis ($m = 0$), that regression line slopes do not differ from zero, for several mice (bold, italicized).

Figure 2.9 – Normalized latencies of Wave V from TBE-CH anesthetized mice

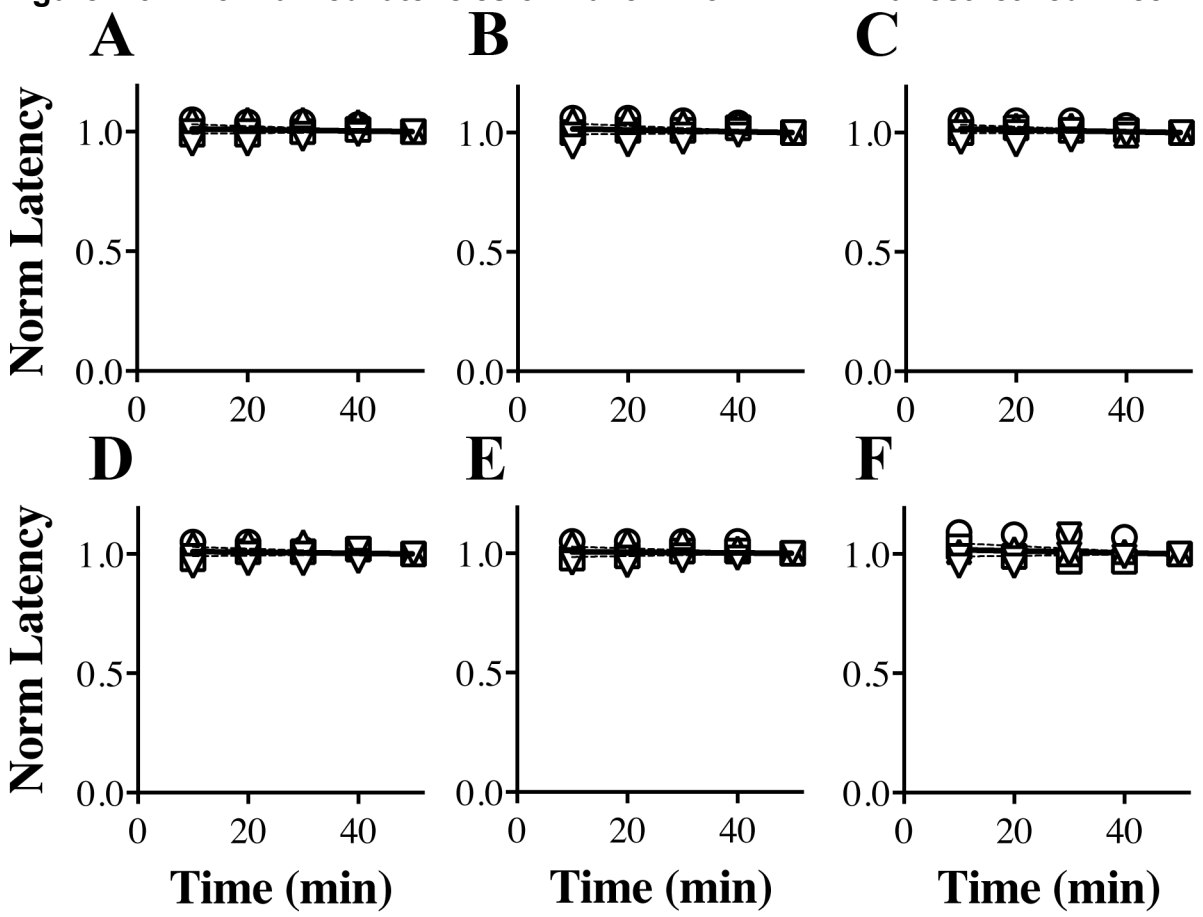

ABR threshold series were obtained at 10 min intervals during anesthesia for 50 min. Normalized Wave V latencies are plotted as a function of time for stimulus intensities of 80 dB SPL (**A**), 70 dB SPL (**B**), 60 dB SPL (**C**) 50 dB SPL (**D**) 40 dB SPL (**E**) and 30 dB SPL (**F**). The data for each mouse are normalized to amplitude at 50 min and the average linear regression line constrained at (50,1) is shown (solid line) ± 95 % CI (dashed lines). See Table 2.9 for corresponding linear regression *p* values.

Table 2.9 – Tabulated *p* values of normalized Wave V latencies from TBE-CH anesthetized mice (Figure 2.9).

Stimulus	*p* values, $F_{1,3}$					
(dB SPL)	Mouse 1	Mouse 2	Mouse 3	Mouse 4	Mouse 5	Group
80	***0.001***	0.178	***0.006***	0.477	***<0.001***	0.257
70	***0.002***	0.288	***0.004***	0.099	***<0.001***	0.180
60	***0.003***	0.145	***0.006***	0.448	***0.001***	0.095
50	***<0.001***	0.914	***0.006***	0.757	***0.002***	0.292
40	***0.011***	0.256	***0.006***	***0.004***	***0.001***	0.546
30	***0.005***	1	***0.046***	0.830	***0.009***	0.216

F-tests were used to identify statistically significant differences between the null hypothesis ($m = 0$), that regression line slopes do not differ from zero, for several mice (bold, italicized).

Rapid recovery of mice from TBE-CH anesthesia and normal weight maintenance

In addition to determining the effect of TBE-CH anesthesia on ABRs, we examined post-anesthesia recovery times and the safety of the anesthesia in terms of mouse weight over the subsequent two days. Consciousness was judged to coincide with several coincident behavioral characteristics: the reappearance of tail and ear pinch reflexes, an increase in respiratory rate and attempts to ambulate. Normal activity coincided with the reacquisition of persistent exploring, foraging, eating and drinking behaviors.

Figure 2.10B shows average times taken for six mice to regain consciousness and resume normal activity in the cage following TBE or TBE-CH anesthesia. Although the time to consciousness doubles from 30 min for TBE to 60 min for the combination anesthetic, there is a modest 20 % increase in the time to regain normal activity for the combination cocktail. Thus, the addition of choral hydrate extends anesthesia but does not markedly increase recovery time from consciousness to normal activity.

A useful indication of the short and medium term effects of anesthesia on mouse health is obtained by monitoring changes in weight during the post anesthesia period. Figure 2.10A shows the weights of six animals anesthetized with TBE-CH normalized to the weight of the mice just prior to injection (Day 0). An average weight gain of 5 % was observed for most mice after two days, and none of them lost more than 1.2 % of their pre-anesthesia body weight in the post-

anesthesia period. Accordingly, we conclude that the acute after effects of the TBE-CH combination is not detrimental to the normal behavior or health of the mice.

Mild peritoneal vasodilation following TBE-CH anesthesia

Finally, we examined the comparative medium term effects of two doses of anesthetic, one day apart, on peritoneal cavity appearance in mice injected with PBS, TBE, or TBE-CH. Figure 2.11 shows the peritoneal cavities of representative mice before (Figure 2.11A, C, and E) and following (Figure 2.11B, D, and F) detailed examination of the abdominal organs. Both observers were in agreement that the superficial appearance of the abdominal organs from the TBE and TBE-CH cohorts are indistinguishable from the controls at three days post-injection and gut content and color indicates that all three cohorts were actively feeding. Further, ascites is absent in all three cohorts, which suggests there is little or no inflammation, and the organs have normal size, shape and color.

The observers identified several areas of apparent vasodilation in the intestinal vasculature for both TBE and TBE-CH cohorts compared to the controls, but the anesthesia cohorts were indistinguishable from each other. Accordingly, we observe persistent damage to the peritoneal cavity of mice following a single dose of TBE or the TBE-CH cocktail, although the pathology is mild and non-inflammatory. This vasodilation likely stems from mild irritation caused by TBE and / or the solvent 2-methylbutan-2-ol because of the similarity of the changes in both anesthetized cohorts.

Figure 2.10 – Post anesthesia effect on recovery time and weight

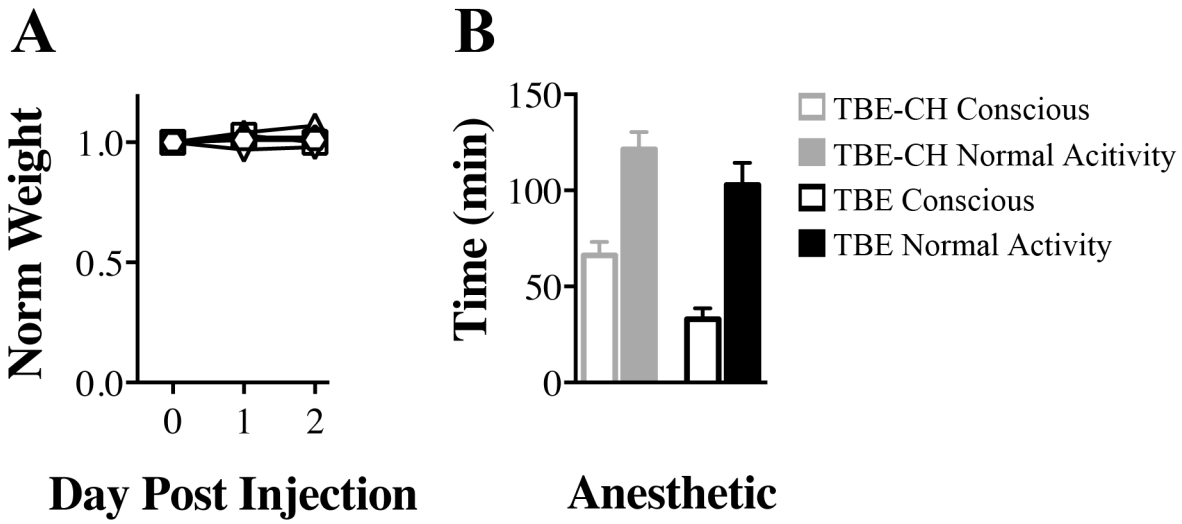

(A) Average times for mice to become conscious from anesthesia and resume normal activity. Averages are for six mice (mean ± SD) for awake and fully recovered states. TBE-CH (TBE-CH) anesthetic combination persists for 60 min with full recovery observed by two hrs, where as TBE alone persists for 30 min with full recovery by an hr and a half. (**B**) The weights of six mice are normalized to their weight on the day of anesthesia. There is no statistically significant change in weight for this cohort over three days following anesthesia (ANOVA; $p = 0.272$).

Figure 2.11 – Mild acute vasodilation in TBE-CH injected abdomens

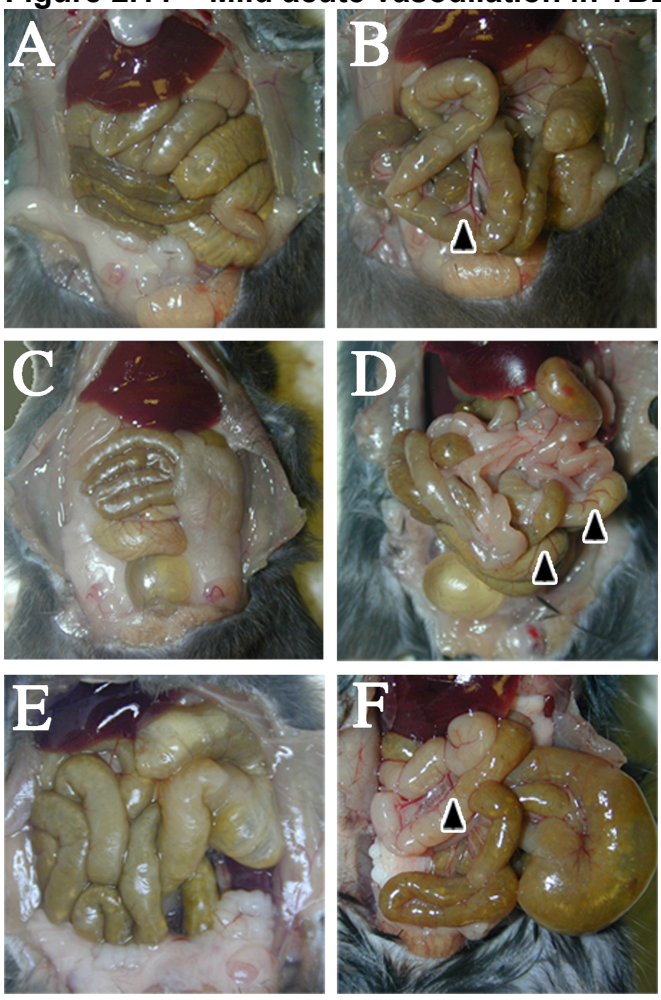

Saline injected (**A and B**), TBE injected (**C and D**) and TBE-CH injected (**E and F**) abdominal cavities post sacrifice indicate normal coloration, morphology and shape of abdominal structures. Control (**B**), TBE injected (**E**), and TBE-CH injected (**F**) intestines upon further examination highlight differences in vasodilation along intestines and septum. Black arrowheads indicate increased vasodilation in the peritoneal cavity.

DISCUSSION

For decades, studies in rodents have employed TBE anesthesia for AEPs because of its ease of preparation and use; TBE is not a controlled substance subjected to State and Federal regulations, is readily available, easily prepared, is safe and rapid-onset anesthetic that can be used over a wider dosage range (Gaertner et al., 2008; Papaioannou and Fox, 1993; Weiss and Zimmermann, 1999). Anesthesia with this drug causes loss of righting reflexes, absence of responses to tail and ear pinching, muscle relaxation and decreased skeletal respiratory activity within 1 – 2 min (Gaertner et al., 2008; Norris and Turner, 1983; Papaioannou and Fox, 1993).

Concerns about the use of TBE have arisen in the past because this drug has been associated with contradictions including intestinal ileus, peritonitis, muscle necrosis, serositis of abdominal organs, and death (Tarin and Sturdee, 1972; Zeller et al., 1998). Detailed examination of previous studies lacked crucial information regarding the preparation, monitoring, and storage conditions of both the stock and working solutions (Buetow et al., 1999; Gaertner et al., 2008; Weiss and Zimmermann, 1999). TBE has a short half-life and can break down into hydrobromic acid and dibromoacetaldehyde. These compounds are hypothesized to decrease the pH of the solution below 5 and likely cause the aforementioned contradictions (Lieggi et al., 2005; Nicol et al., 1965; Norris and Turner, 1983; Papaioannou and Fox, 1993). To minimize complications and increase the efficacy of the anesthetic, TBE should be dissolved in 2-methylbutan-2-ol, stored at 4°C and away from light for

no longer than two weeks, and the pH of the solution checked before use (Lieggi et al., 2005; Weiss and Zimmermann, 1999).

Nevertheless, a single dose of TBE provides only 25 – 30 min of anesthesia, which limits the scope of experiments that can be performed. Our interest in characterizing binaural hearing in mice prompted a search for anesthetics that increase anesthesia time to one hr. Rather than a major change to different drugs, which would yield results that may be difficult to compare with our previous studies, we opted to test a novel cocktail using TBE as a base anesthetic overlaid with low dose CH to extend effective anesthesia time while minimally changing the fundamental characteristics of the centrally derived ABR waveforms.

The routine dose of TBE that is used for AEP studies in our lab is 375 mg / kg (Gow et al., 2004). We have previously observed that significantly increasing the dose to 500 mg / kg, as used by other groups, extends anesthesia time, but at the cost of significant reductions in ABR amplitudes (Zheng et al., 1999). Repeated IP injections of 375 mg / kg within the same testing period are impractical considering the sensitivity of electrode and sound tube placement and lingering anesthesia from the initial dose of TBE can alter the level of overall anesthesia affecting waveforms.

Chloral hydrate has been used as a reliable sedative for more than a century (Gaertner et al., 2008; Hetzler and Dyer, 1984). It is often considered to be a suboptimal anesthetic for rodents because it has poor analgesic properties and, indeed, most contemporary surgical procedures involve anesthetics with strong analgesic properties (Flecknell, 1996). Typical doses of CH for rodents with which a surgical level of anesthesia is induced ranges from 300 – 400 mg / kg and confers

effective anesthesia for 1 – 2 hrs. Numerous studies have demonstrated that the dose of CH has a linear relationship to anesthesia time (Field et al., 1993; Flecknell, 1996; Smith and Kraus, 1987). At greater dosages, above 350 mg / kg, or with repeat injections, CH has been shown to have a proportional impact on various electroencephalography recordings by increasing waveform latencies and altering amplitudes (Field et al., 1993; Smith and Kraus, 1987). However, at low to moderate doses, ≤ 300 mg / kg, CH preserves the electroencephalography waveforms in rats, which is an important consideration for psychoacoustic studies (Sisson and Siegel, 1989).

The least invasive method to collect AEP measurements is via short-term anesthesia. Surgical implantation of a recording device is not required, thus alleviating any deleterious effects from surgery, data collection can begin without delay, and a greater number of data points (animals) can be gathered more efficiently. One compromise by using an acute anesthetic versus a surgically implanted device is the inherent decrease in the signal-to-noise ratio (SNR). Classically defined as SNR = Signal / Noise, this ratio relates the detectability of desired signal in background noise where a greater numerical SNR value indicates increased detectability of signal. To compensate for low SNR in anesthetized animals arising from the use of subdermal electrodes rather than implants, a greater number of recordings can be averaged together.

All forms of anesthesia have their advantages and disadvantages that must be taken into account for specific applications. Herein, our goal was to extend anesthesia time in mice without compromising AEP measurements, however, this

did not seem attainable with the aforementioned alternative anesthetic compounds. Barbiturates tend to increase hearing thresholds, variably affect amplitudes, or strongly suppress EEG waveforms compared to awake animals (Feng et al., 2007; Shaw, 1986; Smith and Kraus, 1987). Likewise, the dissociative agent cocktail ketamine / xylazine, although most commonly employed has been shown to suppress ABR amplitudes by 20 % and increase wave latencies by 1 msec in rodents when compared to awake recordings (McGee et al., 1983; Santarelli et al., 2003; Stronks et al., 2010; van Looij et al., 2004). Using the combination TBE-CH anesthesia, we observe negligible changes in wave latencies and non-systematic changes in amplitude, when compared to TBE alone.

Herein, we demonstrate that 375 mg / kg TBE followed after five min by 200 mg / kg CH is safe for mice, roughly doubles the anesthesia time to around 60 min, and has non-systematic effects on the ABR amplitudes (Maheras and Gow, 2013). A more reliable measure of these waves is to examine latencies as shown in Figures 2.5, 2.7 and 2.9. The regression lines for the averaged latencies have slightly negative or zero slope indicating consistency throughout anesthetic time. Because of the tight relationship between ABR wave amplitudes and latencies, it is reasonable to conclude that variability in amplitude we observe stem from inter-subject effects, such as technical placement of the subdermal electrodes, rather than systematic suppression of the ABRs by the anesthetic combination.

In light of our data, TBE-CH anesthesia is superior to other commonly used anesthetics in AEP studies. Amplitudes and latencies of ABRs measured from awake mice are similar to the values we observed under TBE anesthesia alone (van

Looij et al., 2004). Using the combination TBE-CH anesthesia, we observe negligible increases in wave latencies and non-systematic changes in amplitude, which is a preferable and more consistent method for collecting and analyzing AEPs.

We find that the timing for the administration of TBE and CH to mice is important. Initial experiments involved injecting these anesthetics in quick succession, first TBE then CH. However, this protocol leads to acute gasping and body twitching in some mice and occasionally a failure to induce effective anesthesia. However, administration of TBE to rapidly induce unconsciousness at a level where reflexes are absent, followed by CH, yields no adverse effects. Typically, we use a time delay between TBE and CH injections of approximately 5 min.

The most common side effects from IP injected anesthetics include transient weight loss and peritoneal irritation or inflammation (Gaertner et al., 2008). In Figure 2.10A, we demonstrate using ANOVA that there are no statistically significant changes in weight for TBE-CH injected mice over the three days following anesthesia (p = 0.272). Figure 2.11 shows that the peritoneal cavities of these mice sacrificed three days post injection with TBE-CH (Figure 2.11E and F), TBE alone (Figure 2.11C and D) and even saline injected controls (Figure 2.11A and B) exhibit mild signs of vasodilation around the intestines and normal abdominal organ color and morphology. The similar extent of vasodilation between the TBE and TBE-CH cohorts suggests that CH contributes minimally to peritoneal irritation. Finally, there is no evidence of ascites in the peritoneal cavity of the anesthetized mice, which indicates that inflammatory responses are minimal.

CHAPTER 3 – slowed conduction velocity impacts neural processing

INTRODUCTION

Sensory perception is governed through five classic modalities: vision, hearing, taste, touch, and smell. All five senses begin as a physical event that stimulates receptors, transforming stimulation into electrical impulses that travel to the brain. As a result, the brain forms a perception or conscious experience from the initial stimuli event. When triggered, each sensory modality encodes four elemental characteristics of the stimulus: modality, location, intensity, and timing. Combined with diverse receptors and a fine-tuned network, complex experiences develop in each modality (Kandel et al., 2000). For instance, vivid images can be envisaged, a classical symphony perceived, a delicate touch felt, and bold flavors entertained. This chapter focuses on audition detailing and interrogating key features of sound utilized within this modality.

The auditory pathway differentiates characteristics of sound for processing

Sound perception relies on the ability to localize the spatial positioning of a sound source. Being able to isolate the necessary cues and eliminate redundant or irrelevant sound information improves clarity and aids in the survival instinct, such as the fight or flight response. Sound cues are non-redundant and provide spectral, timing, and intensity information about the sound source. These features have differing levels of importance depending upon the species.

Critical factors determining which sound features are optimally exploited include head shape and relative ear location. The auricle, or outer ear, and shape of

the head filter incoming stimuli that must then be dissociated from the actual spectral information emitted. These physical features are advantageous: the size of the head can cause a shadowing effect, distorting sounds and creating a perceivable intensity difference between ears, and the difference in path length between ears can generate delays in the arrival of a sound to each ear. These physical attributes of an animal generate non-redundant sound cues and increase resolution of the spatial location for a sound source (Schnupp et al., 2011).

There are two major axes pertaining to the head and the location of a sound source: the vertical plane (front / back, above / below) and the horizontal plane, or azimuth (left / center / right). Auditory cues used to isolate the origin of a sound along the vertical axis originate from the frequency and phase of the sound, together with interference patterns generated by the head, torso, and auricle. These physical outer structures produce differential stimulating patterns on inner ear structures, and thereby preserving sound cue information.

The representation of location for the origin of a sound source along the azimuth plane must be computed from the input of signals from both ears. First proposed in the late 1800s, the duplex theory of binaural hearing states that the primary acoustic cues used to lateralize sounds (pure tones) are discrepancies in the arrival (timing) and level (intensity) of signals that reach each ear. As proposed, differences in sound intensity are best discriminated at higher frequencies, whereas timing disparities are best differentiated at lower frequencies (Rayleigh, 1907). These features are known as interaural level differences (ILDs) and interaural timing differences (ITDs) respectively. The generation of intensity and timing differences

arises from the shielding effect of the head, altering the physical dimension of the auditory cue. The head creates a shadowing effect upon the ear farthest away from the sound source, diminishing the sound intensity and delaying its arrival.

Sound information is encoded and relayed through the auditory pathway

The earliest encoding of timing and intensity cues begins in the peripheral auditory pathway with the basilar membrane, which, like most regions of the auditory pathway, is tonotopically structured. Its tapered structure generates a stiffer membrane near the narrow base, and a more relaxed, wider structure near the apex. High frequency sounds cause maximal deflection of the membrane near the base, and low frequency sounds maximally deflect near the apex. Resting on the basilar membrane is the organ of Corti in which inner hair cells reside. These cells further promote the encoding of auditory cues by electrically depolarizing at their best characteristic frequency, or frequency which elicits the greatest response. When an inner hair cell depolarizes, it stimulates the spiral ganglion neurons that innervate each hair cell. The axons of spiral ganglion neurons carry the frequency specific stimulus information established in the periphery to the central auditory pathway via their collective axons, known as the auditory or VIIIth nerve. When the auditory nerve enters the cochlear nucleus, it bifurcates and innervates each division: dorsal (DCN), posteroventral (PVCN), and anteroventral (AVCN) along their tonotopic axes.

Within the AVCN, there are two main cells types that preserve encoded information: stellate and bushy cells (Kandel et al., 2000; Webster and Trune, 1982). As with the majority of classification schemes, gross morphology and electrophysiological properties differentiate these two populations (Oertel, 1983;

Oertel et al., 1990; Webster and Trune, 1982; Wu and Oertel, 1984). Stellate cells have several asymmetrical dendrites and regularly spaced action potentials. They are thought to be the origin of the chopper response by which auditory nerve inputs cause the cells to fire at regular rates despite noise and variations in stimulus frequency. Conversely, bushy cells have a single dendrite with modest branching and elicit only one action potential. Bushy cells receive direct input from the auditory nerve fibers forming the sizeable, quick-response synapse known as the endbulb of Held (Cant and Morest, 1979; Fekete et al., 1984; Tolbert and Morest, 1982). Two classes of bushy cells, spherical and globular, have distinct physiological properties and projections to the pons for binaural processing. Helping to preserve auditory stimulus information, the bushy cells have a unique ability to phase lock with high precision, causing increased synchronization for auditory nerve fibers with similar characteristic frequencies (Joris et al., 1994; Smith et al., 1991; Smith et al., 1993).

From the AVCN, afferents from both the spherical and globular bushy cells innervate principle cells in three key nuclei of the superior olivary complex (SOC): the medial nucleus of the trapezoid body (MNTB), the medial superior olive (MSO) and the lateral superior olive (LSO). Principle cells in the MSO and LSO act as coincidence detectors and process the preserved sound encoded electrical signals from each ear to represent the sound source location on the azimuth plane; the MNTB principle cells act as a signal relay and sign inverter for signals being relayed to the LSO.

The MSO is specialized to process minute differences in the timing of signals arriving from each ear to aid in sound lateralization in the azimuth plane. Three

different cells types are known to exist in the MSO: multipolar, marginal and principle cells. The principle cells are most likely to be the coincidence detecting cell because of a vast dendritic arbor extending in the medial / lateral direction (coronal view), as well as along the rostral / caudal axes (Kiss and Majorossy, 1983). The principle cells receive excitatory glutamatergic input from spherical bushy cells of both the ipsilateral and contralateral AVCN. Ipsilateral spherical bushy cell axons synapse onto the lateral side of the dendritic arbor, whereas contralateral axons synapse towards the midline (Lindsey, 1975; Stotler, 1953). Termed EE (for excitatory-excitatory) cells, the principle cells in the MSO process incoming signals by summation; if the added depolarization from both ears is great enough, the principle cells will fire.

Lateral superior olive principle cells receive ipsilateral information directly from the ipsilateral AVCN (Cant and Benson, 2003; Doucet and Ryugo, 2003), but information from the contralateral cochlea is relayed through afferents that first synapse in the MNTB (Cant and Casseday, 1986; Kandler and Friauf, 1993; Kil et al., 1995; Kuwabara and Zook, 1991). To help preserve the temporal accuracy of contralateral signal transmission to the LSO, giant specialized synapses known as calyces of Held are located within the MNTB (Guinan and Li, 1990; Held, 1893; Kopp-Scheinpflug et al., 2008; Morest, 1968; Smith et al., 1991; Wu and Kelly, 1993). These synapses form between the presynaptic axon terminals of globular bushy cells in the contralateral AVCN and principle cell perikarya in the ipsilateral MNTB. The afferents form a giant cup-like structure with finger-like processes, which surround over half of the principle cell area. Additionally, principle cells of the MNTB

are approximately five times the size of other cells in the mammalian brain. These unique features enable the rapid transmission of signals, with precision, for sound processing in the LSO.

The LSO is specialized to process differences in intensity for sound localization in the azimuth plane. Detection of intensity differences is complimentary to timing differences (MSO specialty), both of which are utilized for sound discrimination in the form of electrical signals from each cochlea arriving onto principle cells. Lateral superior olive principle / binaural cells receive direct, excitatory, intensity encoded, ipsilateral information from spherical bushy cell axons originating in the ipsilateral AVCN (Cant and Benson, 2003; Doucet and Ryugo, 2003). Information from globular bushy cells in the contralateral AVCN starts out glutamatergic when synapsing in the MNTB, however MNTB principle cells invert the signal to inhibitory when projecting onto the LSO. Thus, LSO principle cells are EI (excitatory-inhibitory) in nature and depolarization and subsequent firing depends upon overcoming the inhibitory hyperpolarization of these neurons.

Binaural sound information in the azimuth plane is processed by SOC nuclei

To determine the spatial directionality of a sound source in the azimuth plane, incoming electrical signals from both ears that synapse on SOC principle cells are processed. Two main hypotheses describe how neurons differ in their azimuth coding frequencies and are known as the population and hemifield models (Phillips, 2008). First characterized in barn owls, the population model posits that individual neurons are focally tuned to narrow ranges of ITDs or ILDs, spanning the relevant frequency range for that animal. Responsiveness or sensitivity arises from the

differing path lengths between the two ears and the selective neurons that respond to sound stimuli. This hypothesis supports a coincidence detection model to describe the arrival and processing of sound in MSO principle neurons and is known as the Jeffress model for neural processing (Jeffress, 1948). The model relies on a series of coincidence detecting cells (principle cells) and neural delay lines to these cells, comprised of serial connections of each axon to adjacent coincidence-detecting cells. Coincidence detecting cells receive excitatory neural signals from both the left and right ears and uses the delay lines to equalize the differing distances signals must traverse from each ear. Based on this output, the location of the sound in the azimuth plane can be determined. Importantly, depolarization of a principle cell only occurs when inputs from both neural pathways arrive in near coincidence. Excitatory information synapsing from a single delay line axon from one side is insufficient to generate action potentials; signals must arrive from both ears almost coincidently to depolarize the principle cell.

The Jeffress model is the generally accepted model for neural processing in birds and mammalian MSO, however this hypothesis is controversial. For example, McAlpine and colleagues (2001) used single neuron recordings in guinea pigs to show that some tuning frequencies of the ITD were inconsistent with the Jeffress model and many of the calculated best ITDs were beyond the physiological range of detection. The authors hypothesized this may stem from uncharacterized inhibitory projections that were targeting the MSO neurons. Additional studies that blocked these inhibitory projections from the MNTB and the lateral nucleus of the trapezoid

body (LNTB) were shown to alter ITD tuning curves, once again, shifting peaks outside of their physiological range (Brand et al., 2002).

Modeling how binaural information is processed in the LSO has been more challenging than the MSO. Lateral superior olive principle neurons have a chopper-like response in which a highly regular discharge pattern of repetitive firing is seen. Due to the extensive dendritic arborization of principal cells and diffuse synaptic inputs from the AVCN, MNTB and other nuclei, a simple linear relationship between bilateral inputs and subsequent output is implausible. Rather than passive membrane properties, LSO principle neurons are thought to have active membrane properties allowing for rapid temporal firing patterns (Adam et al., 2001). Thus, the specification of a universal principle cell binaural model for lateralizing sound in space is misleading. An alternate hypothesis, the hemifield model, appears to be more suited for describing binaural information processing in the LSO.

Auditory evoked potential studies in humans and animals have demonstrated that interaural level and timing differences are major determinants for high fidelity acoustic perception near the midline (McAlpine and Grothe, 2003; Mills, 1958; Phillips and Brugge, 1985). In humans, this relationship is linear for small and medium level and timing differences but is non-linear for larger differences (Yost, 1974, 1981). Such data suggest neuronal subpopulations capable of precise acoustic perception along the midline and distinguishing broad hemifield level and timing differences more laterally.

In contrast to the narrow range of intensity differences proposed by the Jeffress model, the hemifield model posits that neurons are tuned to a broad range

of interaural timing and intensity variations, but a subset of neurons are also specialized for sound detection near the midline, or medial boarder between hemifields. A sound source emanating from the midline of the azimuth plane will activate two distinct channels of neurons, in either the left or right hemifield, and those spanning the medial boarder. Contrasting the Jeffress model, where the timing or spike rate of neuronal firing encodes the magnitudes of timing and intensity differences between left and right ears, the responsiveness or sensitivity of neurons in the hemifield model arises from the distribution of firing activity across a small number of neural channels. (Dingle et al., 2012; Phillips, 2008; Phillips and Hall, 2005). A number of recent psychoacoustic studies support the hemifield model of neural processing with two populations of neurons.

Inaccuracies in the perceptual representation of a sound source can be elicited under specific conditions. For example, a phenomenon known as the auditory saltation illusion occurs when the processing of sound from one side of the head interferes with a subsequent sound on the opposite side, causing signal contamination. The perceived sound source is neither from the left nor the right, but along the midline (Bremer et al., 1977; Phillips and Hall, 2005; Shore et al., 1998). Further, a similar illusion is evoked during selective adaptation when a population of neurons within the LSO adapts to a tone at a specific frequency. Once saturated, further stimulation with the adapter tone and frequency causes a shift in perception (Phillips et al., 2006; Phillips and Hall, 2005). Additional support for the hemifield model comes from studies employing gap detection (Boehnke and Phillips, 1999) and spatial release from masking (Phillips et al., 2003) paradigms.

The classic Jeffress model of neural processing posits that neurons are focally tuned to narrow ranges of timing and intensity delays that span the relevant frequency range for that animal. The spatial location in the azimuth can be determined depending upon which principle cells fire maximally. Single cell electrophysiological recordings of MSO principle cells support this population model of neural processing; however firing patterns of LSO principle cells is drastically different. Auditory evoked response recordings from humans and animals propose a two-neuron model to describe how LSO principle cells process differences in level intensities. This model describes two different populations of neurons: those optimized for firing when sound originates from the left or right hemifield, and a second population that spans the midline between the hemifields.

In both models of sound processing, the transmission of auditory signals from both ears to integration centers in the SOC is critical. To achieve temporal fidelity of signal transmission, fibers in the auditory brainstem are myelinated, increasing propagation speed and accuracy of dissemination. Herein, we investigate the consequence of dysfunction myelin on sound lateralization. A decrease in myelin membrane resistance due to the absence of electrically sealing Claudin11 tight junctions produces dysfunctional myelin, most notably for small diameter myelinated fibers. Larger diameter fibers have a greater number of wraps, increasing resistance and offsetting the tight junctions (Devaux and Gow, 2008). Using the *Cldn11*$^{-/-}$*Tg*$^{+/-}$ mouse model, we conclude that sound lateralization mirrors a two-neuron hypothesis. Stimulating sound near the midline elicits a steep, linear pattern neural response, whereas and a non-linear gradual response is perceived as sound is

lateralized to a hemifield. Data collected from dysfunctional myelin mutant mice highlight the importance of small diameter myelinated axons in the auditory pathway.

MATERIALS AND METHODS

Generation of transgenic mice

The *Osp20* transgene construct (GS605) comprises a 22 kb *Sau3A I* fragment of genomic sequence from 5 kb upstream of the transcription start site in exon 1 to 1.9 kb downstream of the first polyadenylation site in exon 3. The unique *Acc65 I* site near the 5' end of intron 1 was blunted – out distinguishing the transgene from the endogenous *Cldn11* gene during qPCR analysis. The genomic fragment was cloned between two *Not I* sites in a *pUC18* – based vector (Gow et al., 1992) and was excised and phenol : chloroform – purified from an agarose gel slice for male pronuclear injection. This allele is referred to as Tg(Cldn11)605Gow (MGI:5306245), and for the purposes of this dissertation as $Tg^{+/-}$. Transgene expression was demonstrated for the testis and inner ear, but not brain (Wu et al., 2012). Additionally, this transgene restored the known male sterility phenotype in $Cldn11^{-/-}$ mice (Gow et al., 1999) and the premature hearing loss stemming from diminished endocochlear potential (Gow et al., 2004) (unpublished data).

Double mutant F1 $Cldn11^{+/-}$:Tg(Cldn11)605Gow$^{Tg/+}$ ($Cldn^{+/-}$:$Tg^{+/-}$) mice were generated by breeding males from Tg(Cldn11)605Gow with $Cldn11^{-/-}$ females. These mice were sib-mated to generate F2 (and beyond) $Cldn11^{-/-}Tg^{+/-}$ mice (as well as control $Cldn11^{+/-}Tg^{+/-}$) for experiments. These mice were used for all experiments except where noted.

Auditory brainstem responses (ABRs) and interaural level delays (ILDs)

Mice were anesthetized by intraperitoneal (i.p.) injection of freshly prepared 2,2,2-tribromoethanol in sterile phosphate buffered saline (PBS) (Cellgro, Manassas,

VA) at a dose of 375 mg / kg. Mice were monitored for the absence of tail, foot, and ear reflexes, as well as reduced respiratory rate, all of which are indicative of effective anesthesia. Once confirmed, mice were injected i.p. with 200 mg / kg chloral hydrate (Sigma, St Louis, MO) in sterile phosphate buffered saline to maximize anesthesia time (Chapter 1), and placed on a 39°C pad (Maheras and Gow, 2013). The fur along the top of the head and middle of the back of each mouse was sterilized / moistened with alcohol pre pads (Triad Group, INC, Harland WI) and subdermal platinum electrodes (Grass Technologies, West Warwick, RI) were positioned at the left and right mastoids (negative), vertex (reference) and hindquarters along the midline (ground) for recording.

For auditory brainstem responses (ABR), mice were presented with 512 pure-tone stimuli in 10 dB SPL decrements from 80 – 20 dB SPL at 32 kHz (102 μsec duration; Blackman envelope) at a stimulus rate of 29.1 / sec. Both right and left ears were tested successively and ipsilateral EEGs were pre-amplified (x 100,000), band pass filtered (0.3 – 3 kHz), and recorded for 12.5 msec (Sepwin software version 5.1, Intelligent Hearing Systems, Miami, FL). Interaural level delay (ILD) measurements were collected once a symmetrical hearing threshold of ≤ 40 dB SPL was confirmed.

For ILDs, mice were presented with 2,048 pure-tone stimuli at 32 kHz (102 μsec duration; Blackman envelope) and a stimulus rate of 29.1 / sec. All EEGs were pre-amplified (x 200,000), band pass filtered (10 – 3000 Hz), and recorded for 25 msec (Sepwin software version 5.1, Intelligent Hearing Systems, Miami, FL). The advanced module was utilized to present ipsilateral and bilateral stimuli of differing intensities to each ear. First, midline level delays were obtained by playing 70 dB

SPL to either the left ear or right ear, then simultaneously. Subsequently, left ear stimulus intensity was decreased to 68, 65, 60, 50, then 40 dB SPL in conjunction with and without a 70 dB SPL stimulus presented to the right ear. This process was reversed and right ear stimuli were reduced to 68, 65, 60, 50, then 40 dB SPL in conjunction with and without a 70 dB SPL stimulus presented to the left ear. See Table 3.1 for clarification.

To obtain binaural interaction components (BICs), we determined that post-filtering traces from 10 – 500 Hz was optimal. First, a midline BIC was acquired by summing monaural left and right ipsilateral traces (μV weighted) obtained at 70 dB SPL, then subtracting this summed trace from the binaural trace obtained when 70 dB SPL was presented bilaterally. Two midline BIC traces were obtained, one from each ear. Subsequent ILD BIC traces were generated in a similar fashion. Left ear BIC were generated by adding the monaural left ipsilateral trace obtained at <70 dB SPL to the monaural right ipsilateral trace obtained at 70 dB SPL. The resulting summed monaural trace was then subtracted from the corresponding binaural trace (See Figure 3.1). This process was repeated for the right ear. After the completion of experiments, the mice were allowed to recover in a separate cage on a 39°C heating pad (Delta phase isothermal pad, Braintree Scientific, Braintree, MA) until they regained normal activity and could be placed back in their home cage.

Figure 3.1 – Schematic for calculation of the BIC

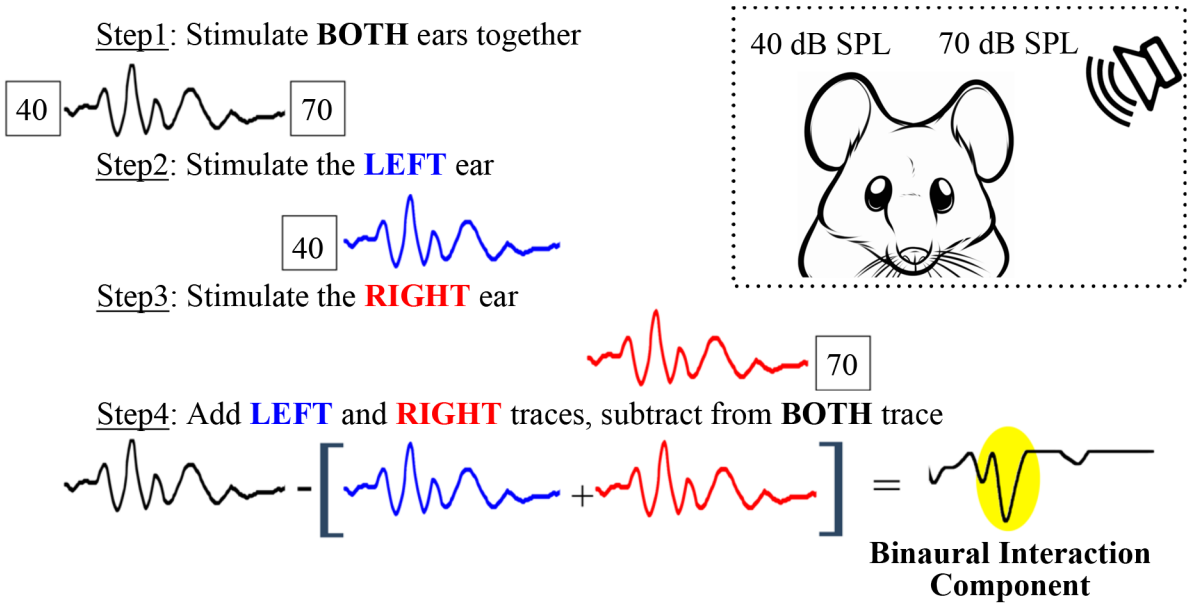

A Binaural traces were obtained by simultaneously stimulating both ears with differing sound intensities and the response recorded. Left and right ear monaurals were obtained by individual stimulation with corresponding sound intensity and traces recorded. The binaural interaction component was generated by summating the two monaural traces and subtracting from the binaural.

Dextran Labeling

CD – 1 female mice (Crl:CD1(ICR) Charles River, Wilmington, MA) were perfused with 10 ml of freshly oxygenated artificial cerebral spinal fluid (aCSF: 126mM NaCl, 3mM KCl, 2mM $CaCl_2$, 2mM $MgSO_4$, 1.25 mM NaH_2PO_4, 26 mM $NaHCO_3$, 10mM dextrose, pH 7.4) at a rate of 2 ml / min (PHD 22/2000 Syringe Pump Infusion, Harvard Apparatus, Holliston, MA). Brains were promptly removed and 2 ml coronal sections isolating the lower auditory brainstem nuclei were harvested extending from interaural -1 to -3 using a mouse anodized aluminum matrice (BS-AL 5000C, Braintree Scientific, Braintree, MA). Coronal sections were allowed to rest for an hr in a 60 x 60 millimeter petri dish (BD Falcon, Franklin Lakes, NJ) filled with aCSF and perfused continuously with carbox gas (95% O_2, 5% CO_2). Custom microinjection needles 10 – 20 μm in diameter were pulled from glass capillary tubes using a puller (Narishige, Tokyo, Japan). Needles were back-filled with 3 μl of a 50 mg / ml solution containing Alexa488 labeled dextran dye (CAT#:D22910, 10000MW, Molecular Probes, Eugene, OR) then attached onto a digital microdispensor (CAT#:53506-121, VRW International, Radnor, PA) clamped onto a micromanipulator (Narishige, Tokyo, Japan).

Mouse brain slices were transferred, one-by-one from the resting dish to a separate 60 mm dish containing freshly carbox-perfused aCSF under a stereomicroscope (Leica Zoom 2000, Leica, Solms, Germany). Approximately 30 to 50 nl of dextran dye was quickly injected into a single location and the brain slice was immediately returned to the resting dish for four hrs to allow sufficient time for endocytosis of the dye and transport along axons. During this time, the carbox-

perfused aCSF was replaced every hr and pH monitored. After labeling, brains were immersion-fixed overnight with shaking at 4°C in a fresh 60 mm dish containing 4 % PFA in phosphate buffer, pH 7.2. The following day, brains underwent five x 15 min washes in PBS in preparation for vibratome sectioning.

Vibratome

Dextran dye-labeled coronal mouse brain sections were removed from PBS, blotted dry, placed into a 15 x 15 mm cryomold (Electron Microscopy Science, Thermo Fisher Scientific, Waltham, MA), and overlaid with 4 % low-melt agarose (Agarose Products, Nesbit, MS). The agarose was allowed to solidify at room temperature for 10 min before being moved to 4°C for 20 min. Molds were removed from 4 C, the gel excised, trimmed, and superglued to a vibratome chuck. Coronal sections of approximately 70 μm thick were cut at room temperature and transferred using an artist brush into individual wells of a 24-well dish (Fisher) containing PBS.

Immunofluorescence staining of vibratome sections

Individual 70 μm vibratome sections were stained in separate wells of a 24-well plate using a minimum of 200 microliters solution during each step. Sections were permeabilized in blocking solution comprised of TBSGBA (1X TBS pH 7.5, 0.1 % gelatin, 1 % BSA, 0.05 % sodium azide, 2 % goat serum) and 0.5 % triton X-100 for one hr. Blocking solution was removed and replaced with primary antibody (See Table 3.2) diluted fresh in blocking solution. Primary antibody incubation was carried out for three overnight periods with gentle agitation at 4 C. Primary antibody liquid was removed and washed with PBS plus 0.5 % triton X-100, twice, for 30 min. Wash solution was removed and replace with the secondary antibody (See Table

3.3) diluted in blocking solution. Slices were incubated with secondary antibody for six hrs at room temp with gentle agitation. The secondary antibody liquid was removed and replaced with DAPI solution diluted in PBS plus 0.5 % triton X-100 for ten min. DAPI solution was removed and the sections washed with PBS plus 0.5 % triton X-100, twice, for thirty min. Sections were free-floated in PBS and carefully mounted to slides using a paintbrush. Sections were covered with Vectashield mounting medium (Vector Labs, cat#H1000), coverslipped, and sealed with nail polish.

Confocal microscopy and axon diameter measurements

Confocal fluorescence image stacks of dextran-labeled axons were captured using a Leica DM5500B microscope equipped with a Plan Apo 63x lens, Yokogawa spinning disk confocal with Argon/He/Ne lasers (QLC100, Visitech International, Sunderland, United Kingdom) and a Hamamatsu Orca ER^2 digital camera. Confocal image stacks were acquired using a 63x Plan Apo oil-immersion objective lens (*n.a.* = 1.4) in 0.2 μm increments through 70 μm vibratome sections.

After collection, stacks were quantified using Image J software. The location of each fiber within a stack was determined and mini stacks were flattened into single through-focus images for analysis of individual fibers. Axons were analyzed only if the entire length could be followed with confidence throughout the image stack. Axon diameters were manually drawn at random along the length of the axon, resulting in 20 – 30 measurements per fiber. To discern contralateral auditory fibers from pyramidal fibers, only axons attached to a calyx of Held were analyzed. Average axon diameters from multiple mice were used to generate the histograms

shown in Figures 3.5 and 3.6 using 0.2 μm as the binning factor and fit with a Gaussian distribution (Graphpad).

Cryostat sectioning of PFA-perfused brain

Cldn11$^{-/-}$*Tg*$^{+/-}$ mice were injected i.p. with 400 mg / kg avertin, and monitored for the absence of reflexes, signifying deep anesthesia. The chest cavity was exposed using scissors, and mice were perfused transcardially with 4 % PFA (Sigma Aldrich, St Louis, MO) in 0.1 M phosphate buffer pH for 15 min. Brains were immediately removed and place in a 25 % sucrose solution over night at 4 C. Sucrose solution was changed the next morning and brains prepped for embedding that afternoon. Brains were removed from the sucrose solution, blotted dry on a Kimwipe (Kimberly-Clark Corp, Roswell, GA) placed in a plastic cryomold (Tissue-tek, cat #4557, Torrance, CA), and covered with OCT (Tissue-tek OCT, Andwin Scientific, Schaumburg, IL). Blocks were gradually frozen using ice-cold 2-methyl butane and stored at - 80°C until cutting.

Frozen blocks were cut using a Shandon Electric Cyrotome (Pittsburgh, PA). Sagittal 10 μm sections were collected on charged superfrost slides (Fisherbrand, Thermo Fisher Scientific, Waltham, MA) beginning at the midline and progressing laterally. Every fifth section (50 μm) was collected and stored at - 80°C until staining.

Immunofluorescence staining for cryostat sections

Superfrost slides were removed from the - 80°C and immediately thawed in a glass vial containing PBS and washed twice for five min. Slides were permeabilized with methanol for 20 min at 4°C. Slides were washed in PBS, excess liquid removed, outlined brains using a pap pen, and immersed with blocking solution (TBSGBA +

2 % goat serum) for an hr. Blocking solution was removed and replaced with primary antibodies (Table 3.4), diluted in blocking solution. Primary antibodies were incubated over night at room temperature while rocking. Primary antibody was removed and slides washed with PBS. Secondary antibodies (Table 3.5) diluted in blocking solution were placed onto sections for three hrs while rocking at room temperature. Slides were washed once more in PBS, the pap pen removed using a cotton bud soaked with chloroform, a drop of Vectashield mounting medium added over the section and coverslipped. Slides rested overnight, excess mounting medium removed, and edges of the coverslip sealed with clear nail polish the following day.

RESULTS

Cldn11$^{-/-}$*Tg*$^{+/-}$ mice have altered ABRs

Evoked potentials can be elicited using a number of sensory modalities, but our interest lies in the well-characterized ascending auditory pathway. Figure 3.2A shows representative ABR threshold series traces from *Cldn11*$^{+/-}$*Tg*$^{+/-}$ and *Cldn11*$^{-/-}$ *Tg*$^{+/-}$ mice and demonstrates several characteristics of an ABR threshold series. First, the five characteristic peaks and troughs of the ABR are discernable for both groups of mice with Wave I arising approximately 1.5 – 2 msec post stimulus and each subsequent waveform in approximate one msec intervals thereafter. Second, the latency of each wave increases slightly as stimulus intensity is progressively decreased. Finally, the lowest stimulus intensity that elicits an identifiable Wave I is regarded as the hearing threshold of the mouse. Figure 3.2B shows that the hearing thresholds between *Cldn11*$^{+/-}$*Tg*$^{+/-}$ and *Cldn11*$^{-/-}$*Tg*$^{+/-}$ mice are indistinguishable.

One detectable difference in the ABR trace of *Cldn11*$^{-/-}$*Tg*$^{+/-}$ mice compared to controls is the increased Wave V latency, indicated by the red 'X' along the *x*-axis (Figure 3.2A). The latencies of Waves I – IV in *Cldn11*$^{-/-}$*Tg*$^{+/-}$ mice are normal at the level of both the absolute ABR and interpeak latencies (Figure 3.2C). Absolute interpeak latency, Wave V – Wave I latency, is calculated to correct for variability in Wave I onset. Figure 3.2C shows the absolute interpeak latency for *Cldn11*$^{+/-}$*Tg*$^{+/-}$ and *Cldn11*$^{-/-}$*Tg*$^{+/-}$ mice, illustrating a significant increase in *Cldn11*$^{-/-}$*Tg*$^{+/-}$ mice: $F_{9,100} = 25.25$, $p < 0.0001$. Post hoc testing using Bonferroni's multiple comparisons test indicates significant differences are present at every intensity level (80 – 40 dB SPL) stimulated. When frequency of the stimulus is varied, the delay in Wave V persists

(data not shown). These data suggest the delay in Wave V is not a function of stimulus parameters, but a consequence of eliminating Cldn11 tight junctions.

The absolute interpeak latency can be separated into two components based on location of signal generators: central (V – II) or peripheral (II – I) nervous system. Similar to absolute interpeak latency, central interpeak latency of *Cldn11*$^{-/-}$*Tg*$^{+/-}$ mice is significantly increased compared to controls: $F_{9,100} = 21.42$, $p < 0.0001$. Bonferroni post hoc tests reveal significant increases for all intensity levels. Contrasting absolute and central interpeak latencies, peripheral interpeak latency was significant ($F_{9,100} = 2.938$, $p = 0.0039$), however post hoc analysis comparing individual intensities is not significant. Together, these data demonstrate that *Cldn11*$^{-/-}$*Tg*$^{+/-}$ mice have an in increase Wave V latency and elongated central interpeak latency, suggesting slowed conduction along central components of the lower auditory brainstem.

Cldn11$^{-/-}$_Tg_$^{+/-}$ mice have altered neural processing in the auditory brainstem

The characteristic waveform traces of the ABR are evoked when auditory information is rapidly transmitted to the generators, persevering the temporal accuracy of signal transmission are myelinated fibers along the auditory brainstem. The function of myelin is to increase the speed of signal transmission, preserving temporal accuracy and increasing long-range signal fidelity. The repetitive delay in central components of the ABR in *Cldn11*$^{-/-}$*Tg*$^{+/-}$ mice suggests that small diameter myelinated fibers are present in the lower auditory brainstem and are associated with the transmission of electrical signals between these components. Because preserving temporal transmission is imperative for the processing of sound

Figure 3.2 – ABRs reveals delayed Wave V latency in *Cldn11*$^{-/-}$*Tg*$^{+/-}$ mice

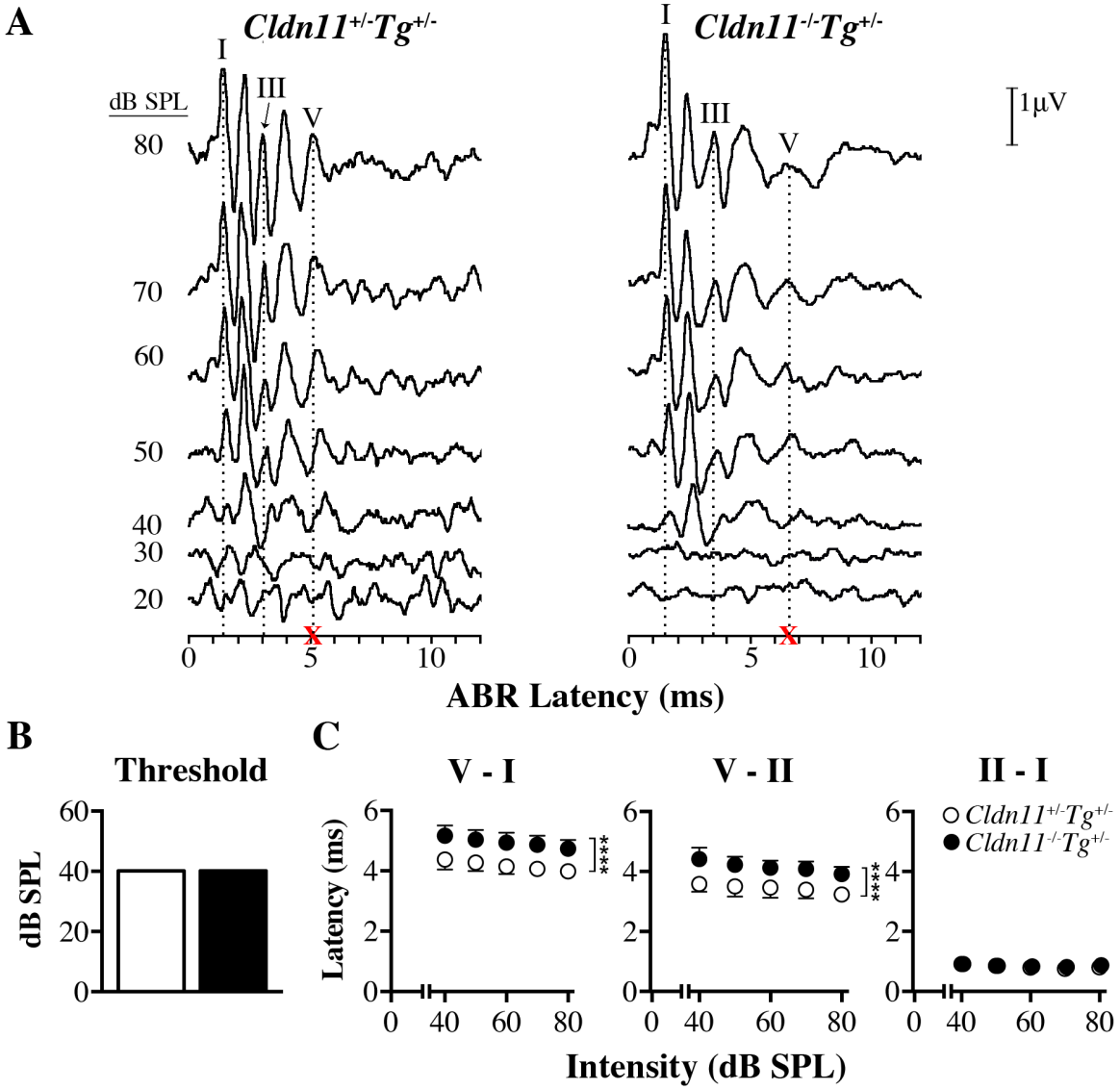

(A) Representative ABR traces collected from *Cldn11*$^{+/-}$*Tg*$^{+/-}$ and *Cldn11*$^{-/-}$*Tg*$^{+/-}$ mice at 32 kHz, 80 – 20 dB SPL. Characteristic Waves I, III, and V are indicated in the 80 dB SPL trace with dotted vertical lines drawn down to convey latencies. The delay in Wave V latency for *Cldn11*$^{-/-}$*Tg*$^{+/-}$ mice is discernible at all intensities. **(B)** Threshold quantification for *Cldn11*$^{+/-}$*Tg*$^{+/-}$ and *Cldn11*$^{-/-}$Tg$^{+/-}$ mice are identical. **(C)** Total interpeak latency, Waves V – I, is significantly different between *Cldn11*$^{+/-}$*Tg*$^{+/-}$ and *Cldn11*$^{-/-}$*Tg*$^{+/-}$ mice at all intensities. Upon further examination, central interpeak components (Waves V – II) remain significantly latent, whereas peripheral components (Wave II – I) are not. *Cldn11*$^{-/-}$*Tg*$^{+/-}$ data points in II – I are right-shifted about the abysses for clarification. Data values are plotted as mean ± SD; 10 ≤ *n* ≤ 12; ****$p < 0.0001$.

localization cues, we explored the ramification of slowed conduction on neural processing.

One method to non-invasively interrogate neural processing is to measure the binaural interaction component (BIC) computed from processed ABR traces (Figure 3.1). Binaural ABR traces contain three pieces of information: ipsilateral transmitted from the ipsilateral ear, contralateral relayed via the MNTB, and finally binaural information. Binaural interaction component information is extracted from binaural ABR traces by summing each monaural component (ipsi- and contra- lateral) and subtracting from the binaural signal. The resulting BIC traces represents the output from LSO principle cells where bilateral information has converged from ipsilateral and contralateral pathways.

Figure 3.3A shows representative BIC traces generated via interaural level delays (ILDs) using difference stimulus intensities for each ear of 0, 2, 5, 10, 20, and 30 ΔdB SPL. The corresponding ABR trace at 70 dB SPL is shown above the BIC trace series is, and is labeled for Waves I, III and V. The characteristic BIC trough, known as the DN1 trough, is indicated by a black dot for each BIC generated. The DN1 trough represents the measured interaction component; the computed output from LSO principle cells to which bilateral sound information has synapsed. The latency of the BIC occurs between Waves IV and V of the ABR trace, indicating the trough is generated immediately after the information reaches the SOC, but precedes termination of lateral lemniscus fibers into the inferior colliculus (Wave V) (Appendix C.1).

The interaction component, DN1, contains two pieces of information reflecting neural processing in the SOC, the amplitude and the latency. Appendix C.2 illustrates the raw latency and amplitude values of the DN1 trough for *Cldn11*$^{+/-}$*Tg*$^{+/-}$ and *Cldn11*$^{-/-}$*Tg*$^{+/-}$ mice. To control for initial waveform onset, each variable between groups, data values are normalized to either the respective latency or amplitude recorded when simulated sound was directly in front of the animal at the midline (Δ0 dB SPL). Figure 3.3B shows the normalized latency of the DN1 trough for *Cldn11*$^{+/-}$ *Tg*$^{+/-}$ and *Cldn11*$^{-/-}$*Tg*$^{+/-}$ mice. A one-way ANOVA comparing normalized latency of the DN1 trough to intensity difference indicates a significant difference between *Cldn11*$^{+/-}$*Tg*$^{+/-}$ and *Cldn11*$^{-/-}$*Tg*$^{+/-}$ mice: $F_{11,120} = 8.334$, $p < 0.0001$. Bonferroni post hoc testing reveals a significant increase in latency when sound intensity varies by 20 or 30 dB SPL for *Cldn11*$^{-/-}$*Tg*$^{+/-}$.

The second feature examined was the amplitude of the DN1 trough. Figure 3.3C shows normalized amplitude of the DN1 trough for *Cldn11*$^{+/-}$*Tg*$^{+/-}$ and *Cldn11*$^{-/-}$ *Tg*$^{+/-}$ mice. Unlike latency values, amplitude is highly variable, indicated by the large deviations present at all ILD intensities stimulated for both groups of animals. There are several strategies for measuring amplitude of a waveform. First, the conventional approach measures amplitude from the bottom of the trough to the tip of the subsequent waveform peak or to the preceding waveform peak. In the BIC, both bounding peak waveforms are inconsistent in both *Cldn11*$^{+/-}$*Tg*$^{+/-}$ and *Cldn11*$^{-/-}$*Tg*$^{+/-}$ mice. The best approach was to measure amplitude from the base of the DN1 trough to the - 5 msec baseline recording prior to sound stimulus presentation (0 msec). This region was unbiased during waveform manipulation. A one-way ANOVA

indicates normalized amplitude of the DN1 trough was similar between *Cldn11*$^{+/-}$*Tg*$^{+/-}$ and *Cldn11*$^{-/-}$*Tg*$^{+/-}$ mice, $F_{11,120} = 0.6553$, $p = 0.7778$.

With neurophysiology data, latency is the stronger parameter measurement compared to amplitude. It is well known that amplitude values, regardless of calculation method, are highly variable in nature. In addition, when a sound source is located in the lateral hemifields (increased intensity difference), amplitude is imprecise in specifying a sound source due to ILDs having a maximal response over a broad lateral azimuth (Makous and Middlebrooks, 1990). This variability is seen between and within mice of both groups, indicated by raw (Appendix C.2) or normalized (Figure 3.3C) amplitudes. Combined, these data sound show that lateralization measured by the DN1 trough is significantly different between *Cldn11*$^{+/-}$ *Tg*$^{+/-}$ and *Cldn11*$^{-/-}$*Tg*$^{+/-}$ mice, suggesting a difference in sound lateralization ability.

The auditory brainstem in mice contains myelinated small and large diameter fibers

The significant increase in Wave V of the ABR in *Cldn11*$^{-/-}$*Tg*$^{+/-}$ mice is indicative of slowed conduction velocity along the auditory pathway. Interpeak latency calculations show a significant increase in central, but not peripheral interpeak latencies. These findings corroborate previous studies examining compound action potentials (CAPs) of *ex vivo* optic nerves from *Cldn11*$^{-/-}$ mice indicating that conduction velocity is severely slowed along small diameter fibers (< 1.2 μm). Furthermore, the difference in sound lateralization ability between CLdn11+/-Tg+/- and Cldn11-/-Tg+/- mice suggests a functional consequence to slowed conduction within the auditory brainstem. The literature has eluded to the

Figure 3.3 – Computed DN1 interaction trough indicates abnormal latency in *Cldn11*$^{-/-}$*Tg*$^{+/-}$ mice

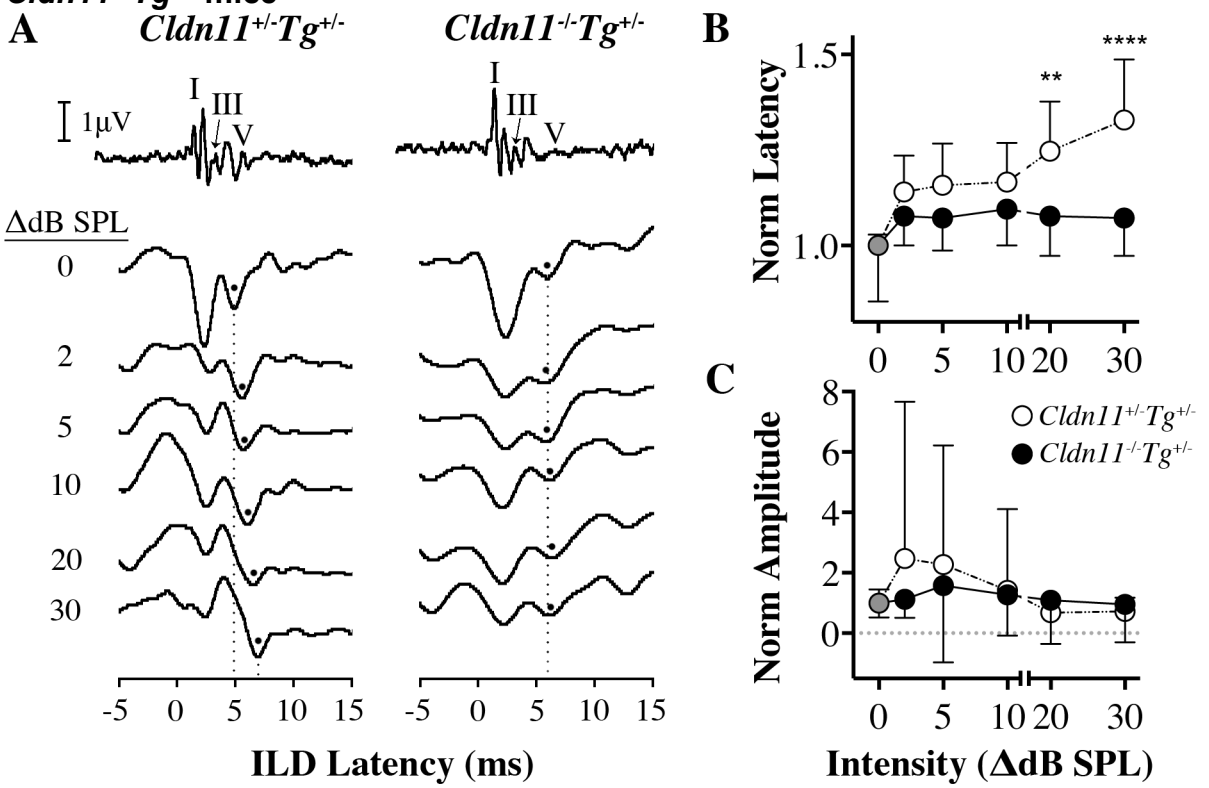

(A) Representative BIC traces calculated for intensity differences ranging from 0 – 30 dB SPL for Cldn11$^{+/-}$*Tg*$^{+/-}$ and *Cldn11*$^{-/-}$*Tg*$^{+/-}$ mice. BIC traces are aligned with corresponding ABR trace to substantiate BIC emergence between Waves IV and V. Crosshatch indicates the binaural trough, DN1. **(B)** Normalized latency of DN1 trough for varying intensity differences. **(C)** Normalized amplitude of DN1 trough for varying intensity differences. Grey circles represent the normalized value for both Cldn11$^{+/-}$*Tg*$^{+/-}$ and *Cldn11*$^{-/-}$*Tg*$^{+/-}$ mice. Data values plotted as mean ± SD; $10 \leq n \leq 12$; $^{**}p < 0.01$, $^{****}p < 0.0001$.

presence of myelinated large diameter contralateral and small diameter ipsilateral fibers, however direct quantitation is lacking (Doucet and Ryugo, 2003; Wu and Kelly, 1991, 1992b; Wu and Oertel, 1984).

Figure 3.4A illustrates the size of key brainstem nuclei using calbindin staining, highlighting the extent to which information must be relayed for neural processing. The simplified schematic in Figure 3.4B depicts the three fiber tracts are responsible for relaying auditory information from each ear for neural processing in the SOC along the contralateral pathway: between the CN and contralateral MNTB, the MNTB and LSO, and from the CN to the LSO along the ipsilateral pathway (blue, pink, and green fiber tracts respectively. Because electrophysiology data alludes to small diameter myelinated fibers within this relay network, methodological studies were undertaken to measure axon diameters between relay nuclei within this network.

Contralateral fibers relaying information from the CN to the contralateral MNTB must be speedy, preserving temporal accuracy of signal transmission (Guinan and Li, 1990; Kopp-Scheinpflug et al., 2008; Wu and Kelly, 1993). Two features important for rapid transmission, and subsequent relaying of information, are the giant calyx of Held synapse and myelination of axons. Figure 3.5 confirms myelination of contralateral fibers by immunofluorescence staining of sagittal sections through the trapezoid body tract. Axons are stained with neurofilament light (NFL, red), myelin is indicated with myelin basic protein (MBP, green), and nuclei identified with DAPI (blue).

Figure 3.4 – Auditory brainstem schematic illustrating key fiber tracts transmitting binaural information

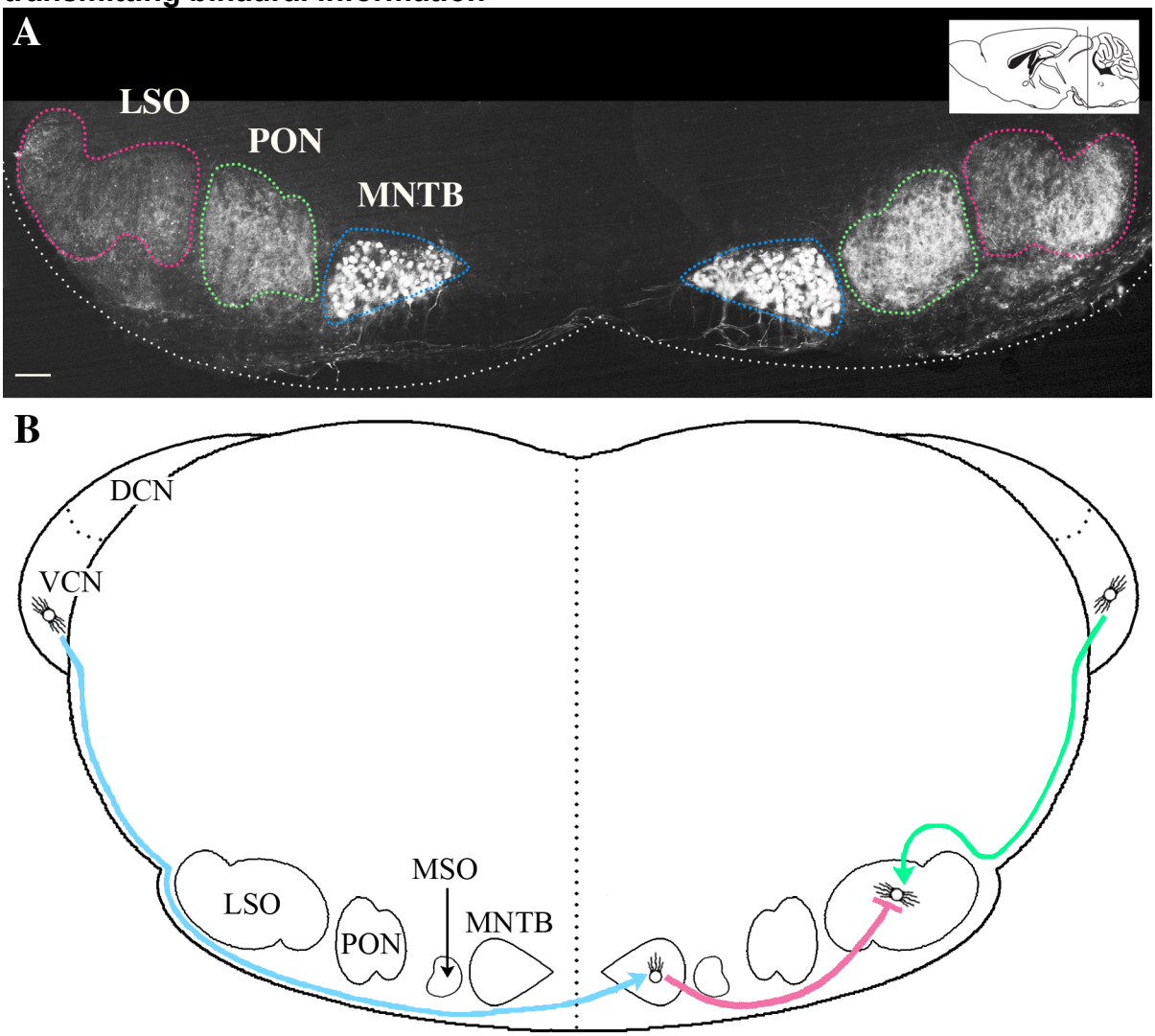

(A) Calbindin staining was used to identify key brainstem nuclei associated with binaural interaction. Principle cells of the MNTB (outlined in blue) are pronounced, as well as their axonal projections. Moreover, the PON (outlined in green) and LSO (outlined in pink) are observable, presumably from MNTB priciple cell innervation. Scale bar = 200 μm. **(B)** Lower brainstem schematic depicting three necessary fiber tracts and their nuclei relays that transmit binaural information to priciple cell integrators in the LSO. The blue trajectory represents contralateral information transmitted from the AVCN to the contralateral MNTB; pink trajectory portrays the subsequent relay of contralateral information from the MNTB to LSO; green trajectory illustrates ipsilateral sound information transferred from the AVCN directly to the LSO.

Figure 3.5 – Myelinated axons are present in the auditory pathway

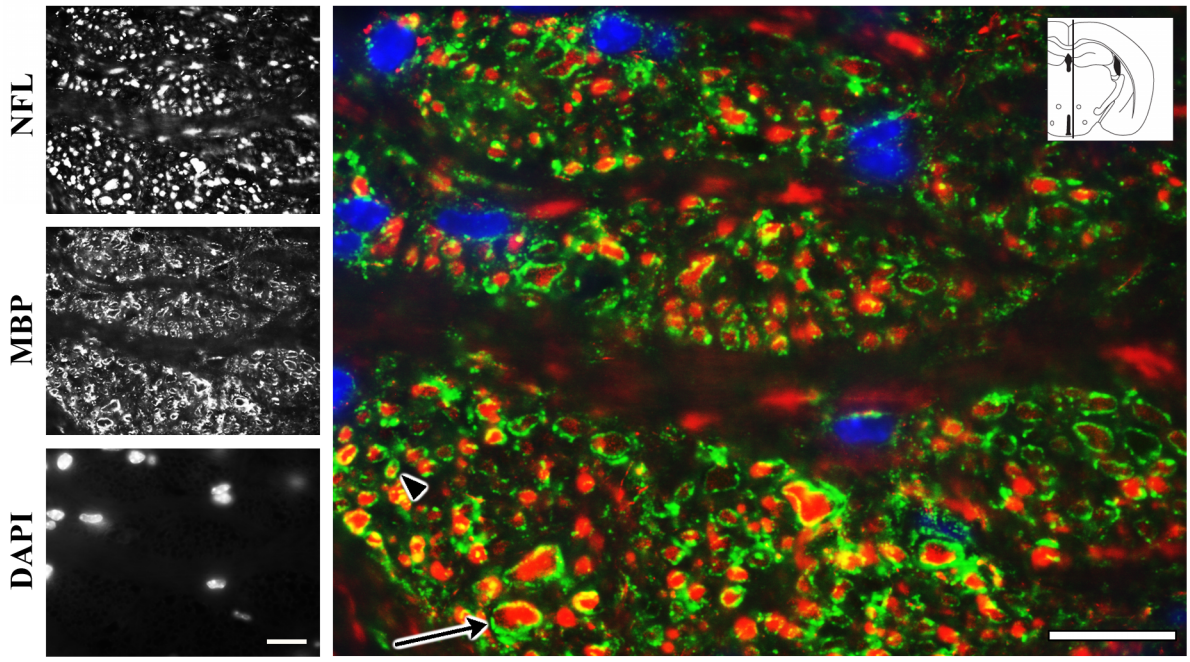

Representative sagittal brainstem section of the trapezoid body fiber tract (see insert). NFL (red) is used to illustrate all axons present, myelin (green) is illustrated with MBP, and nuclei (blue) are visible with DAPI staining. Distinct fiber bundles are evident, interspersed with transverse pyramidal fibers. Scale bar = 20 μm.

Appendix C.3 quantifies the proportion of myelinated axons within the trapezoid body and pyramidal fiber tracts, prior to synapsing with, and in the presence of, MNTB, principle cell innervation. Because axons of AVCN bushy cells (forming the trapezoid body fiber tract) decussate at the midline before innervating contralateral MNTB principle cells, direct midline sagittal sections will contain trapezoid body fiber bundles in the absence of MNTB principle cells. Analyzing sagittal brainstem sections indicates a conservative 98.7 ± 0.64 % of axons are myelinated.

A labeled fluorescent dextran conjugate dye was injected laterally to the MNTB, allowing axonal uptake, transport, and subsequent labeling of contralateral fibers forming calyces of Held. Figure 3.6A illustrates a representative calyx of Held synapse, complete with contralateral fiber labeling from the dextran conjugated dye (green) and co-stained for MNTB principle cells (Calbindin^{+}, red) and nuclei (DAPI, blue). The histogram in Figure 3.6B shows contralateral axon diameters measured from dextran labeled fibers forming a calyx. The distribution was normally distributed, indicated by Gaussian curve fitting, with average diameter 3.33 ± 0.59 μm and ranging 2.22 – 5.13 μm. Figure 3.6C shows variability along individual contralateral axons, consisting of 20 – 25 measurements per fiber. As expected, and implicated for other species from published studies, these data confirm that contralateral fibers diameters are greater than a micron and conduction velocity along contralateral fiber would be minimally affected in *Cldn11*$^{-/-}$*Tg*$^{+/-}$ mice.

Ipsilateral fibers relaying information directly from the CN to the LSO have been alluded to in the literature as being small in diameter, however obtaining a

Figure 3.6 – Morphometric analysis of contralateral trapezoid body fibers reveals axons are large in diameter

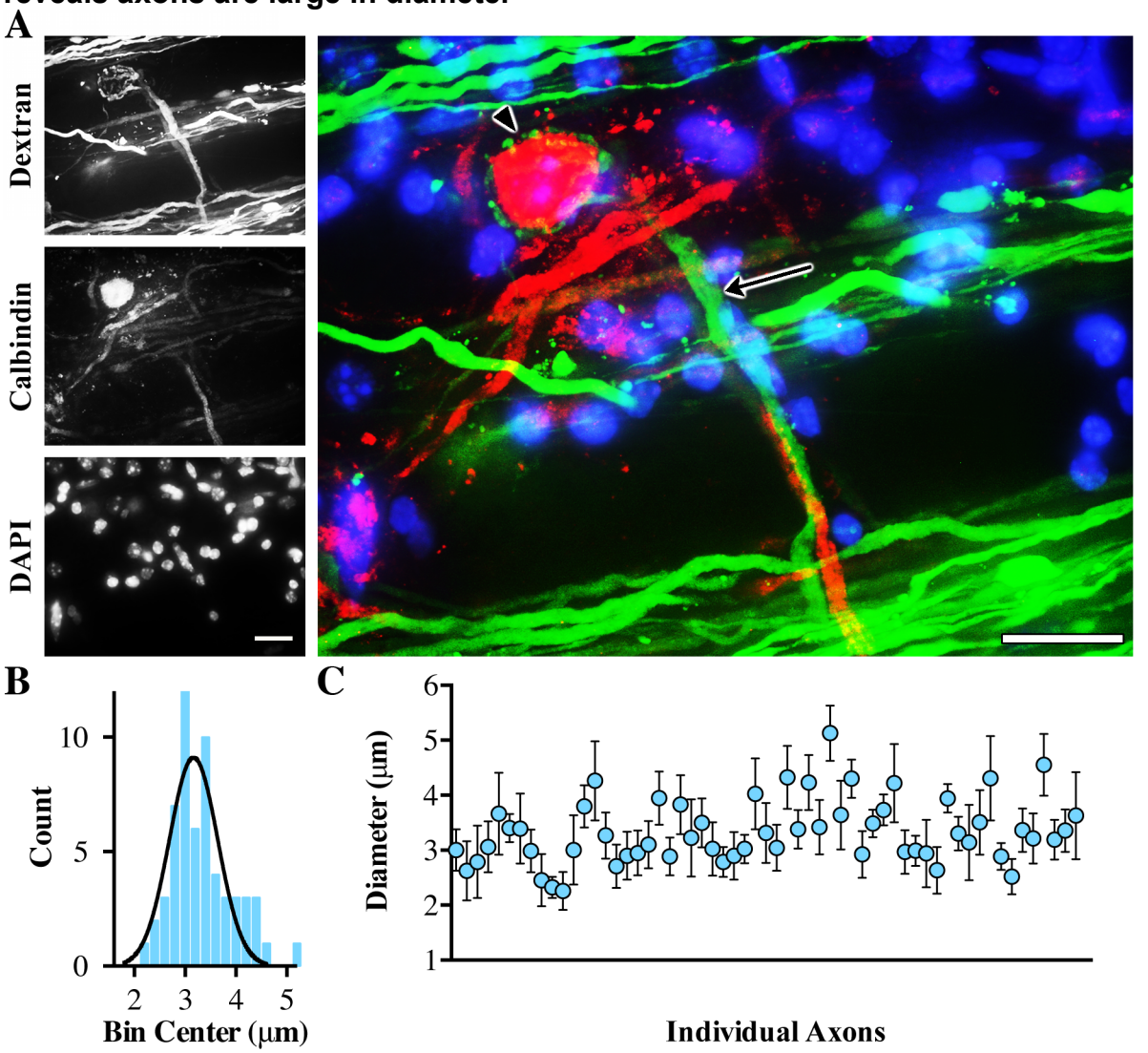

(A) Dextran injected vibratome sections were visualized using spinning disk confocal microscopy. A contralateral dextran labeled fiber (green, arrow) is seen forming the characteristic calyx of Held synapse around a Calbindin^{+} MNTB principle cell (red, arrow head). Nuclei are stained using DAPI (blue). **(B)** Quantitation of axon diameters from contralateral fibers labeled with dextran dye. Histogram is fit with a Gaussian distribution. **(C)** Variation along individual contralateral fibers, labeled with dextran dye and seen forming a calyx of Held. Data values are plotted as mean $\pm$ SD; *n* = 3 mice; 59 total axons, 20 – 25 measurements / axon. Scale bars = 20 μm.

numerical value for small is critical for analysis of *Cldn11*$^{-/-}$*Tg*$^{+/-}$ mice. Previous studies using *ex vivo* optic nerves of *Cldn11*$^{-/-}$ mice indicates a predictable relationship between axon diameter and impact on conduction velocity. Measuring ipsilateral fibers diameters would allow us to build a mathematical model of neural processing in the auditory brainstem, taking into account distance of the fiber tract and axon diameter size.

In a similar fashion to contralateral fibers, ipsilateral fibers were labeled with dextran dye by injecting coronal brainstem slices dorsal and lateral to the LSO. Figure 3.7A illustrates presumed ipsilateral fibers entering the LSO (green), accompanied by labeling of phosphorylated and non-phosphorylated neurofilament (SMI 31 / 32, red) and nuclei (DAPI, blue). The histogram in Figure 3.7B shows ipsilateral axon diameters measured from dextran labeled fibers that entered the LSO. The frequency is normally distributed, as indicated by a Gaussian curve, with average diameter 0.87 ± 0.37 μm and ranging 0.41 – 2.03 μm. Figure 3.7C shows variability along individual ipsilateral axons, consisting of 20 – 25 measurements per fiber. These ipsilateral fibers are less than a micron in diameter and conduction velocity along ipsilateral fibers would be significantly slowed in *Cldn11*$^{-/-}$*Tg*$^{+/-}$ mice, and the likely the cause for the observed abnormal neural processing.

Figure 3.7 – Morphometric analysis of ipsilateral fibers reveals axons are small in diameter

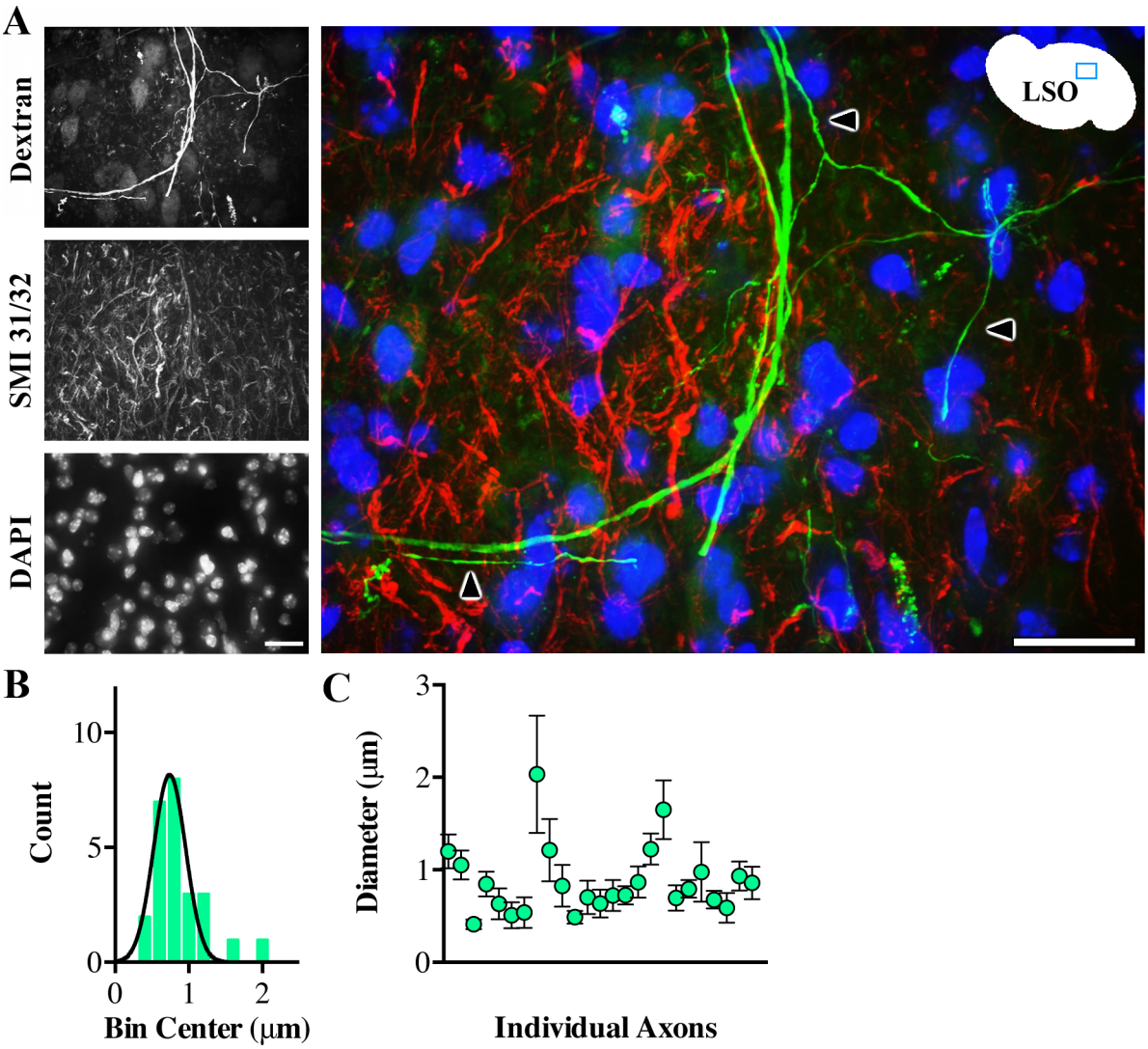

(A) Dextran injected vibratome sections were visualized using spinning disk confocal microscopy. Presumed ipsilateral dextran labeled fibers (green, arrowheads) are seen entering and terminating in the LSO. Insert depicts site of picture in relation to the LSO structure. Contrasting visualizations include all axons using SMI 31 / 32 for phosphorylated and non-phosphorylated neurofilament (red) and nuclei using DAPI (blue). **(B)** Quantitation of axon diameters from presumed ipsilateral fibers entering the LSO and labeled with dextran dye. Histogram of averages is fit with a Gaussian curve. **(C)** Axon diameter variation along individual ipsilateral fibers, labeled with dextran dye and seen entering the LSO. Data values are plotted as mean ± SD; *n* = 3 mice; 25 total axons. Scale bars = 20 μm.

DISCUSSION

Over the past few decades, the mouse has emerged as an important model organism to investigate AEPs and auditory perception (Liu, 2006; Ohlemiller, 2006). With recent advances in molecular genetic manipulation in mouse models producing deletions, duplications, and mutations by homologous recombination and transgene technologies, researchers can explore the contribution of individual abnormalities on audition, aiming to better understand human disease. The lower auditory brainstem is an excellent model to study neural processing because signal transmission along the ascending auditory pathway and their connections are highly conserved and homologous across species, and well-characterized (Christensen-Dalsgaard and Carr, 2008). Direct stimulation and measurement of processing in such an isolated circuit allows extrapolation to higher brain networks that are less accessible to manipulation and more difficult to isolate. Herein, we use auditory brainstem neural circuitry to explore the consequence of dysfunctional myelin on neural processing and its potential ramifications.

Characteristics of the *Cldn11*$^{-/-}$*Tg*$^{+/-}$ ABR

The most well studied auditory evoked potential is the ABR. Elicited within 10 msec following auditory stimulation, the ABR is composed of five, sometimes six waveforms, beginning with Wave I around 1.5 – 2 msec post stimulus. Waves II – V appear in succession at 1 msec intervals thereafter (Willott, 2001). Chapter 2 discusses more extensively the signal generators along the ascending auditory brainstem responsible for the production of each waveform.

The persistent delay in Wave V latency of *Cldn11*$^{-/-}$*Tg*$^{+/-}$ mice suggests conduction velocity is slowed in the auditory brainstem below the level of the inferior colliculus. These findings recapitulate electrophysiological data collected from *ex vivo* optic nerves of *Cldn11*$^{-/-}$ mice computing a slowing of 50 % in myelinated fibers < 0.7 μm and 20 % for those between 0.7 and 1.2 μm (Devaux and Gow, 2008). These quantitative data suggest that within the auditory brainstem, small diameter myelinated fibers < 1.2 μm are responsible for transmission and innervation of ABR signal generating nuclei along the ascending auditory pathway below the level of the inferior colliculus.

Binaural sound processing in the auditory brainstem

Sound is first processed in the lower auditory brainstem at the level of the SOC. Two key nuclei, the MSO and LSO, integrate neural signals arriving from each ear to localize the origin of a sound source on the azimuth plane. Principle cell integrators located in the MSO are responsible for processing the temporal difference in the arrival of signals to each ear. The principle cells are most sensitive for sounds resonating at lower frequencies. In mice, higher frequencies dominate the hearing range resulting from a small head size which lacks the ability to deflect lower frequency sounds. The functional consequence to mice is an underdeveloped MSO, comprised on only 200 neurons (Irving and Harrison, 1967; Ollo and Schwartz, 1979; Wu and Kelly, 1991, 1992a). Accordingly, the examination of binaural processing using interaural timing differences would lack sensitivity, regardless of frequency.

In contrast to the MSO, LSO principle cell integrators discriminate sound intensity, or level, differences arriving at each ear to localize a sound source on the azimuth plane. Principle cells in the LSO are specialized to discriminate higher frequency sounds, which is more appropriate for rodents that have poor hearing below 10 kHz. Equal sound intensities played to each ear simultaneously mimics a sound originating from directly in front, or back, of the animal. As intensity is decreased to one ear and held constant in the other, sound is perceived to be lateralized toward the ear exposed to the louder tone.

The classic Jeffress model for neural processing outlining coincidence detectors and delay lines primarily describes neural processing in the MSO and using those principles to interpret the data presented herein may be incorrect. The measured response from *Cldn11*$^{+/-}$*Tg*$^{+/-}$ and *Cldn11*$^{-/-}$*Tg*$^{+/-}$ mice is similar to humans where a linear response was measured for small and medium disparities of level differences, but continued in a non-linear fashion for larger differences (Yost, 1981). This idea developed into the hemifield model where two populations of neurons are postulated to be responsible for sound localization. Each population / channel of neurons responds broadly across the left or right (ipsilateral versus contralateral) acoustic hemifield, and shares an overlapping boarder along the midline (Boehnke and Phillips, 1999; Phillips, 2008). Each auditory hemifield (left and right) also contains cells that respond to a sound source stemming from the ipsilateral and contralateral hemifield.

The overall shape of the normalized DN1 latency curves for *Cldn11*$^{+/-}$*Tg*$^{+/-}$ and *Cldn11*$^{-/-}$*Tg*$^{+/-}$ mice reflect a two-neuron hypothesis of neural processing. When a

sound source is emulated near the midline, Δ0 – 10 dB SPL (Figure 3.3B), a steep linear increase in latency is evident. These data are similar to those measured in humans and reflect a distinct midline population of neurons that are responding. Because sound lateralization along the azimuth is best near the midline, responding neurons have a steeper response and this is reflected in both *Cldn11*$^{+/-}$*Tg*$^{+/-}$ and *Cldn11*$^{-/-}$*Tg*$^{+/-}$ data collected.

As intensity differences are increased to Δ20 – 30 db SPL, the latency response of *Cldn11*$^{+/-}$*Tg*$^{+/-}$ mice continues to increase while flattening out. These data reflect the hemifield neurons responding to a lateralized sound source. Responding neurons in the lateral hemifields are less precise, generating a broader response as compared to midline neurons. In *Cldn11*$^{-/-}$*Tg*$^{+/-}$ mice, the response from lateral hemifield neurons remains steady with unchanging latency. These data are significantly different from *Cldn11*$^{+/-}$*Tg*$^{+/-}$ mice suggesting that small myelinated fibers either transmit bilateral information for processing, or small myelinated fibers refine the output of the principle cells. These data are important in two ways. First, they support the two-neuron hypothesis of sound lateralization, and second, they highlight the importance of myelin on neural processing

Recent evidence from humans postulates a third group of neurons may aid in sound localization. Located along the midline, this third group is specialized for spatial tuning (Dingle et al., 2010, 2013). The initial jump in latency (Δ0 – 2 dB SPL) may reflect a third population of integrating neurons, however this portion of the curve Is generated from two data points and further resolution is not be plausible using far field recording techniques.

Morphometric analysis of auditory brainstem fiber tracts

Several unique features are evident in the auditory pathway, allowing for robust temporal accuracy of signal relaying, as well as fidelity of signal transmission for processing. First, two large synapses, measuring five times the diameter of normal synapses, preserve and ensure the temporal features of signal transmission: the endbulbs of Held (within the CN) and the calyces of Held (in the MNTB). One understated attribute is the presence of myelinated fibers throughout the auditory pathway (Anniko and Arnesen, 1988; Dinh et al., 2014; Spoendlin and Schrott, 1989, 1990; Wu and Kelly, 1991). Without myelin, signal transmission would be slowed by as much as 10-fold. Our data confirm the presence of myelinated fibers in the auditory pathway (Figure 3.5) and highlight their critical role in neural processing by demonstrating abnormal responses when slowed conduction occurs along myelinated fibers < 1.2 μm.

The electrophysiology data presented suggest *Cldn11*$^{-/-}$*Tg*$^{+/-}$ mice have small diameter myelinated fibers present within the lower auditory brainstem, as indicated by the significant delay in Wave V latency and differential output of LSO signal integrators. The morphometric studies presented in this chapter are the first to quantify axon diameters along the auditory pathway in mice, despite the widespread use of these animals in auditory experiments over the past few decades.

Studies in chick show contralateral axons transmitting information from the AVCN to the MNTB are large in diameter, approximately 2 μm, and small diameter fibers of approximately 1 μm, that relay information from the ipsilateral AVCN directly to the LSO (Seidl et al., 2010). For mice, several published studies make mention of

large diameter myelinated contralateral and small diameter ipsilateral fibers, but quantitative data have not been presented (Doucet and Ryugo, 2003; Wu and Kelly, 1991, 1992b; Wu and Oertel, 1984). Figures 3.6 demonstrates that large contralateral fibers are approximately 3.3 μm in diameter, and Figure 3.7 suggests that the ipsilateral fibers are small, at approximately 0.87 μm in diameter. The significant delay in Wave V latency suggests that small diameter myelinated fibers are found in the auditory brainstem of mice and we confirm the presence of small, as well as large diameter fibers.

There are several caveats associated with the current analysis of the ipsilateral fibers. Unlike the contralateral fiber analysis, where we directly confirmed the identity of axons giving rise to calyces of Held, direct verification of ipsilateral fibers synapsing with the LSO principal neurons has not been possible. These technical difficulties arose in the current study because of our inability to detect synapsing fibers. While it has been shown that LSO principle cells are aligned along the long axes of the nuclei (into and out of the image) (Brown and Liu, 1995; Guinan et al., 1972), the trajectory of ipsilateral fibers is unknown. If fibers enter the LSO, as seen in Figure 3.7, turn 90 degrees to synapse with a principle cell out of the plane of section; a confirmed synapse would not be detectable. What we can verify is a healthy brain slice during, and subsequent to dextran injections, robust labeling of healthy fibers, and correct location within the LSO. These caveats aside, these data suggest that all detectable ipsilateral fibers entering the LSO are small in diameter (< 1 μm), refuting the possibility of large diameter ipsilateral fibers.

Morphometric data confirm the observations that contralateral fiber diameters are large and ipsilateral fibers are small (less than a micron) in diameter. These data are critical for interpreting neural processing the *Cldn11*$^{-/-}$*Tg*$^{+/-}$ mice. Previous studies have extensively detailed and modeled the consequence of ablating Cldn11 tight junctions on conduction velocity along myelinated axons. When Cldn11 tight junctions within myelin sheaths are ablated, conduction velocity along small diameter fibers, (~0.7 μm) is severely reduced by 50 % and medium diameter fibers (~ 1.2 μm) by 20 %, whereas large diameter fibers (>2.1 μm) are minimally affected (< 5 %) (Devaux and Gow, 2008).

In summary, *Cldn11*$^{-/-}$*Tg*$^{+/-}$ mice have dysfunctional myelin in which resistance of the myelin membrane is decreased, severely affecting conduction velocity along small diameter myelinated fibers. Neurophysiological evidence collected in the auditory brainstem of *Cldn11*$^{-/-}$*Tg*$^{+/--}$ mice confirms a decrease in conduction velocity via an increase in Wave V latency of the ABR. This demonstrates the presence of small diameter myelinated fibers along the ascending auditory brainstem. When neural processing is probed using ILDs, the resulting response differs from *Cldn11*$^{+/-}$ *Tg*$^{+/-}$, suggesting alterations in sound lateralization. Interestingly, the response curve from both groups of animals lends to a newly emerged model of neural processing known as the two-neuron model. This model posits that the lateral position of a sound source cannot be encoded by which particular neurons are discharging maximally (population model). Instead, lateral sound is encoded by the relative activation of two channels of neurons: those that are activated maximally by sources favoring the contralateral or ipsilateral side, but both contain a steep boarder

towards the midline (Boehnke and Phillips, 1999; Dingle et al., 2010; McAlpine et al., 2001; Phillips, 2008; Phillips and Hall, 2005; Yost, 1981). Data collected within the chapter supports a hemifield model, as opposed to the classic Jeffress model of population neural processing for sound lateralization.

CHAPTER 4 – slowed conduction velocity can alter behavior

INTRODUCTION

Behavioral disorders are simplistically defined as conduct that deviates from the socially accepted normal. These abnormalities range from internal conflicts to outward expressions of defiant episodes, both of which adversely affect and impinge upon daily functioning. Behavioral abnormalities are present in children and adults and are influenced by environmental stimuli and experiences. Common abnormalities include anxiety, depression, and cognitive impairments. An estimated half of adults will be diagnosed with a behavioral abnormality at some point in their lifetime (Kessler et al., 2005). This translates to an increased annual encumbrance, ranging in the tens of millions of dollars spent annually in the United States alone (W.H.O., 2001).

Behavioral disorders result from a disconnection between brain regions

The etiologies for many behavioral disorders are uncharacterized, however the leading hypothesis is that different parts of the brain do not effectively communicate, known as the disconnection hypothesis. Proponents of this hypothesis contend that behavior is the result of temporal integration of sensory signals; *abnormal* behavior results when there is a disconnection between brain regions or neural circuits (Friston, 1998, 1999). The disconnection hypothesis was originally proposed by Karl Friston to describe the etiology of schizophrenia, but more recently, a number of researchers have promoted and broadened this hypothesis to include numerous neurological illnesses including Alzheimer (Bell and Claudio Cuello, 2006; Bokde et al., 2009; Hof and Bouras, 1991; Reid and Evans,

2013), autism spectrum disorders (Frith, 2004; Just et al., 2007; Melillo and Leisman, 2009), Parkinson disease (Cilia et al., 2011; Cronin-Golomb, 2010; Fogelson et al., 2013) and bipolar disorder (Mahon et al., 2010). To understand the how neural circuits become disconnected and cause behavioral abnormalities, researchers have developed and investigated two main hypotheses for disconnection: altered neurotransmitters and aberrant neurogenesis or neuron biology.

Disconnection can originate from altered neurotransmitters

Neurotransmitters are small molecules that nerve cells (neurons) use to communicate with their targets. They extend across numerous biological categories including cholines, monoamines, amino acids, peptides and purines (Kandel et al., 2000; Webster, 2001). There are several, highly regulated stages involved in neurotransmission. First, a molecule is synthesized from precursors in the axon terminal of the presynaptic neuron, or in rare cases, transported from elsewhere in the cell. After synthesis and before release, a neurotransmitter is packaged and stored in vesicles near the presynaptic terminal (De Camilli and Jahn, 1990; Holtzman, 1977). Upon stimulation, vesicles dock to the presynaptic membrane and release the neurotransmitters into the synaptic cleft (Kelly et al., 1979; Miller and Racker, 1976; Papahadjopoulos et al., 1977; Sudhof, 2004). Finally, neurotransmitters bind to receptors on the postsynaptic membrane, which pass current across the membrane to depolarize or hyperpolarize the postsynaptic terminal.

Evidence of altered neurochemical levels in patients with behavioral abnormalities is evident throughout the literature. In recent years, researchers have

developed molecular imaging techniques to measure neurotransmitters levels in the brains of humans in real time. Using radiolabeled ligands, the binding of a radiolabeled substrate can be measured using positron emission tomography (PET). The amount of ligand binding is proportional to the number of unoccupied receptors and thus, act as a proxy for the amount of native neurotransmitter present (Badgaiyan, 2011). Several human and animal studies have used this technique to investigate diseases in which an onerous behavioral component is evident, including Alzheimer (Jacobs et al., 2003; Wengenack et al., 2008), Parkinson (Elsinga et al., 2006) and schizophrenia (Andreasen et al., 1996; Davis et al., 1991). Moreover, behavioral abnormalities, such as anxiety, have been directly studied using PET demonstrating abnormal neurochemical compositions (Reiman, 1997).

Recently, proton magnetic resonance spectroscopy (H^1MRS) has allowed for a direct quantitation of neurochemical levels in select brain regions associated with behavioral abnormalities including anxiety (Mathew et al., 2004; Pollack et al., 2008), depression (Hasler et al., 2007; Sanacora et al., 1999) and neuropsychiatric disorders (Stanley, 2002). Thus, the advancement of medical imaging techniques has demonstrated altered brain neurochemistry in behavioral disorders suggesting disconnection between brain networks and the emergence of atypical behavior.

Literature advocating for neurochemical alterations as the probable etiology for behavioral abnormalities has lead to the development of drug therapies targeted to correct neurochemical levels in patients. Neural transmission is a highly regulated process in which the timing of release, amount of information (quanta), and precision of targeting is closely monitored. If any stage in the chemical transmission process

becomes modified, the proper information fails to be communicated and subsequently relayed. Drug design has optimization signal transmission through compounds that reduce clearance from the synaptic cleft (Haenisch and Bonisch, 2011; Philip et al., 2010) or inhibit removal (Feighner, 1999; Stahl, 1998; Stahl et al., 2005), thereby modulating signal transmission. With available drug treatments, the major disadvantage is the significant proportion of patients whose symptoms and behaviors are not alleviated.

Selecting the appropriate therapeutic treatment for a behavioral abnormality is complex. Longitudinal epidemiological data are not available for many therapies and predictions for relapse / remitting phases are complicated by factors including comorbid illnesses and traumatic events, which can substantially alter effectiveness. Data collected over a five year period are often used to project the proportion of patients expected to experience full remission with drug therapy. The forecasted level is around 40 % for most behavioral abnormalities (Foa et al., 1983; Yonkers et al., 2000) and, consequently, the majority of patients will struggle to find relief, advocating for alternative etiologies for behavioral abnormalities.

Abnormal neuron biology generates disconnection between neural networks

In addition to aberrant levels of neurotransmitters, abnormal neuron biology can be a driving factor for behavioral abnormality. Neurons are the main communication cell responsible for receiving, processing, and transmitting electrical and chemical encoded information (Waxman et al., 1995). There are different subtypes of neurons (motor, sensory, interneuron), totaling over 200 billion neurons in the adult human brain, and on average each neuron is connected to 5,000 –

200,000 other neurons. Altering the expansive connections established can perturb normal signal processing, modify integration, and conceivably disconnect neural circuitry. Neural connections also can be reshaped by increases or decreases in the number of neurons in a network.

The most widely studied mechanism for reductions in neurons is death through diffuse axonal injury related to a traumatic event. Axonal injury, in its many forms, has a similar pattern of disruption that ultimately leads to the degeneration of the axon and death of the cell. In brief, an expansion of the axonal membrane is seen, followed by an increase in Na^{+} and Ca^{2+} ion permeability. Next, damaging intracellular cascades attributable to the Ca^{2+} influx causes swollen and ruptured mitochondria, and finally, potential indirect effects due to disruption of the axoglial interaction necessary to maintain homeostasis (Buki and Povlishock, 2006; Marmarou et al., 2005; Medana and Esiri, 2003).

It has been assumed that axonal injury impairs brain function, reflecting the extent of damage and the number of neurons injured (Waxman et al., 1995). Axonal damage can be translated to deafferentation, yielding target cell dysfunction as illustrated by presynaptic degeneration; however, the functional significance remains unclear (Erb and Povlishock, 1991). On the opposite end of the spectrum, increasing the number of neurons may lead to dysfunctional neural circuitry via improper signaling cascades and competing signal information. This supposition has been suggested for the etiology of autism where hyperconnectivity has been demonstrated (Belmonte et al., 2004a; Belmonte et al., 2004b). Similarly, increasing

the activity of a neuron can also render circuitry dysfunctional, most notably with illnesses such as epilepsy (McNamara, 1999).

White matter integrity is a key component of properly functioning neural circuitry

There is clear evidence that behavioral abnormalities may arise from mechanisms including aberrant neurotransmitter levels, or other abnormal neuron biology, however, patients receiving treatments to correct these deficits do not always respond. Thus, there may be additional mechanisms by which behavioral abnormalities arise. We know from the clinical literature that white matter diseases, such as leukodystrophies and multiple sclerosis (MS) have known alterations to white matter along with prominent behavioral abnormalities (Baumann et al., 2002; Garside et al., 1999; Hyde et al., 1992; Petersen and Kokmen, 1989; Schiffer and Babigian, 1984; Schubert and Foliart, 1993). We also know that myelin is functionally important in temporal communication, increasing the speed and fidelity at which impulses propagate along a neuron and improving long-range communication between brain regions (Hodgkin, 1964; Hodgkin and Huxley, 1952; Tasaki, 1952). Dysfunctional myelin can cause a disconnection between brain regions, altering the processing of sensory information and contribute to behavioral abnormalities. To better elucidate the link between dysfunctional myelin and behavioral abnormalities; we investigated the *Cldn11*$^{-/-}$ mouse model of dysfunctional myelin.

Animal models play an essential role in understanding the pathophysiological mechanism by which behavioral abnormalities arise (Petters and Sommer, 2000;

Phillips et al., 2002; van der Staay et al., 2009). Modeling abnormalities, whether in their simplest form or a prominent attribute of an illness, is quite challenging due to the complexity of human behavior. Genetic, pharmacological, environmental, or direct manipulation of neural circuitry has been employed to study behavior (Nestler and Hyman, 2010). We can ascertain the anthropomorphic characteristics of human behavior in animal models by quantitative measurements via behavioral testing. Numerous tests have been developed to interrogate behavioral abnormalities such as anxiety, depression, and cognitive ability and we will use such tests to determine if dysfunctional myelin can cause behavioral changes, indicating a potential etiology for these disorders.

Because of the numerous proportions of patents unresponsive to current behavioral drug therapies targeting neurotransmitters and neurons, there must be an alternate hypothesis describing how brain regions become disconnected leading to behavioral abnormalities. Herein, we investigate the *Cldn11*$^{-/-}$ mouse model of dysfunctional myelin to explore the possibility that myelin is critical for the proper functioning of neural circuitry and dysfunction can arise when the integrity of myelin is altered. Our animal model provides the first direct evidence that dysfunctional myelin can contribute to the development of behavioral abnormalities, and can alter brain neurochemistry. These data provide evidence indicating dysfunctional myelin can contribute to the etiology of behavioral abnormalities.

MATERIALS AND METHODS

Mice

The Department of Laboratory and Animal Resources at Wayne State University maintained all mice in this study. All experiments on mice were performed in accordance with an Institutional Animal Care and Use Committee protocol approved by the Wayne State University Animal Investigation Committee. Up to four mice were housed in group I rodent polycarbonate cages (19.05 X 29.21 X 12.7 cm^3, Ancare, Bellmore, NY), or up to nine mice housed in groupII polycarbonate cages (26.67 X 48.26 X 15.56 cm^3, Bellmore, NY). Each cage was given a 2 X 2 in nestlet square (Ancare, Bellmore, NY) to promote nesting behavior and aid in thermoregulation. Food and water were available *ad labium*. Breeding mouse trios or pairs were provided mouse diet (#5015, LabDiet, St. Louis, MO) to support healthy pups and non-breeding mice were provided laboratory rodent chow (#5001, LabDiet, St. Louis MO). All polycarbonate cages, water bottles, and food pellets were changed weekly and as needed.

The *Osp20* transgene construct (GS605) comprises a 22 kb *Sau3A I* fragment of genomic sequence from 5 kb upstream of the transcription start site in exon 1 to 1.9 kb downstream of the first polyadenylation site in exon 3. The unique *Acc65 I* site near the 5' end of intron 1 was blunted-out distinguishing the transgene from the endogenous *Cldn11* gene during qPCR analysis. The genomic fragment was cloned between two *Not I* sites in a *pUC18* – based vector (Gow et al., 1992) and was excised and phenol : chloroform-purified from an agarose gel slice for male pronuclear injection. This allele is referred to as *Tg*(*Cldn11*)605Gow (MGI:5306245),

and for the purposes of this dissertation as *Tg*$^{+/-}$. Transgene expression was confirmed in testis and inner ear, but not brain (Wu et al., 2012). Additionally, this transgene restored the known sterility (Gow et al., 1999) and premature hearing loss resulting from a loss in endocochlear potential in *Cldn11*$^{-/-}$ mice (Gow et al., 2004) (unpublished data). Double mutant mice were generated by breeding males from *Tg*(*Cldn11*)605Gow with *Cldn11*$^{-/-}$ female mice to generate F1 *Cldn11*$^{+/-}$ *:Tg*(*Cldn11*)605Gow*Tg*$^{+/+}$ mice, referred to as *Cldn11*$^{+/-}$*Tg*$^{+/-}$. These mice were sib-mated to generate F2 (and beyond) *Cldn11*$^{-/-}$*Tg*$^{+/-}$ mice (as well as control *Cldn11*$^{+/-}$ *Tg*$^{+/-}$) for experiments. These mice were used for all experiments unless noted.

Open Field

The open field arena consisted of a 61 x 61 x 31 cm black plexiglass box with a matted finish (FT Plastics, Oak Park, MI). The bottom of the arena was lined with white bench top paper (Whatman™ Benchkote™, cat#: 12-007-182B, ThermoFisher, Waltham, MA) and a clear plexigalss insert panel (61 x 61 x 1 cm^3) placed over top for added contrast and ease of cleaning. All mice were habituated to the behavior room one hr before testing. Standard open field protocol consisted of two consecutive days in which mice were placed in the center of the arena, facing the same wall, and video recorded for five min (Samsung SC-MX20L/XAA). Videos were uploaded and the center point of the mouse was post – tracked using Ethovision software (version 8.5, Noldus, Leesburg, VA) to obtain various center square activity, total distance traveled, average velocity, and time spent in each quadrant. All variables for the two days were averaged for each animal.

Conventional center square (CS) analysis designates 50 % of the total area as the center portion, however we find this parameter uncommunicative. To convey practical criteria and a more detailed analysis, we used the average body length of a mobile mouse (7.5 cm) as the determinant for CS boundaries. Half a mouse body length away from the periphery computed to be 83 % of the total area, and thus, designated as 83 % CS. A similar pattern was followed to generate concentric squares of the OF environment, resulting in the following: 66 % (one body length away from the periphery), 48 % (one and a half body lengths), and 32 % (two body lengths).

Figure 4.1 – Open field schematic

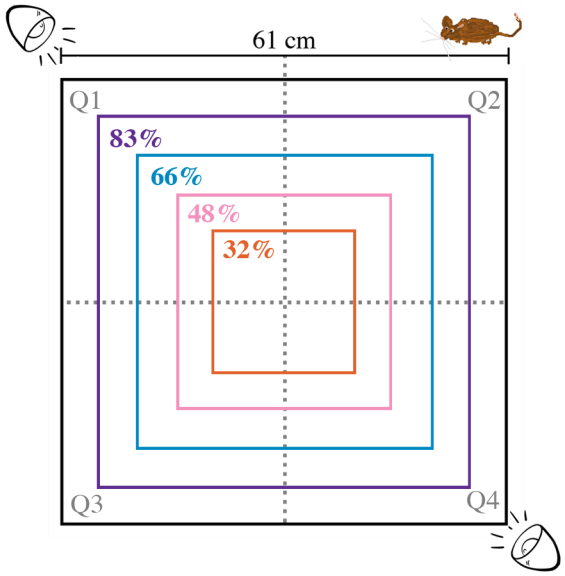

Open field schematic detailing size and location of the various different center square (CS) % used for analysis, location of quadrants and light sources. Schematic is drawn with respect to the mouse in the top right hand corner

Marble Burying

All mice were habituated to the behavior room one hr prior to testing. Marble burying test was carried out in a clean home cage (19.05 X 29.21 X 12.7 cm^3, Ancare, Bellmore, NY) layered with 2 cm of bedding (Bed O'Cobs 1/8", Andersons Lab Bedding, Maumee, OH). Fifteen glass marbles were placed in a grid pattern formed by five rows of three marbles, evenly spaced throughout the cage (See schematic below). A single mouse was placed in the center of the cage and video recorded (Samsung SC-MX20L/XAA) for 30 min. Afterwards, photos of each testing environment were collected and the number of marbles buried at least two-thirds of the way with bedding were tallied.

Figure 4.2 – Marble burying schematic

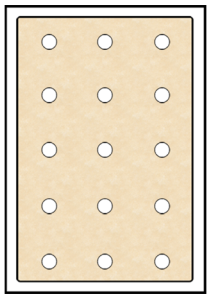

Marble burying schematic illustrating placement of 15 marbles at the start of testing.

Tail Suspension

Tail suspension apparatus was comprised from a metal ring stand rod suspended approximately 18 in from the bench top between two rings stands. All mice were habituated to the behavior room one hr prior to testing. Prior to taping the mouse's tail, a one-inch clear plastic tube was threaded over the tail and placed at the base of each mouse's rear to prevent it from climbing its tail during testing. Mice were suspended by their tails using 15 cm of standard laboratory tape (Thermo Fisher Scientific, Waltham, MA) in which 2.5 – 3 cm of one end was used to secure the tail, and the opposing end secured to the bar. Mice were suspended for six min and video recorded (Samsung SC-MX20L/XAA). Videos were played back and scored, unbiased, for the amount of time mice spent immobile or helpless. Immobility was defined by a lack of movement of the forelimbs, hind limbs, and head, but not whiskers. Pendulum swinging in the absence of limb movement was also evaluated as time immobile. Total time spent immobile was recorded as time out of 360 sec.

Sucrose Preference

Sucrose preference testing was carried out in a polycarbonate cage (26.67 X 48.26 x 15.56 cm^3, Ancare, Bellmore, NY) and spanned a total of eight days. All mice were individually housed during the testing period and given one nestlet (2 X 2 in, Ancare, Bellmore, NY). During habituation (days 1 – 4), mice were acclimated to the presence of two dual bearing sipper tube bottles (Lixit #QLCSA-5, Petsmart, Phoenix, AZ) containing water. Following habituation, one water bottle solution was replaced with a 2 % sucrose solution for remaining testing days. To avoid a side preference, the location of the sucrose solution was counterbalanced during sucrose

testing days (days 5 – 8). Measurements, based on weight difference, were calculated daily for total water, sucrose solution, and food consumption before replenishing. The density of a 2 % sucrose solution is 1.0060 g / cm^3 and is negligible to the density of water (1 g / cm^3). Mice were given 40 grams of rodent chow daily (#5001, LabDiet, St. Louis MO) and 100 milliliters of fluid in each sipper bottle, whether water or sucrose. After testing, mice were returned to group housing. To prevent fighting between males, nestlets were collected every other day from males originally residing in the same home cage, intermixed, divided evenly, and returned.

Barnes Maze

All mice were habituated to the behavior room one hr prior to testing. The Barnes maze was constructed from a circular, white plexiglass (91.4 cm diameter) with twenty holes (5 cm) positioned equidistance from each other and 2 cm from the outer edge (FT Plastics, Oak Park, MI). Located beneath one hole was a removable, sliding black box that served as the goal location. A mesh step was placed inside the black box to aid descending mice. Visual cues adorned the walls or were native to the testing room: a solid black circle, a solid black line, camera stand, experimenter, and trolley. Cues remained constant and unchanged throughout all testing days.

Habituation (day 1): Mice are placed directly in front of the goal hole, enclosed in a glass beaker (Pyrex, Thermo Fisher Scientific, Waltham, MA) placed upside – down. Habituation lasts for five min and mice are allowed to directly explore the goal hole, goal box, and its surrounding environment. If the mouse has not

entered the goal hole after five min, the mouse is gently placed inside, the entrance covered, and remains for 30 sec. One hr later, acquisition training can begin.

Acquisition Training (days 1 – 4): Acquisition training lasts five min, three trials per day, one hr between trials. Mice are placed onto the center of the maze, facing a chosen wall used throughout testing. Latency to find the goal hole, enter the hole, and the number or errors are recorded. If a mouse finds and subsequently enters the goal hole before five min time is up, the training trial can be stopped. If the mouse has not entered the goal hole after five min, the mouse is gently placed inside, the entrance covered, and remains for 30 sec. The location of the goal hole remains constant throughout training. All training trials are video recorded (Samsung SC-MX20L/XAA).

Acquisition Probe (day 5): Before beginning, the goal box is removed and the Barnes maze table is rotate 90 degrees counterclockwise from the training location. Acquisition probe lasts for a single trial, five min in length. Mice are released onto the center of the maze as in prior days and allowed to explore for the full five min. The probe trial is video recorded and post – processed using Ethovision software (version 8.5, Noldus, Leesburg, VA).

Acquisition Retraining (day 6): The goal box is replaced and the location of the goal hole is set up identical to training days 1 – 4. Mice undergo three training trials, one hr apart. If a mouse finds and subsequently enters the goal hole before five min time is up, the training trial can be stopped. If the mouse has not entered the goal hole after five min, the mouse is gently placed inside, the entrance covered, and remains for 30 sec.

Curtain Probe (day 7): Before beginning, the goal box is removed and the maze rotated 90 degrees counterclockwise from training locations. Additionally, bench coat paper is used to surround the maze in two levels, blocking all visual cues. The purpose of the curtain surrounding the maze was to determine if mice were using non-visual intra maze cues or the visual extra maze cues to help them locate the goal hole during training exercises. Mice are then release onto the center of the maze and allowed to explore for five min. Probe trials are video recorded and post – analyzed using Ethovision.

Acquisition Retraining (day 8): The goal box is replaced and the location of the goal hole is set up identical to training days 1 – 4 and day 6. Mice undergo three training trials, one hr apart. If a mouse finds and subsequently enters the goal hole before five min time is up, the training trial can be stopped. If the mouse has not entered the goal hole after five min, the mouse is gently placed inside, the entrance covered, and remains for 30 sec.

Reversal Training (day 9): Similar to acquisition training days, however the location of the goal hole is now 180 degrees from all previous training days. Mice undergo three training trials, one hr apart. If a mouse finds and subsequently enters the goal hole before five min time is up, the training trial can be stopped. If the mouse has not entered the goal hole after five min, the mouse is gently placed inside, the entrance covered, and remains for 30 sec.

Reversal Probe (day 10): Before beginning, the goal box is removed and the maze rotated 90 degrees counterclockwise from reversal training location. Mice are

then release onto the center of the maze and allowed to explore for five min. Probe trials are video recorded and post – analyzed using Ethovision.

During all phases of the Barnes maze, a number of factors are recorded (manually during the test, confirmed via video) including latency to the goal hole, time to enter the goal hole, number of errors pre-hole, and number of errors post – hole. During probe days (days 5, 7, and 10) Ethovision software was used confirm latencies and errors, as well as measure time spent in zones drawn around the goal hole mice were trained to locate, and the actually hole where the box can hook-in at (90 degrees counterclockwise). The number of acquisition training days was determined prior to testing with separate groups of mice. It was concluded that four days of acquisition training was adequate for mice to learn the location of the goal hole, ascend into the goal box, and retain that information.

Figure 4.3 – Barnes maze schematic

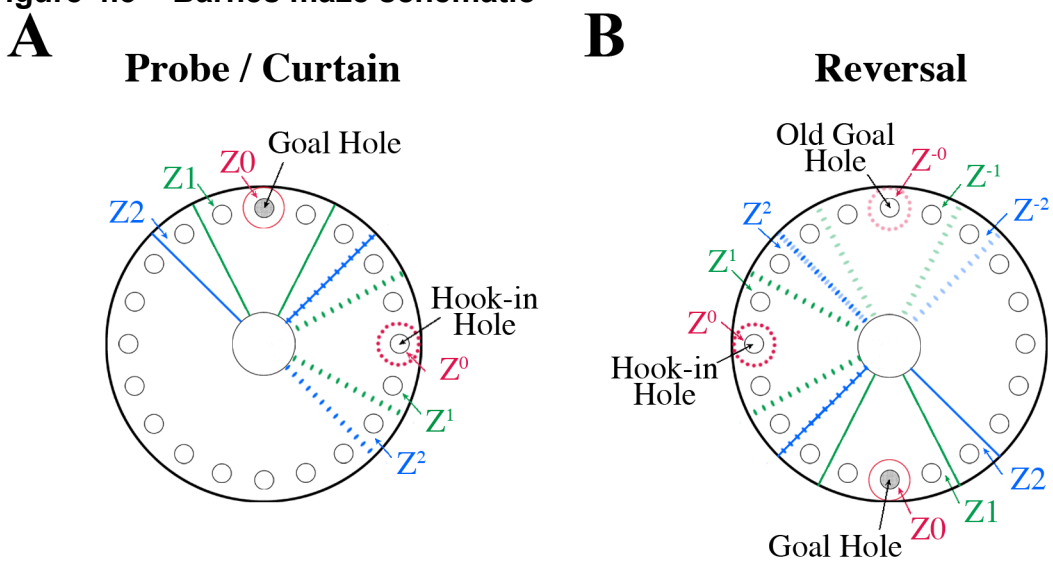

(A) Overview of zone boundaries surrounding the trained goal hole (Goal Hole) or the hole where the training box attaches (Hook-in Hole). This schematic was used for calculating zone analysis for BM probe (day 5) and curtain probe (day 7). **(B)** Overview of zone boundaries surrounding the location of the original goal hole (Old Goal Hole), the location of the re-trained goal hole (Goal Hole), or the hole where the training box attaches (Hook-in Hole). This schematic was used for calculating zone analysis for BM reversal probe (Day 10).

High Resolution Magic Angle Spinning Proton Nuclear Magnetic Resonance (H^1MRS)

Mice were decapitated and brains immediately removed from the skull. Serial coronal slices (2 mm) were obtained using a mouse anodized aluminum matrice (BS-AL 5000C, Braintree Scientific, Braintree, MA) beginning at + 2 bregma and ending at - 8 bregma (see schematic below). Slices were promptly frozen on a block of dry ice. Once frozen, slices were moved onto a wet ice platform. Intact, bilateral punches isolating various brain regions were collected using 1.5 mm diameter disposable biopsy punches (Miltex Inc., Plainsboro, NJ) and stored in 1.7 ml microcentrifuge tubes (Thermo Fisher Scientific, Waltham, MA) at - 80°C until testing. For H^1NMR analysis, tubes were transferred from - 80°C, one bilateral punch was extracted, weighed, and promptly placed into a 10 μl Bruker zirconium rotor containing PAFT buffer (100 mM K_2HPO_4 / KH_2PO_4, 200 mM HCOONa, 1 g / L NaN_3 diluted 50 % with D_2O containing 3 mM trimethylsilyl – propionate (TSP, Sigma Aldrich, St Louis, MO; pH = 7.4). TSP served as an internal chemical shift reference (0.00 ppm), formate (8.44 ppm) was used for autophasing, and D_2O was used to lock on the center frequency. The rotor (with sample) was placed into a Bruker magic angle spinning probe maintained at 4°C in a vertical wide – bore (8.9 cm) Bruker 11.7 T magnet, controlled with an Avance DRX-500 console (Bruker Biospin Corp., Billerica, MA, USA). Rotors were spun at 4.2 ± 0.002 kHz at 54.7° relative to the static magnetic field B_0. After a pre – saturation pulse for water suppression, spectra were acquired with a 1-D Carr–Purcell–Meiboom–Gill pulse sequence (90-(τ-180-τ)n-acquisition) with TR = 6210 ms, τ = 0.15 ms, and n = 12 for total echo

time (TE) of 3.6 ms; spectral bandwidth = 7.0 kHz (14 ppm), 16 k complex data points, and 256 averages for total acquisition time of 7 min 36 s. Data was acquired using Bruker-XWINNMR version 3.6 software. Spectra were analyzed with a custom LCModel version 6.1 – 4, established with a basis set of metabolites over a spectral range of 1.0 – 4.2 ppm. The precision of the LCModel fit to the spectral data was estimated with Cramér–Rao bounds, which are typically less than 10 % for the metabolites reported herein.

Figure 4.4 – Fresh tissue punch schematic

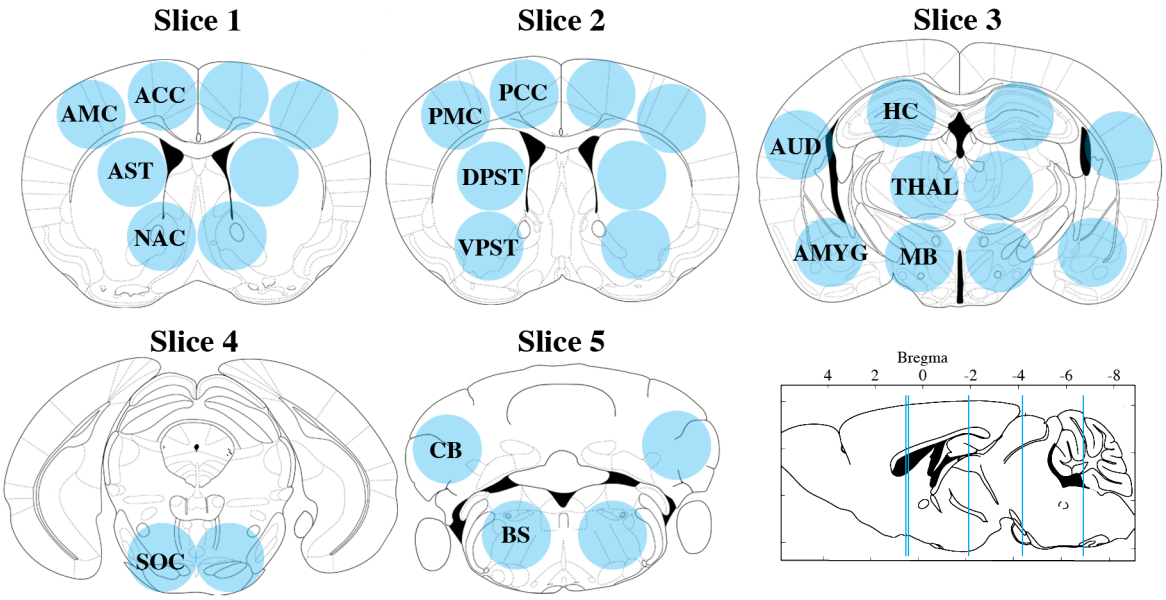

Illustration of individual 2 mm coronal slices and location the bilateral fresh tissue punches collected for H^1NMR and western blots. Blue punches represent the relative size (1.5 mm) collected. Coronal mouse brain slices were edited from the Paxinos mouse atlas.

Western Blotting

Mice were decapitated and brains immediately removed from the skull. Serial coronal slices (2 mm) were obtained using a mouse anodized aluminum matrice (BS-AL 5000C, Braintree Scientific, Braintree, MA) beginning at + 2 bregma and ending at - 8 bregma (see schematic in H^1MRS above). Slices were promptly frozen on a block of dry ice. Once frozen, slices were moved onto a wet ice platform. Intact, bilateral punches isolating various brain regions were collected using 1.5 mm diameter disposable biopsy punches (Miltex Inc., Plainsboro, NJ) and stored in 0.7 ml microcentrifuge tubes (Thermo Fisher Scientific, Waltham, MA) at - 80°C until use. Tissue punches were sonicated (Fisher Scientific sonic dismembrator Model 500) in 50 μl buffer (tris buffered saline (TBS), 2 mM ethylenediaminetetraacetic acid (EDTA), 0.5 mM phenylmethylsulfonyl fluoride (PMSF, Thermo Fisher Scientific, Waltham, MA), 1 % triton X-100 (Thermo Fisher Scientific, Waltham, MA), and P8340 (Sigma Aldrich, St Louis, MO), and protein concentrations measured via Bradford assay on a spectrophotometer (Smartspec3000, Biorad, Hercules, CA). Protein concentrations of 5 – 10 μg per lane were loaded on 6 – 8 % SDS gels, electrophoresed (SE260, Hoefer, Holliston, MA), and transferred onto nitrocellulose (Whatman Protran, GE Healthcare via Thermo Fisher Scientific, Waltham, MA). Membranes were blocked with 5 % nonfat milk (Carnation, Nestle) for one hr, washed in phosphate buffered saline with 1 % tween20 (PBST), then incubated overnight with corresponding primary antibody diluted in 2 % nonfat milk with PBST Membranes were washed of the primary antibody (See Table 4.1) with PBST then incubated in corresponding HRP conjugated secondary antibody (See Table 4.2) for

an additional one hr. Once complete, membranes were washed thoroughly with PBST and protein visualized with enhanced chemiluminescensce (Thermo Fisher Scientific, Waltham, MA) and exposed on film. Film was scanned (Canon canoscan9000F) and band intensity quantified using ImageJ software. For proteins exhibiting multiple bands, intensities were combined.

Lysis solution: TBS, 2 mM EDTA pH 8.0, 0.5 mM PMSF (Thermo Fisher Scientific, Waltham, MA), 1 % triton-100, 0.5 % P8340 (Sigma Aldrich, St Louis, MO).

Sociability

All animals were habituated to the behavioral testing room one hr prior to testing. Two groups of animals were used: test mice and control or unfamiliar mice. Control animals were of a similar mixed background strain, similar ages, gender matched, and housed in a separate room as the test mice. The sociability arena consisted of a 68.5 cm X 27.2 cm rectangular black plexiglass box (FT Plastics, Oak Park, MI) in which two wire mesh cups (11.11 cm X 12.86 cm, Walmart, Bentonville, AR) were turned upside – down in each end (see schematic below). Magnets were attached to the top of the cups for added weight (#BX0X08DCSPC, K&J Magnetics Inc, Plumsteadville, PA).

Sociability testing was carried out in three phases: habituation, trial 1, and trial 2. During habituation, mice were placed in the center of the sociability arena and allowed to explore the arena and empty cups for five min. Afterwards, mice were returned to their home cage. Thirty min later trial 1 began where a control, or unfamiliar mouse, was placed underneath one wire cup while the other remained empty. Test mice were allowed to explore the sociability arena for ten min, then

Table 4.1 – Western blot primary antibodies

Antibody	Company	Catalog #	Species	Dilution
Glutamate decarboxylase (GAD) 65/67	Santa Cruz	sc365180	MsIgG_1	1:1000
gamma-Aminobutyric acid A ($GABA_A$) R receptor α1-6(E-8)	Santa Cruz	sc376282	MsIgG_1	1:1000
gamma- Aminobutyric acid B ($GABA_B$) receptor R1(R300)	Santa Cruz	sc14006	Rb	1:1000
Glutaminase (Gls)	Abcam	ab113509	Rb	1:1000
Glutamine synthetase (GS)	Millipore	MAB302	MsIgG_{2A}	1:1000
4-aminobutyrate aminotransferase (ABAT) (H-161)	Santa Cruz	sc366534	Rb	1:1000
beta-Actin	Sigma	A1978	MsIgG_1	1:1000

Table 4.2 – Western blot secondary antibodies

Antibody	Conjugation	Company	Catalog #	Dilution
Gt α $MsIgG_1$	HRP	Southern Biotech	1070-05	1:2000
Gt α $MsIgG_{2A}$	HRP	Southern Biotech	1080-05	1:2000
Gt α Rb	HRP	Cell Signaling	7074	1:2000

returned promptly to their home cage. Thirty min later trial 2 began. The same control mouse was placed underneath the same wire cup as before, but this time an additional unfamiliar, now novel mouse, was placed underneath the previously empty cup. Control and novel animals were counterbalanced for side of arena and role as control or novel throughout the study between genotypes. Furthermore, control animals were habituated to residing underneath the wire cups.

All phases of sociability were video recorded (Samsung SC-MX20L/XAA) and the center point of the mouse tracked using Ethovision software (version 8.5, Noldus, Leesburg, VA). Videos were analyzed for total distance traveled, average velocity, time spent in a 3.75 cm perimeter circle (half a mouse length or 1.68 X cup diameter) or 5.56 cm perimeter (three-fourths a mouse length, or 2 X cup diameter) around each cup, each zone (left, right, middle), and manual scored for grooming time and location.

Figure 4.5 – Sociability schematic

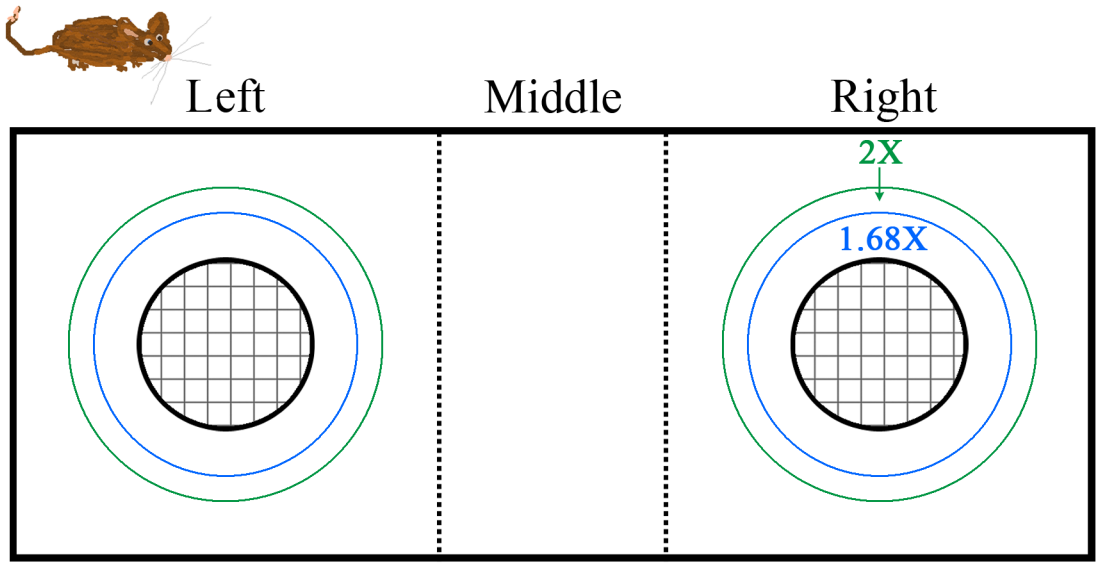

Sociability schematic illustrating the three-chambered arena designating left, middle, and right segments. Zone analyses calculating time spent in the immediate vicinity of the wire cups (black girds) are depicted in blue (1.68 X) and green (2 X) circles representing half and three-fourths a mouse body lengths away from the perimeter of the wire cups. The arena is drawn to scale with respect to the mouse in the top left corner.

RESULTS

Initial behavioral screens suggest *Cldn11*$^{-/-}$*Tg*$^{+/-}$ mice have a reduced anxiety-like phenotype

Initial interactions with *Cldn11*$^{-/-}$*Tg*$^{+/-}$ mice in their home cage suggested that they may exhibit a behavioral abnormality. When lifting the cage top of a large cage of mice, most scattered to the edge, while a few remained in the center. When genotypes of these mice were checked, they were most often *Cldn11*$^{-/-}$*Tg*$^{+/-}$ mice. To quantify this anecdotal observation, we investigated the relative anxiety levels in these mice and littermate controls using behavioral paradigms.

Two behavioral tests were considered, open field (OF) and marble burying (MB). Each test examines anxiety by eliciting a response in a novel or a familiar environment. In the OF paradigm, anxiety level is measured by determining the amount of time rodents spend in the center of a novel open arena (Figure 4.1). Using *t*-tests to compare total time, *Cldn11*$^{-/-}$*Tg*$^{+/-}$ mice at 6 – 8 M of age spent twice as much time in various sized center squares (32, 48, 66, and 83 %) as controls (Figure 4.6, Table 4.3). To determine if this abnormal phenotype was present at younger ages, we examined a separate cohort of 2 and 4 M *Cldn11*$^{+/-}$Tg$^{+/-}$ and *Cldn11*$^{-/-}$Tg$^{+/-}$ mice in the OF paradigm. No significant differences were observed for any of the center square dimensions tested (Figure 4.6, Table 4.3). These data suggest that at 6 – 8 M of age, *Cldn11*$^{-/-}$*Tg*$^{+/-}$ mice exhibit a less anxious phenotype compared to controls that is not detected in the mutants at younger ages.

The validity of behavioral testing depends heavily on control parameters specific to each test. For instance, the OF paradigm relies on a mouse's ability to

Figure 4.6 – *Cldn11*$^{-/-}$*Tg*$^{+/-}$ mice spend significantly more time in center squares of an open field arena, indicating a decreased anxiety-like phenotype

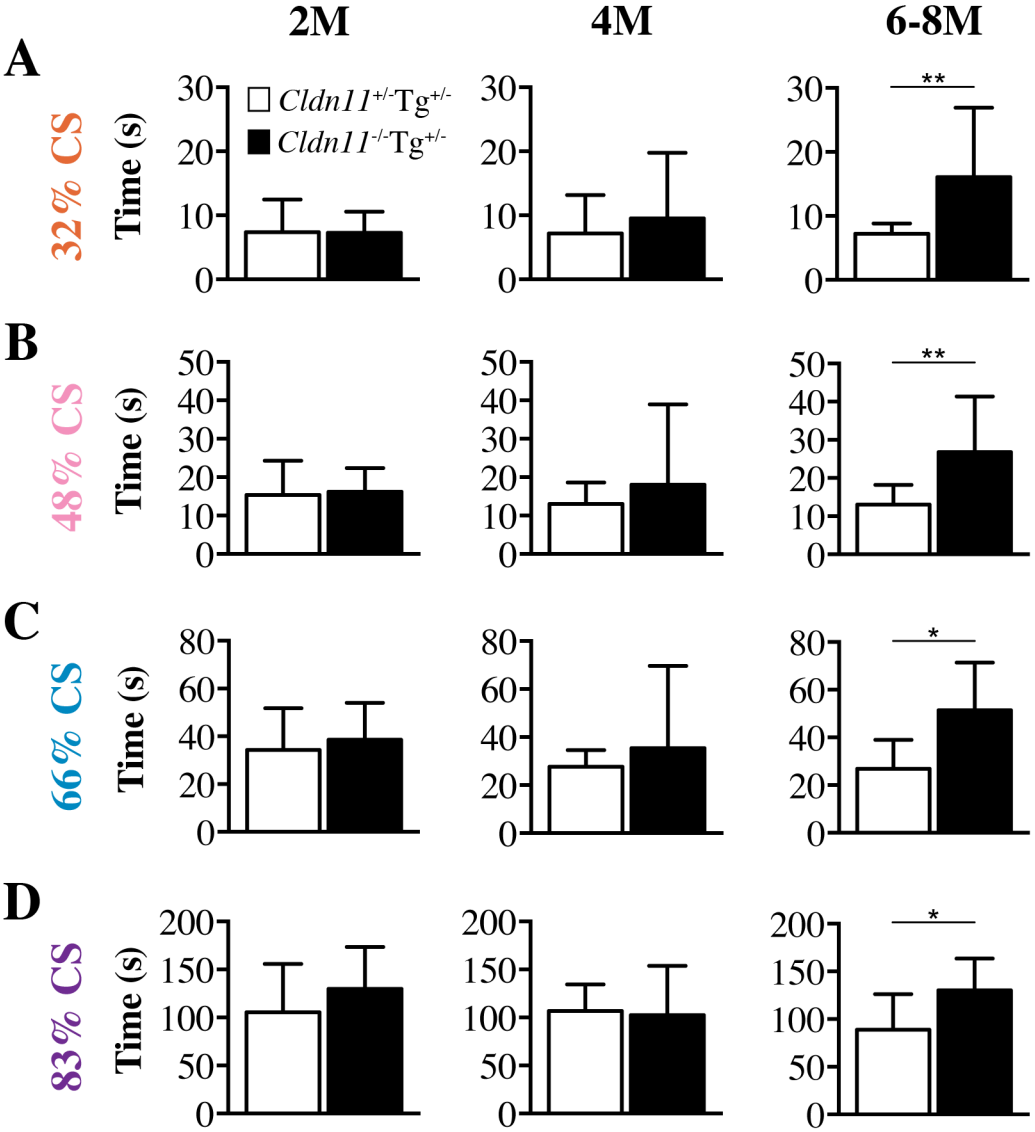

Time spent in concentric center squares of an open field arena reveals that *Cldn11*$^{-/-}$ *Tg*$^{+/-}$ were evident for center squares **(A)** 32 %, **(B)** 48 %, **(C)** 66 %, and **(D)** 83 %. Center square percentages were based on the average mouse body length away from the periphery of the arena: half (83 %), one (66 %), one and a half (48 %), and two (32 %) body lengths. Data values are plotted as mean ± SD, $9 \leq n \leq 10$, $^{*}p < .05$, $^{**}p < .01$.

Table 4.3 – Tabulated *p* values comparing the amount of time *Cldn11*$^{+/-}$*Tg*$^{+/-}$ and *Cldn11*$^{-/-}$*Tg*$^{+/-}$ mice spent in differing CS of the open field arena (Figure 4.6)

	6 – 8 M	
Center Square (%)	t_{17}	*p*
32	***2.483***	***0.0237***
48	***2.747***	***0.0138***
66	***3.067***	***0.0070***
83	***2.545***	***0.0209***
	4 M	
	t_{18}	*p*
32	0.3584	0.7242
48	0.3020	0.7661
66	0.2509	0.8047
83	0.2205	0.8280
	2M	
	t_{18}	*p*
32	0.1371	0.8925
48	0.3874	0.7030
66	0.5750	0.5724
83	1.158	0.2618

A *t*-test was used to identify statistically significant differences (bold, italicized).

explore an unfamiliar, lit arena. The overall interpretation of CS activity can be influenced by two key factors: the speed a mouse travels and the total distance traversed. Appendix D.1 shows the total distance traveled (A) and the average velocity (B) of *Cldn11*$^{+/-}$*Tg*$^{+/-}$ and *Cldn11*$^{-/-}$*Tg*$^{+/-}$ mice at 2, 4, and 6 – 8 M of age. Both groups of mice traverse a similar distance at 2 (t_{18} = 0.2729, p = 0.7880), 4 (t_{18} = 1.1063, p = 0.3021), and 6 – 8 (t_{17} = 1.413, p = 0.1756) M of age. Similarly, when we investigated the average speed of the mice, we find no significant difference at 2 (t_{18} = 0.2887, p = 0.7765), 4 (t_{18} = 1.128, p = 0.2739), and 6 – 8 M (t_{17} = 1.335, p = 0.1996).

Additionally, because ambient lighting is a major contributing factor to anxiety in the OF test, we wanted to verify that differential illumination, if present, did not influence the results. We divided the square arena into four quadrants (Figure 4.1) and performed a quadrant analysis in which the average amount of time spent in each was compared between genotypes within each age group (Appendix D.2). A one-way ANOVA did not detect significant differences for time spent in any quadrant for mice at 2 M of age ($F_{7, 72}$ = 1.330, p =0.2486). Significant overall F values were obtained at 4 ($F_{7, 72}$ = 2.497, p = 0.0235) and 6 – 8 M of age ($F_{7,68}$ = 3.248, p =0.0049), however, Bonferroni post hoc tests comparing individual quadrants between genotypes were not significant. Taken together, the lack of differences between any of the control parameters validates our initial interpretation of the OF data that *Cldn11*$^{-/-}$*Tg*$^{+/-}$ mice appear to have a less anxious phenotype.

Behavioral testing aims to quantify anthropomorphic emotional responses in rodents and relate them to multifaceted and complex human behaviors. The

interpretation of behavioral phenotypes based on a single test may be misleading, and therefore, a secondary behavioral test is always recommended (Ramos, 2008). Because the OF paradigm induces anxiety-like responses through a novel environment, we wanted a second test that could be implemented in a more native, less aversive setting: a home cage. To achieve this, we chose to perform marble burying (MB) analysis.

Marble burying is designed to measure the anxiety-like response of rodents by comparing the number of marbles buried over a designated time period. We analyzed the number of marbles buried for the same cohort of mice that underwent OF testing. Significant differences between *Cldn11*$^{+/-}$*Tg*$^{+/-}$ and *Cldn11*$^{-/-}$*Tg*$^{+/-}$ mice were seen at 6 – 8 M of age (Figure 4.7). *Cldn11*$^{-/-}$*Tg*$^{+/-}$ mice buried significantly fewer marbles as compared to controls, t_{17} = 2.723, p = 0.0145, on average about half as many. At 2 and 4 M of age, *Cldn11*$^{+/-}$*Tg*$^{+/-}$ and *Cldn11*$^{-/-}$*Tg*$^{+/-}$ mice buried a similar amount of marbles: t_{18} = 1.935, p = 0.0689 and t_{18} = 1.306, p = 0.2080 respectively. These data mirror the OF paradigm, supporting the idea that *Cldn11*$^{-/-}$ *Tg*$^{+/-}$ mice have decreased anxiety-like phenotype at 6 – 8 M of age.

Cldn11$^{-/-}$_Tg_$^{+/-}$ mice do not exhibit depression-like symptoms

Behavioral abnormalities are common in white matter diseases, and can be the most debilitating feature of the disease. Changes in anxiety state are frequently comorbid with changes in depression (major depression, major depressive disorder, unipolar depression, clinical depression). A number of behavioral experiments have been developed for studying depression-like behaviors in animal models (Porsolt et al., 1977; Porsolt et al., 1987). Because we observed an altered anxiety-like

Figure 4.7 – Marble burying test reveals *Cldn11*$^{-/-}$*Tg*$^{+/-}$ mice have decreased anxiety-like phenotype compared to controls

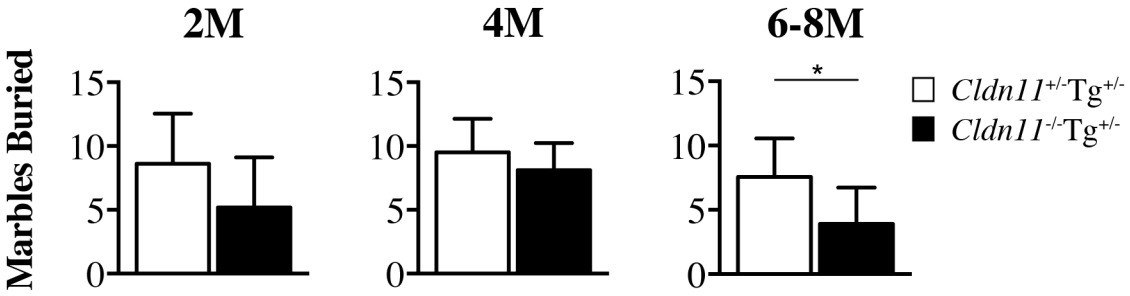

Using a Student's *t*-tests by age, *Cldn11*$^{-/-}$*Tg*$^{+/-}$ mice buried significantly fewer marbles than controls at 6 – 8M of age. At 2M or 4M, there is no significant difference in the number of marbles. Data values are plotted as mean ± SD, $9 \leq n \leq 10$, $*p < .05$.

phenotype in the *Cldn11*$^{-/-}$Tg$^{+/-}$ mice, we next asked if changes in depression were also present. We employed two behavioral tests, the tail suspension test (TST) and the sucrose preference test (SPT). These tests emphasize distinct facets of depression, despair and anhedonia respectively.

In a comparable template to anxiety testing, these tests investigate depression-like phenotypes via different strategies. The TST paradigm has been widely used to screen the effectiveness of antidepressant drugs for their ability to increase mobility time (Cryan et al., 2005; Perrault et al., 1992; Steru et al., 1987; Steru et al., 1985). We calculated the amount of time *Cldn11*$^{+/-}$*Tg*$^{+/-}$ and *Cldn11*$^{-/-}$ *Tg*$^{+/-}$ mice spent immobile over a 360 sec period at 2, 4, and 6 – 8 M of age (Figure 4.8). The average time spent immobility was approximately 220 sec for mice at 2 and 6 – 8 M of age, and 250 sec for mice at 4 M of age. Regardless of age, there was no significant difference in the amount of time spent immobile between *Cldn11*$^{+/-}$ *Tg*$^{+/-}$ and *Cldn11*$^{-/-}$*Tg*$^{+/-}$ mice at 2 (t_{18} = 1.736, p = 0.0996), 4 (t_{18} = 0.1603, p = 0.8745), or 6 – 8 M (t_{18} = 0.5067, p = 0.6185). These data suggests a lack of despair-like phenotype in the *Cldn11*$^{-/-}$*Tg*$^{+/-}$ mice.

Eliminating the aversive stimulus, we tested anhedonia-like behavior in an unobtrusive setting using the SPT. Mice have a propensity for sweeter substances and when given the choice, preferentially drink the sugary option. A sucrose preference percentage was calculated (sucrose liquid consumed / total liquid consumed [water + sucrose]) for each test day and compared between genotypes. Figure 4.9 illustrates the average sucrose preference percentage for *Cldn11*$^{+/-}$*Tg*$^{+/-}$ and *Cldn11*$^{-/-}$*Tg*$^{+/-}$ mice at 2, 4, and 6 – 8 M of age. On any given test day, mice

Figure 4.8 – The tail suspension test suggests a lack of a depression-like phenotype in *Cldn11*$^{-/-}$*Tg*$^{+/-}$ mice

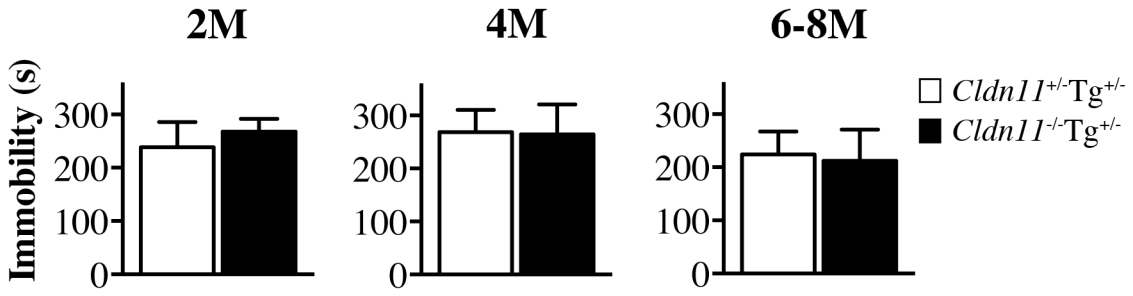

Student's unpaired *t*-test at 2, 4, and 6 – 8M of age reveal both *Cldn11*$^{+/-}$*Tg*$^{+/-}$ and *Cldn11*$^{-/-}$*Tg*$^{+/-}$ mice spend a similar amount of time immobile during tail suspension, suggesting a lack of anhedonia. Data values are plotted as mean ± SD. $9 \leq n \leq 10$.

drank approximately 55 – 70 % sucrose solution compared to water. Using a repeated measures (RM) two-way ANOVA, no significant differences were calculated for preference percentage between genotypes at 2, 4, or 6 – 8 M of age: $F_{1,18}$ = 0.04, p = 0.8536; $F_{1,18}$ = 0.94, p = 0.3445; and $F_{1,18}$ = 0.76, p = 0.3943 respectively. The preference percentages calculated for *Cldn11*$^{+/-}$*Tg*$^{+/-}$ and *Cldn11*$^{-/-}$ *Tg*$^{+/-}$ mice is similar to published values for mice with our background strain performance (Pothion et al., 2004).

The amount of sucrose solution consumed can be influenced by a number of variables, such as weight of the mouse, total liquid consumed, and the amount of food eaten. Each control parameter was monitored during testing, both during acclimation (1 – 4) and testing days (5 – 8) (Appendix D.3). The weight of each animal was normalized to weight on day 1, neutralizing the influence of gender (Appendix D.3, A). Using a RM ANOVA for mice at 2, 4, or 6 – 8 M of age, no significant differences in weight fluctuations was seen (2M: $F_{1,16}$ = 0.15 , p = 0.6991; 4M: $F_{1,18}$ = 0.01, p = 0.9287; and 6 – 8 M: $F_{1,18}$ = 0.58, p = 0.4576).

Next, we examined total liquid consumed, regardless of type, across the testing period (Appendix D.3, B). For any given age, mice consumed approximately 5 – 10 ml of liquid over a 24 – hr period. A RM ANOVA revealed no significant influence of genotype on liquid volume consumed at 2 ($F_{1,16}$ = 0.17 , p = 0.6858) and 6 – 8 M ($F_{1,18}$ = 0.92, p = 0.3493) of age, however, a significant F value was calculated for mice at 4 M of age ($F_{1,18}$ = 6.19, p = 0.0229). Bonferroni post hoc tests comparing genotype versus each test day indicates a lack of significance. The final control parameter monitored was total food intake during SP testing (Appendix D.3,

Figure 4.9 – Sucrose preference testing demonstrates a lack of anhedonia in *Cldn11*$^{-/-}$*Tg*$^{+/-}$ mice

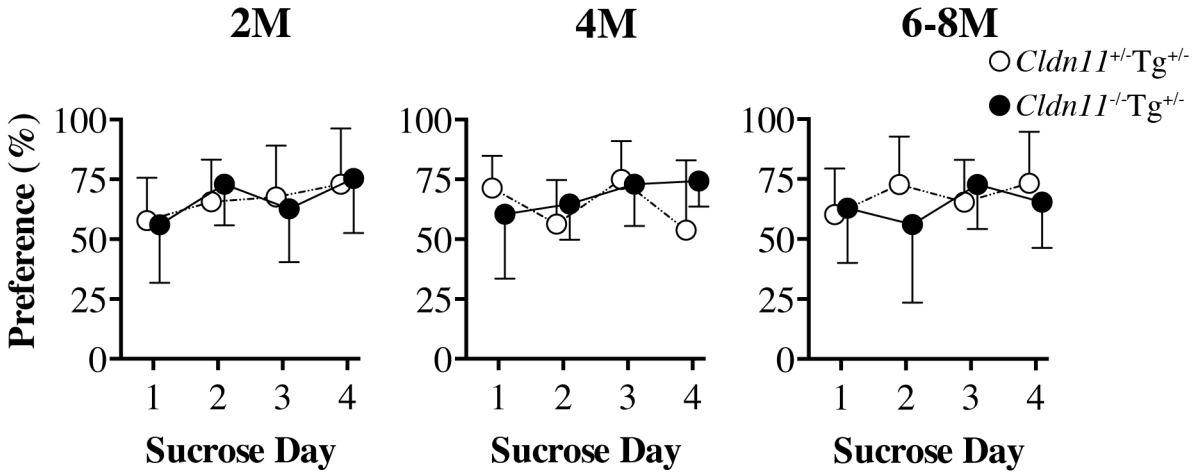

Using a RM two-way ANOVA, it was determined that both *Cldn11*$^{+/-}$*Tg*$^{+/-}$ and *Cldn11*$^{-/-}$*Tg*$^{+/-}$ mice have a similar level of preference for a sucrose solution at 2, 4, and 6 – 8 M of age. Data values are plotted as mean ± SD, *n* = 9 at 2 M, *n* = 10 at 4 and 6 – 8 M. *Cldn11*$^{-/-}$ values are shifted about the abscissa for clarification.

C). In general, mice of all ages consumed approximately 4 – 6 g of food, regardless of phase (acclimation or testing). A RM ANOVA was preformed for each age group and we did not observe significant effects of genotype on food consumed at 2 or 6 – 8 M of age ($F_{1,16}$ = 0.43, p = 0.5196 and $F_{1,18}$ = 0.59, p = 0.4510 respectively). Once more, the overall F values showed a significant difference at 4 M of age ($F_{1,18}$ = 3.21, p = 0.0898), but Bonferroni post hoc tests comparing genotype versus day was not significant. These data suggest that each constraint was neutral and did not influence the overall results of sucrose preference.

A more complex analysis for the breakdown of liquid consumption must be completed, acknowledging the presentation of two sipper bottles and potential effect placement has on total liquid consumption. Appendix D.4, A shows the culmination of liquid drank during acclimation when water is present in both sipper bottles. In our arrangement, the left sipper tube is closest to the long wall of the cage and the right sipper tube is more towards the center. The purpose of examining the differential liquid drank from the left and right side is to determine if one side has preferentially influenced testing, especially given the inherent tendency for *Cldn11*$^{-/-}$*Tg*$^{+/-}$ mice to spend more time in the center. To prevent a side preference while drinking, sipper bottle locations were counterbalanced throughout testing: half of the mice received sucrose beginning in the left sipper bottle, while others started with sucrose on the right. Sipper bottle placement was alternated each day and side preference was computed for acclimation (Appendix D.4, A) and sucrose testing (Appendix D.4, B).

During acclimation (days 1 – 4), a two-way RM ANOVA, shows no significant difference between *Cldn11*$^{+/-}$*Tg*$^{+/-}$ and *Cldn11*$^{-/-}$*Tg*$^{+/-}$ mice at 2 M (2M: $F_{1,16}$ = 0.4213,

p = 0.68). The overall ANOVA comparing left versus right sipper bottle does yield a statistically significant F value ($F_{1,16}$ = 0.4213, p = 0.68), however, Bonferroni post hoc comparing *Cldn11*$^{+/-}$*Tg*$^{+/-}$ versus *Cldn11*$^{-/-}$*Tg*$^{+/-}$ is not statistically significant. At 4 M of age, statistically significant F values were tabulated for a placement difference between left and right ($F_{1,18}$ = 11.09, p = 0.0037), as well as genotype ($F_{1,18}$ = 5.09, p = 0.0367). Bonferroni post hoc tests indicate the only significant finding is between the left and right sipper bottles for both genotypes: both *Cldn11*$^{+/-}$*Tg*$^{+/-}$ and *Cldn11*$^{-/-}$*Tg*$^{+/-}$ mice drank significantly more from the right sipper bottles. With respect to 6 – 8 M animals, there was no statistically significant difference between genotype ($F_{1,18}$ = 1.66, p = 0.2141), but significance in left versus right side preference ($F_{1,18}$ = 25.09, p = <0.0001). Both *Cldn11*$^{+/-}$*Tg*$^{+/-}$ and *Cldn11*$^{-/-}$*Tg*$^{+/-}$ mice preferentially drank more liquid from the right sipper bottle.

Throughout SP testing days (days 5 – 8), one sipper bottle contained a 2 % sucrose solution. To account for a side preference, two-way RM ANOVAs were performed in a similar fashion as the acclimation phase. At 2 M of age, no significant differences were seen for left versus right liquid preference ($F_{1,16}$ = 4.25, p = 0.0533), or between genotypes ($F_{1,16}$ = 0.41, p = 0.5292). At 4 M of age, no significant difference were seen for liquid drank from left versus right sipper bottles ($F_{1,18}$ = 1.66, p = 0.2144), however comparing genotypes yielded a statistically significant F value ($F_{1,18}$ = 6.48, p = 0.0203). Performing a Bonferroni post hoc contrasting *Cldn11*$^{+/-}$*Tg*$^{+/-}$ versus *Cldn11*$^{-/-}$*Tg*$^{+/-}$ revealed no significant difference. And finally, at 6 – 8 M of age, a two-way RM ANOVA indicated a statistically significant difference for left versus right preference ($F_{1,18}$ = 8.71, p = 0.0086). A Bonferroni post hoc test

revealed that *Cldn11*$^{+/-}$*Tg*$^{+/-}$ mice drank significantly more liquid from the right side, as compared to the left. No significant difference was seen between genotype ($F_{1,18}$ = 0.48, p = 0.4962). In summary, the patterning of liquid intake was similar between *Cldn11*$^{+/-}$*Tg*$^{+/-}$ and *Cldn11*$^{-/-}$*Tg*$^{+/-}$ mice, indicating side preference did not influence the overall sucrose preference results.

Combining results from TS and SP, these data indicate a lack of depression-like phenotype in *Cldn11*$^{-/-}$*Tg*$^{+/-}$ mice. The various subcategories of depression examined, despair and anhedonia-like responses, are similar between *Cldn11*$^{+/-}$*Tg*$^{+/-}$ and *Cldn11*$^{-/-}$*Tg*$^{+/-}$ mice. Analyses of confounding variables indicate negligible differences, strongly suggesting a lack of influence of depression-like characteristics in *Cldn11*$^{-/-}$*Tg*$^{+/-}$ mice.

Cognitive learning and memory is similar between *Cldn11*$^{+/-}$*Tg*$^{+/-}$ and *Cldn11*$^{-/-}$*Tg*$^{+/-}$ mice

One of the most distressing symptoms of white matter diseases, despite the probable change in mood, is the loss of cognitive function. Increasing association between white matter dysfunction and cognitive decline / dysfunction is vastly noted throughout the literature, not only in normal aging patients (Gunning-Dixon and Raz, 2000; Hedden and Gabrieli, 2004), but diseases with a predominantly white matter pathology. In multiple sclerosis (MS), for example, cognitive dysfunction is a frequent and often devastating symptom that, arguably, is the most debilitating feature of the disease (Jongen et al., 2012; Lovera and Kovner, 2012).

To determine if our mouse model of dysfunctional myelin exhibited similar deficits, we assessed cognitive learning and memory ability using the Barnes maze

(BM). For this test, a circular platform containing 20 holes along the perimeter is used to assess a mouse's ability to learn and remember the location of a target goal box located underneath a single hole (Figure 4.3). Mice are trained to locate the correct goal hole and the latency is computed for training, as well as probe days (Barnes, 1979). Using a RM ANOVA comparing the effect of genotype on latency to locate the goal hole throughout testing, no significant difference was discerned at 2 ($F_{1,17}$ = 1.48, p = 0.2399), 4 ($F_{1,15}$ = 0.12, p = 0.7293), or 6 – 8 M of age ($F_{1,18}$ = 4.03, p = 0.0601) (Figure 4.10). These data indicate similar cognitive learning and memory ability of *Cldn11*$^{+/-}$*Tg*$^{+/-}$ and *Cldn11*$^{-/-}$*Tg*$^{+/-}$ mice.

During BM testing, three probe days are performed to evaluate a mouse's learning and memory ability under different scenarios. For each, the goal compartment is removed, eliminating reinforcement of a correct selection. Because there is no compartment for a mouse to enter, time spent in various zones surrounding the trained goal hole is analyzed. Zone 0 represents the immediate circular vicinity around the trained goal hole, twice its diameter. Zone 1 is designated as the wedge-shaped portion of maze surrounding the trained goal hole, demarcated by one neighboring hole on each side. Zone 2 is designated as the wedge-shaped section surrounding the goal hole, encompassing Zone 1 and expanding the boundary to two holes flanking the trained goal hole (see Methods for clarification).

The first scenario is a simple probe day (day 5) to test the mouse's ability to remember the location of the trained goal hole (Appendix D.5). Employing Student's *t*-tests to compare time spent in various zones around the trained goal hole, we observe no significant differences at 2, 4, or 6 – 8 M of age for time spent in Zone 0,

Figure 4.10 – Latency to find trained goal hole throughout Barnes maze testing is comparable between *Cldn11*$^{+/-}$*Tg*$^{+/-}$ and *Cldn11*$^{-/-}$*Tg*$^{+/-}$ mice demonstrating indistinguishable spatial learning and memory ability

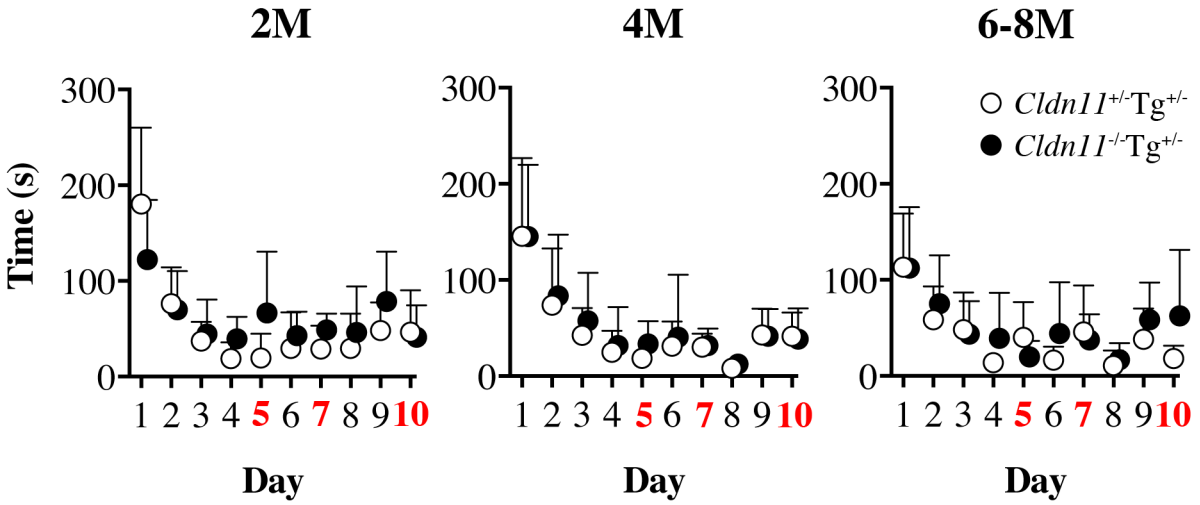

A two-way RM ANOVA comparing genotype by day confirms similar latency for *Cldn11*$^{+/-}$*Tg*$^{+/-}$ and *Cldn11*$^{-/-}$*Tg*$^{+/-}$ mice to reach the learned goal hole across Barnes maze testing at 2, 4, and 6 – 8 M of age. Data values are plotted as mean ± SD; 2 M: $9 \leq n \leq 10$, 4 M: $7 \leq n \leq 10$, 6 – 8 M: $9 \leq n \leq 11$. See Methods section for zone illustration. *Cldn11*$^{-/-}$*Tg*$^{+/-}$ values are shifted about the abscissa for clarification; red numbers indicate probe days.

1, or 2 around the trained goal hole (Table 4.4). These data suggest that both *Cldn11*$^{+/-}$*Tg*$^{+/-}$ and *Cldn11*$^{-/-}$*Tg*$^{+/-}$ mice not only found the goal hole is a similar amount of time, but spend equal time in the zone located immediately around the trained hole.

The second scenario tested was a curtain probe (day 7). In a similar fashion to probe day, time spent in the aforementioned zones was investigated (Appendix D.6). For *Cldn11*$^{+/-}$*Tg*$^{+/-}$ and *Cldn11*$^{-/-}$*Tg*$^{+/-}$ mice at 2 M of age, a comparable amount of time was spent in Zone 0, 1 and 2. The cohort of mice at 4 M of age spent a similar amount of time in Zone 0 and 1, however, *Cldn11*$^{-/-}$*Tg*$^{+/-}$ mice spent significantly more time in Zone 2, about 30 % more, as compared to *Cldn11*$^{+/-}$*Tg*$^{+/-}$ mice. At 6 – 8 M of age, no significant differences were seen for time spent in any zone examined (Table 4.5).

The final scenario examined during BM testing was a reversal probe (day 10). The reversal probe was conducted in a similar format as the probe day (day 5), and the time spent in the aforementioned zones was analyzed for the newly trained hole (Appendix D.7). At 2 M of age, *Cldn11*$^{+/-}$*Tg*$^{+/-}$ mice spent significantly more time in Zone 0 (t_{18} = 1.314, p = 0.0334), a similar amount of time in Zone 1 (t_{18} = 1.944, p = 0.0687) and significantly less time in Zone 2 (t_{18} = 2.118, p = 0.0492) around the newly trained reversal hole. For the cohort at 4 M of age, no significant differences were seen for the amount of time spent in any zone: Zone 0 (t_{16} = 0.6839, p = 0.5045), Zone 1 (t_{16} = 0.1958, p = 0.8474), or Zone 2 (t_{16} = 0.0665, p = 0.9478). Similarly, at 6 – 8 M of age, no significant differences were observed (Zone 0: t_{17} =

Table 4.4 – Tabulated *p* values comparing the amount of time *Cldn11*$^{+/-}$*Tg*$^{+/-}$ and *Cldn11*$^{-/-}$*Tg*$^{+/-}$ mice spent in differing sized zones around the goal hole during BM probe day 5 (Appendix D.5).

	6 – 8 M	
Zone	t_{17}	*p*
0	0.1903	0.8513
1	0.4176	0.6815
2	0.6297	0.5373
	4 M	
	t_{16}	*p*
0	0.8154	0.4268
1	0.3620	0.7221
2	0.0155	0.9878
	2M	
	t_{18}	*p*
0	0.72	0.4808
1	0.9633	0.3482
2	1.062	0.3022

A *t*-test was used to identify statistically significant differences (bold, italicized).

Table 4.5 – Tabulated *p* values comparing the amount of time *Cldn11*$^{+/-}$*Tg*$^{+/-}$ and *Cldn11*$^{-/-}$*Tg*$^{+/-}$ mice spent in differing sized zones around the goal hole during BM curtain probe day 7 (Appendix D.6).

	6 – 8 M	
Zone	t_{17}	*p*
0	0.7320	0.4376
1	0.1658	0.8701
2	0.0165	0.9870
	4 M	
	t_{16}	*p*
0	1.178	0.2560
1	1.819	0.0877
2	***2.236***	***0.04***
	2M	
	t_{18}	*p*
0	0.7701	0.4518
1	0.1132	0.9199
2	0.0309	0.9757

A *t*-test was used to identify statistically significant differences (bold, italicized).

0.4643, p = 0.6480; Zone 1: t_{17} = 0.5227, p = 0.6075; and Zone 2: t_{17} = 1.063, p = 0.3019).

To account for undetectable intra-maze discrepancies, the maze was rotated 90^{O} clockwise on all probe days, ensuring that a hole aligned identically with trained location. To determine the presence of cues, zones were drawn around the hole where the box attaches, the hook-in hole (now at a different location), and zone analysis for time spent was completed. Appendix D.8 shows the zone analysis for probe day for 2, 4, and 6 – 8 M mice. Student's *t*-tests revealed no significant differences in the amount of time *Cldn11*$^{+/-}$*Tg*$^{+/-}$ and *Cldn11*$^{-/-}$*Tg*+/- mice spent around the hook-in hole for Zone^{0}, Zone^{1}, or Zone^{2} at any age (Table 4.6). Appendix D.9 diagrams time spent in each zone around the hook-in hole during curtain probe. Mice at 2 and 6 – 8 M of age spent an indistinguishable amount of time in each region surrounding the hook-in hole, whereas at 4 M of age, *Cldn11*$^{+/-}$*Tg*$^{+/-}$ animals spent significantly more time in every zone surrounding the hook-in hole (Table 4.7). On the final probe day, reversal probe, both groups of animals spent a similar amount of time in the regions around the hook-in hole (Appendix D.10, Table 4.8).

In general, cognitive learning and memory ability of *Cldn11*$^{-/-}$Tg$^{+/-}$ mice is indistinguishable from controls at 2, 4, and 6 – 8 M of age. Barnes maze testing indicates that both genotypes could be trained to locate and remember a target goal hole promptly. The curtain probe trial reveals the use of distal visual cues to be unlikely, and presumably, mice employed a remembered motor reflex to guide them to the target. Introducing a new target location during reversal training and subsequent probe day indicates that both *Cldn11*$^{+/-}$Tg$^{+/-}$ and *Cldn11*$^{-/-}$Tg$^{+/-}$ mice have

Table 4.6 – Tabulated *p* values comparing the amount of time *Cldn11*$^{+/-}$*Tg*$^{+/-}$ and *Cldn11*$^{-/-}$*Tg*$^{+/-}$ mice spent in differing sized zones around the hook-in hole during BM probe day 5 (Appendix D.8).

	6 – 8 M	
Zone	t_{17}	*p*
0	0.5273	0.6048
1	0.5307	0.6025
2	0.3143	0.7571
	4 M	
	t_{16}	*p*
0	0.00009	0.9993
1	0.8202	0.4242
2	0.4174	0.6820
	2M	
	t_{18}	*p*
0	***2.406***	***0.0271***
1	0.04365	0.9657
2	0.1523	0.8806

A *t*-test was used to identify statistically significant differences (bold, italicized).

Table 4.7 – Tabulated *p* values comparing the amount of time *Cldn11*$^{+/-}$*Tg*$^{+/-}$ and *Cldn11*$^{-/-}$*Tg*$^{+/-}$ mice spent in differing sized zones around the hook-in hole during BM curtain probe day 7 (Appendix D.9).

	6 – 8 M	
Zone	t_{17}	*p*
0	0.3207	0.7521
1	0.2527	0.8034
2	0.3207	0.7521
	4 M	
	t_{16}	*p*
0	***5.733***	***<0.0001***
1	***3.788***	***0.0016***
2	***4.639***	***0.0003***
	2M	
	t_{18}	*p*
0	1.785	0.0921
1	0.1690	0.8678
2	0.3035	0.7652

A *t*-test was used to identify statistically significant differences (bold, italicized).

Table 4.8 – Tabulated *p* values comparing the amount of time *Cldn11*$^{+/-}$*Tg*$^{+/-}$ and *Cldn11*$^{-/-}$*Tg*$^{+/-}$ mice spent in differing sized zones around the hook-in hole during BM reversal probe day 10 (Appendix D.10).

	6 – 8 M	
Zone	t_{17}	*p*
0	1.425	0.1712
1	0.3416	0.7366
2	0.6429	0.5284
	4 M	
	t_{16}	*p*
0	0.7512	0.4642
1	0.9394	0.3624
2	1.149	0.2687
	2M	
	t_{18}	*p*
0	0.0753	0.9409
1	0.2331	0.8184
2	0.2369	0.8156

A *t*-test was used to identify statistically significant differences (bold, italicized).

similar short-term memory ability and can focus on a new challenge. This extensive testing and analysis advocates for a lack of cognitive differences between the two groups of animals, for any age examined.

Neurochemical alterations in the brain of *Cldn11*$^{-/-}$*Tg*$^{+/-}$ mice may be responsible for behavioral changes observed

Because we observed abnormal behavior within *Cldn11*$^{-/-}$*Tg*$^{+/-}$ mice, we wanted to determine if neurochemical alterations were present, which could conceivably drive the decreased anxiety we observe. From the same 6 – 8 M animals in which a decreased anxiety-like phenotype was detected, we collected *ex vivo* tissue punches and analyzed the neurochemical composition using high resolution magic angle spinning proton magnetic resolution (magic angle H^1 NMR) (Table 4.9, Figure 4.11). Of importance were brain regions relating to the development of anxiety. Using *t*-tests to compare individual brain regions, *Cldn11*$^{-/-}$ *Tg*$^{+/-}$ mice had significantly increased levels of the main neurotransmitter gamma-aminobutryic acid (GABA) in the VHC, but not the DHC, or ACC (Figure 4.11A): VHC: $t_9 = 2.502$, $p = 0.0338$; DHC: $t_9 = 0.4875$, $p = 0.6378$; ACC: $t_9 = 0.1117$, $p = 0.9138$. Contrasting inhibitory changes, we examined the levels of the principal excitatory neurotransmitter, glutamate, in the VHC, DHC, and ACC, however no significant differences were seen (Figure 4.11B): VHC: $t_9 = 1.359$, $p = 0.2073$; DHC: $t_9 = 0.0365$, $p = 0.9717$; ACC: $t_9 = 2.302$, $p = 0.0503$.

To ascertain the mechanism by which increased levels of GABA could arise, we focused on the metabolic enzymes responsible for synthesizing and breaking

Figure 4.11– Proton Magnetic Resonance Spectroscopy quantification for various brain regions reveals increased GABA levels in the ventral hippocampus of *Cldn11*$^{-/-}$ *Tg*$^{+/-}$ mice

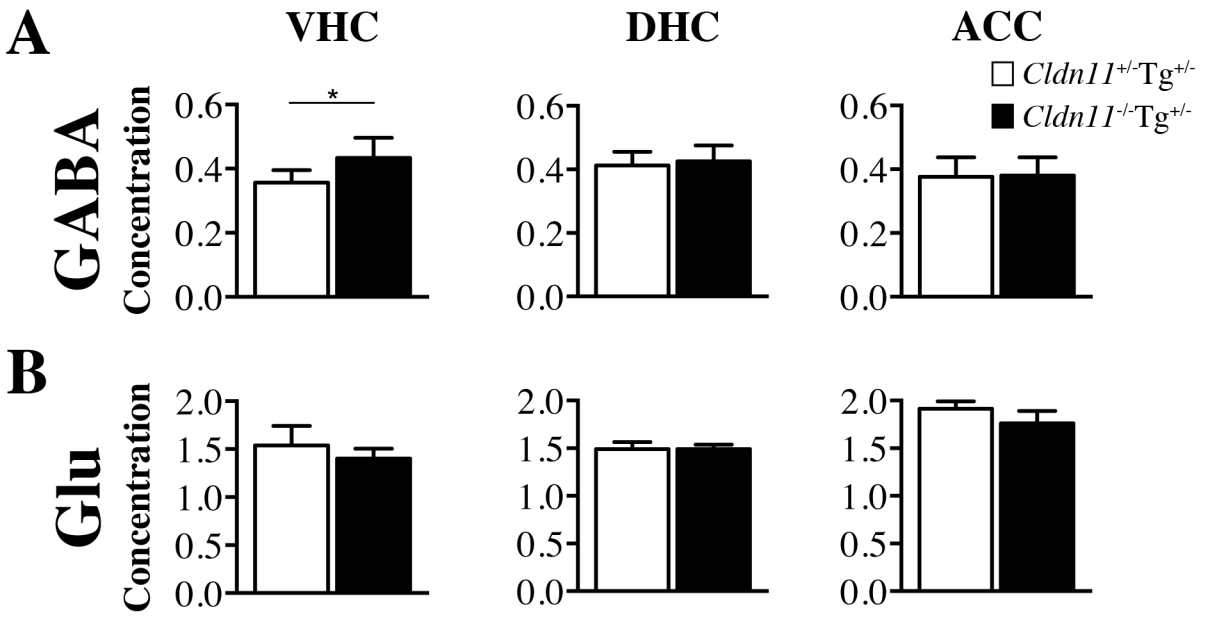

(A) gamma-aminobutryic acid (GABA) levels in select brain regions of *Cldn11*$^{+/-}$*Tg*$^{+/-}$ and *Cldn11*$^{-/-}$ mice. Student's *t*-test for select regions indicates that *Cldn11*$^{-/-}$*Tg*$^{+/-}$ mice have significantly increased GABA levels in the ventral hippocampus (VHC), however comparable amount in the dorsal hippocampus (DHC) and anterior cingulate cortex (ACC). **(B)** Glutamate (Glu) levels in select brain regions of *Cldn11*$^{+/-}$*Tg*$^{+/-}$ and *Cldn11*$^{-/-}$ mice. Student's *t*-test for select regions indicates that *Cldn11*$^{+/-}$*Tg*$^{+/-}$ and *Cldn11*$^{-/-}$*Tg*$^{+/-}$ mice have similar glutamate levels in the VHC, DHC, and ACC. Data values are plotted as mean ± SD; $5 \leq n \leq 6$; $^{*}p < .05$.

Table 4.9 – List of brain regions collected and neurotransmitters analyzable with H^1MRS

	Generalized Brain Region		Neurochemical
ACC	Anterior Cingulate Cortex	Act	Acetate
AMC	Anterior Motor Cortex	Ala	Alanine
AST	Anterior Striatum	Asp	Aspartate
AUD	Auditory Cortex	Bet	Betaine
BS	Brainstem	Cre	Creatine
CB	Cerebellum	Cho	Cholines
DHC	Dorsal Hippocampus	GABA	Gamma-aminobutryic acid
DPST	Dorsal Posterior Striatum	Gln	Glutamine
MidB	Midbrain	Glu	Glutamate
NAC	Nucleus Accumbens	GPC	Glycerophosphocholine
PCC	Posterior Cingulate Cortex	GSH	Glutathione
PMC	Posterior Motor Cortex	Ins	Inositol
SOC	Superior Olivary Complex	Lac	Lactate
THAL	Thalamus	NAA	N-Acetlyaspartate
VHC	Ventral Hippocampus	NAAG	N-Acetlyaspartatylglutamate
VPST	Ventral Posterior Striatum	PEA	Phenylethylamine
		PCh	Phosphocholine
		Suc	Succinate
		Tau	Taurine

down GABA: glutamic acid decarboxylase 65 / 67 (GAD 65 / 67) and 4-aminobutyrate aminotransferase (ABAT) respectively, as well as post-synaptic receptors. Using *t*-tests comparing genotype and individual brain region, no significant differences were seen for the either $GABA_A$ or $GABA_B$ receptor, nor the synthesizing enzyme GAD 65 / 67 (Figure 4.12, Table 4.10). Interestingly, when we compared the protein level of ABAT, a significant increase was seen in the VHC of *Cldn11*$^{-/-}$*Tg*$^{+/-}$ mice (t_8 = 2.570, p = 0.0331), but not the DHC (t_8 = 0.8287, p = 0.4313), or ACC (t_8 = 0.9267, p = 0.3849).

We detected neurochemical alterations at 6 – 8 M of age, correlating with the measureable behavior phenotype, however we wanted to evaluate if this alterations were present in younger animals, preceding a quantifiable behavioral phenotype. Fresh tissue punches were collected from 4 M animals and an abbreviated neurochemical assessment was completed prioritizing the VHC. Appendix D.11 shows GABA and glutamate levels normalized to creatine levels within a given punch. No significant changes were observed within the VHC (GABA: t_{12} = 0.7879, p = 0.4460; Glu: t_{12} = 0.1128, p = 0.9120) or DHC (GABA: t_{15} = 0.0865, p = 0.9322; Glu: t_{15} = 1.337, p = 0.2011). These data support the idea that a neurochemical change may not precede the onset of a detectable behavioral phenotype.

Repeat behavioral analyses of *Cldn11*$^{-/-}$*Tg*$^{+/-}$ mice suggest an undetectable behavioral phenotype

After the initial finding of a decreased anxiety-like phenotype and corresponding increase in GABA level within the VHC of *Cldn11*$^{-/-}$*Tg*$^{+/-}$ mice, we

Figure 4.12 – Western blot analysis of key brain regions associated with an anxiety-like phenotype is similar between *Cldn11*$^{+/-}$*Tg*$^{+/-}$ and *Cldn11*$^{-/-}$*Tg*$^{+/-}$ mice

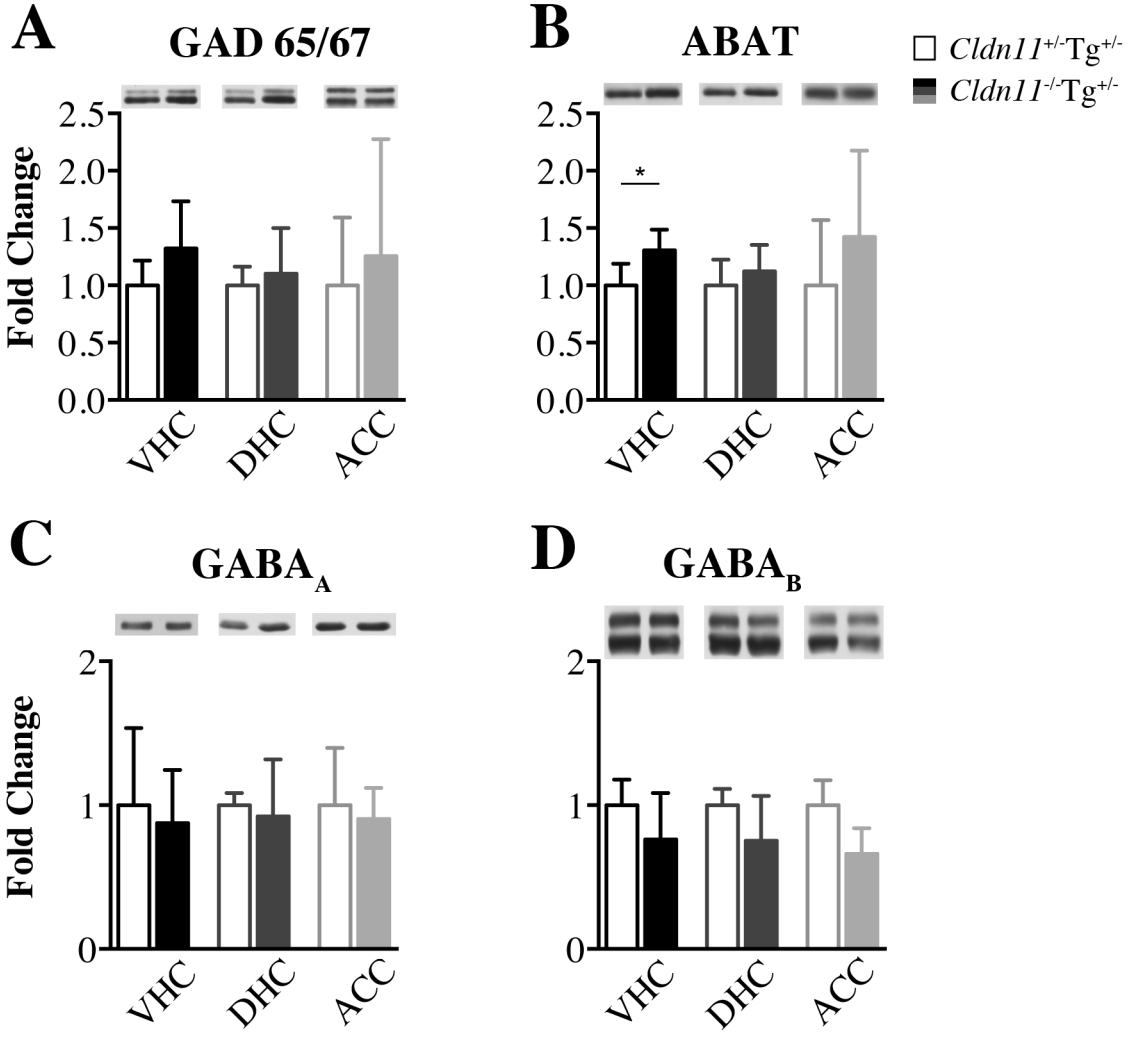

(A) Student's *t*-test comparing GABA's synthesizing protein, GAD 65 / 67, in select brain regions from *Cldn11*$^{+/-}$*Tg*$^{+/-}$ and *Cldn11*$^{-/-}$*Tg*$^{+/-}$ mice at 6 – 8 M of age suggests no difference in protein concentration. **(B)** Student's *t*-test comparing protein concentrations of ABAT, the enzyme responsible for recycling GABA. A significant increase is seen in the ventral hippocampus (VHC) of *Cldn11*$^{-/-}$*Tg*$^{+/-}$ mice, but not in the dorsal hippocampus (DHC) or anterior cingulate cortex (ACC). **(C)** Student's *t*-test comparing $GABA_A$ receptor in select brain regions from *Cldn11*$^{+/-}$*Tg*$^{+/-}$ and *Cldn11*$^{-/-}$*Tg*$^{+/-}$ mice at 6 – 8 M of age indicates a lack of difference in protein concentration. **(D)** Student's *t*-test comparing $GABA_B$ receptor in select brain regions suggests no difference in protein concentration between genotypes. Representative western blot images are shown below each bar graph. Data values are plotted as mean ± SD; $4 \leq n \leq 6$.

Table 4.10 – Tabulated *p* values comparing the protein level of select metabolic enzymes from fresh tissue punches from *Cldn11*$^{+/-}$*Tg*$^{+/-}$ and *Cldn11*$^{-/-}$ *Tg*$^{+/-}$ mice (Figure 4.12).

	$GABA_A$	
Punch Location	t_4	*p*
VHC	0.3299	0.7580
DHC	0.3340	0.7551
ACC	0.3698	0.7303
	$GABA_B$	
	t_4	*p*
VHC	1.114	0.3276
DHC	1.286	0.2677
ACC	2.361	0.0776
	GAD 65/67	
	t_9	*p*
VHC	1.577	0.1458
DHC	0.5337	0.6065
ACC	0.4957	0.6320

A *t*-test was used to identify statistically significant differences (bold, italicized).

hypothesized that excess GABA levels may have originated from dysregulation of metabolizing enzymes; either an increase in synthesis or a decrease in recycling. Examination of the amygdala would have been preferable, however, heavy reciprocal connections are formed between the AMYG and VHC (O'Donnell and Grace, 1995; Pikkarainen et al., 1999). Recent data has uncovered the ability of the AMYG – VHC connection to modulate anxiety-related behaviors, as well as the social nature of rodents, termed sociability (Felix-Ortiz et al., 2013; Felix-Ortiz and Tye, 2014; Moy et al., 2004). By inhibiting AMYG output via pyramidal cells of the basolateral nucleus (BLA) to the VHC, increased social behavior of mice was observed (Felix-Ortiz and Tye, 2014).

Interestingly, the AMYG and VHC have a bidirectional, reciprocal connections thought to modulate social behavior. To ascertain if *Cldn11*$^{-/-}$*Tg*$^{+/-}$ mice have a deficit in social behavior, we preformed a sociability assay on a third cohort of mice 6 – 8 M in age (Figure 4.13). During habituation when both wire cups in the arena remain empty, we find that *Cldn11*$^{+/-}$*Tg*$^{+/-}$ and *Cldn11*$^{-/-}$*Tg*$^{+/-}$ mice spend a similar amount of time in the zones immediately surrounding each cup, as well as each chamber containing a cup (two-way ANOVA; 1.68 X: $F_{1,10} = 0.64$, $p = 0.4428$; 2 X: $F_{1,10} = 1.20$, $p = 0.2948$; chamber: $F_{1,10} = 0.70$, $p = 0.4208$). During trial 1, an unfamiliar mouse is placed underneath one wire cup and we observe that both *Cldn11*$^{+/-}$*Tg*$^{+/-}$ and *Cldn11*$^{-/-}$*Tg*$^{+/-}$ mice spend an indistinguishable amount of time around the empty cup, the cup housing an unfamiliar mouse, and in each arena chamber containing a cup (two-way ANOVA; 1.68X: $F_{1,10} = 1.91$, $p = 0.1970$; 2X: $F_{1,10} = 3.01$, $p = 0.1133$; chamber: $F_{1,10} = 0.29$, $p = 0.6026$).

During the final assessment (trial 2) when mice are underneath both wire cups (now familiar mouse and novel mouse) we find a similar amount of time is spent immediately around each cup and in each chamber, regardless of mouse familiarity (two-way ANOVA; 1.68X: $F_{1,10}$ = 0, p = 0.9856; 2X: $F_{1,10}$ = 0.02, p = 0.8856; chamber: $F_{1,10}$ = 0.02, p = 0.8856). These data suggest that the social nature of *Cldn11*$^{-/-}$*Tg*$^{+/-}$ mice is comparable to controls.

Examining the motor ability of *Cldn11*$^{+/-}$*Tg*$^{+/-}$ and *Cldn11*$^{-/-}$*Tg*$^{+/-}$ mice during sociability testing further supports these results. Appendix D.12 shows the total distance (Appendix D.12, A), average velocity traveled (Appendix D.12, B) and the time spent in each chamber of the sociability arena (Appendix D.12, C). Each parameter was monitored to ensure similarity, eliminating potential influence on time spent in each chamber of the sociability arena. The total distance traveled was proportional between *Cldn11*$^{+/-}$*Tg*$^{+/-}$ and *Cldn11*$^{-/-}$*Tg*$^{+/-}$ animals during habituation (t_{10} = 1.40, p = 0.3229), trial 1 (t_{10} = 0.9836, p = 0.3485), and trial 2 (t_{10} = 0.3858, p = 0.7086). In addition, the average velocity traversed was similar between *Cldn11*$^{+/-}$*Tg*$^{+/-}$ and *Cldn11*$^{-/-}$*Tg*$^{+/-}$ mice during habituation (t_{10} = 1.024, p = 0.33), trial 1 (t_{10} = 0.9141, p = 0.3822), and trial 2 (t_{10} = 0.3106, p = 0.7632).

The last motor parameter examined was the total amount of time spent in each chamber of the sociability arena: left, center, and right. Using a one-way ANOVA to analyze each phase of testing, we find an overall statistically significant F value for habituation ($F_{5,30}$ = 5,704, p = <0.001), trial 1 ($F_{5,30}$ = 23.18, p = <0.0001) and trial 2 ($F_{5,30}$ = 9.622, p = <0.0001), however, Bonferroni post hoc tests comparing genotype versus chamber is not statistically significant for any of the

Figure 4.13 – Time spent in various zones of the sociability arena is similar between *Cldn11*$^{+/-}$*Tg*$^{+/-}$ and *Cldn11*$^{-/-}$*Tg*$^{+/-}$ mice

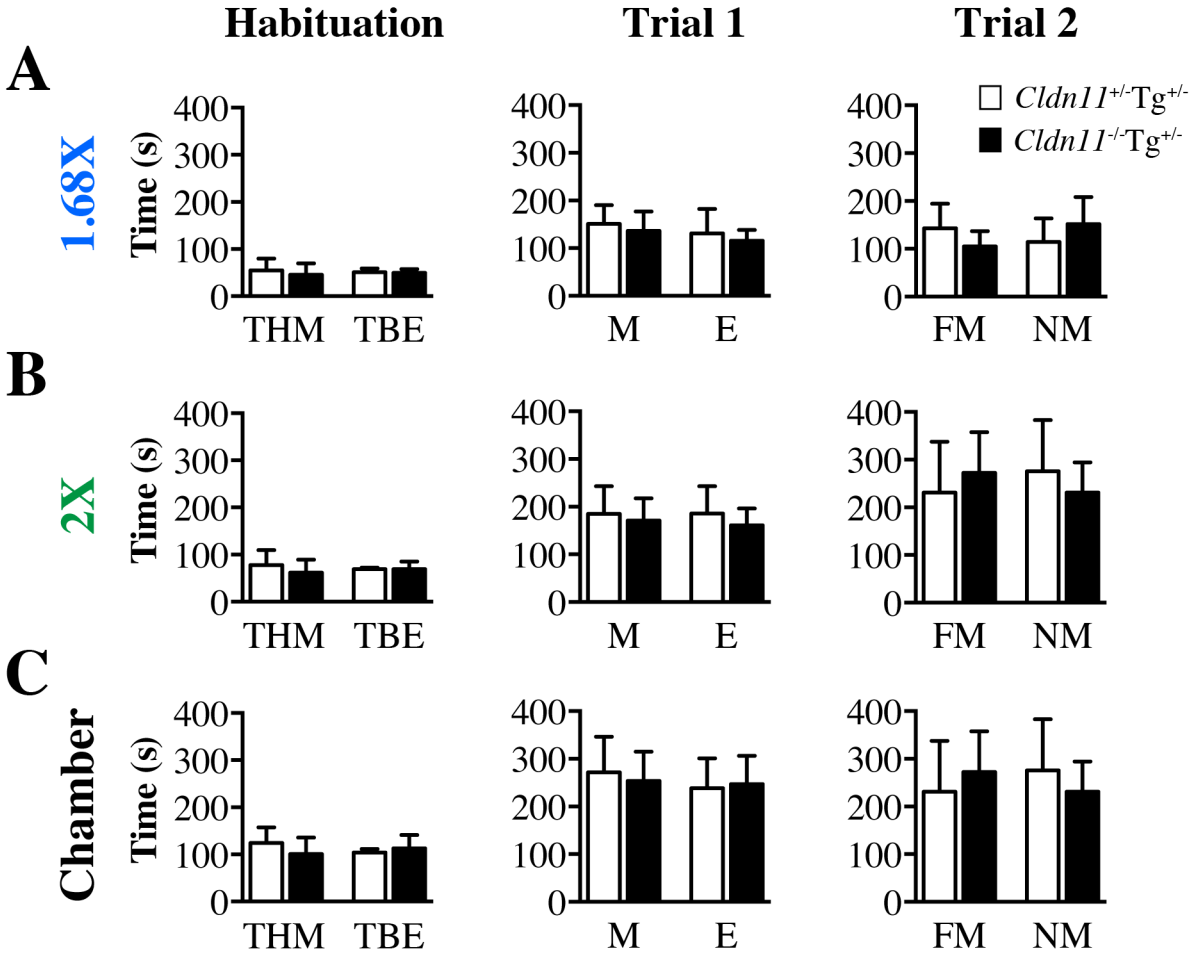

(A) The average amount of time *Cldn11*$^{+/-}$*Tg*$^{+/-}$ and *Cldn11*$^{-/-}$*Tg*$^{+/-}$ mice spend within half a body length (1.68X) around each wire cup is similar throughout each phase of sociability testing: habituation, trial 1, and trial 2. **(B)** The average amount of time mice spend within a body length (2X) of each wire cup is indistinguishable between genotypes. **(C)** The amount of time *Cldn11*$^{+/-}$*Tg*$^{+/-}$ and *Cldn11*$^{-/-}$*Tg*$^{+/-}$ mice spend in each chamber of the sociability arena during each phase is not statistically different between genotypes. Data values are plotted as mean ± SD, *n* = 6. THM to house mouse; TBE to be empty; M mouse; E empty; FM familiar mouse; NM novel mouse

phases. Together, these data suggest that the social nature of *Cldn11*$^{-/-}$*Tg*$^{+/-}$ mice is comparable to controls and uninfluenced by motor ability or arena bias.

Sociability testing involves examining the exploratory preference, and other quantifiable behaviors such as grooming, in the presence of familiar and novel mice (Kaidanovich-Beilin et al., 2011). A secondary analysis was completed on the location and length of grooming behaviors. The amount of time and location of grooming events indicates changes in stress and anxiety levels, differential grooming during various phases of testing could indicate preferential changes in anxiety-like behavior (Kalueff and Tuohimaa, 2005; Moyaho et al., 1995; Moyaho and Valencia, 2002).

Appendix D.13, A diagrams the total time spent grooming for *Cldn11*$^{+/-}$*Tg*$^{+/-}$ and *Cldn11*$^{-/-}$*Tg*$^{+/-}$ mice. No statistically significant differences are observed between genotypes during habituation (t = 1.447, p = 0.1785), trial 1 (t = 1.309, p = 0.22), or trial 2 (t = 1.299, p = 0.2231). We evaluated the proportion of grooming time spent in each chamber of the sociability arena more extensively during trials 1 and 2 because of the added variable (additional mice) and increased overall grooming (Appendix D.13, B). Total grooming time during trial 1 was separated into the fraction of total time spent grooming in the empty chamber, the middle chamber, and the chamber that housed a mouse.

A one-way ANOVA revealed a statistically significant difference in the amount of time spent grooming ($F_{5,30}$ = 1.040, p = <0.0001) and post hoc testing indicated that both *Cldn11*$^{+/-}$*Tg*$^{+/-}$ and *Cldn11*$^{-/-}$*Tg*$^{+/-}$ mice spent significantly more time grooming in the empty chamber as compared to the chamber that housed a mouse

or the middle portion, however, there was no main effect of genotype on location. Total grooming during trial 2 was separated in a similar fashion, but the empty chamber now housed a novel mouse. An ANOVA for time spent in each location was not statistically significant ($F_{5,30}$ = 0.2113, p = 0.5921), suggesting both genotypes groomed for a similar amount of time in all locations.

The persistence of a decreased anxiety-like phenotype was also investigated by repeating the OF and MB paradigms with the third cohort of mice. To determine if the native testing environment can alter anxiety state, we conducted repeat OF testing in two difference locations. During the repeat OF test in location 1, *Cldn11*$^{+/-}$ *Tg*$^{+/-}$ and *Cldn11*$^{-/-}$*Tg*$^{+/-}$ mice spent a similar amount of time in each of center square designation (Figure 4.14, Location 1): 32 % (t_{18} = 0.2850, p = 0.7940), 48 % (t_{18} = 0.3314, p = 0.7441), 66 % (t_{18} = 0.6956, p = 0.4956), and 83 % (t_{18} = 0.0774, p = 0.9391). Control parameters, including total distance traveled, average velocity, and time spent in each quadrant was similar between genotypes (traveled t_{18} = 1.703, p = 0.1058; t_{18} = 1.647, p = 0.1169; and $F_{1,18}$ = 0.03, p = 0.8709 respectively) (Appendix D.15, A).

Likewise, when mice were evaluated for open field activity in a different environment, location 2, *Cldn11*$^{+/-}$*Tg*$^{+/-}$ and *Cldn11*$^{-/-}$*Tg*$^{+/-}$ spent an indistinguishable amount of time in each center square designations (Figure 4.14, Location 2): 32 % (t_{11} = 0.5755, p = 0.5766), 48 % (t_{11} = 1.109, p = 0.2910), 66 % (t_{11} = 1.467, p = 0.1702), and 83 % (t_{11} = 1.466, p = 0.1707). Control variables were not statistically different between genotypes: total distance traveled: t_{11} = 0.4911, p = 0.6330, average velocity: t_{11} = 0.4131, p = 0.875, and quadrant analysis: $F_{1,11}$ = 3.79, p =

0.0776 (Appendix D.14, B). These data suggest it was irrelevant which environment mice were tested in; there was no detectable difference in the anxiety state between mice, uninfluenced by motor ability or exploration constants.

With a lack of significant difference discerned by repeating the OF test, we conducted MB to further investigate this new conclusion (Figure 4.15). Using a Student's *t*-test, we find *Cldn11*$^{+/-}$*Tg*$^{+/-}$ and *Cldn11*$^{-/-}$*Tg*$^{+/-}$ mice bury a similar number of marbles (t_{18} = 1.036, p = 0.3140). The same cohort of OF mice completed the MB task, and results indicate a similar number of marbles buried between *Cldn11*$^{+/-}$Tg$^{+/-}$ and *Cldn11*$^{-/-}$Tg$^{+/-}$ mice. If we compare the MB averages from the original cohort (Figure 4.7) to the repeated cohort of mice, we notice that *Cldn11*$^{+/-}$Tg$^{+/-}$ animals buried, on average, slightly fewer marbles, while *Cldn11*$^{-/-}$Tg$^{+/-}$ mice buried slightly more marbles. Thus the averages are closer together, eliminating significance, and confirming the OF results of an inability to detect the less anxious phenotype in *Cldn11*$^{-/-}$Tg$^{+/-}$ mice.

Figure 4.14 – Repeat analyses of open field center square percentages from two different locations suggest *Cldn11*$^{-/-}$*Tg*$^{+/-}$ mice and controls are similar

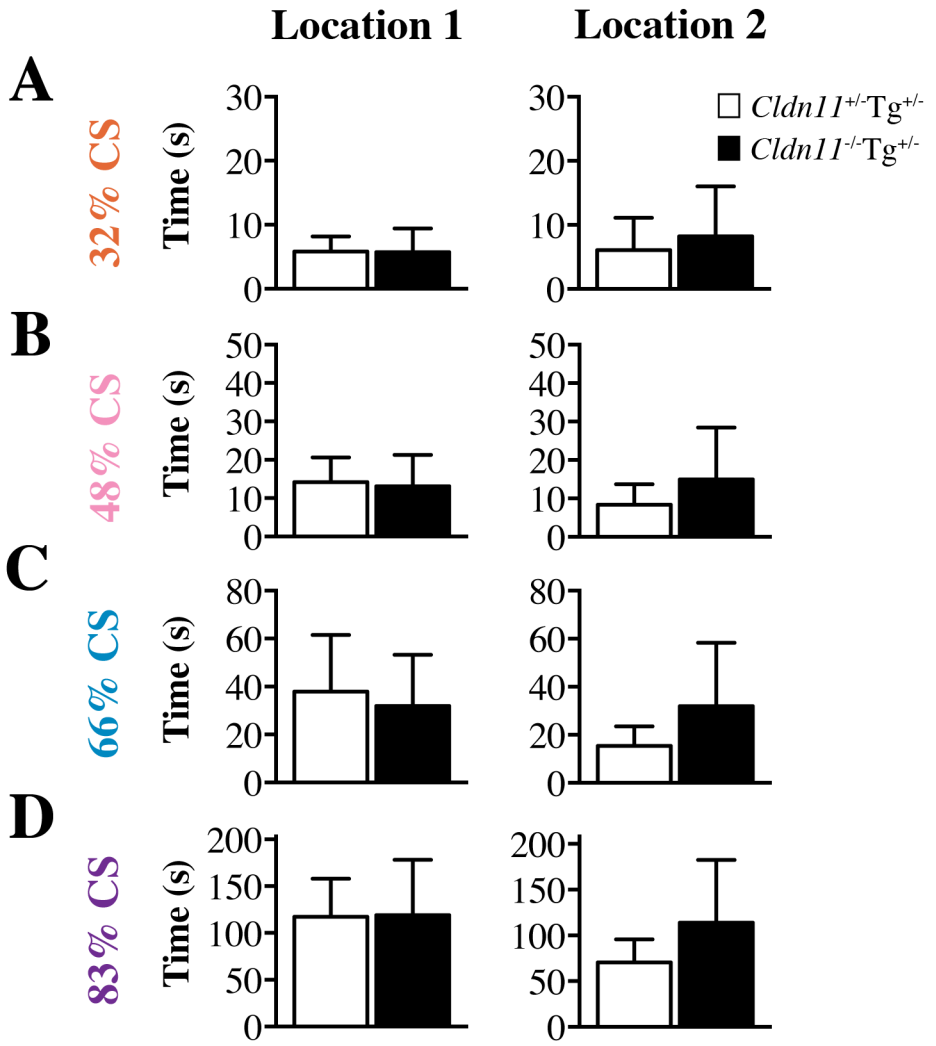

Repeat open field center square analyses for 6 – 8 M *Cldn11*$^{+/-}$*Tg*$^{+/-}$ and *Cldn11*$^{-/-}$ *Tg*$^{+/-}$ mice. Student's *t*-tests indicate similar amount of time spent in **(A)** 32 %, **(B)** 48 %, **(C)** 66 %, and **(D)** 83 % center squares, irrespective of location. Data values are plotted at mean ± SD; Location 1: $n = 10$, Location 2: $6 \leq n \leq 7$.

Figure 4.15 – Repeat marble burying paradigm indicates *Cldn11*$^{+/-}$*Tg*$^{+/-}$ and *Cldn11*$^{-/-}$ *Tg*$^{+/-}$ mice bury a similar amount of marbles

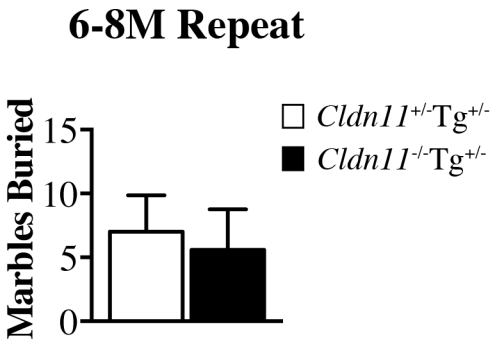

Marble burying analysis was repeated for an additional cohort of *Cldn11*$^{+/-}$*Tg*$^{+/-}$ and *Cldn11*$^{-/-}$*Tg*$^{+/-}$ mice. Using a Student's *t*-test comparing the number of marbles buried, no significant differences were seen. Data values are plotted as mean ± SD; *n* = 10.

Our initial neurochemical data demonstrating GABA alterations was compelling, and a pilot study was conducted to more precisely determine, where GABA changes emanated from in the brains of *Cldn11*$^{-/-}$*Tg*$^{+/-}$ mice. For this analysis, 1 mm coronal brain slices were generated spanning the brain segment of interest (bregma - 1 to - 5), and bilateral punch structures were pooled for magic angle H^1MRS (Figure 4.16A). GABA level was controlled for tissue weight and normalized to the internal control, creatine. Analysis revealed stark different amount of GABA for all segments analyzed (Figure 4.16B): - 1 to - 2, - 2 to - 3, - 3 to - 4, and - 4 to - 5 bregma. Given the pilot study contained only one animal from each genotype, it negates the possibility of statistical analysis, however, we can still discern an increased level of GABA for all slices, regardless of genotype. In addition, the GABA level for the *Cldn11*$^{-/-}$*Tg*$^{+/-}$ mouse in the first two slices was greater than the *Cldn11*$^{+/-}$ *Tg*$^{+/-}$, but decreased within the last two slices.

One momentous question remains, what happened to the behavioral phenotype of the *Cldn11*$^{-/-}$*Tg*$^{+/-}$ mice? Our recent assessment of *Cldn11*$^{-/-}$*Tg*$^{+/-}$ mice reveals our inability to detect a behavioral phenotype or neurochemical alteration within these animals. The aforementioned studies were conducted throughout several years and a number of variables could account for our inability to detect significant differences.

Figure 4.16 – Pilot neurochemical investigation to resolve location of altered GABA points to dissimilarity from original data set

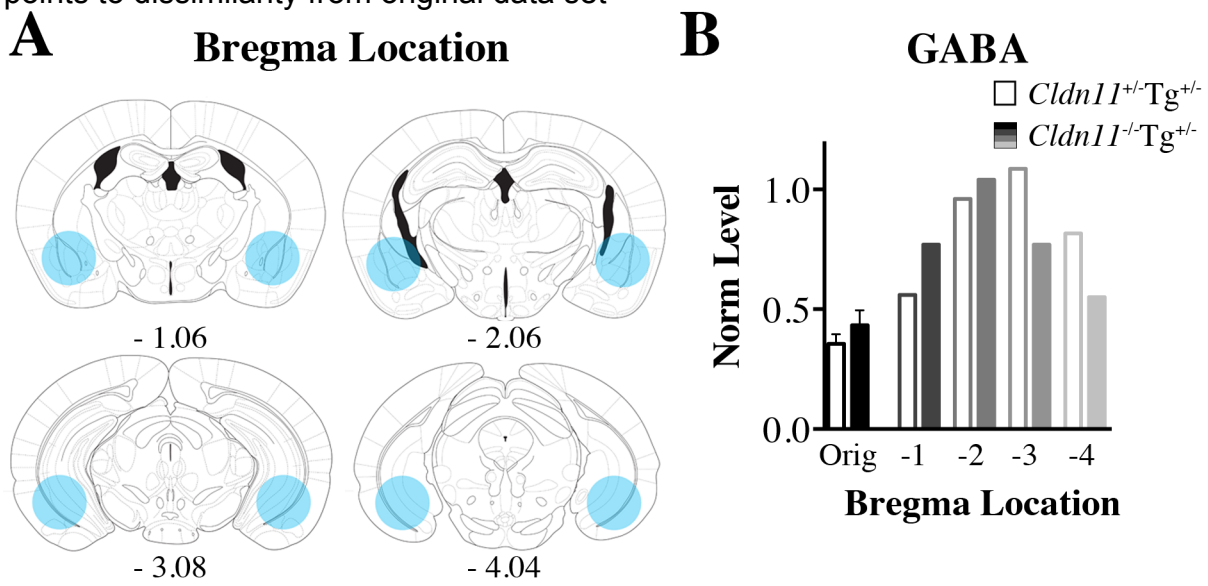

One *Cldn11*$^{+/-}$*Tg*$^{+/-}$ and one *Cldn11*$^{-/-}$*Tg*$^{+/-}$ mouse (age 6 – 8 M) were used to determine precise location for increased GABA expression. **(A)** Coronal slices were generated (1 mm) and bilateral region of interest (blue circles) were collected and analyzed via magic angle H^1MRS. **(B)** GABA expression was quantified, adjusted for tissue weight, then normalized to the internal control marker, creatine.

DISCUSSION

The concept that dysfunctional myelin can lead to behavioral abnormalities has been alluded to throughout the myelin literature. Evidence in clinical literature suggests that myelin may pose an as alternative mechanism for the etiology of behavioral abnormalities. In white matter diseases such as leukodystrophies and multiple sclerosis (MS), the acknowledged component is dysfunctional myelin, however the prominent features are the accompanying behavioral abnormalities. Direct evidence supporting dysfunctional myelin as a causative component for behavioral abnormalities is difficult to obtain due to the compound nature of neurological illnesses and the challenge of separating dysfunctional myelin to disease etiology from behavior. Our *Cldn11*$^{-/-}$*Tg*$^{+/-}$ mouse model is ideal for partitioning dysfunctional myelin from a complex disease state to investigate its contribution to manifestation of behavioral abnormalities.

Dysfunctional myelin has the ability to generate behavioral abnormalities

The etiology of behavioral abnormalities is hypothesized to emanate from a disconnection between neural circuits. As stated in the disconnection hypothesis: behavior is the result of temporal integration of sensory signals; *abnormal* behavior results when there is a disconnection between brain regions or neural circuits (Friston, 1998, 1999). Chapter 3 of this dissertation demonstrates that dysfunctional myelin alters signal integration and neural processing within the auditory brainstem. If we extrapolating those findings and apply them to higher-order brain networks, we envisage a similar deficit is present. Higher-order cortical networks contain a vast network of small diameter, myelinated fibers, that transmit sensory information to

various integration centers within the brain. If integration of sensory signals becomes altered, a behavioral abnormality will arise. This chapter proposes evidence in favor of dysfunctional myelin as an etiology for manifestation of abnormal behavior

Chronicling the behavioral abnormalities of *Cldn11*$^{-/-}$*Tg*$^{+/-}$ mice

Initial behavioral analyses of 2, 4, and 6 – 8 M *Cldn11*$^{+/-}$*Tg*$^{+/-}$ and *Cldn11*$^{-/-}$ *Tg*$^{+/-}$ mice reveals a distinct abnormality resulting from dysfunctional myelin. Irrespective of the inability to detect a phenotype in subsequent cohorts of animals, (see below), *Cldn11*$^{-/-}$*Tg*$^{+/-}$ mice have a less anxious phenotype at 6 – 8 M. This reduced anxiety-like phenotype is not detectable at younger ages, 2 or 4 M. This robust finding is supported by two technically distinct behavioral tests eliciting anxiety-like responses from different methods: OF and MB. While *Cldn11*$^{-/-}$*Tg*$^{+/-}$ mice have no apparent change in depressive-like phenotype based on tests of anhedonia and depressive-like (TST and SPT respectively), or differences in cognitive ability, an alteration in anxiety state is still noteworthy. Furthermore, throughout all behavioral tests require motor activity, we did not detect difference in distance traveled or velocity of *Cldn11*$^{-/-}$Tg+/- mice, negating the known hind limb weakness (Gow et al., 1999). A number of mutant myelin mouse models have been generated and studied for abnormal phenotypes under a similar battery of behavioral analyses.

Alternative mouse models of dysfunctional myelin emanate behavioral abnormalities

Proteolipid protein (PLP) is a major myelin protein constituting about half of total protein within the myelin sheath. Several different mouse strains of mutated PLP have been generated to study potential behavioral abnormalities via gene

knockout (*PLP1*) and overexpression (Boison and Stoffel, 1994; Inoue et al., 1996; Readhead et al., 1994). Studies involving overexpression of PLP indicate abnormal anxiety-like phenotype; interestingly, an increase in anxiety is seen when evoked with the light / dark transition test, while a decrease is identified by the elevated plus maze. In addition, decreased spatial learning and memory is noted using the Barnes maze test (Tanaka et al., 2009). In contrast, knocking out *PLP* causes an increase in anxiety-like behavior in mice (Boison and Stoffel, 1994).

The second major protein found within myelin sheaths is myelin basic protein (MBP). Mutant mice harboring genetic alterations to the MBP gene have also been studied for behavioral abnormalities (Privat et al., 1979; Rosenbluth, 1980). Variations in protein expression cause severe tremors and seizures, as well as a decrease learning ability via the T-maze test (Inagawa et al., 1988).

A direct comparison between our dysfunctional myelin mutant and those is complex. When altered, each of these proteins (PLP and MBP) cause changes in the ultrastructure of the myelin membrane, along with a neurodegenerative phenotypes. Also pronounced are the varying degrees of shakes and tremors exhibited by mutant animals and premature death in MBP mutants (Kirschner and Ganser, 1980; Klugmann et al., 1997; Privat et al., 1979; Readhead et al., 1994).

Consequently, these myelin mutants do not have the ability to separate out compounding structural and disease-causing phenotypes. It is implausible to separate out the contribution of dysfunctional myelin on behavioral abnormalities with additional variables present. These data attempt to illustrate the idea that dysfunctional myelin leads to behavioral abnormalities, however our data is the first

to show definitive evidence. The *Cldn11*$^{-/-}$ mice lack any ultrastructure abnormalities or neurodegenerative component at older time points; leaving a straightforward model to directly study the behavioral ramifications of dysfunctional myelin (Gow et al., 1999).

Dysfunctional myelin causes neurochemical alterations

The leading hypothesis for the etiology of behavioral abnormalities is largely based on altered neurochemical levels present in the brain. Variations include an increase or decrease in amount, as well as modifications in the quanta released at a synapse, inherently causing an imbalance and the physical manifestation of abnormal behavior (Sarter et al., 2007). Pharmaceutical companies have taken advantage of this hypothesis and developed drugs to counteract the incorrect levels for various illnesses including anxiety and depression. However, about 30 % of patients actively being treated relapse during treatment, suggesting an alternative explanation for the etiology must exist.

Anxiety, like many emotion based feelings, are generated from a complex network of brain regions and their connections, known as the limbic system. Consisting of the hypothalamus, amygdala, hippocampus and limbic cortex, the limbic system is responsible for processing emotional and motivational behaviors (LeDoux, 2003; Morgane et al., 2005). Alterations in the neurochemical composition of certain brain regions has been connected to anxiety (Hoehn-Saric, 1982; Hyman, 1998; Pratt, 1992) including increased norepinephrine, increased serotonin (Graeff, 1993) and altered GABA levels (Depino et al., 2008; Hoehn-Saric, 1982).

While the amygdala was not analyzed, the VHC plays a critical role in regulation of anxiety-like phenotypes. Notably, the analyzed VHC punch is composed of roughly 40 % subiculum, which contains a large population of GABAergic neurons that perhaps account for the measured increase. The subiculum is the major output structure of the VHC, sending projections to cortical and subcortical targets such as thalamic nuclei (O'Mara, 2005; O'Mara et al., 2001; Witter and Groenewegen, 1990). A unique feature of the subiculum is the presence of long-range projection GABAergic neurons. Typically, GABAergic neurons are small interneurons that regulate local neural circuitry within a nucleus, however the subiculum is one of few nuclei in the brain containing GABAergic projection neurons (Buzsaki and Chrobak, 1995; Jinno et al., 2007). The target of these GABAergic projections is the cortical limbic system, imposing inhibition on the hypothalamic-pituitary-adrenal (HPA) axis, which in turn, dampens the HPAs response to stress (Lowry, 2002). Coming full circle, there are extensive reciprocal connections between the AMYG and VHC regions; thus, the increase in the less anxious phenotype we observed is still related to the neurochemical alterations in the VHC punch.

Analysis of *ex vivo* tissue punches indicates that *Cldn11*$^{-/-}$*Tg*$^{+/-}$ mice have significantly increased GABA levels, about 20 %, in the VHC region (Figure 4.11 and Table 4.11). In patients suffering from anxiety disorders, a similar significant increase within the AMYG is noted throughout the published literature (Lydiard, 2003; Nemeroff, 2003; Nutt and Malizia, 2001). An increase of GABA by 20 % in the VHC is not only statistically significant, but suggestive of being biologically relevant.

Evidence in the literature establishes a 10 % change in GABA levels in the AMYG is sufficient to cause altered detectable anxiety-like phenotype (Ackermann et al., 2008; Sherif and Oreland, 1995). Further support has been shown when excess GABA remains in the synaptic cleft in the absence of GABA transporters or receptors (Liu et al., 2007; Sur et al., 2001). The function of inhibitory interneurons, and discernably GABA, is to modulate and alter the excitability of neural circuitry (Bloom et al., 1995). Excess neurotransmitters, whether excitatory, or in this case inhibitory, can have dramatic effects on overall neural circuitry, leading to dysregulation and the manifestation of a behavioral abnormality.

These data support the hypothesis that dysfunctional myelin within *Cldn11*$^{-/-}$ mice generates detectable alterations in neurotransmitter levels. They suggest that dysfunctional myelin may be an important etiology for behavioral abnormalities because it can generate the types of neurotransmitter alterations that are found in patients and are commonly targeted by pharmaceutical companies. However, it remains to be determined what proportion of the disease burden might be associated with this etiology.

The vanishing phenotype of *Cldn11*$^{-/-}$*Tg*$^{+/-}$ mice

Initial behavioral experiments describe a consistent story and reveal novel findings attributable to dysfunctional myelin. A decrease in anxiety level correlated with increased inhibitory GABA levels present in the VHC of *Cldn11*$^{-/-}$*Tg*$^{+/-}$ mice at 6 – 8 M of age. These data suggested, for the first time, that dysfunctional myelin plays a critical role in the etiology of behavioral abnormalities, as well as causes alterations in neurotransmitter levels. Undermining these findings are the ensuing

experiments attempting to formulate a mechanism by which an increase in GABA originates.

Performing longitudinal studies on the same group of mice would have introduced a potential learned behavior, failing to reflect genuine behavioral abnormalities (Bailey et al., 2006; Bolivar et al., 2000; Voikar et al., 2004). This necessitates the need for separate cohorts of mice to age, replicate behavioral testing, and tissue collected for protein analysis to determine mechanism of GABA increase. The time to complete a second round of experiments can take upwards of a year, pending optimal breeding. During this time frame, several infections occurred, modifying the perspective of data collected.

Second, throughout behavioral testing data collection, several infections occurred in the vivarium. With each ailment and subsequent management regime, the possibility arises that treatment could affect the behavior of both *Cldn11*$^{+/-}$*Tg*$^{+/-}$ and *Cldn11*$^{-/-}$*Tg*$^{+/-}$ mice. Most notable was the presence of pinworms (*Syphacia muris* and *Aspiculuris tetraplera*) and treatment with Ivermectin (MediGel IVR gel cups). The anthelmintic ivermectin, from the superfamily avermectin, exerts its antiparasitic effect by activating glutamate-gated chloride channels receptors (GluClRs) present exclusively in the invertebrate nervous system (Cully et al., 1994). Recently, our understanding of the precise location where ivermectin binds and how it modulates cys-loop ion channels has expanded with publication of the crystal structure of ivermectin bound to the *C.elegans* GluClR (Hibbs and Gouaux, 2011). Ivemectin binds at the transmembrane domain between two adjacent subunits

forming hydrogen bonds and van der Waals interactions with select amino acids within the channel's transmembrane domain. The binding of ivermectin between subunits has been suggested to wedge open the pore, permitting the passing of chloride ions, cause hyperpolarization of the neurons, paralysis, and ultimate demise of the pinworm species (Fisher and Mrozik, 1992; Martin, 1997). Nevertheless, it has been demonstrated that ivermectin can bind to and alter glycine receptors (GlyRs), as well as $GABA_A$ receptors ($GABA_AR$) in vertebrate animals (Dawson et al., 2000; Shan et al., 2001).

While there may be no overt signs of a pinworm infection, such as hair loss or weight fluctuation, altering internal receptor modulation could influence behavioral outcomes in the host species, in our case the mice. It has been demonstrated that the mere presence of an active pinworm infection can modify the behavior of mice, decreasing exploration during OF testing. Likewise, treatment with ivermectin has been shown to have the opposite result, increasing exploration of an OF arena during pinworm treatment (Davis et al., 1999; McNair and Timmons, 1977). Consequently, if the mice became infected and behavioral analyses performed; data would be difficult to interpret. No behavioral test was carried out while pinworm treatment was in effect, however it is unknown at what point mice contracted the illness before being detected. Furthermore, the perpetual effect of treating animals with ivermectin has not been investigated. Thus, we do not know what lasting effects ivermectin may have on host GlyR and $GABA_AR$.

In spite of the difficulties with this project, our data, in part, suggests that dysfunctional myelin is associated with behavioral abnormalities and alters

neurotransmitter levels. Data collected from the initial cohorts of *Cldn11*$^{+/-}$*Tg*$^{+/-}$ and *Cldn11*$^{-/-}$*Tg*$^{+/-}$ mice is robust and experiments were conducted within a short time frame, so we do not expect technical difficulties such as infections to have confounded the data. These studies await re-examination using mice that have not been exposed to ivermectin and we plan to use a new inducible *Cldn11*$^{-/-}$ colony of mice currently being generated at Baylor School of Medicine.

APPENDIX A – Abbreviation

aa	amino acid
ABAT	4 – aminobutyrate aminotransferase
ABR	auditory brainstem response
ACC	anterior cingulate cortex
aCSF	artificial cerebral spinal fluid
Act	acetate
AEP	auditory evoked potential
Ala	alanine
AMC	anterior motor cortex
AMYG	amygdala
ANOVA	analysis of variance
Asp	aspartate
AST	anterior striatum
AUD	auditory cortex
AVCN	anteroventral cochlear nucleus
Bet	betaine
BIC	binaural interaction component
BLA	basolateral amygdala
BS	brainstem
CAP	compound action potential
CB	cerebellum
CH	chloral hydrate
Cho	cholines
Cldn	claudin
cm	centimeter
CN	cochlear nucleus
CNS	central nervous system
Cre	creatine
CS	center square
dB	decibel
DCM	double cable model
DCN	dorsal cochlear nucleus
DPST	dorsal posterior striatum
DTI	diffusion tensor imaging
EE	excitatory-excitatory
EEG	electroencephalography
EI	excitatory-inhibitory
fMRI	functional magnetic resonance imaging
GABA	gamma-aminobutryic acid
GAD	glutamic acid decarboxylase
Gln	glutamine
Glu	glutamate
GPC	gycerophosphocholine
GSH	glutathione

H^1MRS	proton magnetic resonance spectroscopy
HC	hippocampus
HC	hippocampus
HPA	hypothalamic pituitary adrenal
i.p.	intraperiotoneal
IC	inferior colliculus
ILD	interaural level delay
in	inch
Ins	Inositol
IPL	intraperiod line
ITD	interaural time delay
JP	juxtaparanode
kg	kilogram
kHz	kilo Hertz
Lac	lactate
LL	lateral lemniscus
LLR	late / long latency response
LNTB	lateral nucleus of the trapezoid body
LSO	lateral superior olive
M	month
MAG	myelin associated glycoprotein
MB	marble burying
MidB	midbrain
MBP	myelin basic protein
MDL	major dense line
mg	milligram
MGN	medial geniculate nucleus
min	minute
ml	milliliter
MLR	middle latency response
MNTB	medial nucleus of the trapezoid body
MS	multiple sclerosis
msec	millisecond
MSO	medial superior olive
NAA	N-acetlyaspartate
NAAG	N-acetlyaspartatylglutamate
NAC	nucleus accumbens
OF	open field
PBS	phosphate buffered saline
PCC	posterior cingulate cortex
PCh	phosphocholine
PDZ	PSD95 / Dlgs / ZO-1
PEA	phenylethylamine
PET	positron emission tomography
PLP	proteolipid protein
PMC	posterior motor cortex

ppm	parts per million
PVCN	posteroventral cochlear nucleus
sec	second
SEP	somatosensory evoked potential
SL	sensation level
SNR	signal to noise ratio
SOC	superior olivary complex
SP	sucrose preference
SPL	sound pressure level
Suc	succinate
SZ	Schizophrenia
Tau	taurine
TBE	2,2,2 – tribromoethanol
TBSGBA	tris buffered saline, goat serum, bovine albumin
THAL	thalamus
TJM	tight junction model
TS	tail suspension
TSP	trimethyl silyl – propionate
VEP	visual evoked potential
VHC	ventral hippocampus
VPST	ventral posterior striatum
ZO	zonula occludens
μm	micron
μsec	microsecond
μV	microvolt

APPENDIX B – Chapter 2 Supplemental Figures

Appendix B.1 – Sensation level for Wave III amplitudes is highly variable

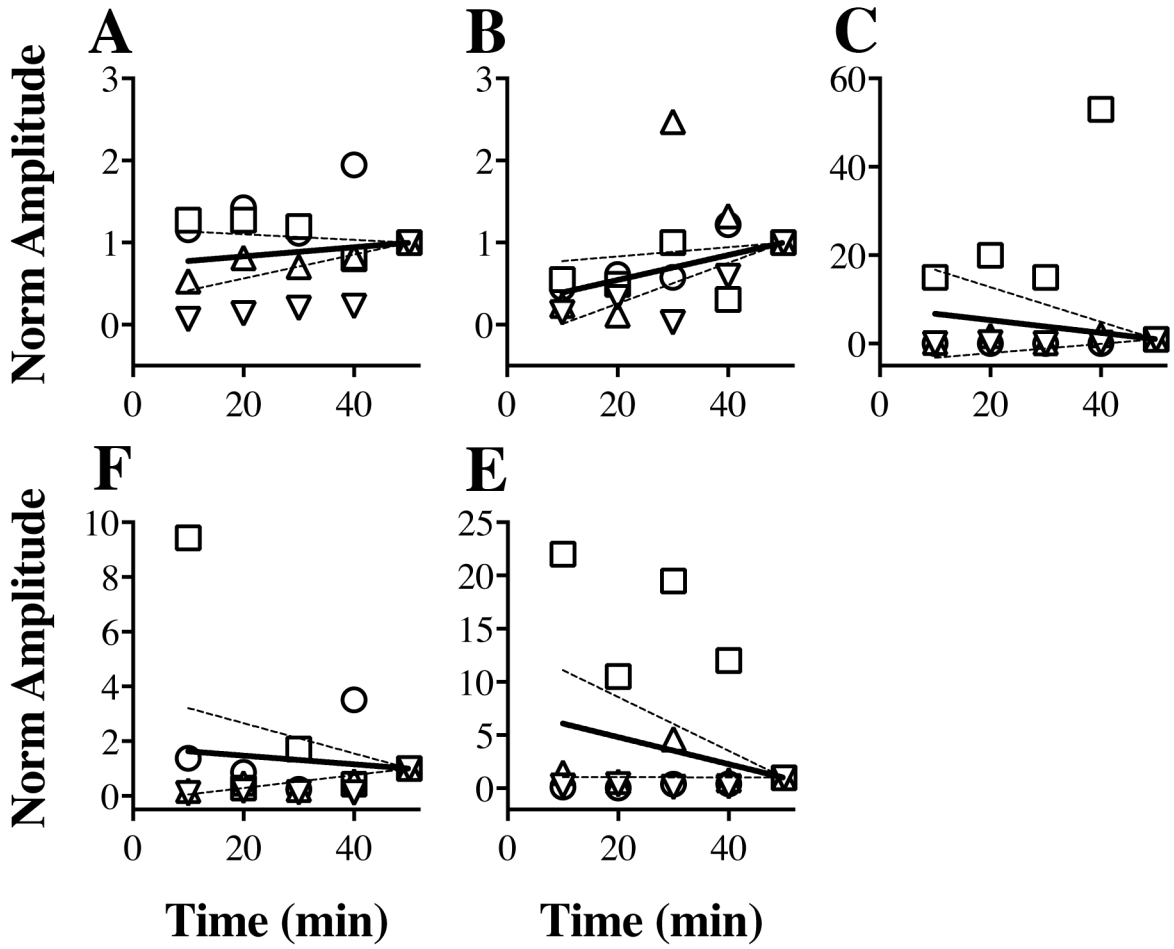

Normalized Wave III amplitudes are plotted as a function of time for calculated sensation level at 80 dB SPL (**A**), 70 dB SPL (**B**), 60 dB SPL (**C**) 50 dB SPL (**D**) 40 dB SPL (**E**) and 30 dB SPL (**F**). Data for each mouse are normalized to amplitude at 50 min and the average linear regression line constrained at (50,1) is shown (solid line) ± 95 % CI (dashed lines).

Appendix B.2 – Sensation level for Wave V amplitudes is highly variable

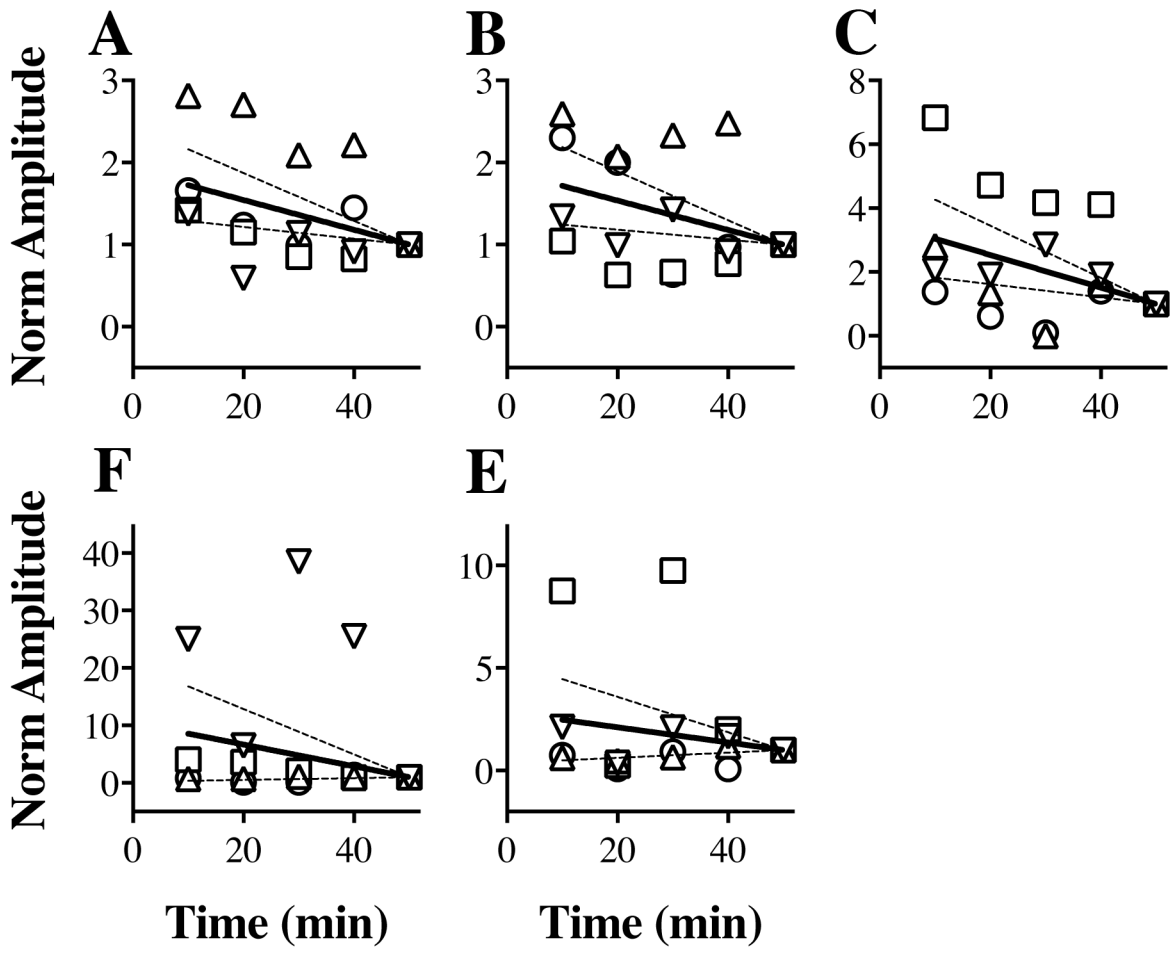

Normalized Wave V amplitudes are plotted as a function of time for calculated sensation level at 80 dB SPL (**A**), 70 dB SPL (**B**), 60 dB SPL (**C**) 50 dB SPL (**D**) 40 dB SPL (**E**) and 30 dB SPL (**F**). Data for each mouse are normalized to amplitude at 50 min and the average linear regression line constrained at (50,1) is shown (solid line) ± 95 % CI (dashed lines).

APPENDIX C – Chapter 3 Supplemental Figures

Appendix C.1 – Raw DN1 latency occurs between latencies of Waves IV and V

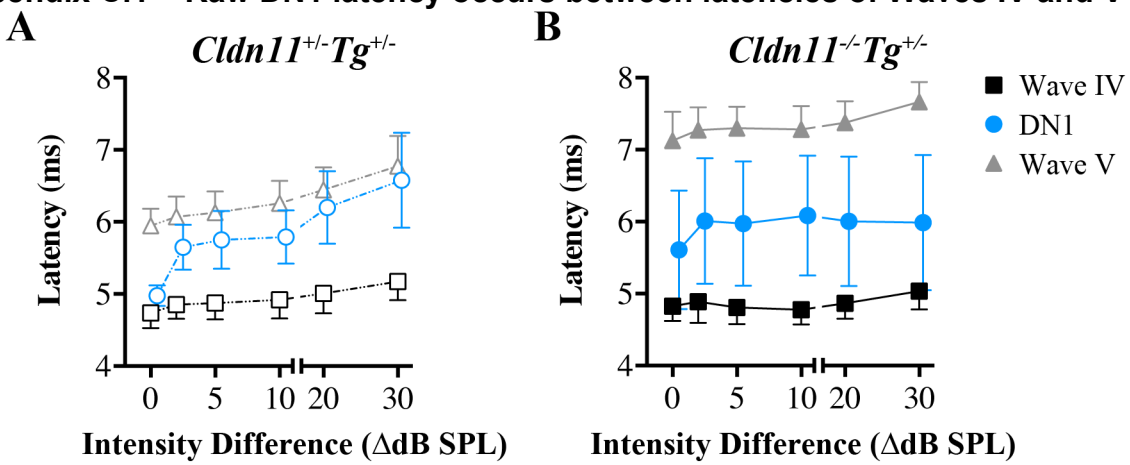

(A) Raw latencies plotted for Wave IV and V, as well as the calculated DN1 trough, as a function of the various intensity differences (ΔdB SPL) tested for *Cldn11*$^{+/-}$*Tg*$^{+/-}$ *Cldn11*$^{+/-}$*Tg*$^{+/-}$ mice. **(B)** Raw latencies are plotted for Wave IV and V, as well as the calculated DN1 trough at the various intensity differences tested (ΔdB SPL) for *Cldn11*$^{-/-}$*Tg*$^{+/-}$ mice. Data values are plotted as mean ± SD; $10 \leq n \leq 12$.

Appendix C.2 – Raw DN1 latency and amplitude for *Cldn11*$^{+/-}$Tg$^{+/-}$ and *Cldn11*$^{-/-}$ Tg$^{+/-}$ mice

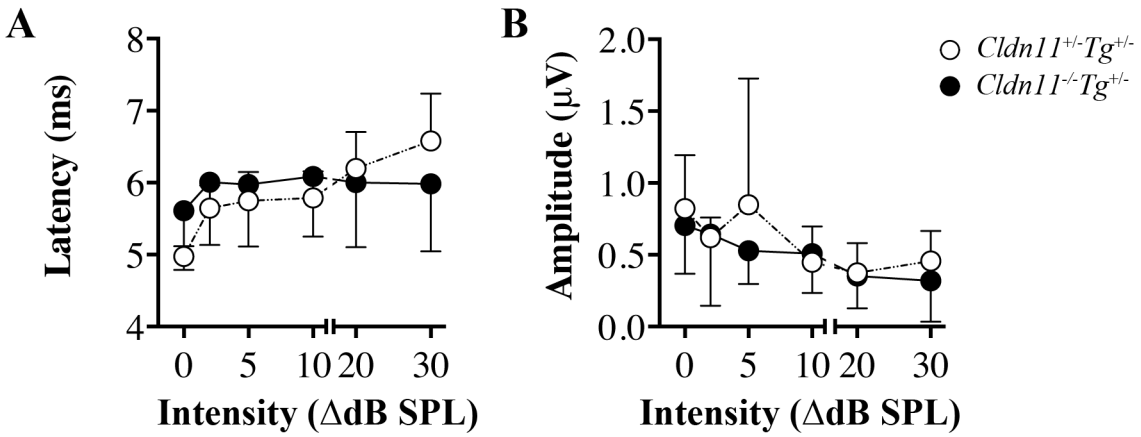

(A) Raw DN1 trough latency plotted as a function of intensity difference (ΔdB SPL) for *Cldn11*$^{+/-}$*Tg*$^{+/-}$ and *Cldn11*$^{-/-}$*Tg*$^{+/-}$ mice. **(B)** Raw DN1 amplitude plotted as a function of intensity difference (ΔdB SPL) for *Cldn11*$^{+/-}$*Tg*$^{+/-}$ and *Cldn11*$^{-/-}$*Tg*$^{+/-}$ mice. Data values are plotted as mean ± SD; $10 \leq n \leq 12$

Appendix C.3 – Proportion of myelinated fibers in trapezoid body fiber tract

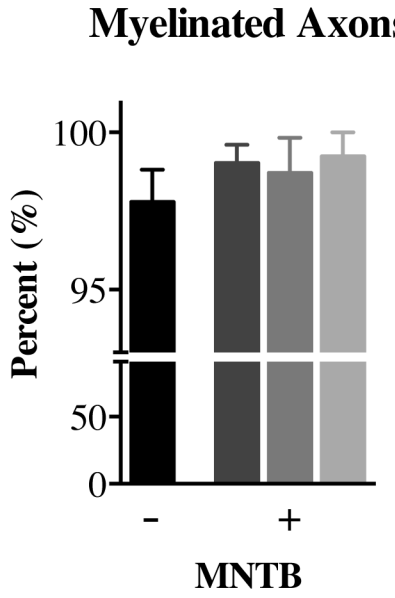

Percentage of myelinated fibers traversing through the trapezoid body tract are displayed. Negative sign indicates sagittal cryostat section medial to the MNTB, whereas the plus sign indicates slides in which posses MNTB principle cells. Data are plotted as mean ± SD; *n* = 3 fields / slide; ~ 100 axons / slide.

APPENDIX D – Chapter 4 Supplemental Figures

Appendix D.1 – *Cldn11*$^{+/-}$*Tg*$^{+/-}$ and *Cldn11*$^{-/-}$*Tg*$^{+/-}$ mice travel a similar distance and velocity during the open field paradigm

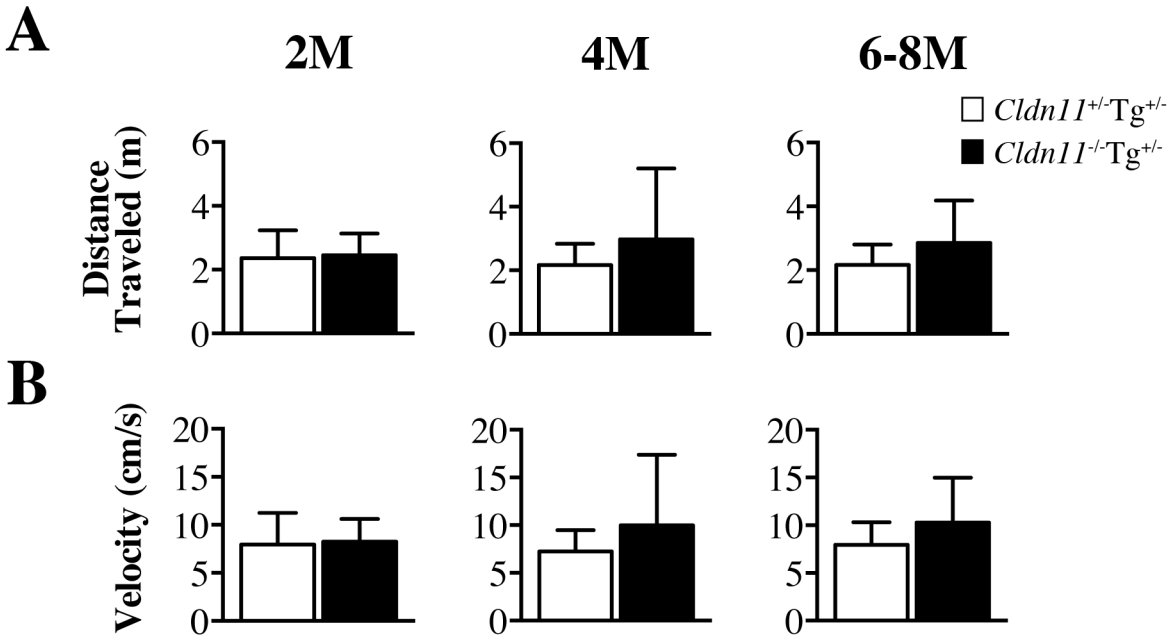

(A) The total distance traveled during the open field test was similar between *Cldn11*$^{+/-}$*Tg*$^{+/-}$ and *Cldn11*$^{-/-}$*Tg*$^{+/-}$ mice at 2, 4, and 6 – 8 M of age. **(B)** Similarly, the average velocity was indistinguishable between genotypes at 2, 4, and 6 – 8 M. Data values are plotted as mean ± SD, $9 \leq n \leq 10$.

Appendix D.2 –Time spent in each quadrant of the open field arena is similar between *Cldn11*$^{+/-}$*Tg*$^{+/-}$ and *Cldn11*$^{-/-}$*Tg*$^{+/-}$ mice

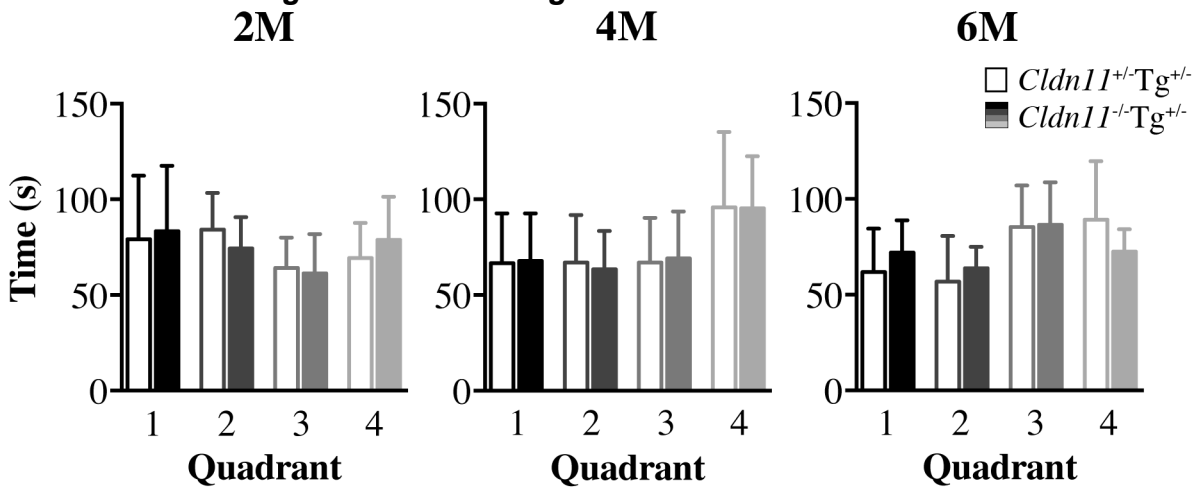

The average time spent in each quadrant of the OF arena (Figure 4.1) was similar between *Cldn11*$^{+/-}$*Tg*$^{+/-}$ and *Cldn11*$^{-/-}$ mice at 2, 4, and 6 – 8 M of age. Data values are plotted as mean ± SD, $9 \leq n \leq 10$.

Appendix D.3 – Standard sucrose testing variables including weight fluctuation, food consumed and liquid drank are indistinguishable between *Cldn11*$^{+/-}$*Tg*$^{+/-}$ and *Cldn11*$^{-/-}$*Tg*$^{+/-}$ mice

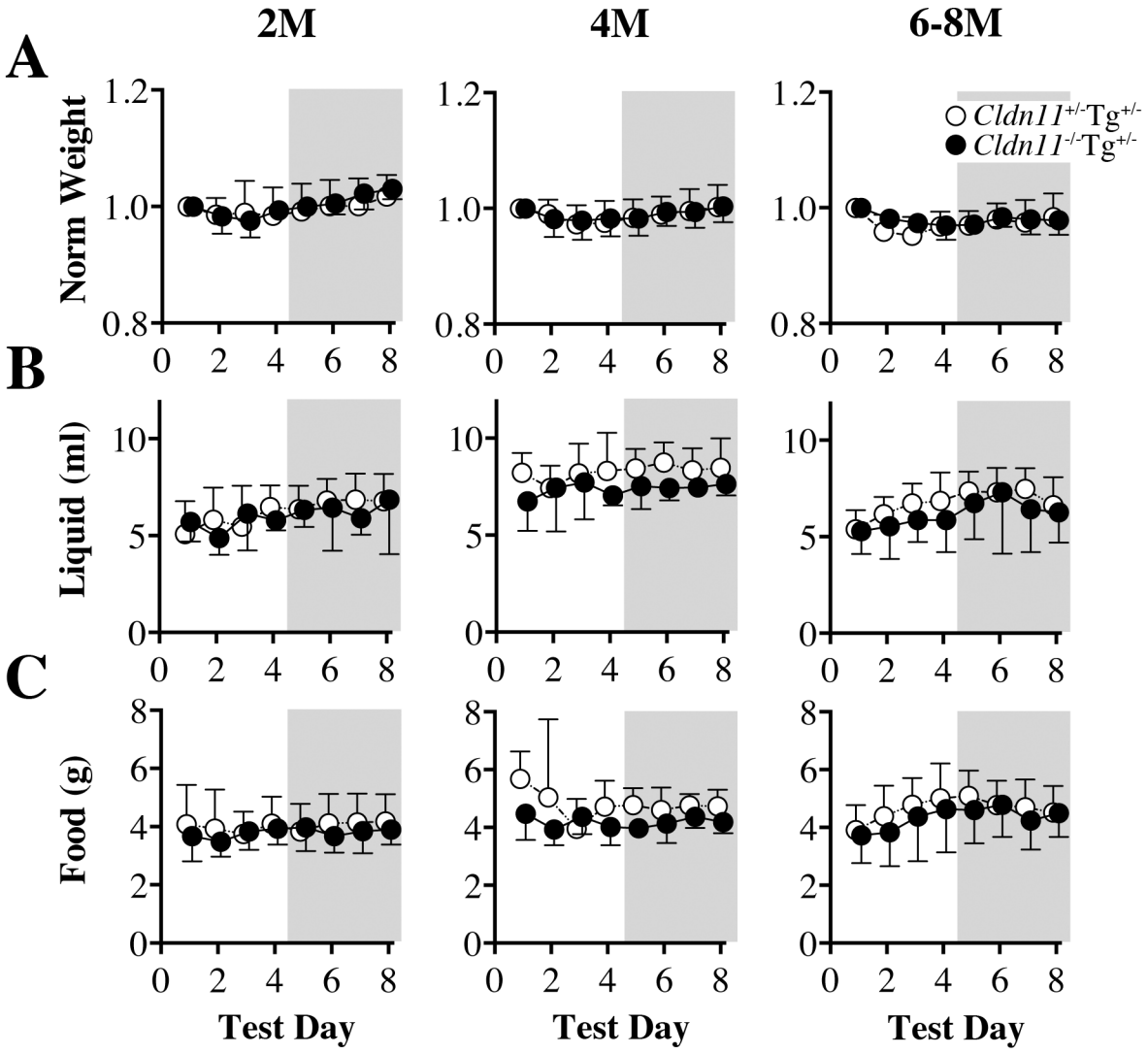

(A) Normalized weight fluctuation for *Cldn11*$^{+/-}$*Tg*$^{+/-}$ and *Cldn11*$^{-/-}$*Tg*$^{+/-}$ mice during the eight days of sucrose preference testing at 2, 4, and 6 – 8 M of age. A mouse's weight was normalized to its starting weight before the testing period began to control for gender differences. **(B)** Total liquid intake during the eight days of sucrose preference testing at 2, 4, and 6 – 8 M of age. **(C)** Total amount of food consumed during the eight days of sucrose preference testing for 2, 4, and 6 – 8 M of age mice. Using repeated measures ANOVAs, no statistically significant differences were seen for any variable, at any age tested. Shaded portion of graphs reflects portion of test when a sucrose solution was present. All data values are plotted as mean ± SD, n = 9 at 2 M, n = 10 at 4 and 6 – 8 M. *Cldn11*$^{-/-}$*Tg*$^{+/-}$ values are shifted about the abscissa for clarification.

Appendix D.4 – Side preference for liquid consumption during sucrose preference testing is similar for *Cldn11*$^{+/-}$*Tg*$^{+/-}$ and *Cldn11*$^{-/-}$*Tg*$^{+/-}$ mice

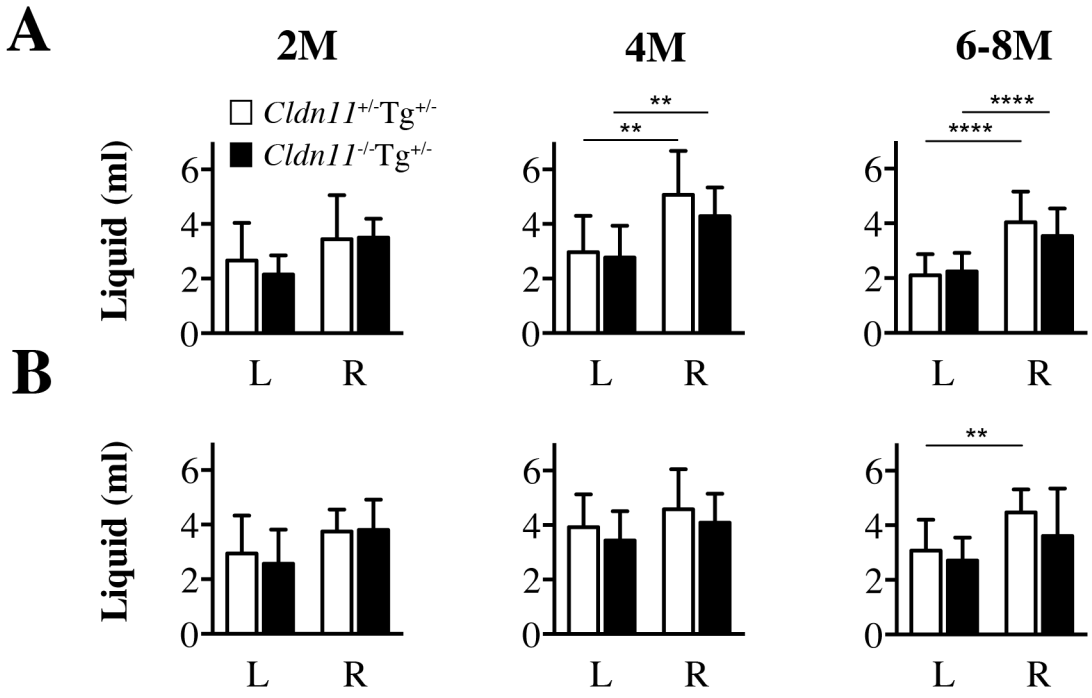

(A) Acclimation phase (days 1 – 4) during sucrose preference testing when water is present in both the L and R sipper tubes. Using a two-way repeated measures ANOVA, the average amount of liquid (water) drank on either the L or R side, or between sides within a genotype, is indistinguishable between *Cldn11*$^{+/-}$*Tg*$^{+/-}$ and *Cldn11*$^{-/-}$*Tg*$^{+/-}$ mice at 2 M of age. At 4 and 6 – 8 M of age, both *Cldn11*$^{+/-}$*Tg*$^{+/-}$ and *Cldn11*$^{-/-}$*Tg*$^{+/-}$ mice drink a similar amount of liquid (water) from either the L or R sipper tubes, however, within a genotype, both groups drink significantly more from the R sipper tube. **(B)** Sucrose phase (days 5 – 8) of testing when one sucrose and one water sipper tube was present each day, counterbalanced by day. Employing a two-way repeated measures ANOVA, the average amount of liquid drank, irrespective of type, was similar between *Cldn11*$^{+/-}$*Tg*$^{+/-}$ and *Cldn11*$^{-/-}$*Tg*$^{+/-}$ mice at 2 and 4 M of age. At 6 – 8 M, there was no significant difference between the amount of liquid drank from either the L or R sipper tubes between genotypes; however, within genotypes, the *Cldn11*$^{+/-}$*Tg*$^{+/-}$ animals drank significantly more liquid from the R sipper tube, than L, as compared to *Cldn11*$^{-/-}$*Tg*$^{+/-}$. All data values are plotted as mean $\pm$ SD, n = 9 at 2 M, n = 10 at 4 and 6 – 8 M; $^{**}p < .01$, $^{****}p < 0.0001$.

Appendix D.5 – Zone analysis of Barnes probe trial (day 5) conveys similar time is spent in various sections around the goal hole

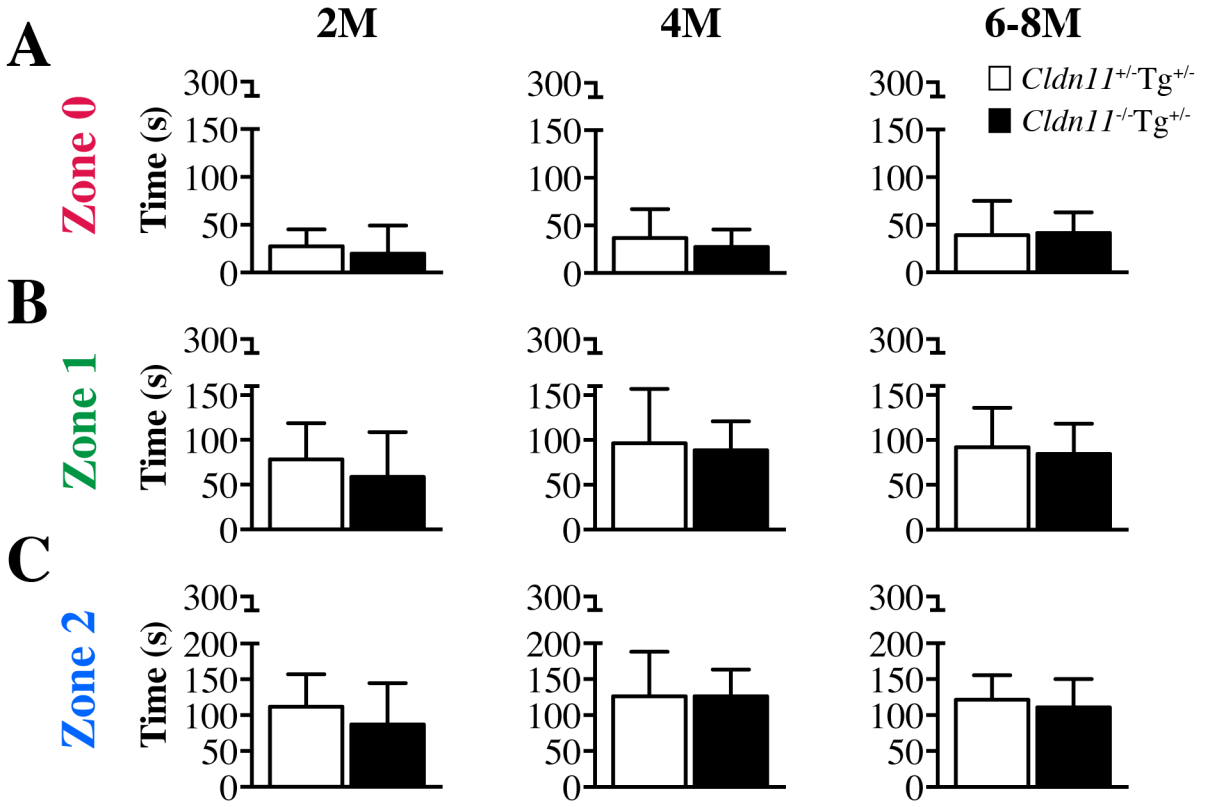

Student's unpaired *t*-tests reveal that at 2, 4, and 6 – 8 M of age, *Cldn11*$^{+/-}$*Tg*$^{+/-}$ and *Cldn11*$^{-/-}$*Tg*$^{+/-}$ mice spend a similar amount of time in **(A)** 'Zone 0,' **(B)** 'Zone 1,' and **(C)** 'Zone 2' during Barnes probe trial (day 5). Data values are plotted as mean ± SD; 2 M: $9 \leq n \leq 10$, 4 M: $7 \leq n \leq 10$, 6 – 8 M: $9 \leq n \leq 11$. See Methods section for zone illustration.

Appendix D.6 – Zone analysis of Barnes curtain trial (day 7) conveys similar time is spent in various sections around the goal hole

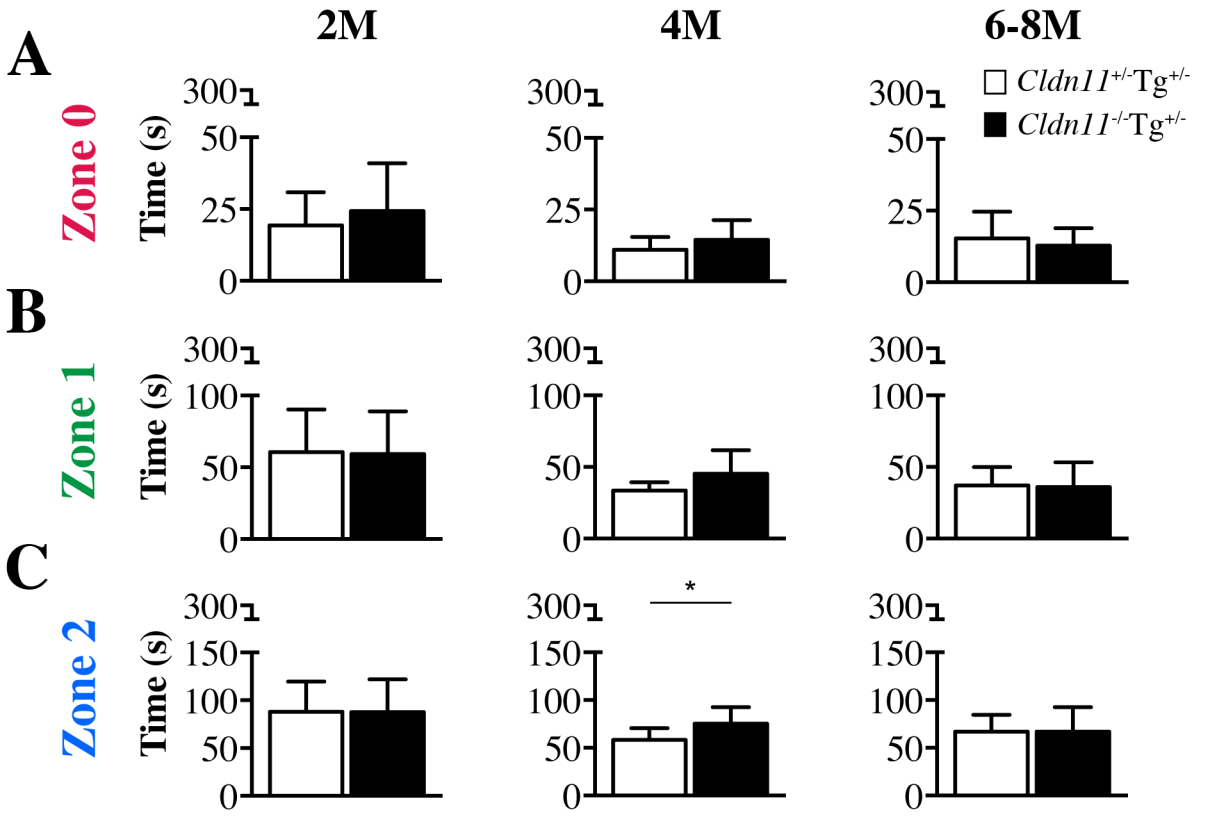

Student's unpaired *t*-tests reveal that at 2, 4, and 6 – 8 M of age, *Cldn11*$^{+/-}$*Tg*$^{+/-}$ and *Cldn11*$^{-/-}$*Tg*$^{+/-}$ mice spend a similar amount of time in **(A)** 'Zone 0' and **(B)** 'Zone 1' during Barnes curtain trial (day 7). Time spent in **(C)** 'Zone 2' is similar at 2 and 6 – 8 M of age, however, 4 M analyses of time reveals that *Cldn11*$^{-/-}$*Tg*$^{+/-}$ mice spend significantly more time in 'Zone 2' than controls. Data values are plotted as mean ± SD; 2 M: $9 \leq n \leq 10$, 4 M: $7 \leq n \leq 10$, 6 – 8 M: $9 \leq n \leq 11$; $^{*}p < .05$. See Methods for zone illustration.

Appendix D.7 – Zone analysis of Barnes reversal trial (day 10) reveals comparable time spent in various sections around the newly learned goal hole

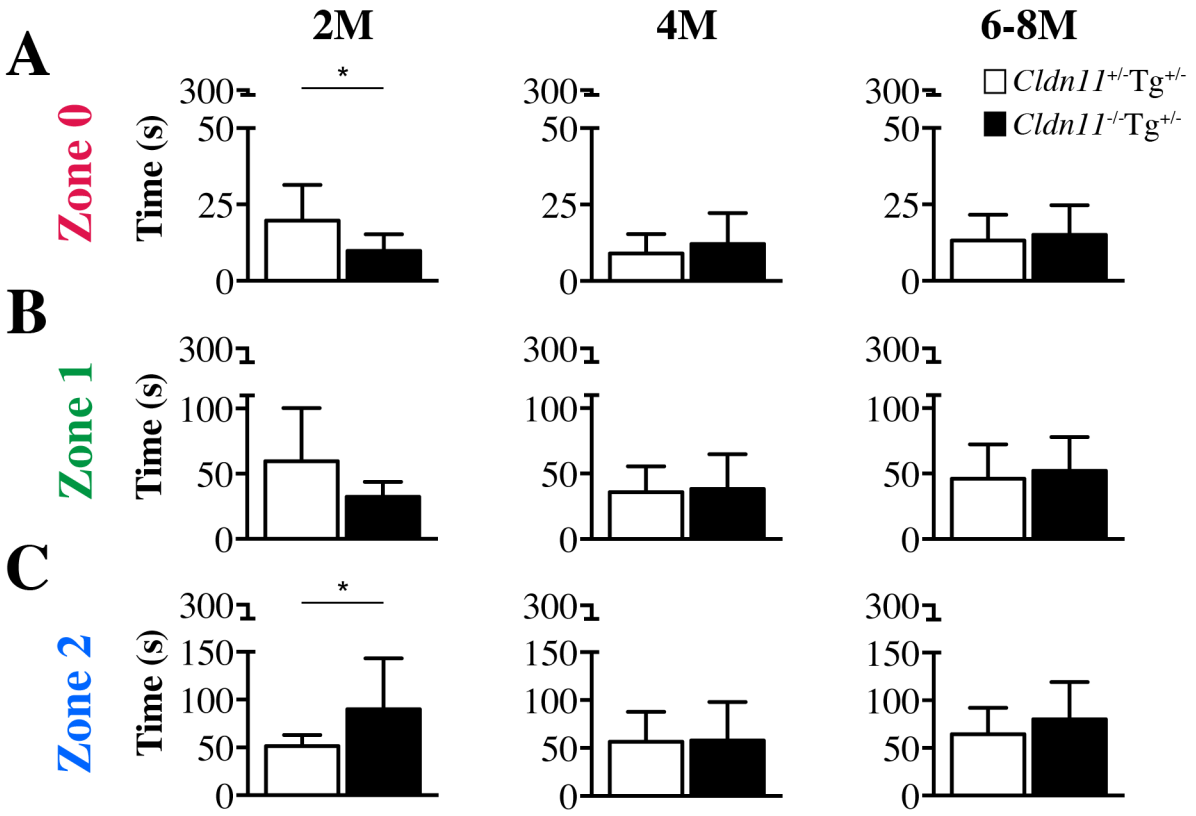

Student's unpaired *t*-tests indicate that time spent in **(A)** 'Zone 0,' **(B)** 'Zone 1,' and **(C)** 'Zone 2' is similar between *Cldn11*$^{+/-}$*Tg*$^{+/-}$ and *Cldn11*$^{-/-}$*Tg*$^{+/-}$ mice at 4 and 6 – 8 M of age. Of note, 2 M animals spend similar amount of time in 'Zone 1,' however controls spend significantly more time in 'Zone 0' and *Cldn11*$^{-/-}$*Tg*$^{+/-}$ mice spend significantly more time in 'Zone 2.' Data values are plotted as mean ± SD; 2M: $9 \leq n \leq 10$, 4M: $7 \leq n \leq 10$, 6 – 8M: $9 \leq n \leq 11$; $^{*}p < .05$. See Methods section for zone illustration.

Appendix D.8 – Zone analysis of Barnes probe trial (day 5) conveys similar time spent in various sections around the hook-in hole

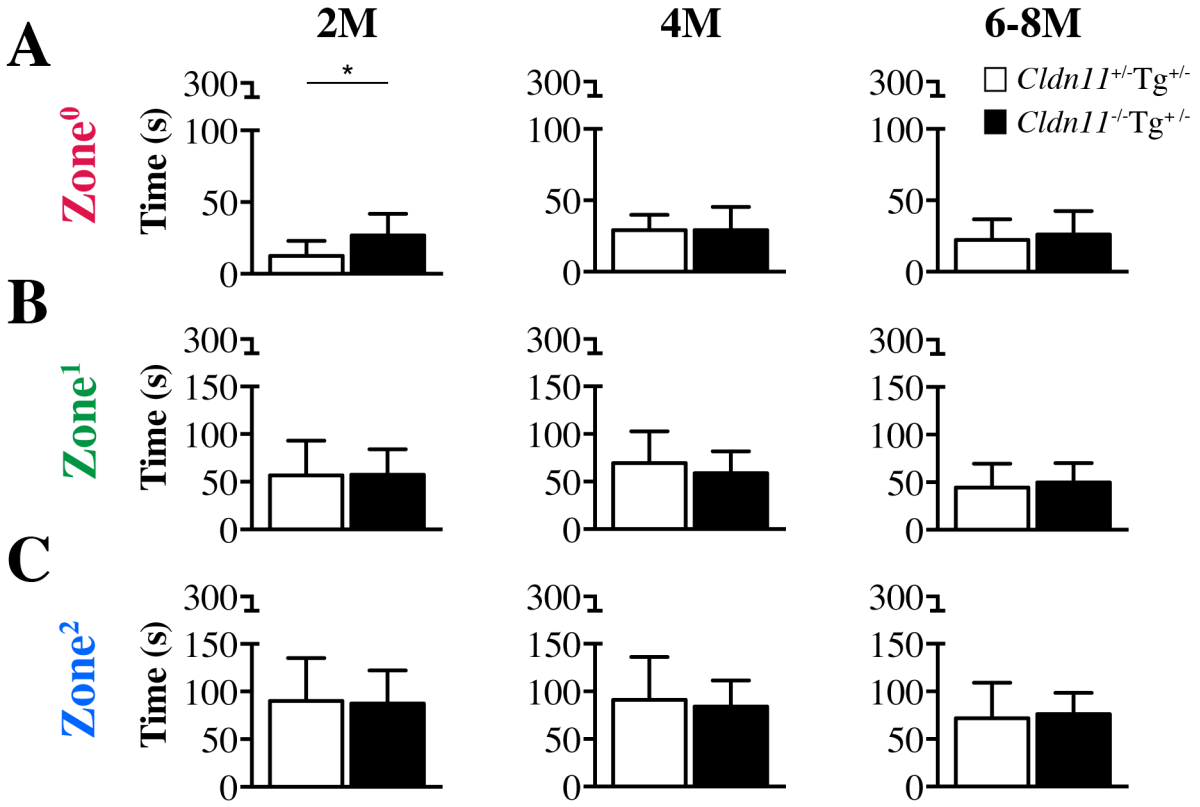

Student's unpaired *t*-tests reveal that at 2, 4, and 6 – 8 M of age, $Cldn11^{+/-}Tg^{+/-}$ and $Cldn11^{-/-}Tg^{+/-}$ mice spend a similar amount of time in **(A)** $Zone^0$, **(B)** $Zone^1$, and **(C)** $Zone^2$ surrounding the hook-in hole during the probe trial. Data values are plotted as mean ± SD; 2 M: $9 \leq n \leq 10$, 4 M: $7 \leq n \leq 10$, 6 – 8 M: $9 \leq n \leq 11$. See Methods for zone illustration.

Appendix D.9 – Zone analysis of Barnes curtain probe (day 7) conveys *Cldn11*$^{+/-}$*Tg*$^{+/-}$ mice spent more time around the in zones surrounding the hook-in hole

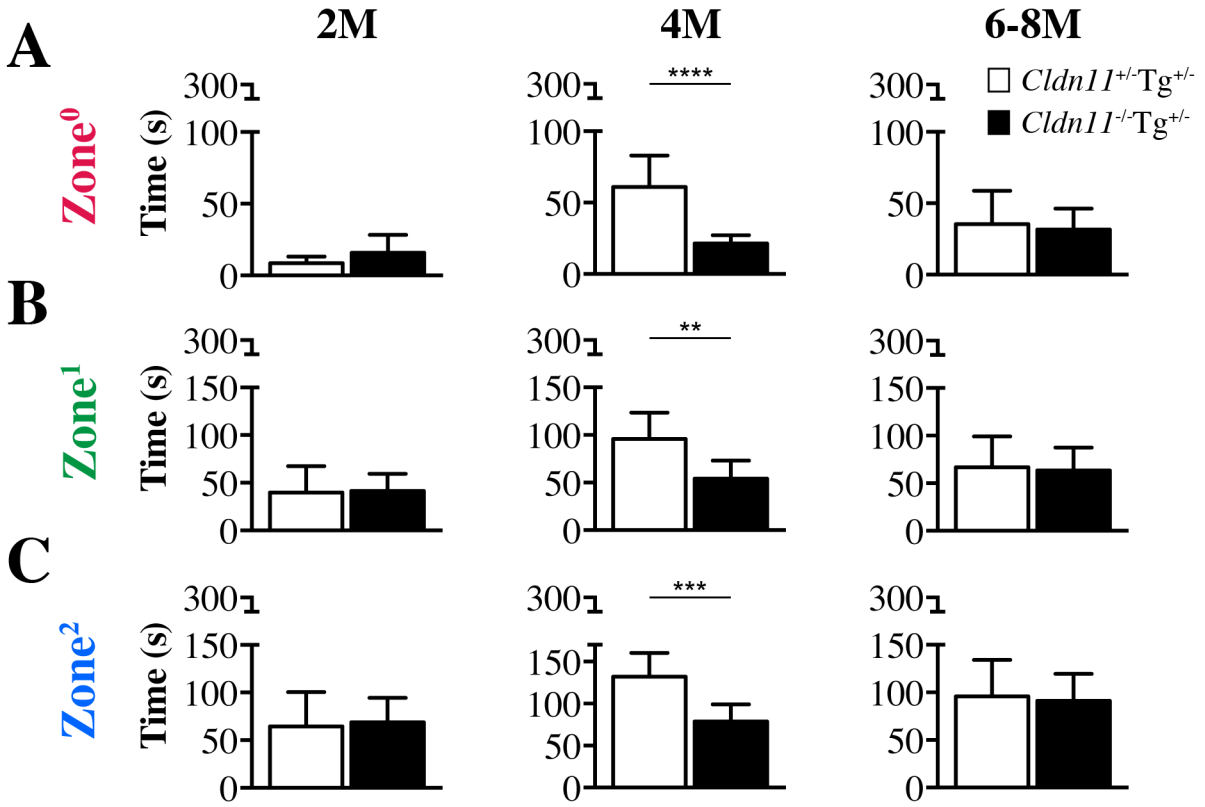

Student's unpaired *t*-tests reveal that at 2 and 6 – 8 M of age, *Cldn11*$^{+/-}$*Tg*$^{+/-}$ and *Cldn11*$^{-/-}$*Tg*$^{+/-}$ mice spend a similar amount of time in **(A)** Zone^0, **(B)** Zone^1, and **(C)** Zone^2 surrounding the hook-in hole during the curtain probe trial. At 4 M of age, *Cldn11*$^{+/-}$*Tg*$^{+/-}$ mice spent significantly more time in each zone surrounding the hook-in hole. Data values are plotted as mean ± SD; 2 M: $9 \leq n \leq 10$, 4 M: $7 \leq n \leq 10$, 6 – 8 M: $9 \leq n \leq 11$; $^{**}p < .01$, $^{***}p < .001$, $^{****}p < .0001$. See Methods for zone illustration.

Appendix D.10 – Zone analysis of Barnes reversal trial (day 10) conveys similar time spent in various sections around the hook-in hole

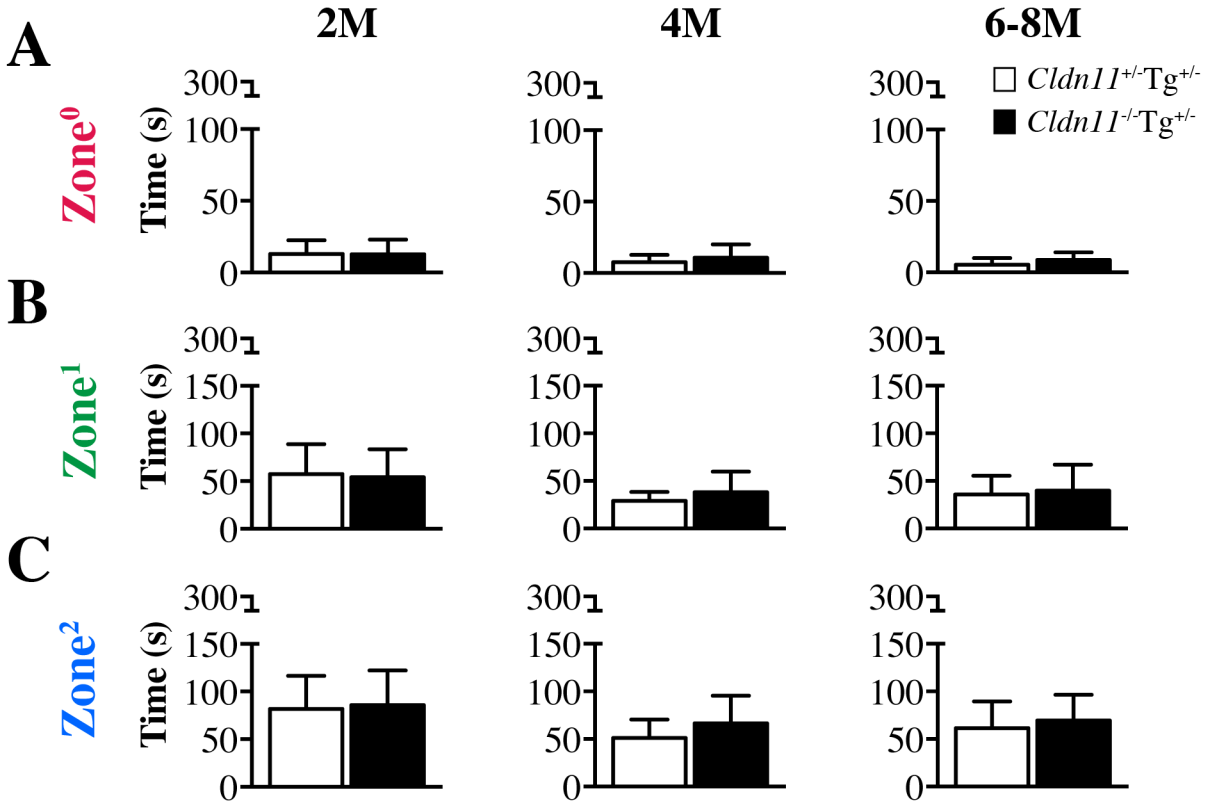

Student's unpaired *t*-tests reveal that at 2, 4, and 6 – 8 M of age, *Cldn11*$^{+/-}$*Tg*$^{+/-}$ and *Cldn11*$^{-/-}$*Tg*$^{+/-}$ mice spend a similar amount of time in **(A)** Zone^{0}, **(B)** Zone^{1}, and **(C)** Zone^{2} surrounding the hook-in hole during the reversal probe trial. Data values are plotted as mean ± SD; 2 M: $9 \leq n \leq 10$, 4 M: $7 \leq n \leq 10$, 6 – 8 M: $9 \leq n \leq 11$. See Methods for zone illustration.

Appendix D.11 – Concentration of GABA and glutamate within select brain regions of 4 M *Cldn11*$^{+/-}$*Tg*$^{+/-}$ and *Cldn11*$^{-/-}$*Tg*$^{+/-}$ mice reveals similar levels

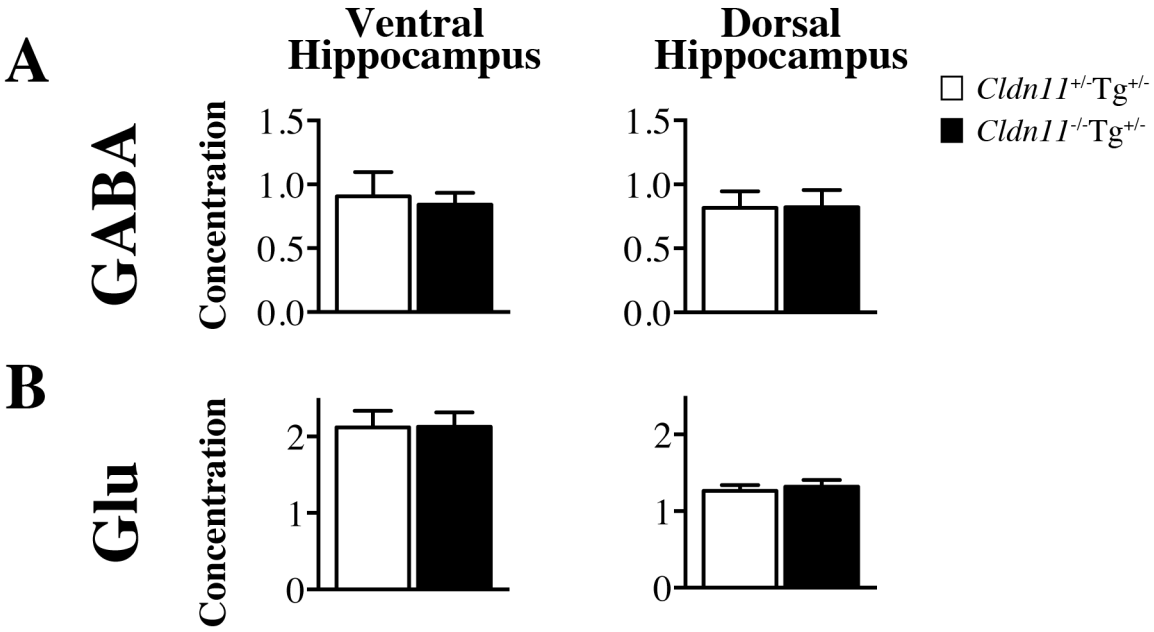

(A) gamma-aminobutryic acid (GABA) levels in the ventral and dorsal hippocampus of 4 M *Cldn11*$^{+/-}$*Tg*$^{+/-}$ and *Cldn11*$^{-/-}$*Tg*$^{+/-}$ mice. Student's *t*-test for select regions indicates no significant difference in concentration for either brain regions. **(B)** Glutamate (Glu) levels in the ventral and dorsal hippocampus of 4 M *Cldn11*$^{+/-}$*Tg*$^{+/-}$ and *Cldn11*$^{-/-}$*Tg*$^{+/-}$ mice. Student's *t*-tests indicate both groups have similar glutamate levels. Data values are plotted as mean $\pm$ SD; $6 \leq n \leq 8$.

Appendix D.12 – Sociability testing control parameters do not influence overall results

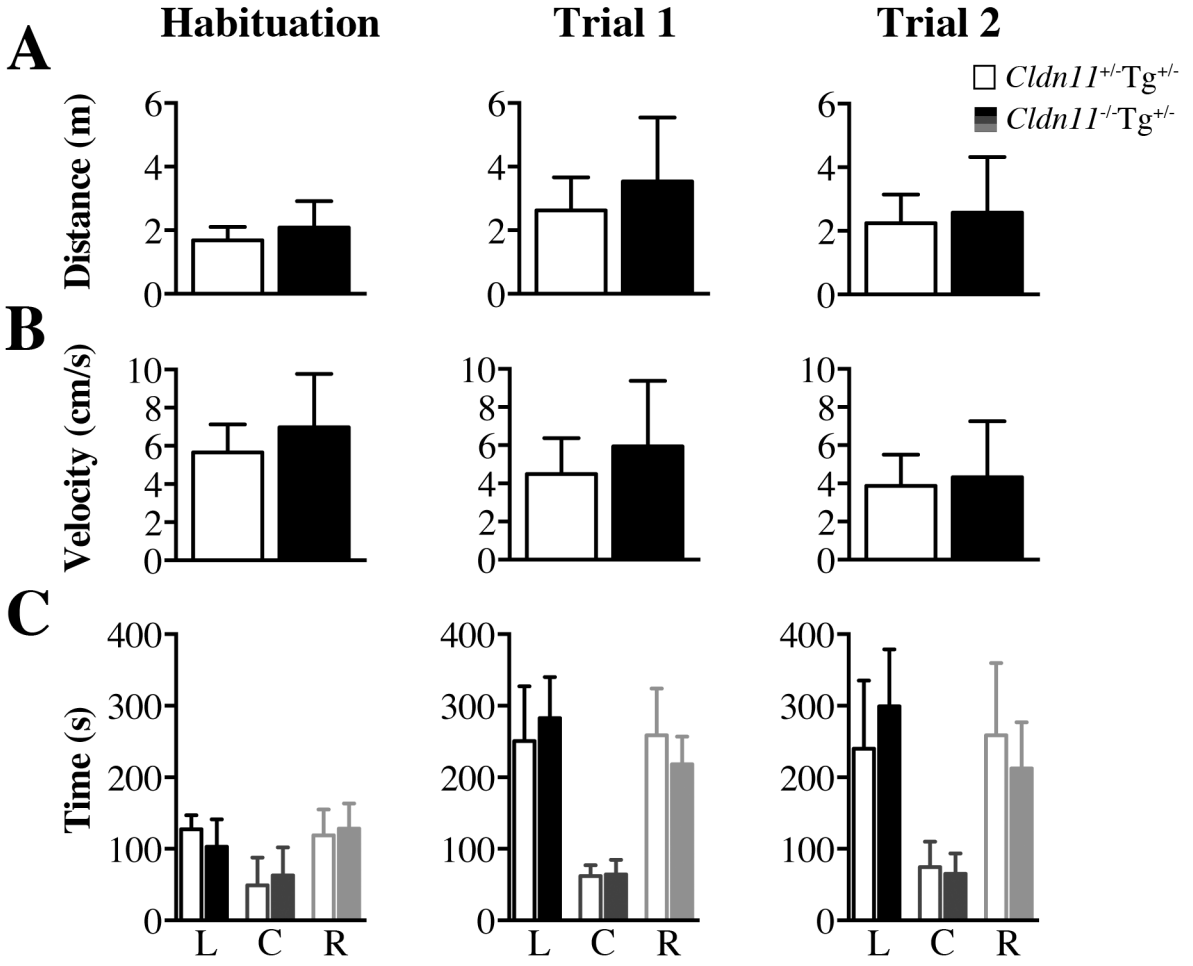

(A) Using a *t*-test, the average distance traveled during each phase of sociability testing (habituation, trial 1, and trial 2) is similar between *Cldn11*$^{+/-}$*Tg*$^{+/-}$ and *Cldn11*$^{-/-}$ *Tg*$^{+/-}$ mice. **(B)** Similar to average distance, the average velocity of the mice is alike between genotypes during each phase of testing. **(C)** A one -way ANOVA comparing total time spent each chamber of the sociability arena during habituation, trial 1, and trial 2 is equivalent between *Cldn11*$^{+/-}$*Tg*$^{+/-}$ and *Cldn11*$^{-/-}$*Tg*$^{+/-}$ mice. Data values are plotted as mean ± SD; *n* = 6.

Appendix D.13 – Grooming during sociability testing reveals similar anxiety-like behaviors

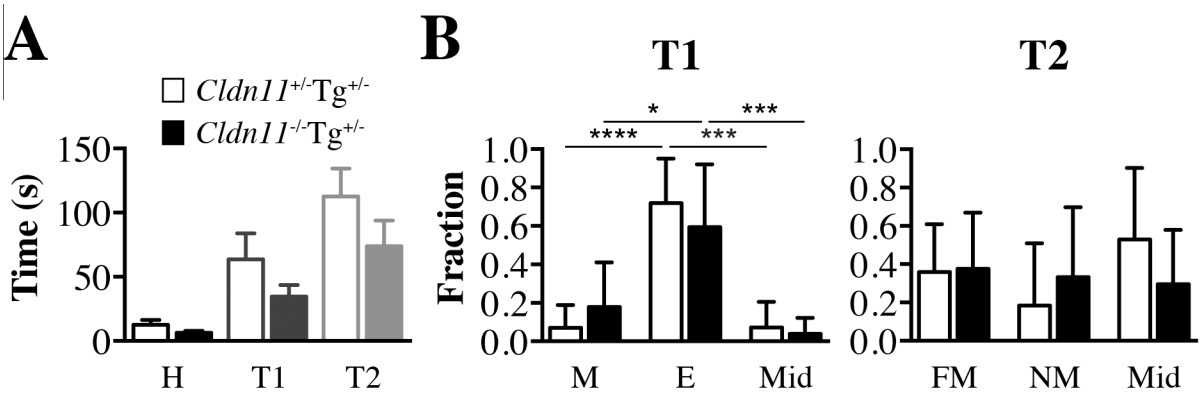

(A) Individual *t*-tests by session (habituation, trial 1, and trial 2) disclose similar total grooming time between *Cldn11*$^{+/-}$*Tg*$^{+/-}$ and *Cldn11*$^{-/-}$*Tg*$^{+/-}$ mice. **(B)** Using a one – way ANOVA comparing genotype versus compartment, the fraction of time mice spend grooming is not different during trial 1 or trial 2. Individual Bonferroni post – hoc testing indicates select differences within a genotype between various compartments. Data values are plotted as mean ± SD; $n = 6$; *$p < .05$, ***$p < .001$, ****$p < .0001$. H habituation, T1 trial 1, T2 trial 2, M mouse, E empty, Mid middle, FM familiar mouse, NM novel mouse

Appendix D.14 – Control variables during repeat open field test reveals parameters do not influence center square activity

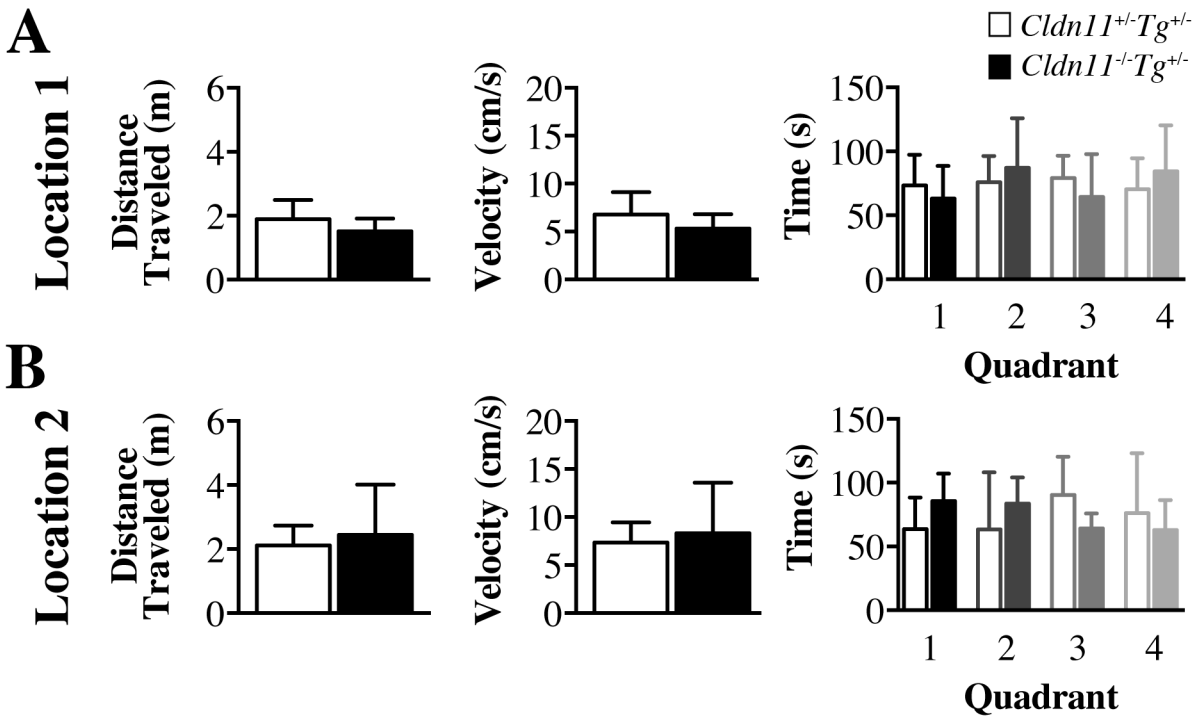

(A) A Student's *t*-test comparing average distance traveled and velocity was similar between *Cldn11*$^{+/-}$*Tg*$^{+/-}$ and *Cldn11*$^{-/-}$*Tg*$^{+/-}$ mice in Location 1. A two – way ANOVA comparing time spent in each quadrant of the open field was also indistinguishable between genotypes. **(B)** A Student's *t*-test comparing average distance traveled and velocity was similar between *Cldn11*$^{+/-}$*Tg*$^{+/-}$ and *Cldn11*$^{-/-}$*Tg*$^{+/-}$ mice in Location 2. A two -way ANOVA comparing time spent in each quadrant of the open field was also indistinguishable between genotypes. Data values are plotted as mean ± SD; Location 1 $n = 10$, Location 2 $6 \leq n \leq 7$.

REFERENCES

(2008). Anesthesia and Analgesia in Laboratory Animals, Second edn (San Diego, CA: Academic Press).

Aboitiz, F., Scheibel, A.B., Fisher, R.S., and Zaidel, E. (1992). Fiber composition of the human corpus callosum. Brain Res *598*, 143-153.

Ackermann, T.F., Hortnagl, H., Wolfer, D.P., Colacicco, G., Sohr, R., Lang, F., Hellweg, R., and Lang, U.E. (2008). Phosphatidylinositide dependent kinase deficiency increases anxiety and decreases GABA and serotonin abundance in the amygdala. Cellular physiology and biochemistry : international journal of experimental cellular physiology, biochemistry, and pharmacology *22*, 735-744.

Adam, T.J., Finlayson, P.G., and Schwarz, D.W. (2001). Membrane properties of principal neurons of the lateral superior olive. J Neurophysiol *86*, 922-934.

Adrian, E.D., and Matthews, B.H.C. (1934). The berger rhythm: potential changes from the occipital lobes in man. Brain *57*, 355-385.

Alberts, B., Wilson, J.H., and Hunt, T. (2008). Molecular biology of the cell, 5th edn (New York: Garland Science).

Andreasen, N.C., O'Leary, D.S., Cizadlo, T., Arndt, S., Rezai, K., Ponto, L.L., Watkins, G.L., and Hichwa, R.D. (1996). Schizophrenia and cognitive dysmetria: a positron-emission tomography study of dysfunctional prefrontal-thalamic-cerebellar circuitry. Proc Natl Acad Sci U S A *93*, 9985-9990.

Angelow, S., Ahlstrom, R., and Yu, A.S. (2008). Biology of claudins. Am J Physiol Renal Physiol *295*, F867-876.

Angelow, S., and Yu, A.S. (2007). Claudins and paracellular transport: an update. Curr Opin Nephrol Hypertens *16*, 459-464.

Anniko, M., and Arnesen, A.R. (1988). Cochlear nerve topography and fiber spectrum in the pigmented mouse. Arch Otorhinolaryngol *245*, 155-159.

Badgaiyan, R.D. (2011). Neurotransmitter imaging: basic concepts and future prospectives. Current Medical Imaging Reviews *7*, 98-103.

Bailey, K.R., Rustay, N.R., and Crawley, J.N. (2006). Behavioral phenotyping of transgenic and knockout mice: practical concerns and potential pitfalls. ILAR J *47*, 124-131.

Barnes, C.A. (1979). Memory deficits associated with senescence: a neurophysiological and behavioral study in the rat. J Comp Physiol Psychol *93*, 74-104.

Baumann, N., Turpin, J.C., Lefevre, M., and Colsch, B. (2002). Motor and psycho-cognitive clinical types in adult metachromatic leukodystrophy: genotype/phenotype relationships? J Physiol Paris *96*, 301-306.

Bell, K.F., and Claudio Cuello, A. (2006). Altered synaptic function in Alzheimer's disease. Eur J Pharmacol *545*, 11-21.

Belmonte, M.K., Allen, G., Beckel-Mitchener, A., Boulanger, L.M., Carper, R.A., and Webb, S.J. (2004a). Autism and abnormal development of brain connectivity. J Neurosci *24*, 9228-9231.

Belmonte, M.K., Cook, E.H., Jr., Anderson, G.M., Rubenstein, J.L., Greenough, W.T., Beckel-Mitchener, A., Courchesne, E., Boulanger, L.M., Powell, S.B., Levitt, P.R., *et al.* (2004b). Autism as a disorder of neural information processing: directions for research and targets for therapy. Mol Psychiatry *9*, 646-663.

Ben-Yosef, T., Belyantseva, I.A., Saunders, T.L., Hughes, E.D., Kawamoto, K., Van Itallie, C.M., Beyer, L.A., Halsey, K., Gardner, D.J., Wilcox, E.R., *et al.* (2003). Claudin 14 knockout mice, a model for autosomal recessive deafness DFNB29, are deaf due to cochlear hair cell degeneration. Hum Mol Genet *12*, 2049-2061.

Benes, F.M. (2000). Emerging principles of altered neural circuitry in schizophrenia. Brain Res Brain Res Rev *31*, 251-269.

Berger, H. (1929). Über das Elektrenkephalogramm des Menschen. Archiv fur Psychiatrie und Nervenkrankheiten *87*, 527-570.

Blight, A.R. (1985). Computer simulation of action potentials and afterpotentials in mammalian myelinated axons: the case for a lower resistance myelin sheath. Neuroscience *15*, 13-31.

Bloom, F.E., Kupfer, D.J., and American College of Neuropsychopharmacology. (1995). Psychopharmacology : the fourth generation of progress (New York: Raven Press).

Boehnke, S.E., and Phillips, D.P. (1999). Azimuthal tuning of human perceptual channels for sound location. J Acoust Soc Am *106*, 1948-1955.

Boison, D., Bussow, H., D'Urso, D., Muller, H.W., and Stoffel, W. (1995). Adhesive properties of proteolipid protein are responsible for the compaction of CNS myelin sheaths. J Neurosci *15*, 5502-5513.

Boison, D., and Stoffel, W. (1994). Disruption of the compacted myelin sheath of axons of the central nervous system in proteolipid protein-deficient mice. Proc Natl Acad Sci U S A *91*, 11709-11713.

Bokde, A.L., Ewers, M., and Hampel, H. (2009). Assessing neuronal networks: understanding Alzheimer's disease. Prog Neurobiol *89*, 125-133.

Bolivar, V.J., Caldarone, B.J., Reilly, A.A., and Flaherty, L. (2000). Habituation of activity in an open field: A survey of inbred strains and F1 hybrids. Behav Genet *30*, 285-293.

Borradori, L., and Sonnenberg, A. (1999). Structure and function of hemidesmosomes: more than simple adhesion complexes. J Invest Dermatol *112*, 411-418.

Brand, A., Behrend, O., Marquardt, T., McAlpine, D., and Grothe, B. (2002). Precise inhibition is essential for microsecond interaural time difference coding. Nature *417*, 543-547.

Bremer, C.D., Pittenger, J.B., Warren, R., and Jenkins, J.J. (1977). An illusion of auditory saltation similar to the cutaneous "rabbit". The American journal of psychology *90*, 645-654.

Brill, M.H., Waxman, S.G., Moore, J.W., and Joyner, R.W. (1977). Conduction velocity and spike configuration in myelinated fibres: computed dependence on internode distance. J Neurol Neurosurg Psychiatry *40*, 769-774.

Bronstein, J.M., Micevych, P.E., and Chen, K. (1997). Oligodendrocyte-specific protein (OSP) is a major component of CNS myelin. J Neurosci Res *50*, 713-720.

Brown, M.C., and Liu, T.S. (1995). Fos-like immunoreactivity in central auditory neurons of the mouse. J Comp Neurol *357*, 85-97.

Buchwald, J.S., and Huang, C. (1975). Far-field acoustic response: origins in the cat. Science *189*, 382-384.

Buetow, B.S., Chen, L.I., Maggio-Price, L., and Swisshelm, K. (1999). Peritonitis in Nude Mice in a Xenograft Study. Contemporary topics in laboratory animal science / American Association for Laboratory Animal Science *38*, 47-49.

Buki, A., and Povlishock, J.T. (2006). All roads lead to disconnection?--Traumatic axonal injury revisited. Acta Neurochir (Wien) *148*, 181-193; discussion 193-184.

Buxton, R.S., Cowin, P., Franke, W.W., Garrod, D.R., Green, K.J., King, I.A., Koch, P.J., Magee, A.I., Rees, D.A., Stanley, J.R.*, et al.* (1993). Nomenclature of the desmosomal cadherins. J Cell Biol *121*, 481-483.

Buzsaki, G., and Chrobak, J.J. (1995). Temporal structure in spatially organized neuronal ensembles: a role for interneuronal networks. Curr Opin Neurobiol *5*, 504-510.

Camchong, J., MacDonald, A.W., 3rd, Bell, C., Mueller, B.A., and Lim, K.O. (2011). Altered functional and anatomical connectivity in schizophrenia. Schizophr Bull *37*, 640-650.

Cant, N.B., and Benson, C.G. (2003). Parallel auditory pathways: projection patterns of the different neuronal populations in the dorsal and ventral cochlear nuclei. Brain Res Bull *60*, 457-474.

Cant, N.B., and Casseday, J.H. (1986). Projections from the anteroventral cochlear nucleus to the lateral and medial superior olivary nuclei. J Comp Neurol *247*, 457-476.

Cant, N.B., and Morest, D.K. (1979). The bushy cells in the anteroventral cochlear nucleus of the cat. A study with the electron microscope. Neuroscience *4*, 1925-1945.

Chen, M.S., Huber, A.B., van der Haar, M.E., Frank, M., Schnell, L., Spillmann, A.A., Christ, F., and Schwab, M.E. (2000). Nogo-A is a myelin-associated neurite outgrowth inhibitor and an antigen for monoclonal antibody IN-1. Nature *403*, 434-439.

Chiappa, K.H. (1997). Evoked potentials in clinical medicine, 3rd edn (Philadelphia: Lippincott-Raven).

Christensen-Dalsgaard, J., and Carr, C.E. (2008). Evolution of a sensory novelty: tympanic ears and the associated neural processing. Brain Res Bull *75*, 365-370.

Cilia, R., Cho, S.S., van Eimeren, T., Marotta, G., Siri, C., Ko, J.H., Pellecchia, G., Pezzoli, G., Antonini, A., and Strafella, A.P. (2011). Pathological gambling in patients with Parkinson's disease is associated with fronto-striatal disconnection: a path modeling analysis. Mov Disord *26*, 225-233.

Clark, W.A., Brown, R.M., Goldstein, M.H., Jr., Molnar, C.E., O'Brien, D.F., and Zieman, H.E. (1961). The average response computer (ARC): a digital device for computing averages and amplitude and time histograms of electrophysiological response. IRE transactions on bio-medical electronics *BME-8*, 46-51.

Cronin-Golomb, A. (2010). Parkinson's disease as a disconnection syndrome. Neuropsychol Rev *20*, 191-208.

Cryan, J.F., Mombereau, C., and Vassout, A. (2005). The tail suspension test as a model for assessing antidepressant activity: review of pharmacological and genetic studies in mice. Neurosci Biobehav Rev *29*, 571-625.

Cully, D.F., Vassilatis, D.K., Liu, K.K., Paress, P.S., Van der Ploeg, L.H., Schaeffer, J.M., and Arena, J.P. (1994). Cloning of an avermectin-sensitive glutamate-gated chloride channel from Caenorhabditis elegans. Nature *371*, 707-711.

Davis, H.D., AL, Loomis AL, Harvey EN, Hobart, G (1939). Electrical reactions of the human brain to auditory stimulation during sleep. Journal of Neurophysiology *2*, 500-514.

Davis, J.A., Paylor, R., McDonald, M.P., Libbey, M., Ligler, A., Bryant, K., and Crawley, J.N. (1999). Behavioral effects of ivermectin in mice. Lab Anim Sci *49*, 288-296.

Davis, K.L., Kahn, R.S., Ko, G., and Davidson, M. (1991). Dopamine in schizophrenia: a review and reconceptualization. Am J Psychiatry *148*, 1474-1486.

Davis, K.L., Stewart, D.G., Friedman, J.I., Buchsbaum, M., Harvey, P.D., Hof, P.R., Buxbaum, J., and Haroutunian, V. (2003). White matter changes in schizophrenia: evidence for myelin-related dysfunction. Arch Gen Psychiatry *60*, 443-456.

Dawson, G.D. (1947). Investigations on a patient subject to myoclonic seizures after sensory stimulation. J Neurol Neurosurg Psychiatry *10*, 141-162.

Dawson, G.R., Wafford, K.A., Smith, A., Marshall, G.R., Bayley, P.J., Schaeffer, J.M., Meinke, P.T., and McKernan, R.M. (2000). Anticonvulsant and adverse effects of avermectin analogs in mice are mediated through the gamma-aminobutyric acid(A) receptor. J Pharmacol Exp Ther *295*, 1051-1060.

De Camilli, P., and Jahn, R. (1990). Pathways to regulated exocytosis in neurons. Annu Rev Physiol *52*, 625-645.

Denier, C., Orgibet, A., Roffi, F., Jouvent, E., Buhl, C., Niel, F., Boespflug-Tanguy, O., Said, G., and Ducreux, D. (2007). Adult-onset vanishing white matter leukoencephalopathy presenting as psychosis. Neurology *68*, 1538-1539.

Depino, A.M., Tsetsenis, T., and Gross, C. (2008). GABA homeostasis contributes to the developmental programming of anxiety-related behavior. Brain Res *1210*, 189-199.

Dermietzel, R. (1974). Junctions in the central nervous system of the cat. I. Membrane fusion in central myelin. Cell Tissue Res *148*, 565-576.

Devaux, J., and Gow, A. (2008). Tight junctions potentiate the insulative properties of small CNS myelinated axons. J Cell Biol *183*, 909-921.

Dingle, R.N., Hall, S.E., and Phillips, D.P. (2010). A midline azimuthal channel in human spatial hearing. Hear Res *268*, 67-74.

Dingle, R.N., Hall, S.E., and Phillips, D.P. (2012). The three-channel model of sound localization mechanisms: interaural level differences. J Acoust Soc Am *131*, 4023-4029.

Dingle, R.N., Hall, S.E., and Phillips, D.P. (2013). The three-channel model of sound localization mechanisms: interaural time differences. J Acoust Soc Am *133*, 417-424.

Dinh, M.L., Koppel, S.J., Korn, M.J., and Cramer, K.S. (2014). Distribution of glial cells in the auditory brainstem: normal development and effects of unilateral lesion. Neuroscience *278*, 237-252.

Doucet, J.R., and Ryugo, D.K. (2003). Axonal pathways to the lateral superior olive labeled with biotinylated dextran amine injections in the dorsal cochlear nucleus of rats. J Comp Neurol *461*, 452-465.

Elsinga, P.H., Hatano, K., and Ishiwata, K. (2006). PET tracers for imaging of the dopaminergic system. Curr Med Chem *13*, 2139-2153.

Erb, D.E., and Povlishock, J.T. (1991). Neuroplasticity following traumatic brain injury: a study of GABAergic terminal loss and recovery in the cat dorsal lateral vestibular nucleus. Exp Brain Res *83*, 253-267.

Fanning, A.S., Jameson, B.J., Jesaitis, L.A., and Anderson, J.M. (1998). The tight junction protein ZO-1 establishes a link between the transmembrane protein occludin and the actin cytoskeleton. J Biol Chem *273*, 29745-29753.

Farquhar, M.G., and Palade, G.E. (1963). Junctional complexes in various epithelia. J Cell Biol *17*, 375-412.

Feighner, J.P. (1999). Mechanism of action of antidepressant medications. J Clin Psychiatry *60 Suppl 4*, 4-11; discussion 12-13.

Feinstein, A., du Boulay, G., and Ron, M.A. (1992). Psychotic illness in multiple sclerosis. A clinical and magnetic resonance imaging study. Br J Psychiatry *161*, 680-685.

Fekete, D.M., Rouiller, E.M., Liberman, M.C., and Ryugo, D.K. (1984). The central projections of intracellularly labeled auditory nerve fibers in cats. J Comp Neurol *229*, 432-450.

Felix-Ortiz, A.C., Beyeler, A., Seo, C., Leppla, C.A., Wildes, C.P., and Tye, K.M. (2013). BLA to vHPC inputs modulate anxiety-related behaviors. Neuron *79*, 658-664.

Felix-Ortiz, A.C., and Tye, K.M. (2014). Amygdala inputs to the ventral hippocampus bidirectionally modulate social behavior. J Neurosci *34*, 586-595.

Feng, Y., Wang, J., and Yin, S. (2007). General anesthesia changes gap-evoked auditory responses in guinea pigs. Acta Otolaryngol *127*, 143-148.

Field, K.J., White, W.J., and Lang, C.M. (1993). Anaesthetic effects of chloral hydrate, pentobarbitone and urethane in adult male rats. Laboratory animals *27*, 258-269.

Fisch, U.P., and Ruben, R.J. (1962). Electrical acoustical response to click stimulation after section of the eighth nerve. Acta Otolaryngol *54*, 532-542.

Fisher, M.H., and Mrozik, H. (1992). The chemistry and pharmacology of avermectins. Annual review of pharmacology and toxicology *32*, 537-553.

Flecknell, P. (1996). Laboratory Animal anaesthesia (Academic Press).

Flynn, S.W., Lang, D.J., Mackay, A.L., Goghari, V., Vavasour, I.M., Whittall, K.P., Smith, G.N., Arango, V., Mann, J.J., Dwork, A.J.*, et al.* (2003). Abnormalities of myelination in schizophrenia detected in vivo with MRI, and post-mortem with analysis of oligodendrocyte proteins. Mol Psychiatry *8*, 811-820.

Foa, E.B., Grayson, J.B., Steketee, G.S., Doppelt, H.G., Turner, R.M., and Latimer, P.R. (1983). Success and failure in the behavioral treatment of obsessive-compulsives. J Consult Clin Psychol *51*, 287-297.

Fogelson, N., Li, L., Li, Y., Fernandez-Del-Olmo, M., Santos-Garcia, D., and Peled, A. (2013). Functional connectivity abnormalities during contextual processing in schizophrenia and in Parkinson's disease. Brain Cogn *82*, 243-253.

Folch, J., and Lees, M. (1951). Proteolipides, a new type of tissue lipoproteins; their isolation from brain. J Biol Chem *191*, 807-817.

Forrest, D., Erway, L.C., Ng, L., Altschuler, R., and Curran, T. (1996). Thyroid hormone receptor beta is essential for development of auditory function. Nat Genet *13*, 354-357.

Friston, K.J. (1998). The disconnection hypothesis. Schizophr Res *30*, 115-125.

Friston, K.J. (1999). Schizophrenia and the disconnection hypothesis. Acta Psychiatr Scand Suppl *395*, 68-79.

Frith, C. (2004). Is autism a disconnection disorder? Lancet Neurol *3*, 577.

Fujimoto, K. (1995). Freeze-fracture replica electron microscopy combined with SDS digestion for cytochemical labeling of integral membrane proteins. Application to the immunogold labeling of intercellular junctional complexes. J Cell Sci *108 (Pt 11)*, 3443-3449.

Furuse, M. (2009). Knockout animals and natural mutations as experimental and diagnostic tool for studying tight junction functions in vivo. Biochim Biophys Acta *1788*, 813-819.

Furuse, M., Fujita, K., Hiiragi, T., Fujimoto, K., and Tsukita, S. (1998). Claudin-1 and -2: novel integral membrane proteins localizing at tight junctions with no sequence similarity to occludin. J Cell Biol *141*, 1539-1550.

Furuse, M., Hata, M., Furuse, K., Yoshida, Y., Haratake, A., Sugitani, Y., Noda, T., Kubo, A., and Tsukita, S. (2002). Claudin-based tight junctions are crucial for the mammalian epidermal barrier: a lesson from claudin-1-deficient mice. J Cell Biol *156*, 1099-1111.

Furuse, M., Hirase, T., Itoh, M., Nagafuchi, A., Yonemura, S., Tsukita, S., and Tsukita, S. (1993). Occludin: a novel integral membrane protein localizing at tight junctions. J Cell Biol *123*, 1777-1788.

Furuse, M., Itoh, M., Hirase, T., Nagafuchi, A., Yonemura, S., Tsukita, S., and Tsukita, S. (1994). Direct association of occludin with ZO-1 and its possible involvement in the localization of occludin at tight junctions. J Cell Biol *127*, 1617-1626.

Furuse, M., and Tsukita, S. (2006). Claudins in occluding junctions of humans and flies. Trends in cell biology *16*, 181-188.

Gaertner, D., Hallman, T., Hankenson, F., and Batchelder, M. (2008). Anesthesia and Analgesia in Laboratory Animals, 2 edn (Burlington: Academic Press).

Garside, S., Rosebush, P.I., Levinson, A.J., and Mazurek, M.F. (1999). Late-onset adrenoleukodystrophy associated with long-standing psychiatric symptoms. J Clin Psychiatry *60*, 460-468.

Goldstein, R., and Rodman, L.B. (1967). Early components of averaged evoked responses to rapidly repeated auditory stimuli. Journal of speech and hearing research *10*, 697-705.

Gow, A. (2008). Major components of myelin in the mammalian central and peripheral nervous systems. In Neuroimmunology in clinical practice, B. Kalman, and T.H. Brannagan III, eds. (Maden : Blackwell Publishing), pp. 12 - 25.

Gow, A., Davies, C., Southwood, C.M., Frolenkov, G., Chrustowski, M., Ng, L., Yamauchi, D., Marcus, D.C., and Kachar, B. (2004). Deafness in Claudin 11-null mice reveals the critical contribution of basal cell tight junctions to stria vascularis function. J Neurosci *24*, 7051-7062.

Gow, A., and Devaux, J. (2008). A model of tight junction function in central nervous system myelinated axons. Neuron Glia Biol *4*, 307-317.

Gow, A., Friedrich, V.L., Jr., and Lazzarini, R.A. (1992). Myelin basic protein gene contains separate enhancers for oligodendrocyte and Schwann cell expression. J Cell Biol *119*, 605-616.

Gow, A., Southwood, C.M., Li, J.S., Pariali, M., Riordan, G.P., Brodie, S.E., Danias, J., Bronstein, J.M., Kachar, B., and Lazzarini, R.A. (1999). CNS myelin and sertoli cell tight junction strands are absent in Osp/claudin-11 null mice. Cell *99*, 649-659.

Graeff, F.G. (1993). Role of 5-HT in defensive behavior and anxiety. Rev Neurosci *4*, 181-211.

Greer, J.M., and Lees, M.B. (2002). Myelin proteolipid protein--the first 50 years. Int J Biochem Cell Biol *34*, 211-215.

Guinan, J.J., Jr., and Li, R.Y. (1990). Signal processing in brainstem auditory neurons which receive giant endings (calyces of Held) in the medial nucleus of the trapezoid body of the cat. Hear Res *49*, 321-334.

Guinan, J.J., Jr., Norris, B., and Guinan, S.S. (1972). Single auditory units in the superior olivary complex: II: locations of unit categories and tonotopic organization. International Journal of Neuroscience *4*, 147-166.

Gunning-Dixon, F.M., and Raz, N. (2000). The cognitive correlates of white matter abnormalities in normal aging: a quantitative review. Neuropsychology *14*, 224-232.

Haenisch, B., and Bonisch, H. (2011). Depression and antidepressants: insights from knockout of dopamine, serotonin or noradrenaline re-uptake transporters. Pharmacol Ther *129*, 352-368.

Hall, J.W. (1992). Handbook of auditory evoked responses (Allyn and Bacon).

Halter, J.A., and Clark, J.W., Jr. (1991). A distributed-parameter model of the myelinated nerve fiber. J Theor Biol *148*, 345-382.

Haroutunian, V., Katsel, P., Dracheva, S., Stewart, D.G., and Davis, K.L. (2007). Variations in oligodendrocyte-related gene expression across multiple cortical regions: implications for the pathophysiology of schizophrenia. Int J Neuropsychopharmacol *10*, 565-573.

Hartline, D.K., and Colman, D.R. (2007). Rapid conduction and the evolution of giant axons and myelinated fibers. Curr Biol *17*, R29-35.

Hashimoto, I., Ishiyama, Y., Yoshimoto, T., and Nemoto, S. (1981). Brain-stem auditory-evoked potentials recorded directly from human brain-stem and thalamus. Brain *104*, 841-859.

Hasler, G., van der Veen, J.W., Tumonis, T., Meyers, N., Shen, J., and Drevets, W.C. (2007). Reduced prefrontal glutamate/glutamine and gamma-aminobutyric acid levels in major depression determined using proton magnetic resonance spectroscopy. Arch Gen Psychiatry *64*, 193-200.

Hedden, T., and Gabrieli, J.D. (2004). Insights into the ageing mind: a view from cognitive neuroscience. Nat Rev Neurosci *5*, 87-96.

Held, H. (1893). Die zentrale Gehorleitung. Arch Anat Physiol Anat Abtheil *17*, 201 - 258.

Hetzler, B.E., and Dyer, R.S. (1984). Contribution of hypothermia to effects of chloral hydrate on flash evoked potentials of hooded rats. Pharmacol Biochem Behav *21*, 599-607.

Hibbs, R.E., and Gouaux, E. (2011). Principles of activation and permeation in an anion-selective Cys-loop receptor. Nature *474*, 54-60.

Hodgkin, A.L. (1964). The conduction of the nervous impulse (C. C. Thomas).

Hodgkin, A.L., and Huxley, A.F. (1952). A quantitative description of membrane current and its application to conduction and excitation in nerve. J Physiol *117*, 500-544.

Hoehn-Saric, R. (1982). Neurotransmitters in anxiety. Arch Gen Psychiatry *39*, 735-742.

Hof, P.R., and Bouras, C. (1991). Object recognition deficit in Alzheimer's disease: possible disconnection of the occipito-temporal component of the visual system. Neurosci Lett *122*, 53-56.

Holton, J.L., Kenny, T.P., Legan, P.K., Collins, J.E., Keen, J.N., Sharma, R., and Garrod, D.R. (1990). Desmosomal glycoproteins 2 and 3 (desmocollins) show N-terminal similarity to calcium-dependent cell-cell adhesion molecules. J Cell Sci *97 (Pt 2)*, 239-246.

Holtzman, E. (1977). The origin and fate of secretory packages, especially synaptic vesicles. Neuroscience *2*, 327-355.

Hyde, T.M., Ziegler, J.C., and Weinberger, D.R. (1992). Psychiatric disturbances in metachromatic leukodystrophy. Insights into the neurobiology of psychosis. Arch Neurol *49*, 401-406.

Hyman, S.E. (1998). Brain neurocircuitry of anxiety and fear: implications for clinical research and practice. Biol Psychiatry *44*, 1201-1203.

Inagawa, K., Watanabe, S., Tsukada, Y., and Mikoshiba, K. (1988). The role of myelination in learning performance observed in two strains of myelin-deficient mutant mice (shiverer and mld). Behav Neural Biol *50*, 184-192.

Inoue, Y., Kagawa, T., Matsumura, Y., Ikenaka, K., and Mikoshiba, K. (1996). Cell death of oligodendrocytes or demyelination induced by overexpression of proteolipid protein depending on expressed gene dosage. Neurosci Res *25*, 161-172.

Irving, R., and Harrison, J.M. (1967). The superior olivary complex and audition: a comparative study. J Comp Neurol *130*, 77-86.

Itoh, M., Nagafuchi, A., Yonemura, S., Kitani-Yasuda, T., Tsukita, S., and Tsukita, S. (1993). The 220-kD protein colocalizing with cadherins in non-epithelial cells is identical to ZO-1, a tight junction-associated protein in epithelial cells: cDNA cloning and immunoelectron microscopy. J Cell Biol *121*, 491-502.

Jacobs, A.H., Li, H., Winkeler, A., Hilker, R., Knoess, C., Ruger, A., Galldiks, N., Schaller, B., Sobesky, J., Kracht, L.*, et al.* (2003). PET-based molecular imaging in neuroscience. Eur J Nucl Med Mol Imaging *30*, 1051-1065.

Jacobson, J.T. (1994). Principles and applications in auditory evoked potentials (Boston: Allyn and Bacon).

Jalabi, W., Kopp-Scheinpflug, C., Allen, P.D., Schiavon, E., DiGiacomo, R.R., Forsythe, I.D., and Maricich, S.M. (2013). Sound localization ability and glycinergic innervation of the superior olivary complex persist after genetic deletion of the medial nucleus of the trapezoid body. J Neurosci *33*, 15044-15049.

Jeffress, L.A. (1948). A place theory of sound localization. J Comp Physiol Psychol *41*, 35-39.

Jewett, D.L., and Williston, J.S. (1971). Auditory-evoked far fields averaged from the scalp of humans. Brain *94*, 681-696.

Jinno, S., Klausberger, T., Marton, L.F., Dalezios, Y., Roberts, J.D., Fuentealba, P., Bushong, E.A., Henze, D., Buzsaki, G., and Somogyi, P. (2007). Neuronal diversity in GABAergic long-range projections from the hippocampus. J Neurosci *27*, 8790-8804.

Jongen, P.J., Ter Horst, A.T., and Brands, A.M. (2012). Cognitive impairment in multiple sclerosis. Minerva medica *103*, 73-96.

Joris, P.X., Carney, L.H., Smith, P.H., and Yin, T.C. (1994). Enhancement of neural synchronization in the anteroventral cochlear nucleus. I. Responses to tones at the characteristic frequency. J Neurophysiol *71*, 1022-1036.

Just, M.A., Cherkassky, V.L., Keller, T.A., Kana, R.K., and Minshew, N.J. (2007). Functional and anatomical cortical underconnectivity in autism: evidence from an FMRI study of an executive function task and corpus callosum morphometry. Cereb Cortex *17*, 951-961.

Kaidanovich-Beilin, O., Lipina, T., Vukobradovic, I., Roder, J., and Woodgett, J.R. (2011). Assessment of social interaction behaviors. J Vis Exp.

Kalueff, A.V., and Tuohimaa, P. (2005). Mouse grooming microstructure is a reliable anxiety marker bidirectionally sensitive to GABAergic drugs. Eur J Pharmacol *508*, 147-153.

Kandel, E.R., Schwartz, J.H., and Jessell, T.M. (2000). Principles of neural science, 4th edn (New York: McGraw-Hill, Health Professions Division).

Kandler, K., and Friauf, E. (1993). Pre- and postnatal development of efferent connections of the cochlear nucleus in the rat. J Comp Neurol *328*, 161-184.

Katsel, P., Davis, K.L., and Haroutunian, V. (2005). Variations in myelin and oligodendrocyte-related gene expression across multiple brain regions in schizophrenia: a gene ontology study. Schizophr Res *79*, 157-173.

Kelly, R.B., Deutsch, J.W., Carlson, S.S., and Wagner, J.A. (1979). Biochemistry of neurotransmitter release. Annu Rev Neurosci *2*, 399-446.

Kessler, R.C., Berglund, P., Demler, O., Jin, R., Merikangas, K.R., and Walters, E.E. (2005). Lifetime prevalence and age-of-onset distributions of DSM-IV disorders in the National Comorbidity Survey Replication. Arch Gen Psychiatry *62*, 593-602.

Kil, J., Kageyama, G.H., Semple, M.N., and Kitzes, L.M. (1995). Development of ventral cochlear nucleus projections to the superior olivary complex in gerbil. J Comp Neurol *353*, 317-340.

Kirschner, D.A., and Ganser, A.L. (1980). Compact myelin exists in the absence of basic protein in the shiverer mutant mouse. Nature *283*, 207-210.

Kiss, A., and Majorossy, K. (1983). Neuron morphology and synaptic architecture in the medial superior olivary nucleus. Light- and electron microscope studies in the cat. Exp Brain Res *52*, 315-327.

Kitajiri, S., Miyamoto, T., Mineharu, A., Sonoda, N., Furuse, K., Hata, M., Sasaki, H., Mori, Y., Kubota, T., Ito, J.*, et al.* (2004). Compartmentalization established by claudin-11-based tight junctions in stria vascularis is required for hearing through generation of endocochlear potential. J Cell Sci *117*, 5087-5096.

Klugmann, M., Schwab, M.H., Puhlhofer, A., Schneider, A., Zimmermann, F., Griffiths, I.R., and Nave, K.A. (1997). Assembly of CNS myelin in the absence of proteolipid protein. Neuron *18*, 59-70.

Koch, P.J., Walsh, M.J., Schmelz, M., Goldschmidt, M.D., Zimbelmann, R., and Franke, W.W. (1990). Identification of desmoglein, a constitutive desmosomal glycoprotein, as a member of the cadherin family of cell adhesion molecules. Eur J Cell Biol *53*, 1-12.

Konrad, M., Schaller, A., Seelow, D., Pandey, A.V., Waldegger, S., Lesslauer, A., Vitzthum, H., Suzuki, Y., Luk, J.M., Becker, C.*, et al.* (2006). Mutations in the tight-junction gene claudin 19 (CLDN19) are associated with renal magnesium wasting, renal failure, and severe ocular involvement. Am J Hum Genet *79*, 949-957.

Kopala, L.C., Tan, S., Shea, C., Orlik, H., Vandorpe, R., and Honer, W.G. (2000). Adrenoleukodystrophy associated with psychosis. Schizophr Res *45*, 263-265.

Kopp-Scheinpflug, C., Tolnai, S., Malmierca, M.S., and Rubsamen, R. (2008). The medial nucleus of the trapezoid body: comparative physiology. Neuroscience *154*, 160-170.

Kuwabara, N., and Zook, J.M. (1991). Classification of the principal cells of the medial nucleus of the trapezoid body. J Comp Neurol *314*, 707-720.

Lawrie, S.M., and Abukmeil, S.S. (1998). Brain abnormality in schizophrenia. A systematic and quantitative review of volumetric magnetic resonance imaging studies. Br J Psychiatry *172*, 110-120.

LeDoux, J. (2003). The emotional brain, fear, and the amygdala. Cell Mol Neurobiol *23*, 727-738.

Lev, A., and Sohmer, H. (1972). Sources of averaged neural responses recorded in animal and human subjects during cochlear audiometry (electro-cochleogram). Archiv fur klinische und experimentelle Ohren- Nasen- und Kehlkopfheilkunde *201*, 79-90.

Lieggi, C.C., Fortman, J.D., Kleps, R.A., Sethi, V., Anderson, J.A., Brown, C.E., and Artwohl, J.E. (2005). An evaluation of preparation methods and storage conditions of tribromoethanol. Contemporary topics in laboratory animal science / American Association for Laboratory Animal Science *44*, 11-16.

Lindsey, B.G. (1975). Fine structure and distribution of axon terminals from the cochlear nucleus on neurons in the medial superior olivary nucleus of the cat. J Comp Neurol *160*, 81-103.

Liu, G.X., Cai, G.Q., Cai, Y.Q., Sheng, Z.J., Jiang, J., Mei, Z., Wang, Z.G., Guo, L., and Fei, J. (2007). Reduced anxiety and depression-like behaviors in mice lacking GABA transporter subtype 1. Neuropsychopharmacology *32*, 1531-1539.

Liu, R.C. (2006). Prospective contributions of transgenic mouse models to central auditory research. Brain Res *1091*, 217-223.

Lovera, J., and Kovner, B. (2012). Cognitive impairment in multiple sclerosis. Current neurology and neuroscience reports *12*, 618-627.

Lowry, C.A. (2002). Functional subsets of serotonergic neurones: implications for control of the hypothalamic-pituitary-adrenal axis. Journal of neuroendocrinology *14*, 911-923.

Lydiard, R.B. (2003). The role of GABA in anxiety disorders. J Clin Psychiatry *64 Suppl 3*, 21-27.

Maheras, K.J., and Gow, A. (2013). Increased anesthesia time using 2,2,2-tribromoethanol-chloral hydrate with low impact on mouse psychoacoustics. J Neurosci Methods *219*, 61-69.

Mahon, K., Burdick, K.E., and Szeszko, P.R. (2010). A role for white matter abnormalities in the pathophysiology of bipolar disorder. Neurosci Biobehav Rev *34*, 533-554.

Makous, J.C., and Middlebrooks, J.C. (1990). Two-dimensional sound localization by human listeners. J Acoust Soc Am *87*, 2188-2200.

Marmarou, C.R., Walker, S.A., Davis, C.L., and Povlishock, J.T. (2005). Quantitative analysis of the relationship between intra- axonal neurofilament compaction and impaired axonal transport following diffuse traumatic brain injury. J Neurotrauma *22*, 1066-1080.

Martin, R.J. (1997). Modes of action of anthelmintic drugs. Vet J *154*, 11-34.

Mathew, S.J., Mao, X., Coplan, J.D., Smith, E.L., Sackeim, H.A., Gorman, J.M., and Shungu, D.C. (2004). Dorsolateral prefrontal cortical pathology in generalized anxiety disorder: a proton magnetic resonance spectroscopic imaging study. Am J Psychiatry *161*, 1119-1121.

McAlpine, D., and Grothe, B. (2003). Sound localization and delay lines--do mammals fit the model? Trends Neurosci *26*, 347-350.

McAlpine, D., Jiang, D., and Palmer, A.R. (2001). A neural code for low-frequency sound localization in mammals. Nat Neurosci *4*, 396-401.

McCarthy, K.M., Skare, I.B., Stankewich, M.C., Furuse, M., Tsukita, S., Rogers, R.A., Lynch, R.D., and Schneeberger, E.E. (1996). Occludin is a functional component of the tight junction. J Cell Sci *109 (Pt 9)*, 2287-2298.

McCullumsmith, R.E., Gupta, D., Beneyto, M., Kreger, E., Haroutunian, V., Davis, K.L., and Meador-Woodruff, J.H. (2007). Expression of transcripts for myelination-related genes in the anterior cingulate cortex in schizophrenia. Schizophr Res *90*, 15-27.

McGee, T.J., Ozdamar, O., and Kraus, N. (1983). Auditory middle latency responses in the guinea pig. Am J Otolaryngol *4*, 116-122.

McIntyre, C.C., Richardson, A.G., and Grill, W.M. (2002). Modeling the excitability of mammalian nerve fibers: influence of afterpotentials on the recovery cycle. J Neurophysiol *87*, 995-1006.

McNair, D.M., and Timmons, E.H. (1977). Effects of Aspiculuris tetraptera dn Syphacia obvelata on exploratory behavior of an inbred mouse strain. Lab Anim Sci *27*, 38-42.

McNamara, J.O. (1999). Emerging insights into the genesis of epilepsy. Nature *399*, A15-22.

Medana, I.M., and Esiri, M.M. (2003). Axonal damage: a key predictor of outcome in human CNS diseases. Brain *126*, 515-530.

Melillo, R., and Leisman, G. (2009). Autistic spectrum disorders as functional disconnection syndrome. Rev Neurosci *20*, 111-131.

Michaelson, M.D., Bieri, P.L., Mehler, M.F., Xu, H., Arezzo, J.C., Pollard, J.W., and Kessler, J.A. (1996). CSF-1 deficiency in mice results in abnormal brain development. Development *122*, 2661-2672.

Miller, C., and Racker, E. (1976). Fusion of phospholipid vesicles reconstituted with cytochrome c oxidase and mitochondrial hydrophobic protein. J Membr Biol *26*, 319-333.

Mills, A. (1958). On the minimum audible angle. Journal of Acoustical Socitey of America *30*, 237-246.

Moller, A.R. (1985). Origin of latency shift of cochlear nerve potentials with sound intensity. Hear Res *17*, 177-189.

Moller, A.R., and Jannetta, P.J. (1981). Compound action potentials recorded intracranially from the auditory nerve in man. Exp Neurol *74*, 862-874.

Moller, A.R., and Jannetta, P.J. (1982). Auditory evoked potentials recorded intracranially from the brain stem in man. Exp Neurol *78*, 144-157.

Moller, A.R., and Jannetta, P.J. (1983a). Interpretation of brainstem auditory evoked potentials: results from intracranial recordings in humans. Scandinavian audiology *12*, 125-133.

Moller, A.R., and Jannetta, P.J. (1983b). Monitoring auditory functions during cranial nerve microvascular decompression operations by direct recording from the eighth nerve. J Neurosurg *59*, 493-499.

Moller, A.R., Jannetta, P.J., and Sekhar, L.N. (1988). Contributions from the auditory nerve to the brain-stem auditory evoked potentials (BAEPs): results of intracranial recording in man. Electroencephalogr Clin Neurophysiol *71*, 198-211.

Moller, A.R., Jho, H.D., Yokota, M., and Jannetta, P.J. (1995). Contribution from crossed and uncrossed brainstem structures to the brainstem auditory evoked potentials: a study in humans. Laryngoscope *105*, 596-605.

Moore, J.K. (1987). The human auditory brain stem as a generator of auditory evoked potentials. Hear Res *29*, 33-43.

Morest, D.K. (1968). The growth of synaptic endings in the mammalian brain: a study of the calyces of the trapezoid body. Zeitschrift fur Anatomie und Entwicklungsgeschichte *127*, 201-220.

Morgane, P.J., Galler, J.R., and Mokler, D.J. (2005). A review of systems and networks of the limbic forebrain/limbic midbrain. Prog Neurobiol *75*, 143-160.

Morita, K., Furuse, M., Fujimoto, K., and Tsukita, S. (1999a). Claudin multigene family encoding four-transmembrane domain protein components of tight junction strands. Proc Natl Acad Sci U S A *96*, 511-516.

Morita, K., Sasaki, H., Fujimoto, K., Furuse, M., and Tsukita, S. (1999b). Claudin-11/OSP-based tight junctions of myelin sheaths in brain and Sertoli cells in testis. J Cell Biol *145*, 579-588.

Morita, K., Sasaki, H., Furuse, M., and Tsukita, S. (1999c). Endothelial claudin: claudin-5/TMVCF constitutes tight junction strands in endothelial cells. J Cell Biol *147*, 185-194.

Moy, S.S., Nadler, J.J., Perez, A., Barbaro, R.P., Johns, J.M., Magnuson, T.R., Piven, J., and Crawley, J.N. (2004). Sociability and preference for social novelty in five inbred strains: an approach to assess autistic-like behavior in mice. Genes Brain Behav *3*, 287-302.

Moyaho, A., Eguibar, J.R., and Diaz, J.L. (1995). Induced grooming transitions and open field behaviour differ in high- and low-yawning sublines of Sprague-Dawley rats. Animal behaviour *50*, 61 - 72.

Moyaho, A., and Valencia, J. (2002). Grooming and yawning trace adjustment to unfamiliar environments in laboratory Sprague-Dawley rats (Rattus norvegicus). J Comp Psychol *116*, 263-269.

Mugnaini, E., and Schnapp, B. (1974). Possible role of zonula occludens of the myelin sheath in demyelinating conditions. Nature *251*, 725-727.

Nelson, W.J., and Fuchs, E. (2010). Cell-cell junctions : a subject collection from Cold Spring Harbor perspectives in biology (Cold Spring Harbor, N.Y.: Cold Spring Harbor Laboratory Press).

Nemeroff, C.B. (2003). The role of GABA in the pathophysiology and treatment of anxiety disorders. Psychopharmacol Bull *37*, 133-146.

Nestler, E.J., and Hyman, S.E. (2010). Animal models of neuropsychiatric disorders. Nat Neurosci *13*, 1161-1169.

Nicol, T., Vernon-Roberts, B., and Quantock, D.C. (1965). Protective effect of oestrogens against the toxic decomposition products of tribromoethanol. Nature *208*, 1098-1099.

Niedermeyer, E., and Lopes da Silva, F.H. (2005). Electroencephalography : basic principles, clinical applications, and related fields, 5th edn (Philadelphia: Lippincott Williams & Wilkins).

Norris, M.L., and Turner, W.D. (1983). An evaluation of tribromoethanol (TBE) as an anaesthetic agent in the Mongolian gerbil (Meriones unguiculatus). Laboratory animals *17*, 324-329.

Nuechterlein, K.H., and Dawson, M.E. (1984). Information processing and attentional functioning in the developmental course of schizophrenic disorders. Schizophr Bull *10*, 160-203.

Nutt, D.J., and Malizia, A.L. (2001). New insights into the role of the GABA(A)-benzodiazepine receptor in psychiatric disorder. Br J Psychiatry *179*, 390-396.

O'Donnell, P., and Grace, A.A. (1995). Synaptic interactions among excitatory afferents to nucleus accumbens neurons: hippocampal gating of prefrontal cortical input. J Neurosci *15*, 3622-3639.

O'Mara, S. (2005). The subiculum: what it does, what it might do, and what neuroanatomy has yet to tell us. J Anat *207*, 271-282.

O'Mara, S.M., Commins, S., Anderson, M., and Gigg, J. (2001). The subiculum: a review of form, physiology and function. Prog Neurobiol *64*, 129-155.

Oertel, D. (1983). Synaptic responses and electrical properties of cells in brain slices of the mouse anteroventral cochlear nucleus. J Neurosci *3*, 2043-2053.

Oertel, D., Wu, S.H., Garb, M.W., and Dizack, C. (1990). Morphology and physiology of cells in slice preparations of the posteroventral cochlear nucleus of mice. J Comp Neurol *295*, 136-154.

Ohlemiller, K.K. (2006). Contributions of mouse models to understanding of age- and noise-related hearing loss. Brain Res *1091*, 89-102.

Ollo, C., and Schwartz, I.R. (1979). The superior olivary complex in C57BL/6 mice. The American journal of anatomy *155*, 349-373.

Omlin, F.X., Webster, H.D., Palkovits, C.G., and Cohen, S.R. (1982). Immunocytochemical localization of basic protein in major dense line regions of central and peripheral myelin. J Cell Biol *95*, 242-248.

Papahadjopoulos, D., Vail, W.J., Newton, C., Nir, S., Jacobson, K., Poste, G., and Lazo, R. (1977). Studies on membrane fusion. III. The role of calcium-induced phase changes. Biochim Biophys Acta *465*, 579-598.

Papaioannou, V.E., and Fox, J.G. (1993). Efficacy of tribromoethanol anesthesia in mice. Lab Anim Sci *43*, 189-192.

Perrault, G., Morel, E., Zivkovic, B., and Sanger, D.J. (1992). Activity of litoxetine and other serotonin uptake inhibitors in the tail suspension test in mice. Pharmacol Biochem Behav *42*, 45-47.

Peters, A. (1961). A radial component of central myelin sheaths. The Journal of biophysical and biochemical cytology *11*, 733-735.

Peters, A. (1964). Further Observations on the Structure of Myelin Sheaths in the Central Nervous System. J Cell Biol *20*, 281-296.

Petersen, R.C., and Kokmen, E. (1989). Cognitive and psychiatric abnormalities in multiple sclerosis. Mayo Clin Proc *64*, 657-663.

Petters, R.M., and Sommer, J.R. (2000). Transgenic animals as models for human disease. Transgenic Res *9*, 347-351; discussion 345-346.

Philip, N.S., Carpenter, L.L., Tyrka, A.R., and Price, L.H. (2010). Pharmacologic approaches to treatment resistant depression: a re-examination for the modern era. Expert Opin Pharmacother *11*, 709-722.

Phillips, D.P. (2008). A perceptual architecture for sound lateralization in man. Hear Res *238*, 124-132.

Phillips, D.P., and Brugge, J.F. (1985). Progress in neurophysiology of sound localization. Annu Rev Psychol *36*, 245-274.

Phillips, D.P., Carmichael, M.E., and Hall, S.E. (2006). Interaction in the perceptual processing of interaural time and level differences. Hear Res *211*, 96-102.

Phillips, D.P., and Hall, S.E. (2005). Psychophysical evidence for adaptation of central auditory processors for interaural differences in time and level. Hear Res *202*, 188-199.

Phillips, D.P., Quinlan, C.K., and Dingle, R.N. (2012). Stability of central binaural sound localization mechanisms in mammals, and the Heffner hypothesis. Neurosci Biobehav Rev *36*, 889-900.

Phillips, D.P., Vigneault-MacLean, B.K., Boehnke, S.E., and Hall, S.E. (2003). Acoustic hemifields in the spatial release from masking of speech by noise. J Am Acad Audiol *14*, 518-524.

Phillips, T.J., Belknap, J.K., Hitzemann, R.J., Buck, K.J., Cunningham, C.L., and Crabbe, J.C. (2002). Harnessing the mouse to unravel the genetics of human disease. Genes Brain Behav *1*, 14-26.

Pikkarainen, M., Ronkko, S., Savander, V., Insausti, R., and Pitkanen, A. (1999). Projections from the lateral, basal, and accessory basal nuclei of the amygdala to the hippocampal formation in rat. J Comp Neurol *403*, 229-260.

Pollack, M.H., Jensen, J.E., Simon, N.M., Kaufman, R.E., and Renshaw, P.F. (2008). High-field MRS study of GABA, glutamate and glutamine in social anxiety disorder: response to treatment with levetiracetam. Prog Neuropsychopharmacol Biol Psychiatry *32*, 739-743.

Porsolt, R.D., Bertin, A., and Jalfre, M. (1977). Behavioral despair in mice: a primary screening test for antidepressants. Arch Int Pharmacodyn Ther *229*, 327-336.

Porsolt, R.D., Chermat, R., Lenegre, A., Avril, I., Janvier, S., and Steru, L. (1987). Use of the automated tail suspension test for the primary screening of psychotropic agents. Arch Int Pharmacodyn Ther *288*, 11-30.

Pothion, S., Bizot, J.C., Trovero, F., and Belzung, C. (2004). Strain differences in sucrose preference and in the consequences of unpredictable chronic mild stress. Behav Brain Res *155*, 135-146.

Pratt, J.A. (1992). The neuroanatomical basis of anxiety. Pharmacol Ther *55*, 149-181.

Privat, A., Jacque, C., Bourre, J.M., Dupouey, P., and Baumann, N. (1979). Absence of the major dense line in myelin of the mutant mouse "shiverer". Neurosci Lett *12*, 107-112.

Ramos, A. (2008). Animal models of anxiety: do I need multiple tests? Trends Pharmacol Sci *29*, 493-498.

Rayleigh, L. (1907). On our perception of sound direction. Philosophical Magazine *13*, 214 - 232.

Readhead, C., Schneider, A., Griffiths, I., and Nave, K.A. (1994). Premature arrest of myelin formation in transgenic mice with increased proteolipid protein gene dosage. Neuron *12*, 583-595.

Reale, E., Luciano, L., and Spitznas, M. (1975). Zonulae occludentes of the myelin lamellae in the nerve fibre layer of the retina and in the optic nerve of the rabbit: a demonstration by the freeze-fracture method. J Neurocytol *4*, 131-140.

Reid, A.T., and Evans, A.C. (2013). Structural networks in Alzheimer's disease. Eur Neuropsychopharmacol *23*, 63-77.

Reiman, E.M. (1997). The application of positron emission tomography to the study of normal and pathologic emotions. J Clin Psychiatry *58 Suppl 16*, 4-12.

Rosenbluth, J. (1980). Central myelin in the mouse mutant shiverer. J Comp Neurol *194*, 639-648.

Saitou, M., Fujimoto, K., Doi, Y., Itoh, M., Fujimoto, T., Furuse, M., Takano, H., Noda, T., and Tsukita, S. (1998). Occludin-deficient embryonic stem cells can differentiate into polarized epithelial cells bearing tight junctions. J Cell Biol *141*, 397-408.

Sanacora, G., Mason, G.F., Rothman, D.L., Behar, K.L., Hyder, F., Petroff, O.A., Berman, R.M., Charney, D.S., and Krystal, J.H. (1999). Reduced cortical gamma-aminobutyric acid levels in depressed patients determined by proton magnetic resonance spectroscopy. Arch Gen Psychiatry *56*, 1043-1047.

Santarelli, R., Arslan, E., Carraro, L., Conti, G., Capello, M., and Plourde, G. (2003). Effects of isoflurane on the auditory brainstem responses and middle latency responses of rats. Acta Otolaryngol *123*, 176-181.

Sarter, M., Bruno, J.P., and Parikh, V. (2007). Abnormal neurotransmitter release underlying behavioral and cognitive disorders: toward concepts of dynamic and function-specific dysregulation. Neuropsychopharmacology *32*, 1452-1461.

Schiffer, R.B., and Babigian, H.M. (1984). Behavioral disorders in multiple sclerosis, temporal lobe epilepsy, and amyotrophic lateral sclerosis. An epidemiologic study. Arch Neurol *41*, 1067-1069.

Schnupp, J., Nelken, I., and King, A. (2011). Auditory neuroscience : making sense of sound (Cambridge, Mass. ; London: MIT Press).

Schubert, D.S., and Foliart, R.H. (1993). Increased depression in multiple sclerosis patients. A meta-analysis. Psychosomatics *34*, 124-130.

Seidl, A.H., Rubel, E.W., and Harris, D.M. (2010). Mechanisms for adjusting interaural time differences to achieve binaural coincidence detection. J Neurosci *30*, 70-80.

Shan, Q., Haddrill, J.L., and Lynch, J.W. (2001). Ivermectin, an unconventional agonist of the glycine receptor chloride channel. J Biol Chem *276*, 12556-12564.

Shaw, N.A. (1986). The effect of pentobarbital on the auditory evoked response in the brainstem of the rat. Neuropharmacology *25*, 63-69.

Sherif, F., and Oreland, L. (1995). Effect of the GABA-transaminase inhibitor vigabatrin on exploratory behaviour in socially isolated rats. Behav Brain Res *72*, 135-140.

Shin, K., Fogg, V.C., and Margolis, B. (2006). Tight junctions and cell polarity. Annual review of cell and developmental biology *22*, 207-235.

Shore, D.I., Hall, S.E., and Klein, R.M. (1998). Auditory saltation: a new measure for an old illusion. J Acoust Soc Am *103*, 3730-3733.

Simon, D.B., Lu, Y., Choate, K.A., Velazquez, H., Al-Sabban, E., Praga, M., Casari, G., Bettinelli, A., Colussi, G., Rodriguez-Soriano, J.*, et al.* (1999). Paracellin-1, a renal tight junction protein required for paracellular Mg2+ resorption. Science *285*, 103-106.

Sisson, D.F., and Siegel, J. (1989). Chloral hydrate anesthesia: EEG power spectrum analysis and effects on VEPs in the rat. Neurotoxicol Teratol *11*, 51-56.

Smith, D.I., and Kraus, N. (1987). Effects of chloral hydrate, pentobarbital, ketamine, and curare on the auditory middle latency response. Am J Otolaryngol *8*, 241-248.

Smith, P.H., Joris, P.X., Carney, L.H., and Yin, T.C. (1991). Projections of physiologically characterized globular bushy cell axons from the cochlear nucleus of the cat. J Comp Neurol *304*, 387-407.

Smith, P.H., Joris, P.X., and Yin, T.C. (1993). Projections of physiologically characterized spherical bushy cell axons from the cochlear nucleus of the cat: evidence for delay lines to the medial superior olive. J Comp Neurol *331*, 245-260.

Sohmer, H., and Feinmesser, M. (1967). Cochlear action potentials recorded from the external ear in man. Ann Otol Rhinol Laryngol *76*, 427-435.

Spoendlin, H., and Schrott, A. (1989). Analysis of the human auditory nerve. Hear Res *43*, 25-38.

Spoendlin, H., and Schrott, A. (1990). Quantitative evaluation of the human cochlear nerve. Acta Otolaryngol Suppl *470*, 61-69; discussion 69-70.

Staehelin, L.A. (1974). Structure and function of intercellular junctions. International review of cytology *39*, 191-283.

Stahl, S.M. (1998). Basic psychopharmacology of antidepressants, part 1: Antidepressants have seven distinct mechanisms of action. J Clin Psychiatry *59 Suppl 4*, 5-14.

Stahl, S.M., Grady, M.M., Moret, C., and Briley, M. (2005). SNRIs: their pharmacology, clinical efficacy, and tolerability in comparison with other classes of antidepressants. CNS Spectr *10*, 732-747.

Stanley, J.A. (2002). In vivo magnetic resonance spectroscopy and its application to neuropsychiatric disorders. Can J Psychiatry *47*, 315-326.

Steru, L., Chermat, R., Thierry, B., Mico, J.A., Lenegre, A., Steru, M., Simon, P., and Porsolt, R.D. (1987). The automated Tail Suspension Test: a computerized device which differentiates psychotropic drugs. Prog Neuropsychopharmacol Biol Psychiatry *11*, 659-671.

Steru, L., Chermat, R., Thierry, B., and Simon, P. (1985). The tail suspension test: a new method for screening antidepressants in mice. Psychopharmacology (Berl) *85*, 367-370.

Stotler, W.A. (1953). An experimental study of the cells and connections of the superior olivary complex of the cat. J Comp Neurol *98*, 401-431.

Strain, G.M., and Tedford, B.L. (1993). Flash and pattern reversal visual evoked potentials in C57BL/6J and B6CBAF1/J mice. Brain Res Bull *32*, 57-63.

Stronks, H.C., Aarts, M.C., and Klis, S.F. (2010). Effects of isoflurane on auditory evoked potentials in the cochlea and brainstem of guinea pigs. Hear Res *260*, 20-29.

Sudhof, T.C. (2004). The synaptic vesicle cycle. Annu Rev Neurosci *27*, 509-547.

Sur, C., Wafford, K.A., Reynolds, D.S., Hadingham, K.L., Bromidge, F., Macaulay, A., Collinson, N., O'Meara, G., Howell, O., Newman, R.*, et al.* (2001). Loss of the major GABA(A) receptor subtype in the brain is not lethal in mice. J Neurosci *21*, 3409-3418.

Tabira, T., Cullen, M.J., Reier, P.J., and Webster, H.d. (1978). An experimental analysis of interlamellar tight junctions in amphibian and mammalian C.N.S. myelin. J Neurocytol *7*, 489-503.

Tamura, A., Kitano, Y., Hata, M., Katsuno, T., Moriwaki, K., Sasaki, H., Hayashi, H., Suzuki, Y., Noda, T., Furuse, M.*, et al.* (2008). Megaintestine in claudin-15-deficient mice. Gastroenterology *134*, 523-534.

Tanaka, H., Ma, J., Tanaka, K.F., Takao, K., Komada, M., Tanda, K., Suzuki, A., Ishibashi, T., Baba, H., Isa, T.*, et al.* (2009). Mice with altered myelin proteolipid protein gene expression display cognitive deficits accompanied by abnormal neuron-glia interactions and decreased conduction velocities. J Neurosci *29*, 8363-8371.

Tarin, D., and Sturdee, A. (1972). Surgical anaesthesia of mice: evaluation of tribromo-ethanol, ether, halothane and methoxyflurane and development of a reliable technique. Laboratory animals *6*, 79-84.

Tasaki, I. (1952). Conduction of impulses in the myelinated nerve fiber. Cold Spring Harb Symp Quant Biol *17*, 37-41.

Tetzlaff, W. (1978). The development of a zonula occludens in peripheral myelin of the chick embryo. A freeze-fracture study. Cell Tissue Res *189*, 187-201.

Tkachev, D., Mimmack, M.L., Ryan, M.M., Wayland, M., Freeman, T., Jones, P.B., Starkey, M., Webster, M.J., Yolken, R.H., and Bahn, S. (2003). Oligodendrocyte dysfunction in schizophrenia and bipolar disorder. Lancet *362*, 798-805.

Tolbert, L.P., and Morest, D.K. (1982). The neuronal architecture of the anteroventral cochlear nucleus of the cat in the region of the cochlear nerve root: electron microscopy. Neuroscience *7*, 3053-3067.

van der Staay, F.J., Arndt, S.S., and Nordquist, R.E. (2009). Evaluation of animal models of neurobehavioral disorders. Behav Brain Funct *5*, 11.

Van Itallie, C.M., and Anderson, J.M. (2004). The molecular physiology of tight junction pores. Physiology (Bethesda) *19*, 331-338.

Van Itallie, C.M., and Anderson, J.M. (2006). Claudins and epithelial paracellular transport. Annu Rev Physiol *68*, 403-429.

van Looij, M.A., Liem, S.S., van der Burg, H., van der Wees, J., De Zeeuw, C.I., and van Zanten, B.G. (2004). Impact of conventional anesthesia on auditory brainstem responses in mice. Hear Res *193*, 75-82.

Voikar, V., Vasar, E., and Rauvala, H. (2004). Behavioral alterations induced by repeated testing in C57BL/6J and 129S2/Sv mice: implications for phenotyping screens. Genes Brain Behav *3*, 27-38.

W.H.O. (2001). The world health report 2001 - Mental Health: New Understanding, New Hope. 19 - 45.

Waxman, S.G., and Bennett, M.V. (1972). Relative conduction velocities of small myelinated and non-myelinated fibres in the central nervous system. Nature: New biology *238*, 217-219.

Waxman, S.G., Kocsis, J.D., and Stys, P.K. (1995). The axon : structure, function, and pathophysiology (New York: Oxford University Press).

Weber, S., Hoffmann, K., Jeck, N., Saar, K., Boeswald, M., Kuwertz-Broeking, E., Meij, II, Knoers, N.V., Cochat, P., Sulakova, T.*, et al.* (2000). Familial hypomagnesaemia with hypercalciuria and nephrocalcinosis maps to chromosome 3q27 and is associated with mutations in the PCLN-1 gene. Eur J Hum Genet *8*, 414-422.

Webster, D.B., and Trune, D.R. (1982). Cochlear nuclear complex of mice. The American journal of anatomy *163*, 103-130.

Webster, R.A. (2001). Neurotransmitters, drugs, and brain function (Chichester ; New York: Wiley).

Weiss, J., and Zimmermann, F. (1999). Tribromoethanol (Avertin) as an anaesthetic in mice. Laboratory animals *33*, 192-193.

Wengenack, T.M., Jack, C.R., Jr., Garwood, M., and Poduslo, J.F. (2008). MR microimaging of amyloid plaques in Alzheimer's disease transgenic mice. Eur J Nucl Med Mol Imaging *35 Suppl 1*, S82-88.

Wilcox, E.R., Burton, Q.L., Naz, S., Riazuddin, S., Smith, T.N., Ploplis, B., Belyantseva, I., Ben-Yosef, T., Liburd, N.A., Morell, R.J.*, et al.* (2001). Mutations in the gene encoding tight junction claudin-14 cause autosomal recessive deafness DFNB29. Cell *104*, 165-172.

Williams, H.L., Tepas, D.I., and Morlock, H.C., Jr. (1962). Evoked responses to clicks and electroencephalographic stages of sleep in man. Science *138*, 685-686.

Willott, J.F. (2001). Handbook of mouse auditory research : from behavior to molecular biology (Boca Raton: CRC Press).

Witter, M.P., and Groenewegen, H.J. (1990). The subiculum: cytoarchitectonically a simple structure, but hodologically complex. Prog Brain Res *83*, 47-58.

Wong, V., and Gumbiner, B.M. (1997). A synthetic peptide corresponding to the extracellular domain of occludin perturbs the tight junction permeability barrier. J Cell Biol *136*, 399-409.

Wu, S.H., and Kelly, J.B. (1991). Physiological properties of neurons in the mouse superior olive: membrane characteristics and postsynaptic responses studied in vitro. J Neurophysiol *65*, 230-246.

Wu, S.H., and Kelly, J.B. (1992a). Binaural interaction in the lateral superior olive: time difference sensitivity studied in mouse brain slice. J Neurophysiol *68*, 1151-1159.

Wu, S.H., and Kelly, J.B. (1992b). Synaptic pharmacology of the superior olivary complex studied in mouse brain slice. J Neurosci *12*, 3084-3097.

Wu, S.H., and Kelly, J.B. (1993). Response of neurons in the lateral superior olive and medial nucleus of the trapezoid body to repetitive stimulation: intracellular and extracellular recordings from mouse brain slice. Hear Res *68*, 189-201.

Wu, S.H., and Oertel, D. (1984). Intracellular injection with horseradish peroxidase of physiologically characterized stellate and bushy cells in slices of mouse anteroventral cochlear nucleus. J Neurosci *4*, 1577-1588.

Wu, X., Peppi, M., Vengalil, M.J., Maheras, K.J., Southwood, C.M., Bradley, M., and Gow, A. (2012). Transgene-Mediated Rescue of Spermatogenesis in Cldn11-Null Mice. Biol Reprod.

Yonkers, K.A., Dyck, I.R., Warshaw, M., and Keller, M.B. (2000). Factors predicting the clinical course of generalised anxiety disorder. Br J Psychiatry *176*, 544-549.

Yoshida, C., and Takeichi, M. (1982). Teratocarcinoma cell adhesion: identification of a cell-surface protein involved in calcium-dependent cell aggregation. Cell *28*, 217-224.

Yoshida-Noro, C., Suzuki, N., and Takeichi, M. (1984). Molecular nature of the calcium-dependent cell-cell adhesion system in mouse teratocarcinoma and embryonic cells studied with a monoclonal antibody. Dev Biol *101*, 19-27.

Yost, W.A. (1974). Discriminations of interaural phase differences. J Acoust Soc Am *55*, 1299-1303.

Yost, W.A. (1981). Lateral position of sinusoids presented with interaural intensive and temporal differences. The Journal of the Acoustical Socitey of America, 397-409.

Zeller, W., Meier, G., Burki, K., and Panoussis, B. (1998). Adverse effects of tribromoethanol as used in the production of transgenic mice. Laboratory animals *32*, 407-413.

Zheng, Q.Y., Johnson, K.R., and Erway, L.C. (1999). Assessment of hearing in 80 inbred strains of mice by ABR threshold analyses. Hear Res *130*, 94-107.

ABSTRACT

NEURAL CIRCUITRY DEFICITS ASSOCIATED WITH MYELIN DYSFUNCTION

by

KATHLEEN JUNE MAHERAS

August 2015

Advisor: Dr Alexander Gow

Major: Molecular Biology and Genetics

Degree: Doctor of Philosophy

In the current study, we have generated mutant mice that lack Claudin 11 (Cldn11) tight junctions in CNS myelin sheaths. In myelin sheaths, Cldn11 forms tight junctions located along the outer and inner edges of the membrane spiral, preventing ions and small molecules from entering the intramyelinic space. The function of Cldn11 tight junctions is to improve the passive properties of the myelin membrane, by increasing membrane resistance and reducing capacitance, thereby improving the speed of saltatory conduction. In the absence of Cldn11, conduction velocity is slowed, most dramatically in small diameter myelinated fibers, somewhat analogous to reducing myelin thickness. Notably, the absence of Cldn11 is without degenerative myelin pathology, enabling direct study on the impact of dysfunctional myelin on neural processing.

Undoubtedly, slowed conduction velocity along myelinated axons increases temporal dispersion and, consequently, degrades information transfer between neural circuits. Herein, this dissertation work explores the impact of dysfunctional myelin on neural processing in the conserved integration circuit of the auditory

brainstem. We find that dysfunctional myelin alters neural processing, generating an inability to lateralize sound sources on the azimuth plane. Extrapolating this information to higher order circuitry within the cortex, we find that dysfunctional myelin generates a disconnection between brain regions, manifesting in behavioral abnormalities and alteration in neurotransmitter levels.

Together, these data demonstrate that non-degenerative changes in myelin membrane passive properties can lead to neurochemistry changes that perturb behavior/perception. Second, they have important implications for the etiology of behavioral disorders in general, and more specifically for the behavioral components of hypomyelinating and demyelinating diseases like multiple sclerosis.

AUTOBIOGRAPHICAL STATEMENT

EDUCATION

Doctor of Philosophy — Wayne State University, Detroit, MI 48201
2009 – present — Molecular Medicine & Genetics

Bachelors of Science — Alma College, Alma, MI 48801
2009 — Double Major: Biochemistry & Biology

PROFESSIONAL MEMBERSHIPS

Society for Neuroscience	2010 – present
American Association for the Advancement of Science	2011 – present
Association for Research in Otolaryngology	2013 – present
International Society for Neurochemistry	2015 – present

PUBLICATIONS

Maheras, K.J., Brigolin, C., Pindola, K., Gow, A., Wolf, B. (2015). Hearing deficits associated with biotinidase deficiency. *In preparation.*

Denninger, A.R., Breglio, A., **Maheras, K.J.**, LeDuc, G., Cristiglio, V., Demé, B., Gow, A., and Kirschner, D.A. (2015). Claudin-11 tight junctions in myelin provide a barrier to diffusion and lack adhesive properties. *Under Review.*

Maheras, K.J., and Gow, A. (2013). Increased anesthesia time using 2,2,2-tribromoethanol-chloral hydrate with low impact on mouse psychoacoustics. J Neurosci Methods *219*, 61-69.

Wu, X., Peppi, M., Vengalil, M.J., **Maheras, K.J.**, Southwood, C.M., Bradley, M., and Gow, A. (2012). Transgene-Mediated Rescue of Spermatogenesis in Cldn11-Null Mice. Biol Reprod.

GRANTS

Carls Foundation — 2013 – 2015

FELLOWSHIPS AND AWARDS

Graduate Research Assistantship	2009 – 2010, 2011 – 2015
Thomas C. Rumble Fellowship	2010 – 2011